PHYSICAL ACOUSTICS SUMMER SCHOOL

30 Sep 2001
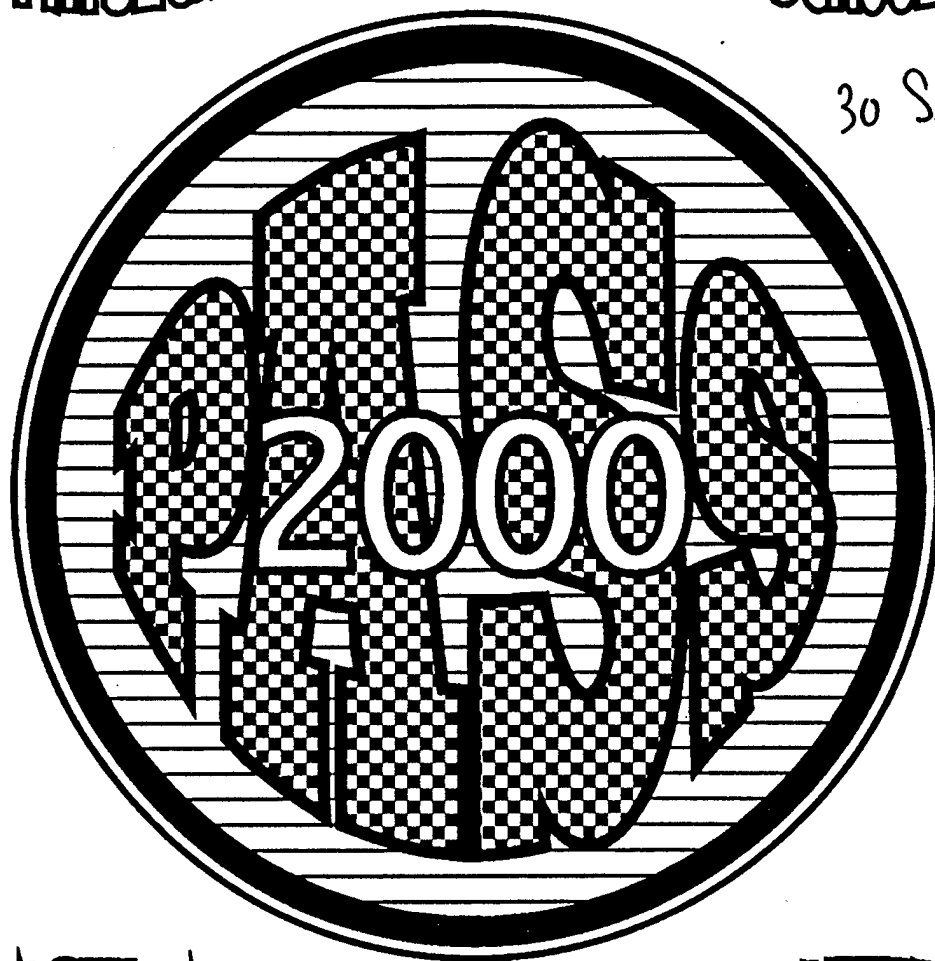
2000

ASILOMAR CONFERENCE CENTER

VOLUME III

BACKGROUND MATERIALS

20011030 085

2000 PHYSICAL ACOUSTICS SUMMER SCHOOL (PASS 00)

VOLUME III: BACKGROUND MATERIALS

TABLE OF CONTENTS

INTRODUCTION TO PHYSICAL ACOUSTICS

Anthony A. Atchley
Graduate Program in Acoustics
The Pennsylvania State University

ABSTRACT

It is rare that an abstract begins with a disclaimer. However, in this case, this author feels that is necessary.

Disclaimer: Considering the purview of acoustics as being any process involving the generation, propagation, reception, and perception of mechanical waves and vibrations, it would be arrogant indeed to suppose that this lecturer could give an adequate introduction of the whole of physical acoustics in a lecture of any duration (finite or otherwise). Limiting the scope to an introduction to PASS 2000 might be only slightly less foolhardy. Abraham Lincoln is reported to have said "better to remain silent and be thought a fool then to speak out and remove all doubt." There will be little doubt after this lecture.

Hereto, the author wishes to revise the title and presumed content of his lecture to be

CONNECTIONS IN PHYSICAL ACOUSTICS
An Introduction to PASS 2000

ABSTRACT

The purpose of this lecture is to introduce the lectures that comprise PASS 2000. An attempt will be made to set the context of the Summer School by connecting the various lecture topics by following the progression of a theme beginning with the "acoustics of a single atom" and leading the wave equation. An important vehicle for this journey will be the development of the well-known, lumped parameter description of acoustics processes. Lumped parameter models provide intuitive solution methods for many complex problems and serve as the starting point for computational acoustics. As this introductory lecture progresses through topics, the sophistication of the "lumps" will increase to accommodate the requisite physics. Eventually, the lumped parameters will lead to a continuum description of wave phenomena.

As an example of connections in physical acoustics, consider the following chain of thought. The principles of conservation of momentum and conservation of mass lead to the lumped parameter concepts of inertness and compliance. These impedance elements can be used to construct a discrete model of lossless acoustic systems. Consider a sequence of impedance elements that mimics a homogeneous, isotropic acoustic system. Such a lumped parameter model allows one to determine, among other things, the resonance frequencies of the system. An inhomogeneous system can be modeled by modifying the values of some of the initially identical impedance elements. If one makes the changes, it will be found that the resonance frequencies change. One branch of this discussion can be followed to high amplitude standing waves in anharmonic resonators, to be discussed in Dr. Garrett's **Nonlinear Acoustics** lecture. It is also recognized that if one knows the resonance frequencies of a system, one can determine something about the internal structure of the system. This concept is the principle underlying **Resonant Ultrasound Spectroscopy** (Dr. Migliori). Applying conservation of energy allows us to modify our lumped parameters to include dissipation mechanisms. Introducing dissipation into a system necessarily leads to fluctuations, leading to Dr. Gabrielson's lecture on **Noise and Sensors**. The improved lumped parameter model can be used to describe propagation in small diameter tubes, a simplistic version of **Porous Media**, the topic of Dr. Sabatier's lecture. Dr. Keolian will discuss **Thermoacoustics**, which can be described by modifying the model used to describe porous media to include the effects of a temperature gradient. Temperature gradients are often encountered in the **Atmospheric and Meteorological Acoustics**, as explained by Dr. Gilbert. (Yes, I realize that the connection has been strained at this point, but I have until June to work on it.) As sound propagates through the inhomogeneous atmosphere, the wavefronts are distorted. One type of wavefront distortion is focusing, which as Dr. Crum will describe has practical **Medical Applications of Acoustics**. Medical acoustics usually rely upon high amplitude sound fields to achieve the desired result. Such high amplitudes can induce other phenomena, such as **Sonoluminescence**, Dr. Matula's topic. Dr. Denardo's **Acoustics Demonstrations** will also illustrate the connections of some of the subfields of Physical Acoustics.

The intent of this lecture is bring the students to a point of embarkation for the subsequent lectures. Because of its nature, there are no references or background material unique to this talk. Reviewing the materials suggested by other lecturers will offer an excellent foundation.

NONLINEAR ACOUSTICS

Steven L. Garrett
United Technologies Corporation Professor of Acoustics
Graduate Program in Acoustics - Applied Research Laboratory
The Pennsylvania State University

ABSTRACT and SYLLABUS

Linearization of the hydrodynamic mass and momentum conservation equations, along with the equation-of-state for a fluid, lead to the familiar linear, homogeneous wave equation that has acoustic solutions which obey the Principle of Superposition. Those waves are stable, and even in the presence of dissipative effects, waves that are initially monochromatic remain monochromatic and maintain their shape, even if they decrease in amplitude over time and distance. When two or more such waves interact, they interfere only in their region of interaction to produce a resultant waveform that is the sum of their independent waveforms. Once the waves propagate beyond their region of mutual interaction, they possess no residual evidence of their former interaction nor have they produced any new disturbances that propagate out of the interaction region.

Those amplitude-independent results of "linear acoustics" can account for most of the phenomena associated with the propagation, attenuation, scattering, reflection, transmission, refraction, production, and reception of sound wave encountered in gases, liquids and solid under "ordinary" conditions in the laboratory and beyond. Such linear waves can introduce scale factors involving length and time, such as wavelength, period, and exponential attenuation distances, but they never introduce scale factors that are related to the amplitudes of the waves. If terms higher than linear order in the hydrodynamic and constitutive equations are retained, then new and interesting amplitude-dependent acoustic solutions occur.

The purpose of these lectures will be to introduce some of these nonlinear acoustic phenomena in simple one-dimensional systems and to provide several complementary perspectives for their understanding and analysis. Topics to be covered include the production of harmonic distortion and the formation of repeated shock waves; the dissipation of acoustic energy by repeated shock waves and their non-exponential attenuation in space; nonlinear wave

mixing and parametric end-fire arrays; large-amplitude standing waves; acoustic forces and torques on solid objects in intense standing wave fields; and the effects of occlusion by such objects on the frequency spectrum of resonators.

The lectures will start with an analysis of shallow water (gravity) waves to introduce the two effects that cause waves to modify the "local" value of their own propagation speed. The effects of convection (self-Doppler shift) and the change in the "thermodynamic sound speed" are shown to accumulate with distance and result in the formation of shock waves. A characteristic discontinuity length, known as the shock inception distance, will be introduced as a scale that determines the importance of these nonlinear effects. The results for distortion of water waves will be generalized to ideal gases and other fluids through definition of the Grüneisen constant, a dimensionless distortion parameter. The Goldberg Number, the dimensionless ratio of the shock inception distance to the exponential length characteristic of the thermoviscous and relaxational attenuation in linear acoustics, will determine whether dissipation or nonlinear effects will dominate a wave's propagation away from its source.

Armed with these conceptual tools, the "life cycle" of an acoustic wave that is dominated by nonlinear effects will be investigated. We start by revisiting the early stages of nonlinear waveform distortion to apply an iterative scheme for calculation of second harmonic distortion that was first employed by Earnshaw [Phil. Trans. Roy. Soc. (London) **150**, 133 (1860)]. Calculation of the accumulation of second and higher-harmonic distortion products will employ Fourier analysis using a simple graphical representation of the progressive distortion [Hargrove, J. Acoust. Soc. Am. **32**, 511 (1960)].

Once the repeated (sawtooth) shock wave is fully developed, its attenuation and subsequent decay back to the realm of linear acoustics will be shown to be independent of the magnitude of the dissipative transport coefficients (shear viscosity, thermal conductivity, and internal molecular relaxation effects). The Rankine-Hugoniot relations can be used to show that the non-exponential decay rate is caused by the large gradients in pressure, temperature, sound speed, and particle velocity across the shock front, but a more intuitive graphical technique will be employed. Thickness of a shock front is related to the dissipative coefficients and, in an ideal gas, the thickness is shown to be on the order of ten times the mean-free-paths of the gas molecules.

A general expression for one-dimensional nonlinear propagation will be derived from the hydrodynamics through a perturbation expansion. That approach results in a linear wave equation for the second-order density variations "driven" by a geometrically-resonant inhomogeneous term for non-dispersive media that depends on quadratic combinations of the first-order (linear) sound field variables.

$$\frac{\partial^2 \rho_2}{\partial t^2} - \frac{\partial^2 \rho_2}{\partial x^2} = \frac{c_0^2}{\rho_0}\left[1 + \frac{\rho_0}{c_0}\left(\frac{\partial c}{\partial \rho}\right)_s\right]\nabla^2 \rho_1^2$$

In addition to the generation of harmonic distortion, this view provides a means of understanding nonlinear wave mixing effects. One such effect, called a "parametric end-fire array," will be described as an application of nonlinear acoustics that can produce highly directional, low-frequency sound source from an aperture which is significantly smaller than the wavelength of the radiated low-frequency sound. That effect will be generalized to media that support two wave modes with different sound speeds, such as longitudinal and transverse sound waves in solids [Rollins, *et al.,* Phys. Rev. **136A**, 597 (1964)], leading to resonant, nonlinear conversion from one mode to the other.

The lecture will conclude with a consideration of non-zero time-averaged nonlinear acoustic effects in resonators driven at large amplitudes. First, the connection between the distortion of progressive plane waves and shock waves in resonators [Coppens and Atchley, *Encyclopedia of Acoustics*, Chapter 22 (Wiley, 1997)] will be established. The presence of solid objects within the resonator and/or variations in resonator cross-sectional area will be described as a means of suppressing shock waves in thermoacoustic devices [Gaitan and Atchley, J. Acoust. Soc. Am. **93**, 2489 (1993)] and tailoring waveforms for use in resonant acoustic compressors [Ilinski, *et al.,* J. Acoust. Soc. Am **104**(5), 2664 (1998)].

Analysis of the time-averaged forces and torques on solid objects will be based on Bernoulli's Law which produces time-averaged pressures that are proportional to the square of the acoustic flow velocity,

$$\frac{\partial \phi}{\partial t} + \frac{1}{2}v^2 + h = const.$$

where ϕ is the velocity potential and h is the enthalpy density. Consideration of classical effects, such as the appearance of striation bands in cork dust observed in Kundt Tubes and measurement of the torque on a Rayleigh Disk [Rayleigh, *Theory of Sound*, Vol. II], will be followed by a more modern application: acoustic levitation for containerless processing. The connection between the frequency shift caused by the levitated obstacle and the acoustic forces and torques will be made through the Boltzmann-Ehrenfest Adiabatic Principle [Putterman, *et al.*, J. Acoust. Soc. Am. **85**(1), 68 (1988); Greenspan, J. Acoust. Soc. Am. **27**, 34 (1955)]. Levitation instability and superstability will be explained through the interaction of the resonator de-tuning, produced by the position of the levitated object, and the de-phasing of the force/position relation due to the finite time for the growth or decay of the resonant sound field [Rudnick and Barmatz, J. Acoust. Soc. Am. **87**(1), 81 (1990); Barmatz and Garrett, US Pat. No. 4,577,266 (Sept. 27, 1988)].

It is hoped that the study of these nonlinear acoustical phenomena will not only introduce some interesting acoustical phenomena, but will also provide the student with a better understanding of the foundations of linear acoustics and its limitations.

PHYSICAL ACOUSTICS

Principles and Methods

Edited by WARREN P. MASON

BELL TELEPHONE LABORATORIES, INCORPORATED,
MURRAY HILL, NEW JERSEY

VOLUME II—PART B

*Properties of Polymers
and Nonlinear Acoustics*

1965

7

—12—

Use of Light Diffraction in Measuring the Parameter of Nonlinearity of Liquids and the Photoelastic Constants of Solids

L. E. HARGROVE† and K. ACHYUTHAN‡

Department of Physics, Michigan State University, East Lansing, Michigan

I. Nonlinearity of Liquids

A. INTRODUCTION

It is now well known that the ultrasonic waveform changes from its initial (say, sinusoidal) form as the wave propagates in a liquid. The bases for this "distortion" are that the exact equation of motion is nonlinear and in general the equation of state of the medium is nonlinear. In the usual "infinitesimal-amplitude acoustics" the simplifying assumptions give results which do not predict this change in waveform.

† *Present address:* Bell Telephone Laboratories, Incorporated, Murray Hill, New Jersey.

‡ *Present address:* Research and Development Organization, Ministry of Defense, New Delhi, India.

Ultrasonic waves of sufficiently high frequency and large amplitude that the nonlinear effects become appreciable are commonly referred to as "finite-amplitude" waves.

Optical methods have been important in investigating finite-amplitude distortion. The various optical methods for determining the ultrasonic waveform are rather sensitive to small changes in waveform and have the advantage that the measuring device, light, does not disturb the sound field. From determinations of the waveform the nonlinearity (i.e., the nonlinear equation of state) of the liquid may be determined.

In this section we shall review the distortion of the waveform arising from nonlinearity, the diffraction of light by distorted ultrasonic waves, and the various optical methods for determining the ultrasonic waveform and the parameter B/A describing the nonlinearity of the equation of state.

B. DISTORTION OF THE ULTRASONIC WAVEFORM ARISING FROM NONLINEARITY

1. Phenomenological Description of Finite-Amplitude Distortion

The change in waveform of an ultrasonic wave as it progresses in a liquid results from the fact that the propagation velocity differs from point to point within one wavelength. The regions of compression travel faster than the regions of rarefaction with the result that the waveform approaches a saw-tooth form. A wave of any amplitude might be considered "finite" in a dissipationless medium, as the change in waveform accumulates as the wave progresses and appreciable distortion would develop at sufficiently large distances. With the action of some dissipative process, an initially small-amplitude wave may be dominated by absorption and the nonlinear effects never become noticeable. However, even in moderately dissipative liquids, significant distortions of the waveform occur at smaller amplitudes than were previously expected.

An important consequence of the distortion of the waveform is a change in rate of dissipation of the wave as it progresses. Qualitatively, at least, one may think of this change as resulting from change in the frequency spectrum of the wave (transfer of energy to higher harmonics) and greater rates of dissipation of the higher frequency components.

With these general remarks about finite-amplitude distortion we shall turn to a more detailed treatment of the problem, with emphasis on the relationships between the waveform and the equation of state.

2. Propagation of Plane, Finite-Amplitude Waves in a Dissipationless Nondispersive Medium

Here we shall give only some details of the theory which are useful in understanding the optical methods for determining nonlinearity of

liquids. The interested reader should consult the many papers in the literature.[1]

Consider an initially sinusoidal finite-amplitude wave as indicated in Fig. 1a. The *phase* velocity for such a wave is not constant; it is approximated by

$$c = c_0 + Ku \qquad (1)$$

where c_0 is the velocity of sound for infinitesimal amplitudes, K is a constant depending on the equation of state, and u is the particle
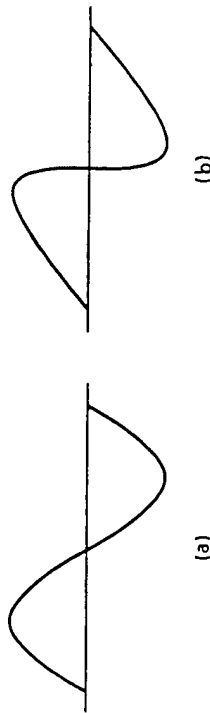
FIG. 1. (a) Initially sinusoidal waveform, and (b) the waveform after having propagated to the discontinuity distance in a dissipationless medium.

velocity. Equation (1) neglects terms in u^2 and higher. From Eq. (1) it is seen that to each value of u in the instantaneous waveform there corresponds a different propagation velocity. The points on the wave characterized by greater particle velocity tend to overtake points having lesser values, while the whole (changing) waveform propagates with a velocity c_0. Neglecting effects of dissipation, an initially sinusoidal wave propagating according to Eq. (1) attains the waveform indicated in Fig. 1b when it has traveled a distance (the so-called "discontinuity distance")

$$L = \frac{c_0^2}{KU\omega^*} \qquad (2)$$

where U is the peak particle velocity of the initially sinusoidal wave, and ω^* is the circular frequency. In the presence of dissipation, the infinite slope at the center of the waveform shown in Fig. 1b is never attained, as dissipative effects act more strongly in this region of greater velocity and temperature gradients.

The phase velocity of a plane acoustic wave is given by the local values of $(dp/d\rho)$ and the particle velocity,

$$c = (dp/d\rho)^{1/2} + u \qquad (3)$$

where p is the pressure and ρ is the density. The relationship expressed in Eq. (3) is independent of the equation of state. By assuming an

[1] See the papers by Zarembo and Krasilnikov (1959), Keck and Beyer (1960), and Blackstock (1962) and the references given therein.

equation of state to second-order terms

$$p = p_0 + A\left(\frac{\rho-\rho_0}{\rho_0}\right) + \frac{B}{2}\left(\frac{\rho-\rho_0}{\rho_0}\right)^2 \quad (4)$$

one obtains

$$c = c_0 + [1+(B/2A)]u \quad (5)$$

to terms of first-order in u. An alternative form for the equation of state is

$$p/p_0 = (\rho/\rho_0)^\gamma \quad (6)$$

for which the phase velocity is

$$c = c_0 + [(\gamma+1)/2]u \quad (7)$$

to the same degree of approximation. For a perfect gas, γ is the ratio of specific heats. For a liquid γ must be regarded as an empirical constant equivalent to $(B/A)+1$. From Eqs. (5) and (7) we see that the constant K used in Eqs. (1) and (2) is

$$K = 1 + (B/2A) = (\gamma+1)/2. \quad (8)$$

Here, we shall use the form involving the ratio B/A and call this ratio the "parameter of nonlinearity," following the terminology of Beyer (1960). Beyer (1960) has tabulated some values of this parameter.

The terms in u^2 which were neglected in Eq. (5) are usually small. The linear and quadratic terms become comparable for $u \sim 10^4$ sec/cm if $B/A \sim 10$, $c_0 \sim 10^5$ cm/sec, and $\rho_0 \sim 1$ gm/cm³. These conditions correspond to a peak acoustic pressure amplitude $P \sim 10^3$ atm in a typical liquid. If the quadratic terms must be included in Eq. (5) then the second-order equation of state, Eq. (4), would probably be inadequate. The errors committed in using the

$$p = \rho_0 c_0 u \quad (9)$$

relationship are comparable to those involved in a quadratic equation of state and a linear dependence of phase velocity on the particle velocity, in the absence of dissipation.

Experimental determination of the nonlinearity parameter is usually made from the change in ultrasonic waveform with distance and/or initial pressure amplitude. The second harmonic component is most commonly used in such determinations. Theoretical relationships between the ultrasonic waveform and the nonlinearity parameter are required. Thus the problem is twofold: experimental determination of the ultrasonic waveform² and the relationship between change in waveform and the nonlinearity parameter B/A.

² Optical methods for studying the ultrasonic waveform have been reviewed by Hiedemann and Zankel (1961).

Fubini-Ghiron (1935), Hargrove (1960), and Keck and Beyer (1960) have independently obtained a useful expression for the finite-amplitude ultrasonic waveform in a dissipationless medium. Using the equation of state (4), the phase velocity expressed by Eq. (5), and the relationship in Eq. (9), the acoustic pressure may be written

$$P = P_1(0) \sum_{n=1}^{\infty} b_n \sin[2\pi n(f^*t - x/\lambda^*)] \quad (10)$$

where the b_n's are given by

$$b_n = \frac{2}{nk} J_n(nk) \quad (11)$$

and

$$k = x/L \quad (12)$$

is the ratio of propagation distance to discontinuity distance. $P_n(k)$ is a notation for the amplitude of the nth harmonic at reduced distance k. These results are valid for

$$0 \leq k \leq 1 \quad \text{or} \quad 0 \leq x \leq L. \quad (13)$$

Beyond the distance L, without dissipation, Eq. (5) predicts that the initially sinusoidal wave becomes multivalued, a condition which has no physical significance. This dissipationless theory has been useful under limited conditions where the effects of dissipation may be neglected or simply accounted for, and as a starting point for theories which account for the dissipation. Figure 2 shows the first four Fourier coefficients calculated from Eq. (11).

3. Propagation of Plane, Finite-Amplitude Waves in a Dissipative, Nondispersive Medium

Several theories have been proposed for predicting the harmonic structure of finite-amplitude ultrasonic waves in dissipative liquids. Where dissipation must be accounted for, the problem of determining the nonlinearity parameter becomes that of choosing a theory and adjusting the nonlinearity parameter to get the best fit to experimental data, usually measurements of the second harmonic component. Some of the theories will be briefly reviewed here.

Keck and Beyer (1960) used a perturbation analysis and obtained (written here in terms of the acoustic pressure)

$$|b_n'| = e^{-n\alpha_1 x} \sum_{s=0}^{\infty} \frac{(-1)^s [nN(1-e^{-2\alpha_1 x})]^{n-1+2s}}{s!(n+s)!} C_{ns} \quad (14)$$

where

$$N = \frac{K\omega^* P_1(0)}{4\alpha_0 \rho_0 c_0^3} = (4\alpha_0 L)^{-1} \quad (15)$$

as in the dissipationless theory and $B_n(k), C_n(k),...$ involve the frequency dependence of the amplitude absorption coefficient, the initial pressure amplitude $P_1(0)$, and sums of Bessel functions of argument (nk) as was the case in the dissipationless theory. The terms $B_n(k)$, etc. are also functions of the product ($\alpha_0 L$), as are the b'_n's given by Keck and Beyer, Eqs. (14) and (15).

Cook (1962) developed an iterative procedure for calculating the waveform of plane, finite-amplitude ultrasonic waves in a dissipative medium. The method consists of considering distortion of the incident

(a) DISSIPATIONLESS THEORY ($\alpha_0 = 0$)
(b) LESTER ($\alpha_0 L = 0.185$)
(c) KECK & BEYER ($\alpha_0 L = 0.185$)
(d) COOK ($\alpha_0 L = 0.185$)
(e) LESTER ($\alpha_0 L = 0.370$)

FIG. 3. Calculated second harmonic Fourier coefficients b_2 versus reduced distance k (Lester, 1961; Cook, 1962).

waveform over a small spatial interval according to dissipationless theory, approximately correcting for absorption of the various frequency components, and repeating the procedure for the new waveform in the next spatial interval. This procedure allows calculations of the waveform into the region beyond the discontinuity distance L.

Figure 3 shows the second harmonic Fourier coefficient b_2 versus k as given by Eq. (11) (dissipationless theory), Eq. (16) (Lester), Eq. (14) (Keck and Beyer), and by Cook. It may be noted at this point that the various theoretical predictions of the second harmonic component shown in Fig. 3 are not significantly different for small values of k and ($\alpha_0 L$). In this region determination of the nonlinearity parameter B/A may be made from experimental determinations of the second harmonic component, using the considerably simpler dissipationless theory. In the following discussions greater emphasis will be placed on methods for obtaining the ultrasonic waveform and lesser emphasis

and α_0 is the infinitesimal-amplitude absorption coefficient at the fundamental frequency. The coefficients $C_{n,s}$ are polynomials in $R = \exp(-2\alpha_0 x)$, the first few of which are given by Keck and Beyer (1960). Equations (14) and (15) are displayed here to demonstrate how the parameters K and L (containing the nonlinearity parameter) enter into the theory. It should be noted that in the absence of dissipation ($\alpha_0 = 0$) all the $C_{n,s}$ are unity and Eq. (14) reduces to Eq. (11).
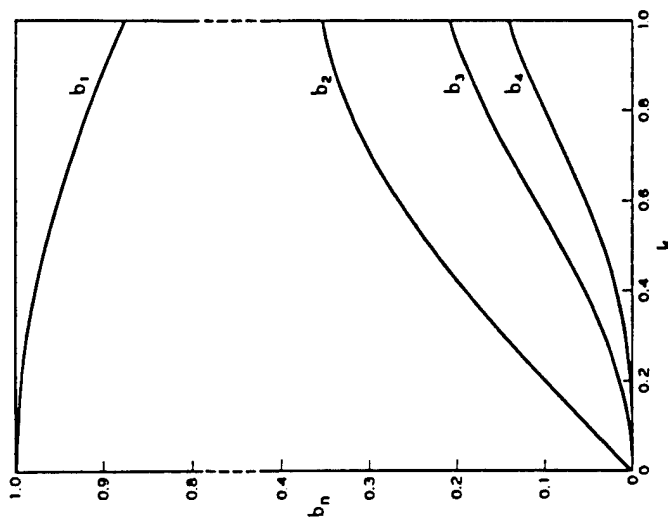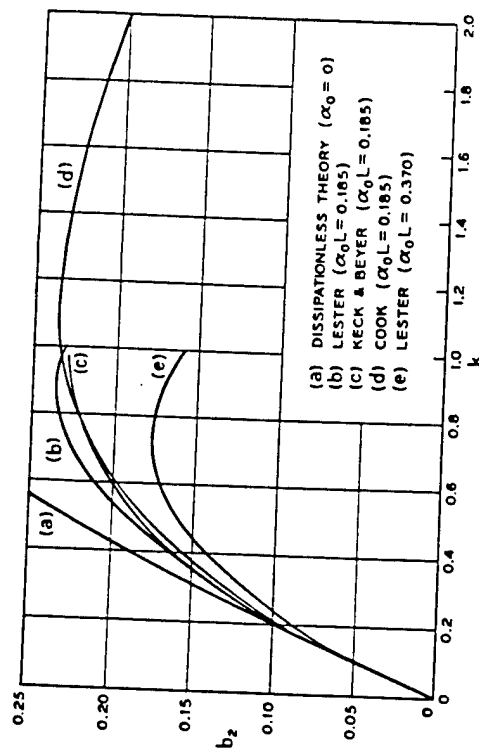

FIG. 2. Calculated Fourier coefficients b_n versus reduced distance k for an initially sinusoidal plane progressive wave of finite amplitude in a dissipationless medium (Hargrove, 1960).

Lester (1961) used the dissipationless theory [Eq. (11)] as a basis for calculation of the harmonic components of a plane, finite-amplitude ultrasonic wave in a dissipative fluid. The results are expressed in the form

$$P_n(k) = A_n(k) - B_n(k) + C_n(k) - ... + ... \quad (16)$$

where

$$A_n(k) = b_n P_1(0) \quad (17)$$

Barnes, J. M., Mayer, W. G., and Hiedemann, E. A. (1959). *J. Opt. Soc. Am.* **48**, 663.

Bergmann, L., and Fues, E. (1936). *Naturwissenschaften* **24**, 492.

Beyer, R. T. (1960). *J. Acoust. Soc. Am.* **32**, 719.

Bhagavantam, S. (1942). *Proc. Indian Acad. Sci.* **A16**, 359.

Bhagavantam, S. (1949). *Acta Cryst.* **2**, 21.

Bhagavantam, S. (1952). *Acta Cryst.* **5**, 591.

Bhagavantam, S., and Suryanarayana, D. (1947). *Proc. Indian Acad. Sci.* **A26**, 97.

Bhagavantam, S., and Suryanarayana, D. (1948). *Nature* **162**, 740.

Bhagavantam, S., and Suryanarayana, D. (1949). *Acta Cryst.* **2**, 26.

Blackstock, D. T. (1962). *J. Acoust. Soc. Am.* **34**, 9.

Breazeale, M. A. (1961). *J. Acoust. Soc. Am.* **33**, 700.

Breazeale, M. A., Hargrove, L. E., and Hiedemann, E. A. (1960). *U.S. Navy J. Underwater Acoust.* **10**, 381.

Burstein, E., and Smith, P. L. (1948). *Phys. Rev.* **74**, 229, 1880.

Burstein, E., Smith, P. L., and Henvis, B. (1948). *Phys. Rev.* **73**, 1262.

Carpenter, R. O'B. (1951). Ph.D. Thesis, Harvard Univ., Cambridge, Massachusetts.

Coker, E. G., and Filon, L. N. G. (1931). "Treatise on Photoelasticity." Cambridge Univ. Press, London and New York.

Colbert, H. M., and Zankel, K. L. (1961). *J. Acoust. Soc. Am.* **33**, 1679. Abstract.

Cook, B. D. (1960). *J. Acoust. Soc. Am.* **32**, 336.

Cook, B. D. (1961). *J. Acoust. Soc. Am.* **33**, 832. Abstract.

Cook, B. D. (1962). *J. Acoust. Soc. Am.* **34**, 941.

Cook, B. D., and Hiedemann, E. A. (1961). *J. Acoust. Soc. Am.* **33**, 945.

Eppendahl, R. (1920). *Ann. Physik* **61**, 591.

Extermann, R., and Wannier, G. (1930). *Helv. Phys. Acta* **9**, 520.

Fykman, M. F. J. (1895). *Rec. trav. chim.* **14**, 177.

Fubini-Ghiron, E. (1935). *Alta Frequenza* **4**, 530.

Fumi, F. G. (1952). *Nuovo cimento* **9**, 184.

Galt, J. K. (1948). *Phys. Rev.* **73**, 1460.

Gates, H. F., and Hiedemann, E. A. (1956). *J. Acoust. Soc. Am.* **28**, 1222.

Gibson, R. E., and Kincaid, R. F. (1938). *J. Am. Chem. Soc.* **60**, 511.

Govansow, R. W., and Adams, L. H. (1933). *J. Franklin Inst.* **216**, 475.

Hagelberg, M. P. (1961). Ph.D. Thesis, Michigan State Univ.

Hargrove, I. E. (1960). *J. Acoust. Soc. Am.* **32**, 511.

Hargrove, L. E., Zankel, K. L., and Hiedemann, E. A. (1959). *J. Acoust. Soc. Am.* **31**, 1366.

Hiedemann, E. (1938). *Z. Physik* **108**, 592.

Hiedemann, E., and Hoesch, K. H. (1935a). *Naturwissenschaften* **23**, 511.

Hiedemann, E., and Hoesch, K. H. (1935b). *Naturwissenschaften* **23**, 577.

Hiedemann, E., and Hoesch, K. H. (1935c). *Naturwissenschaften* **23**, 705.

Hiedemann, E., and Hoesch, K. H. (1935d). *Z. Physik* **96**, 268.

Hiedemann, E., and Hoesch, K. H. (1935e). *Z. Physik* **96**, 273.

Hiedemann, E., and Hoesch, K. H. (1936). *Naturwissenschaften* **24**, 60.

Hiedemann, E. A., and Zankel, K. L. (1961). *Acustica* **11**, 213.

Jahn, H. A. (1949). *Acta Cryst.* **2**, 30.

Keck, W., and Beyer, R. T. (1960). *Phys. Fluids* **3**, 346.

Klein, W. R. (1962). M.S. Thesis, Michigan State Univ.

Krasilinikov, V. A., Shklovskaya-Kordi, V. V., and Zarembo, L. K. (1957). *J. Acoust. Soc. Am.* **29**, 642.

Lester, W. W. (1961). *J. Acoust. Soc. Am.* **33**, 1196.

Lester, W. W., and Hiedemann, E. A. (1962). *J. Acoust. Soc. Am.* **34**, 265.

Lorentz, H. (1880). *Ann. Physik* **9**, 641.

Lorenz, L. (1880). *Ann. Physik* **11**, 70.

12. Use of Light Diffraction

Melngailis, J., Maradudin, A. A., and Seeger, A. (1963). *Phys. Rev.* **131**, 1972.

Mikhailov, I. G., and Shutilov, V. A. (1957). *Soviet Phys.-Acoust.* (*English Transl.*) **3**, 217.

Mikhailov, I. G., and Shutilov, V. A. (1958). *Soviet Phys.-Acoust.* (*English Transl.*) **4**, 174.

Mueller, H. (1938). *Z. Krist.* **99**, 122.

Narasimhamurty, T. S., and Ziauddin, M. (1961). *J. Opt. Soc. Am.* **51**, 574.

Neumann, F. E. (1841). *Abhandl. Kön. Acad. Wiss. Berlin*, Pt. II, pp. 1–254.

Pockels, F. (1889). *Ann. Physik* **37**, 144, 372.

Pockels, F. (1906). "Lehrbuch der Krystalloptik." Teubner, Leipzig and Berlin.

Ramachandran, G. N. (1947). *Proc. Indian Acad. Sci.* **A25**, 208.

Ramachandran, G. N. (1950). *Proc. Indian Acad. Sci.* **A32**, 171.

Ramachandran, G. N., and Chandrasekhavan, V. (1951). *Proc. Indian Acad. Sci.* **A33**, 199.

Raman, C. V., and Nath, N. S. (1935). *Proc. Indian Acad. Sci.* **A2**, 406.

Raman, C. V., and Nath, N. S. (1936). *Proc. Indian Acad. Sci.* **A3**, 75.

Ramaseshan, S. (1954). *Proc. Indian Acad. Sci.* **A40**, 184.

Schaefer, C., and Bergmann, L. (1934). *Naturwissenschaften* **22**, 685.

Schaefer, C., and Bergmann, L. (1935). *Naturwissenschaften* **23**, 799.

Schaefer, C., and Dransfeld, K. (1953). *Z. Naturforsch.* **8a**, 90.

Schaefer, C., and Nassenstein, H. (1953). *Z. Naturforsch.* **8a**, 90.

Shutilov, V. A. (1959). *Soviet Phys.-Acoust.* (*English Transl.*) **5**, 230.

Vedam, K. (1950). *Proc. Indian Acad. Sci.* **A31**, 450.

Vedam, K. (1951). *Proc. Indian Acad. Sci.* **A32**, 161.

Vedam, K., and Ramachandran, G. N. (1951). *Proc. Indian Acad. Sci.* **A34**, 250.

Waxler, R. M., and Napolitano, A. (1957). *J. Research Natl. Bur. Standards* **59**, 121.

Willard, G. W. (1949). *J. Acoust. Soc. Am.* **21**, 101.

Zankel, K. L., and Hiedemann, E. A. (1958a). *Naturwissenschaften* **45**, 157.

Zankel, K. L., and Hiedemann, E. A. (1958b). *Naturwissenschaften* **45**, 329.

Zankel, K. L., and Hiedemann, E. A. (1958c). *J. Acoust. Soc. Am.* **30**, 582.

Zankel, K. L., and Hiedemann, E. A. (1959). *J. Acoust. Soc. Am.* **31**, 44.

Zarembo, L. K., and Krasilinikov, V. A. (1959). *Soviet Phys.-Usp.* (*English Transl.*) **2**, 580.

References

Achynthan, K., and Breazeale, M. A. (1961a). *J. Opt. Soc. Am.* **51**, 914.

Achyuthan, K., and Breazeale, M. A. (1961b). *J. Acoust. Soc. Am.* **33**, 1673. Abstract.

Adler, L., and Hiedemann, E. A. (1962). *J. Acoust. Soc. Am.* **34**, 410.

Bachem, C., Hiedemann, E., and Asbach, H. R. (1934). *Z. Physik* **87**, 734.

Bansigir, K. G., and Iyengar, K. S. (1958). *Proc. Phys. Soc.* (*London*) **B71**, 225.

Nonlinear acoustics and its applications: A historical perspective.

Leif Bjørnø
Department of Industrial Acoustics
Technical University of Denmark
Building 425
DK-2800 Lyngby, Denmark
prof.lb@get2net.dk

SUMMARY

The most important contributions to nonlinear acoustics since Euler's formulation of his equations of motion in 1755 and until 1960 are reviewed briefly in this paper. The review includes the works by Lagrange (1760), Poisson (1808), Stokes (1848), Earnshaw (1860), Riemann (1860), Rankine (1870), Hugoniot (1889), Rayleigh (1910), Taylor (1910), Fay (1931), Fubini (1935), Thuras, Jenkins & O'Neil (1935), Burgers' (1948), Hopf (1950) and Cole (1951), and Beyer (1960). The development in the mathematical basis and in the understanding of the physics behind nonlinear acoustics will be emphasised and the potential applications of nonlinear acoustics will be discussed. The discussions have been restricted to nonlinear acoustics of fluids, and relations between nonlinear acoustics, as an important discipline of acoustics, and fluid mechanics are pointed out.

INTRODUCTION

While description and exploitation of acoustical phenomena can be traced more than 2000 years back in time, nonlinear acoustics is a 'rather new' discipline being only about 250 years old. In 1755 Euler [1] formulated the equation of continuity and the equation of momentum for the motion of fluids. His equations are:

$$D\rho/Dt + \rho \nabla \bullet u = 0 \qquad (1)$$

$$\rho(Du/Dt) + \nabla p = F \qquad (2)$$

If supplemented with an equation of state, the equation (1) and (2) may lead to the wave equation for lossless propagation of acoustical waves in a fluid. In (1) and (2), ρ and t denote the fluid density and the time, respectively, D/Dt is the material derivative, u and F denote the particle velocity vector and the external body force vector per unit volume, respectively, and p is the pressure. The nonlinearity of the equations is included in the convective part of the first term of (2).

In 1759 Euler, in spite of his interests in linear acoustics, developed an equation describing the propagation of plane, finite-amplitude waves in a lossless fluid. Paradoxically, this equation is expressed in a material coordinate system, today termed a Lagrange coordinate system, and it writes:

$$b^2(\partial^2\xi/\partial a^2) - \{1 + (\partial\xi/\partial a)^2\}(\partial^2\xi/\partial t^2) = 0 \qquad (3)$$

where a denotes the material coordinate and where b is the speed of sound in an isothermal gas obeying Boyle's Law, $p/p_0 = \rho/\rho_0$, where p_0 and ρ_0 denote the ambient pressure and density, respectively. Later on in 1765 Euler [I] corrected his equation to the form:

$$b^2(\partial^2\xi/\partial a^2) - \{1 + \partial\xi/\partial a\}^2(\partial^2\xi/\partial t^2) = 0 \qquad (4)$$

From Euler's remarks to this equation he was aware of the fact that if the nonlinear term was taken into account, the speed of propagation would exceed the isothermal velocity, b.

Lagrange [4] also studied waves of finite amplitudes, and in 1761 he obtained an equation of the form:

$$b^2(\partial^2\xi/\partial a^2) - \{1 + \partial\xi/\partial a\}(\partial^2\xi/\partial t^2) = 0 \qquad (5)$$

which, in spite of being incorrect, led Lagrange to an important second order solution of the form:

$$\xi = \varphi(a - bt) + \tfrac{1}{4}bt\{\varphi'(a - bt)\}^2 \qquad (6)$$

where φ is an arbitrary function. This solution he rewrote as:

$$\xi = \varphi\{a - (b + \tfrac{1}{4}u)t\} \qquad (7)$$

where u is the particle velocity and where $b + \tfrac{1}{4}u$ correctly was interpreted as the velocity of propagation (phase velocity) of the waves. However, Lagrange did not believe in his own result as he felt it would destroy the uniformity of the concept of sound velocity because the velocity would be dependent on the nature of the disturbance causing the acoustic signal. For Lagrange "the hypothesis of infinitely small disturbances was the only one acceptable in the theory of sound propagation".

In (1808) Poisson [5] worked with an equation of the type as (8), where η is a velocity potential related to the particle velocity u by $u = \partial\eta/\partial x$, for progressive waves of finite amplitudes.

$$b^2(\partial^2\eta/\partial x^2) - \partial^2\eta/\partial t^2 = 2(\partial\eta/\partial x)(\partial^2\eta/\partial x\partial t) + (\partial\eta/\partial x)^2(\partial^2\eta/\partial x^2) \qquad (8)$$

In (8), x denotes the spatial coordinate (in an Eulerian coordinate system). For one-dimensional, isothermal propagation of waves of finite amplitudes he found the exact solution:

13

$$\partial \eta / \partial x = f\{x - (b + \partial \eta / \partial x)t\} \qquad (9)$$

valid for waves travelling in the direction of increasing values of x. In order to obtain a full solution to his differential equation (8), Poisson found it necessary to couple the solution (9) to an auxiliary equation (10) being a reduced form of the wave equation for lossless propagation of waves in the positive x direction.

$$\partial \eta \partial t + b(\partial \eta / \partial x) + \frac{1}{2}\{\partial \eta / \partial x\}^2 = 0 \qquad (10)$$

During the years around 1848, when the revolutions spread like wildfire over Europe, a prosperity in activity took place in nonlinear acoustics. It is difficult to say if there were any relation between these two events, but at least both were characterised by the break through of new ideas. A discussion between Airy and Challis [6] about the existence of plane sound waves, inspired Stokes [7] to study the waveform distortion described by Poisson's solution (9) and (10). Stokes produced the first sketches showing the distortion of a finite-amplitude wave during its propagation, see figure 1.
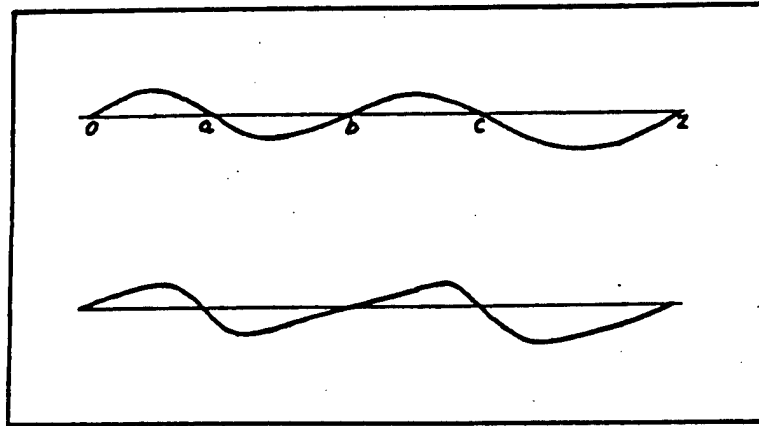
Figure 1. *Stokes' sketches showing the distortion course for a wave under influence of the particle velocity u in the wave.*

Figure 1 shows the original waveform in the upper trace, while the lower trace shows the waveform after some distance of propagation. A steepening of the wave takes place as parts of the wave with a positive particle velocity u travel faster than the parts of the wave having a negative particle velocity. Moreover, parts of the wave with a higher positive particle velocity travel faster than parts of the wave having a lower positive particle velocity. This distortion course would, as defined by Stokes, lead to the formation of a shock (by Stokes termed a "surface of discontinuity"). However Stokes was not able to explain the thermodynamical consequences of a shock formation, in spite of the fact that he was able to derive the conservation laws, conservation of mass and momentum, across the shock. A deeper knowledge about thermodynamics was the key to the solution, but thermodynamics was not developed far enough in 1848. Another 30 years had to elapse to solve the fundamental problems of thermodynamics.

A contribution by Airy [8] from the time around 1848 should also be mentioned. Using a successive approximation method he found a solution to the propagation and distortion of finite-amplitude waves originally generated by the sinusoidal motion of an infinitely rigid plane. He found the, now generally accepted, result that the amplitude of the 2nd harmonic is increasing linearly with propagation distance.

In 1860 the mathematician Earnshaw, who was going to influence the development in nonlinear acoustics over the next decades, brought the thermodynamics closer to the mathematical basis for wave propagation. The thermodynamic state of the fluid was represented by an expression (11) valid for any arbitrary relation between the density ρ and the pressure p.

$$\lambda = \int (c/\rho) \, d\rho \qquad (11)$$

where the boundaries for the integration is from ρ_o to ρ. In (11), c denotes the isentropic velocity of sound, which for an adiabatic gas with the relation: $p/p_o = (\rho/\rho_o)^\gamma$, where γ is the ratio between the specific heats C_p and C_v, leads to $c = \sqrt{\gamma p/\rho}$.

Introducing the adiabatic gas relation into (11) and inserting (11) into Euler's equations (1) and (2) lead to the symmetric expressions for one-dimensional wave propagation:

$$\partial\lambda/\partial t + u(\partial\lambda/\partial x) + c(\partial u/\partial x) = 0 \qquad (12)$$

$$\partial u/\partial t + u(\partial u/\partial x) + c(\partial\lambda/\partial x) = 0 \qquad (13)$$

where λ is expressed by:

$$\lambda = 2(c - c_o)/(\gamma - 1) \qquad (14)$$

From the equations (12) and (13) Earnshaw concluded that for finite-amplitude waves propagation in the positive x-direction, the phase velocity dx/dt of a point in the wave having the particle velocity u will be:

$$(dx/dt)_u = u + c \qquad (15)$$

and

$$(dx/dt)_u = u - c \qquad (16)$$

for the propagation in the negative x-direction.

Earnshaw, moreover, showed that for simple wave regions, i.e. regions where wave propagation takes place in one and the same direction, the thermodynamics and the kinematics will be connected in an unambiguous way through the expressions:

$$u = +\lambda \text{ and } u = -\lambda \qquad (17)$$

for positively and negatively propagating waves, respectively.

For waves propagating in the positive x-direction Earnshaw showed that the local velocity of sound c in (18) will be the sum of the infinitesimal velocity of sound c_o and a term expressing a

15

contribution from the local thermodynamical conditions representing the lack of linearity between p and ρ in the equation of state for the fluid. For an adiabatic gas relation (18) is obtained as:

$$c = c_0 + \tfrac{1}{2}(\gamma - 1)u \qquad (18)$$

If the expression (18) is inserted into the expression (15) for the phase velocity, the following expression is obtained:

$$(dx/dt)_{u=constant} = c_0 + \tfrac{1}{2}(\gamma + 1)u \qquad (19)$$

Expression (19) is important in the sense that it comprises two contributions to the distortion course for a finite-amplitude wave during its propagation. The thermodynamical contribution arising from the nonlinear pressure-density relation and expressed by $\tfrac{1}{2}(\gamma - 1)u$, and a convective contribution caused by the fact that a local disturbance propagating with the local velocity of sound c is convected with the local particle velocity u, thus leading to a phase velocity of c + u for a local phase in the wave. The key to the understanding of the change of the wave form in nonlinear acoustics is governed by a thermodynamical and by a kinematic contribution to the phase velocity of the wave.

Earnshaw also derived a nonlinear partial differential equation (20) describing the propagation of plane waves of finite amplitudes in an ideal gas:

$$\partial u/\partial t + c_0(\partial u/\partial x) + \tfrac{1}{2}(\gamma + 1)u\, \partial u/\partial x = 0 \qquad (20)$$

which has the same form as the auxiliary equation derived by Poisson.

Insertion of the pressure-density relation for an adiabatic gas into expression (17) leads to the relation (21):

$$p/p_0 = \{1 + \tfrac{1}{2}(\gamma - 1)u/c_0\}^{2\gamma/(\gamma - 1)} \qquad (21)$$

expressing the connection between p and u in a finite-amplitude wave. From (21) may be seen that the characteristic impedance p/u for a finite-amplitude wave propagating in the positive x-direction varies from point to point in the wave. Only for infinitesimal wave amplitudes (i.e. u ≪ c_0) expression (21) leads to the constant characteristic impedance of $\rho_0 c_0$.

Earnshaw, moreover, recognised that a formation of a shock was possible and that the propagation velocity for the shock would exceed the infinitesimal velocity of sound c_0. However, what happened after the formation of a shock was unknown to Earnshaw.

The German mathematician Riemann [10] contributed in 1860 with an important generalisation of the expression (19) for the phase velocity in a compound (i.e. non-simple) wave field, where propagation of waves takes place in the negative and in the positive x-direction simultaneously. He showed that in a compound wave field the two linear combinations R and S of λ and u given by:

$$R = \tfrac{1}{2}(\lambda + u) \quad \text{and} \quad S = \tfrac{1}{2}(\lambda - u) \qquad (22)$$

will propagate with the velocities:

$$(dx/dt)_{R=constant} = u + c, \text{ and } (dx/dt)_{S=constant} = u - c \quad (23)$$

which means that not u nor λ individually, but their linear combination will propagate with the velocities $u + c$ and $u - c$. Riemann's generalisation forms one of the most important contributions to the basis for the later development of the methods of characteristics used for solving hyperbolic partial differential equations. A simple wave field constitutes a special case of Riemann's generalised expression.

A deeper understanding of thermodynamics was necessary in order to be able to understand what happens after the formation of a shock. It was obvious to Riemann and Earnshaw that a discontinuity or a shock could develop. But this was not the only problem. If a discontinuity developed, reflection of waves would take place at the discontinuity and a simple wave field would be transformed into a compound wave field. The concept of dissipation was not understood in depth.

THE POST-CLASSICAL PERIOD 1860 – 1960

The years after 1870 brought the understanding of the shock a great step further. Rankine's [11] works dealing with steady shocks in an inviscid, but heat conducting gas, and some year later also Hugoniot's [12] studies of the necessary conditions for the existence of steady discontinuities led to the establishment of the Rankine-Hugoniot relations. These relations are conservation relations connecting the thermodynamic and the kinematic variables on the two sides of a shock, however without specifying the course of processes in the shock. For the steady flow through a shock at rest and with index 1 and index 2 denoting variables before and after the shock, respectively, the conservation equations may be written as:

$$\rho_1 v_1 = \rho_2 v_2 \qquad\qquad (24) \quad [\text{Conservation of mass}]$$

$$p_1 + \rho_1 v_1^2 = p_2 + \rho_2 v_2^2 \qquad (25) \quad [\text{Conservation of momentum}]$$

In (24) and (25), $v_1 = u_1 = U_s$ and $v_2 = u_2 - U_s$, where U_s is the constant propagation velocity of the shock, brought to rest by superposition of the velocity $-U_s$ to the flow field. The conservation equations (24) and (25) do not involve losses, and (25) expresses a form of Bernoulli's equation for a compressible fluid.

In order to avoid to end up with solutions like the ones obtained by Stokes and Riemann due to use of a lossless theory, Rankine and later on Hugoniot introduced an energy equation including losses. Their equation may be written as:

$$\tfrac{1}{2}v_1^2 + e_1 + p_1/\rho_1 = \tfrac{1}{2}v_2^2 + e_2 + p_2/\rho_2 \quad (26) \quad [\text{Conservation of energy}]$$

where e denotes the internal energy per unit mass. For a perfect gas (26) may be written as:

$$v_2^2 - v_1^2 = \{2\gamma/(\gamma - 1)\}\{p_1/\rho_1 - p_2/\rho_2\} \quad (27)$$

17

which connects the thermodynamic and the kinematic variables across the shock.

The equations (24), (25) and (27) form the basis for the later developed "theory of weak shocks" frequently used in nonlinear acoustics. If a weak shock is assumed, i.e. $u \ll c_0$, an expression for the velocity of propagation of the shock may be derived as:

$$U_s = c_0 + \tfrac{1}{4}(\gamma + 1)\{u_1 + u_2\} \qquad (28)$$

which shows that a weak shock will propagate with a velocity being the sum of the infinitesimal velocity of sound and the mean value of the particle velocities in the flow just before and just after the shock. It can, moreover, be shown [13] that the increase in entropy across a weak shock is small to the third order in the pressure variation across the shock. Thus, for shocks with an acoustical Mach number $u/c < 0.1$ the propagation may be considered as isentropic. This fact is useful when dealing with weak shocks in nonlinear acoustics.

Rankine made an attempt to describe the shock profile, i.e. the variation of the variables inside and across the shock. His basis was a heat conducting, but inviscid gas. The applicability of his solution is, however, limited to lower pressure jumps across the shock as dissipation by heat conduction alone is not sufficient to avoid the shock to become multi-valued, i.e. that several pressure values appear at the same position in the shock, as pointed out by Rayleigh [14].

Rayleigh was the first to introduce viscosity in the calculation of a shock profile. He calculated the thickness of a shock with a pressure jump of $p_2/p_1 = 5.67$ to be of a magnitude of around 30 μm, in reasonable agreement with measured results using modern optical techniques.

A break-through in the description of the shock profile, i.e. the variation in thermodynamic and kinematic quantities in a shock, was made by G.I. Taylor [15]. For weak shocks in a viscous, heat conducting gas Taylor found an analytical solution for the shock profile. For a shock travelling into a quiet gas the particle velocity variation through the shock may be written as:

$$u = \tfrac{1}{2}u_2 \{1 - \tanh [(\tfrac{1}{2}(\gamma + 1) u_2 X)/2\delta]\} \qquad (29)$$

where X denotes the moving coordinate in the shock with $X = 0$ at the centre of the shock, and δ describes the dissipation due to viscous and heat conducting effects in the shock, given by:

$$\delta = (\mu/\rho_0)\{4/3 + \mu_B/\mu + (\gamma - 1)Pr\} \qquad (30)$$

In (30) μ is the shear viscosity and μ_B the bulk viscosity, respectively, while Pr denotes the Prandtl number, $Pr = \mu c_p/\kappa$, where κ is the thermal conductivity. From (29) the thickness h of the shock expressed by the distance between the points of 10% and 90% change in the variables across the shock may be written as:

$$h = (2\delta \ln 9)/(\tfrac{1}{2}(\gamma + 1) u_2) \qquad (31)$$

Expression (31) shows clearly the nonlinear (the denominator) and the dissipative (the numerator) effects on the thickness of a shock. The nonlinear effects are steepening the shock, while the dissipative effect is flattening the shock. Strong shocks are thin, while weak shocks are

thick. As the dissipative effect is the winner, even strong shocks will after some distance of propagation end up as infinitesimal amplitude waves.

The contributions to our knowledge on the processes in a shock produced by Rayleigh and G.I. Taylor were very important, but they were limited to the variations in variables in the "step" formed by the shock. The dissipation process in a propagating finite-amplitude wave had not been studied in depth. A major contribution to nonlinear acoustics was published by Fay [16] in the, at that time new, Journal of the Acoustical Society of America. For a plane wave of finite amplitude, propagating in a viscous gas Fay sought the most stable waveform. The balance between nonlinear and dissipative effects in the wave was recognised by Fay, and the fact that the dissipation would be the final winner meant, that only a comparatively stable waveform was possible. Considering only the shear viscosity as a contributor to dissipation, Fay obtained the solution (32).

$$(p - p_0)/(\rho_0 c_0^2) = (2\alpha\, c_0)/(\tfrac{1}{2}(\gamma + 1)\,\omega)\, \Sigma_{n=1}\, (\sin n(\omega t - kx))/(\sinh n\alpha\, (x + x_0)) \quad (32)$$

where ω is the angular velocity and where $\alpha = 2\omega^2\,\mu/(3\rho_0 c_0^3)$. The quantity x_0 is a constant related to the discontinuity distance, i.e. the distance for the first formation of a discontinuity (a vertical tangent to the waveform) at a 0-crossing under lossless propagation conditions. n denotes the number of the harmonics formed.

An important contribution to nonlinear acoustics, which did not received so much attention as it deserved as it was published in the Italian language in a journal not directly related to acoustics, was written by Fubini [17]. He found an explicit solution to the wave equation for the propagation of plane waves of finite amplitudes in a lossless fluid. While using boundary conditions of the sinusoidal type he obtained for the particle velocity in the wave:

$$u = 2u_0\, \Sigma_{n=1}\, \{J_n(n\sigma)/n\sigma\} \sin (n(\omega t - kx)) \quad (33)$$

where $\sigma = \tfrac{1}{2}(\gamma + 1)\, u_0 kx/c_0$ is the dimensionless discontinuity distance. J_n is the Bessel function of order n, where n is the number of the harmonic formed during the propagation of the finite-amplitude wave out from the source. Due to the lossless conditions this solution is only valid to the discontinuity distance where $\sigma = 1$. While Fubini's solution is a nearfield solution, Fay's solution constitutes a farfield solution.

Some of the first experiments reported on finite-amplitude wave propagation in air, and produced by a sinusoidal vibrating piston source, were performed by Jenkins et al [18]. Their measurements were performed in a tube terminated at the end opposite to the piston source in order to avoid reflections and thus the establishment of a compound wave field. They measured the formation of the amplitude of the second harmonic for various fundamental frequencies with propagation distance from the source. They found a linear growth of the second harmonic amplitude with propagation distance, with frequency and with original source amplitude as predicted by Fubini (and earlier by Airy). They also reported the formation of a sum and difference frequency component when the source generated a two-frequency signal. The last finding is also fundamental to the operation of the later introduced parametric acoustic array by Westerveld [19]

A track of great importance in nonlinear acoustics was established based on Burgers' [20] equation. This equation (34):

$$\partial v/\partial t + v\,\partial v/\partial x = \zeta\,\partial^2 v/\partial x^2 \qquad (34)$$

was originally developed by Burgers to be used for describing certain characteristics of turbulence. However, the equation turned out to be very useful for description of propagation of finite-amplitude waves under simultaneous influence of nonlinearity and dissipation. Burgers' equation has formed a strong basis over the past for the study of nonlinear acoustical phenomena, and it is still one of the "key tools" for investigations of progressive finite-amplitude waves in materials of various physical qualities.

Some decisive contributions to the general applications of Burgers' equation in nonlinear acoustics were given by Mendousse [21], who worked out a form of the equation applicable for viscous fluid, while Lighthill [24] gave Burgers' equation a form making it applicable for waves in thermoviscous gases.

While Burgers' equation in its original form was most applicable for solving initial value problems, and as most problems encountered in relation to wave propagation are boundary value problems, an approximate of Burgers' equation, applicable for boundary value problems, may be written as:

$$\partial V/\partial\sigma - V\,\partial V/\partial y = \Gamma^{-1}\,(\partial^2 V/\partial y^2) \qquad (35)$$

where: $V = u/u_o$, $\sigma = \tfrac{1}{2}(\gamma + 1)\,u_o kx/c_o$ and $y = (\omega t - kx)$

$\Gamma = (\gamma + 1)\,u_o\rho_o/bk$, where $b = 4\mu/3 + \mu_B + \kappa\{1/c_v - 1/c_p\}$

Equation (35) is given in a dimensionless form and the propagation distance parameter $\sigma = x/\vartheta$, where ϑ is the discontinuity distance, $\vartheta = 2c_o^2/(\gamma + 1)\omega u_o$. The parameter Γ may be written as:

$$\Gamma = (\gamma + 1)\,\{u_o\rho_o/bk\} = (\gamma + 1)\,Re_a \qquad (36)$$

where Re_a is an acoustical Reynolds number, analogous to the hydrodynamic one. The quantity Γ describes the ratio of the influence of nonlinearity (including 'equation of state' and 'convective' nonlinearity contributions), represented by the nonlinear strength term $\tfrac{1}{2}(\gamma + 1)u_o/c_o$, to the influence of dissipation. Γ was first introduced by Gol'dberg [26] as a criterion such that shock formation is not likely to take place if $\Gamma < 1$.

A solution to Burgers' equation was produced by Hopf [22] and Cole [23], who used the similarity between Burgers' equation and the equation for heat conduction. Their analytical solution included the propagation of finite-amplitude, plane waves under influence of dissipation.

One of the major players in nonlinear acoustics in this century, professor R.T. Beyer, developed the so-called second-order nonlinearity ratio, B/A, describing the degree of material nonlinearity shown by gases, liquids and solids [25]. Starting from a relation between the pressure p, the density ρ and the entropy s for a fluid, a development in a Taylor series of the relation and assuming a nearly isentropic wave motion, which is justified by the fact that for pressure waves in a fluid the change in entropy is small to the third order in the pressure change, it is possible to write the following relation between p and ρ:

$$p - p_0 = A[(\rho - \rho_0)/\rho_0] + B[(\rho - \rho_0)/\rho_0]^2 + \dots \quad (37)$$

where only the first two terms in the Taylor series have been included. The quantities A and B now write:

$$A = \rho_0[\{\partial p/\partial \rho\}_s]_{\rho=\rho_0} = \rho_0 c_0^2, \text{ and } B = \rho_0^2[\{\partial^2 p/\partial \rho^2\}_s]_{\rho=\rho_0} \quad (38)$$

Based on thermodynamical relations, B/A may be written on the form:

$$B/A = 2\rho_0 c_0[\{\partial c/\partial p\}_T]_{\rho=\rho_0} + (2c_0 T\beta/c_p)[\{\partial c/\partial T\}_p]_{\rho=\rho_0} \quad (39)$$

where the most important contribution comes from the first term. The development of the expressions (38) and (39) gave rise to a substantial increase world-wide in the study of the acoustical nonlinearity of materials and to relate the nonlinear acoustical qualities to the molecular structures of materials.

CONCLUSIONS

Nearly 250 years have passed since the first significant contribution to nonlinear acoustics was made. However, a fast, nearly explosive, development in nonlinear acoustics has taken place over the last 40 years, reflected in an increasing number of papers published in international journals and conference proceedings, related to various aspects of nonlinear acoustics as for instance progressing and standing waves of finite amplitudes, material nonlinearity, acoustical streaming, radiation pressure and acoustical levitation, parametric acoustic arrays etc. The "tools" for solving the nonlinear wave equations have been considerably improved over the past 40 years by development of fast and reliable methods for solving the Burgers' equation, the KZK equation, the KdV equation etc. The practical applications of nonlinear acoustics have, however, not been able to keep pace with the theoretical and numerical development. Only the parametric acoustic array and focused fields in lithotripters have profited to some extent from the development in nonlinear acoustics. However, nonlinear acoustics research has been able to explain observations related to various processes in industry, in medicine, in geophysics and in oceanology, but without any major break-through in direct applications. It is fair to say that the "tools" in nonlinear acoustics have been going through a enormous development over the past 40 years, based on the important fundamental contributions to nonlinear acoustics produced over the 200 years period 1760 – 1960, but we still need to see the "tools" being used to their full extent in the service of the society. This is one of the most important challenges in nonlinear acoustics in the years to come.

REFERENCES

1. Truesdell, C., "Prologue" to L. Euler, OPERA OMNIA, Ser. II, Vol. 12 and 13, Orell Füssli, Zürich, 1954 and 1956.

2. Bjørnø, L., Nonlinear Acoustics: A summary for non-specialists. Department of Fluid Mechanics, Technical University of Denmark, Internal Report No. AFM 74 – 20, Dec. 1974, 1– 44.

3.   Bjørnø L., Nonlinear Acoustics. In R.W.B. Stephens & H.G. Leventhall, "Acoustics and Vibration Progress, Vol. 2, Chapman and Hall, London 1976, 101 – 198.

4.   Oeuvres de Lagrange, Vol. 1, Gauthier-Villars, Paris 1867, 151 – 316.

5.   Poisson, S.D., Mémoire sur la théorie du son. J. l'Ecole Polytechnique, Vol. 7, 1808, 365.

6.   Challis, J., On the velocity of sound, in reply to the remarks of the Astronomer Royal. Phil. Mag., Ser. 3, Vol. 32, 1848, 494 – 499.

7.   Stokes, G.G., On a difficulty in the theory of sound. Phil. Mag., Ser. 3, Vol. 33, 1848, 349-356

8.   Airy, G.B., On a difficulty in the problem of sound. Phil. Mag., Ser. 3, Vol. 34, 1849, 401-405.

9.   Earnshaw, S., On the mathematical theory of sound. Trans. Royal Soc. (London), Vol. 150, 1860, 133 – 148.

10. Riemann, B., Über the Fortpflanzung ebener Luftwellen von Endlischer Schwingungsweite. Abhandl. Ges. Wiss. Göttingen, Math.-Physik, Vol 8, 1860, 43 – 65.

11. Rankine, W.J.M., On the thermodynamic theory of waves of finite longitudinal disturbance. Phil. Trans. Royal Soc., Vol. 160, 1870, 277 – 288.

12. Hugoniot, H., Mémoire sur la propagation du mouvement dans les corps et spécialement dans les gaz parfaits. J. l'Ecole Polytechnique (Paris), Vol. 57, 1887, 3 – 97, and J. l'Ecole Polytechnique (Paris), Vol. 59, 1889, 1 – 125.

13. Landau L.D. and Lifshitz, E.M., Fluid Mechanics. Pergamon Press, 1963, pp. 322.

14. Rayleigh, Lord, Aerial plane waves of finite amplitude. Proc. Royal Soc., Vol. A 84, 1910, 247 – 284.

15. Taylor, G.I., The conditions necessary for discontinuous motion in gases. Proc. Royal. Soc.,Vol. A 84, 371 – 377.

16. Fay, R.D., Plane sound waves of finite amplitude. J. Acoust. Soc. Amer., Vol 3, 1931, 222 - 241.

17. Fubini, E., Anomalie nella propagazione di ande acustiche de grande ampiezza. Alta Frequenza, Vol. 4, 1935, 530 – 581.

18. Thuras, A.L., Jenkins, R.T. and O'Neil, H.T., Extraneous frequencies generated in air carrying intense sound waves. J. Acoust. Soc. Amer., Vol. 6, 1935, 173 – 180.

19. Westerveld, P., Scattering of sound by sound. J. Acoust. Soc. Amer., Vol. 29, 1957, 199 – 203.

20. Burgers, J.M., A mathematical model illustrating the theory of turbulence. In Advances in Applied Mechanics, R. von Mises & T. von Kármán (Eds.), Vol. 1, Academic Press, New York, 1948, 171 – 199.

21. Mendousse, J.S., Nonlinear dissipative distortion of progressive sound waves at moderate amplitudes. J. Acoust. Soc. Amer., Vol. 25, 1953, 51 - 54.

22. Hopf, E., The partial differential equation $u_t + uu_x = \mu u_{xx}$. Comm. Pure and Appl. Math., Vol. 3, 1950, 201 – 230.

23. Cole, J.D., On a quasi-linear parabolic equation occurring in aerodynamics. Quart. Appl. Math., Vol. 9, 1951, 225 – 236.

24. Lighthill, M.J., Viscosity effects in sound waves of finite amplitude. In Surveys in Mechanics. G.K. Batchelor & R.M. Davies (Eds.), Cambridge University Press, 1956, 250 – 351.

25. Beyer, R.T., Parameter of nonlinearity in fluids. J. Acoust. Soc. Amer., Vol. 32, 1960, 719 – 721.

26. Gol'dberg, Z. A., On the propagation of plane waves of finite amplitude. Soviet Phys. (Acoust.), Vol. 2, 1956, 346 – 350.

ACOUSTICS DEMONSTRATIONS

Bruce Denardo
Department of Physics
Naval Postgraduate School

ABSTRACT

Physical acoustics deals with fundamental aspects of acoustics. Current research areas include atmospheric acoustics, nonlinear acoustics, porous media acoustics, sonoluminescence, thermoacoustics, and ultrasonic diagnosis of materials. Due to their fundamental knowledge, physical acousticians may engage in research in other areas of acoustics, such as musical and physiological acoustics, as well as in areas that are usually considered to be outside of acoustics, for example, optics, surface and lattice waves, and nonlinear oscillations and dynamics. It is thus important for a physical acoustician to have a detailed and broad knowledge of oscillations and waves. In accord with this, the demonstrations lecture will include oscillations of few-degree-of-freedom systems, sound in air, and mechanical waves in media other than air.

The main purpose of the demonstrations lecture is to provide a greater understanding of physical acoustics by exhibiting the phenomena with actual apparatus. A secondary purpose is to prepare students to perform demonstrations, which have a long oral tradition in acoustics due to its experimental accessibility and connection with music. To lead to both a greater understanding of physical acoustics and the performance of demonstrations, students will be encouraged ask questions during the lecture. In addition, there are expected to be many discussions due to the challenging explanations of some of the demonstrations.

The lecture will be split into three parts of roughly equal duration. Each part is intended to represent a different basic aspect important for the study of physical acoustics, although in some cases the categorizations are artificial. The parts are: (i) few-degree-of-freedom oscillations, (ii) mechanical waves not including sound in air, and (iii) sound in air. These are described below. The notes for the lecture will be in the form of preliminary pages from the book *Physics Lecture Demonstrations*, second edition (in progress), by the lecturer. Each write-up describes an apparatus and demonstration, and includes an explanation. The write-ups will not be displayed during the lecture. Students may want to glance at them prior to or during the lecture. Any comments about the write-ups during or after the lecture will be appreciated. A digital scope

connected to a computer projector will be used for demonstrations with microphones and other detection transducers, so that the results can be easily observed by the audience.

Most of the demonstrations in the first part (few-degree-of-freedom oscillations) involve mechanical oscillators. The demonstrations are planned to include the following. Collisions with two identical side-by-side billiard ball pendulums show the connection between uniform circular and simple harmonic motion. A spherical pendulum precesses at finite amplitudes due to the dependence of period upon amplitude. A vibrating rod attached to a rotatable table offers a model of Foucault pendulum, where rods with circular, I-beam, and square cross sections exhibit different behavior. A rectangular plate with a concentric hole serves as a physical pendulum whose period is independent of the location of the pivot at the rim. A torsional oscillator is used to illustrate the most accurate arrangement for the determination of the universal constant of gravitation. Coupled linear oscillations are demonstrated with a V-coupled pendulum apparatus, a Wilberforce oscillator, and a double pendulum. Relaxation oscillations are shown with an RC circuit and a neon bulb. Electromagnetically coupled oscillators show the importance of the relative damping of modes. Resonance is demonstrated with a system of pendulums of different lengths driven by a common force, and by the acoustic breaking of a glass. A transverse mass-and-spring system shows the nonlinear phenomena of bent resonance curves and hysteresis. Parametric excitation is demonstrated with a normal and inverted pendulum. Internal parametric instabilities are shown with a spring pendulum and the V-coupled pendulums above. Finally, mode locking is shown with two magnetically-coupled metronomes, and an organ pipe driven by loudspeaker.

Demonstrations planned for the second part (mechanical waves not including sound in air) include the following. A collision ball apparatus with the balls touching in equilibrium fails to function properly because the collision time exceeds the time required for sound to travel the diameter of a ball. A lattice of magnetically-coupled pendulums illustrates a strong dispersive effect of the group and phase velocities being substantially different near the lower-frequency cutoff mode. Longitudinal and transverse vibrational modes of aluminum rods are demonstrated, and overtones are shown to be present. Three demonstrations of waves in nonuniform systems are shown: a pulse on a vertical torsional wave apparatus accelerates and spreads as it travels upward, a standing wave on a nonuniform torsional wave apparatus has a wavelength and amplitude that vary with position, and different resonance frequencies occur for acoustic

resonators when the nonuniformity in cross-sectional area is varied. Finally, solitons are demonstrated on a pendulum lattice as well as on the surface of water.

Demonstrations planned for the third part (sound in air) include the following. The velocity nodes and antinodes of standing waves are demonstrated with a hot-wire Kundt's tube. Linear propagation is demonstrated with a multipole source (monopole, dipole, and quadrupole), an unbaffled and baffled loudspeaker, and pulsed wave propagation above the first cutoff frequency in an acoustics tube. A photoacoustics effect is demonstrated with a strobe light shining on glass with a layer of carbon. Thermoacoustics effects are shown with a Rijke tube and a Hofler tube. There are many dramatic nonlinear acoustics phenomena that will be demonstrated. Distortion and shocks, sum and difference frequency generation, and absorption of sound by noise are shown in a propagating wave tube. In addition, a single sine burst develops into either an N-wave or single shock front, depending upon the polarity of the burst. An ultrasonic ring source generates audible sound through nonlinearity, and dramatically demonstrates a well-defined beam similar to that from a parametric end-fire array. Standing sound waves exert a torque on a Rayleigh disk, and cause antinodal bunching and levitation in a Kundt's tube. The acoustically-generated steady flow in and out of a Helmholtz resonator can extinguish the flame of a match, and can also be employed to create an acoustic motor. Spinning cups in an acoustic enclosure demonstrate acoustic streaming. In the same enclosure, radiation pressure is shown with an acoustic radiometer that is analogous to Crooke's electromagnetic radiometer. Radiation pressure is also demonstrated by the attraction of two plates analogous to the Casimir effect in quantum electrodynamics. Finally, standing waves in a tube driven by a loudspeaker affect the height of flames from the tube.

NOISE AND SENSORS

Thomas B. Gabrielson
Applied Research Laboratory
The Pennsylvania State University

ABSTRACT

Various techniques for converting acoustic or vibration signals to electronic or optical signals (and vice versa) are treated in detail in many papers and books. Frequently, a superficial understanding of the conversion processes is all that is required; however, there is a depth to the physics of transduction that can only be appreciated by closer examination. While the physics of electromechanical signal conversion is rich enough, the study of noise is equally rewarding.

Because the subject of sensor self-noise integrates concepts in mechanics, solid-state physics, quantum mechanics, and thermodynamics, the study of self-noise would be fascinating even if there were no direct application of the principles. For high-performance sensors, however, the achievable noise floor is a critical parameter and so an understanding of sensor self-noise is essential for design, construction, and application of such sensors.

Equilibrium thermal noise is an inevitable consequence of the Second Law of Thermodynamics and, as such, is perhaps the most fundamental source of noise in any system. Equilibrium thermal noise is the noise produced by the normal thermal motion of the molecules that make up the sensor structure or the surrounding liquid or gas. It has a long history of both theoretical and experimental study and so it is remarkable that this mechanism is frequently ignored in the design and analysis of new sensor types. Presumably the reason for this omission is that there are many conventional sensors for which the limiting noise is some other mechanism and the familiarity with this other mechanism has led to the assumption that it is the only important mechanism. This belief does not cause problems until a significant technology shift is introduced and the relative importance of different noise mechanisms changes.

A critical aspect of equilibrium thermal noise is that *every resistance-like term contributes a fluctuating force* in accordance with Nyquist's Theorem. This includes fluid damping, structural damping, acoustic radiation resistance, an acoustic or mechanical load having a real component in the impedance, or thermal radiation. Any path that permits energy transfer from the sensor to the

environment, whether it involves ordered motion (*e.g.*, radiation) or disordered motion (*e.g.*, viscous damping), introduces a fluctuating force.

Sometimes this noise component is called Brownian noise; this can lead to the impression that its sole source is the collision of gas or liquid molecules with the moving element. Even if the element were operated in a vacuum, though, there would still be an equilibrium thermal noise associated with damping in the structure. Frequently, "thermal noise" is cited as a component of the ambient noise (particularly in descriptions of underwater ambient noise). This component is completely accounted by associating the proper fluctuation force with the radiation resistance of the transducer. Also, this component should not be assumed to contain all "thermal noise" fluctuations; it only accounts for those fluctuations associated with the radiation path.

Equilibrium-thermal noise is not only observed in miniature sensors. It can be important in any system designed for ultimate detection performance. At one extreme is the Laser Interferometric Gravitational-Wave Observatory (LIGO), with masses expected to be 10 000 kilograms on suspensions with Q's from 10^7 to 10^9. Because of the extremely small signals anticipated, molecular agitation of those large masses is still a significant source of noise. At the other extreme, the 50 picogram "proof mass" in the geotactic protozoan *Loxodes* is just large enough to permit distinguishing of up from down in the background of equilibrium noise.

Because equilibrium thermal noise is a consequence of classical thermodynamics, its calculation does not depend on any particular model of the physical process. The noise that results from molecular bombardment of a suspended mass in thermal equilibrium with a fluid can be described with complete accuracy by continuum models from fluid dynamics (in terms of the mechanical damping resulting from viscosity in the fluid, or in terms of the continuum radiation resistance into the surrounding fluid, for example). There is no need to accurately describe the microscopic behavior of the fluid. In contrast, *shot noise* is critically dependent on two specific aspects of a particular physical model. First, the carriers (molecules, electrons, photons) must be discrete objects and, second, these discrete objects must act independently: the action of any one carrier must not depend on the presence or absence of any other carrier. Low levels of electron emission from the cathode of a vacuum tube, low levels of current flow across a reverse-biased semiconductor junction, current flows in nondegenerate semiconductors, photoelectric excitation of photodiodes, and tunneling of electrons represent instances in which the carriers can be considered to be acting independently. Molecular impacts at normal gas pressures (because of the very small

mean free path) and electron flow in metals (because of the interdependence forced by the exclusion principle) are situations in which there is a very high degree of dependence between carriers; applying simple shot-noise analyses to these phenomena leads to substantial overestimation of the noise.

Shot noise can be an equilibrium phenomenon or a nonequilibrium phenomenon. In equilibrium shot noise, the calculated noise will be identical to that obtained by an equilibrium thermal noise analysis. For example, a piece of semiconductor with no applied voltage (hence, no *measurable* average current) exhibits a noise voltage that can be calculated in two ways: (1) by considering the Johnson noise associated with the semiconductor's resistance, or (2) by considering two equal (on average) but oppositely directed random currents related to the independent (thermally excited) motion of the carriers and then calculating the root-mean-square value of the voltage produced by these two noise currents. Often, there is no *observable* average current that can be associated with equilibrium shot noise. (An important exception to this is the case of pressure fluctuations in the free-molecular regime; here, the noise is directly related to the observable pressure.) In the equilibrium case, the equilibrium-thermal analysis is fundamental; equilibrium shot noise is a special case and must, in any event, lead to the same answer, not to an additional component.

For current in a semiconductor, application of an external voltage forces the system away from equilibrium, and the forward current (applied plus random) dominates over the reverse current (random). The current noise expression rapidly approaches the standard shot-noise expression in terms of the measurable current for applied voltages greater than k_BT/q (about 25 mV at room temperature). This is a classic example of nonequilibrium shot noise.

Since the voltage (25 mV) beyond which shot noise would dominate over Johnson noise is relatively small, serious errors can be introduced by ascribing a shot-noise component to a material with an inherently high degree of dependence in the carrier flows. Devices such as inductors, capacitors, resistors (carbon, carbon-film, metal-film, wirewound), and degenerate (very highly doped) semiconductors have well-populated conduction bands. Since no two electrons can occupy the same spin-state (the exclusion principle) and most electrons in a well-populated band will be surrounded by occupied states, only those few electrons near the band edge are capable of moving to vacant states. Therefore, only a very small fraction of the conduction electrons exhibit

29

fluctuations. The resultant noise can be much lower than that predicted by the usual shot-noise expression.

Currents associated with potential jumps (currents through PN junctions, gate leakage currents in FETs, tunneling currents) or currents composed of carriers that are thermally excited out of their "rest" bands into sparsely populated conduction bands (currents in intrinsic or normally doped semiconductors) will exhibit full shot noise. In these cases, there are plenty of unoccupied states near the occupied ones and the carriers can act independently even if they are electrons obeying the exclusion principle.

If a system is in thermal equilibrium, then its noise is completely and accurately described by equilibrium thermal noise (mechanical, electrical, or otherwise). Once a system is forced away from equilibrium, the noise frequently increases over the equilibrium value. In addition to non-equilibrium shot noise, another common form of this excess noise is *1/f noise*, so called because its power spectrum goes roughly as f^1 (where f is frequency). There is no satisfactory unifying theory for 1/f noise as there is for equilibrium thermal noise or shot noise. Besides the spectral dependence, one frequently observed characteristic of 1/f noise is that the power spectrum of that noise is proportional to the applied power. While processes are observed in which a 1/f behavior is observed to extremely low frequency, if the noise power spectrum were 1/f all the way to zero frequency, the total noise power would be infinite. Consequently, a universal model for 1/f noise must not only account for the 1/f spectral shape, it must also predict a very-low-frequency roll-off. Unfortunately, since the power is concentrated at the low frequencies, small errors in the location and nature of the roll-off can lead to large errors in the predicted magnitude of the noise. In addition, the roll-off itself is poorly understood because of the difficulty of making measurements at extremely low frequencies.

KEY TO INCLUDED REFERENCES

Uhlenbeck and Goudsmit, "A problem in Brownian motion," Phys. Rev. **34**, 145-151, 1929. On of many classic papers on the fundamentals of noise. Don't be put off by the math. Read the text and find the thought processes and the conclusions. Footnote number 5 is very important. Take note of the importance of independence in applying the methods they use.

T. Gabrielson, "Fundamental noise limits for miniature acoustic and vibration sensors," ASME J. Vibration and Acoustics **117**, 405-410, 1995. A summary of various principles and noise mechanisms. No new information but a reasonable selection of references for further study.

A PROBLEM IN BROWNIAN MOTION

By G. E. Uhlenbeck and S. Goudsmit

Department of Physics, University of Michigan

(Received April 26, 1929)

Abstract

Gerlach investigated the rotatorial Brownian motion of a small mirror suspended on a fine wire. It follows from the theorem of equipartition that the average square deviation of the mirror will depend on the temperature alone of the surrounding gas. Gerlach verified this for a large range of pressures (1 to 10^{-6} atm). The analogy which we found that exists between this problem and the well-known treatment of the shot effect by Schottky enables us to give a more detailed theory of this phenomenon. If the displacement, registered during a time, long compared with the characteristic period of the mirror, is developed into a Fourier series, we find the square of the amplitude of each Fourier component to be a function of the pressure and molecular weight of the surrounding gas as well as of its temperature, (formula 18). The sum of the squares, however, is a function of the temperature alone (proved in section 4). This explains why the curves registered by Gerlach at different pressures, though all giving the same mean square deviation, are quite different in appearance. To get the fluctuating torque on the mirror, the expression:

$$\overline{\delta_p{}^2} = \frac{16}{\pi} \cdot \frac{1}{n} \cdot \frac{1}{\bar{c}\Delta t \Delta o}$$

is obtained for the fluctuation in time of the pressure of a gas on the wall (section 5). In this n represents the number of molecules per cc, $\bar{c}$ is the mean velocity and Δo is the surface of the wall.

I. Introduction

INTERESTING experiments on Brownian motion around a position of equilibrium have been performed by Zeeman and Houdyk[1] in Amsterdam and by Gerlach[2] in Tübingen. The former registered the motion of the loose end of a suspended wire, the latter photographed by means of reflected light the rotational Brownian movement of a little mirror fixed on a very fine wire. The first experiment is theoretically more complicated, because one has to consider the many natural frequencies of the observed body. In the experiment of Gerlach on the other hand the observed system has only *one* characteristic frequency. We will restrict ourselves therefore in the following treatment to the latter case.

In both cases one can immediately predict by means of the equipartition —theorem what the average square of the deflection will be. This will depend on the properties of the observed system and on *the temperature only* of the surrounding gas, *not* for instance on its pressure or molecular weight. The experiments however give *more* than merely the average square deviation; the registered curves show to some extend at least the time-dependence of

[1] P. Zeeman and A. Houdyk, Proc. Acad. Amsterdam, **28**, 52 (1925).

[2] W. Gerlach, Naturwiss. **15**, 15 (1927).

the irregular Brownian motion. As Professor Gerlach kindly communicated to us, the general appearance of these curves is quite different at different pressures of the surrounding gas, though the average square deviation remains the same for any given temperature. The problem is therefore to give a more detailed theory of these curves.

It has occurred to us that this problem may be treated in a manner quite analogous to the method employed by Schottky,[3] to describe the well-known shot-effect. In the experiments of Hull and Williams,[4] the fluctuating voltage in the shot-circuit is coupled inductively with the amplification-circuit, which possesses only one characteristic frequency. In the experiments of Gerlach the fluctuating moment of momentum around the mirror-axis of the gas-molecules, is coupled, by means of collisions, with the "amplifying" mirror, which has also only one characteristic frequency.

The analogy is complete only when *the surrounding gas is much rarefied*, because only then are the moments of momentum given by the gas-molecules to the mirror in successive time-elements independent of each other.[5]

By applying the method of Schottky, we will show in Sections II and III that for this case the amplitudes of the Fourier components of the motion depend on the pressure and the molecular weight of the surrounding gas. This will explain the different forms of the observed curves under various circumstances.

II. THE FOURIER-ANALYSIS OF THE BROWNIAN MOTION

The equation of motion of the mirror is given by:

$$I\ddot{\phi}+f\dot{\phi}+D\phi=M(t), \tag{1}$$

where: I is the moment of inertia around the mirror-axis; ϕ is the angle of deflection; f the friction-coefficient; D the directional force; and $M(t)$ the fluctuating torque, caused by the collisions of the gas molecules. When we introduce the frequency in 2π sec:

$$\omega=(D/I)^{1/2} \tag{2}$$

and the angular acceleration:

$$T(t)=M(t)/I \tag{3}$$

and put:

$$r=f/I \tag{4}$$

Eq. (1) becomes:

$$\ddot{\phi}+r\dot{\phi}+\omega^2\phi=T(t). \tag{5}$$

For our further purposes it is essential to give now a more detailed discussion of the meaning of $M(t)$ or $T(t)$.

[3] W. Schottky, Ann. der Phys. 57, 541 (1918); 68, 157 (1922). Comp. also: J. Tinbergen, Physica, 5, 361 (1925).

[4] A. W. Hull and N. H. Williams, Phys. Rev. 25, 147 (1925). Comp. also N. H. Williams and H. B. Vincent, Phys. Rev. 28, 1250 (1926).

[5] For higher pressures, the problem becomes analogous to the problem of the shot effect for high current densities. Because of the space charge the numbers of electrons hitting the anode in successive time elements are then not more independent of each other, and the fluctuations decrease. Comp. N. H. Williams and H. B. Vincent, ref.[4] p. 1262 and N. H. Williams and W. S. Huxford, Phys. Rev. 33, 773 (1929).

The actual microscopic $M^*(t)$ consists of a large number of sharp peaks, each corresponding to the impulse moment transferred to the mirror by the collision of one (or a few) molecules. We introduce now a "physically infinitely small" time-element Δt,[6] very small compared with the characteristic period $2\pi/\omega$ of the mirror but within which many collisions occur.[7] Our function $M(t)$ consists of the averages of all $M^*(t)$ values included in each time-element Δt. The actual value of $M(t_i)$ for the time-element Δt_i is of course unknown *a priori*, but we can tell some of its properties:

(*a*) $M(t_i)$ will have equal chance of being positive or negative, so that the average over all the time-elements is zero.

(*b*) In our case, when the surrounding gas is rarefied, the $M(t_i)$ in the time-element Δt_i will be independent of the value $M(t_j)$ in the time-element Δt_j.

(*c*) In Section V we will show that the mean of $M^2(t_i)$ over all the time-elements is given by:

$$\overline{M^2(t_i)} = 4m\bar{c}pI/\rho\Delta t \tag{6}$$

where: m is the mass of the gas molecules; $\bar{c}$ their mean velocity; p the pressure of the surrounding gas, and ρ the mass of the mirror per square cm.

Let τ be the time of observation, which must be long compared with the period of the mirror, so that:

$$\Delta t \ll 2\pi/\omega \ll \tau. \tag{7}$$

Develop $T(t)$ within the interval $(0,\tau)$ in a Fourier series:

$$T(t) = \sum_{k=0}^{\infty}(A_k \cos \omega_k t + B_k \sin \omega_k t) \tag{8}$$

where:

$$\omega_k = 2\pi k/\tau$$

$$\left.\begin{array}{l} A_k = \dfrac{2}{\tau} \displaystyle\int_0^\tau T(t) \cos \omega_k t \cdot dt \\[4mm] B_k = \dfrac{2}{\tau} \displaystyle\int_0^\tau T(t) \sin \omega_k t \cdot dt \end{array}\right\} \tag{9}$$

We can now replace these integrals by the following sums:

$$A_k = \frac{2}{\tau} \sum_1^z T(t_i) \cos \omega_k t_i \cdot \Delta t_i$$

$$B_k = \frac{2}{\tau} \sum_1^z T(t_i) \sin \omega_k t_i \cdot \Delta t_i \tag{10}$$

where Δt_i are the successive, equal time-elements, and $T(t_i)$, $\cos \omega_k t_i$, $\sin \omega_k t_i$ are evaluated at a time t_i included within the ith element Δt_i. Z

---

[6] We suppose them all equal.

[7] The introduction of such an "physically infinitely small" time element is characteristic in the kinetic theory of gases. Comp. e.g., P. and T. Ehrenfest, Enc. der Math. Wiss. Vol. IV, Art. 32, p. 39.

is the total number of time-elements. The motion of the mirror is then expressed by:

$$\phi(t) = \sum_k \phi_k(t) = \sum_k \frac{1}{(\omega^2 - \omega_k{}^2)^2 + r^2\omega_k{}^2} [\{A_k(\omega^2 - \omega_k{}^2) - B_k r\omega_k\} \cos \omega_k t$$
$$+ \{A_k r\omega_k + B_k(\omega^2 - \omega_k{}^2)\} \sin \omega_k t] \tag{11}$$

which is the solution of (5) under the conditions $\phi = \dot{\phi} = 0$ for $t = 0$. These conditions mean that we start our observations only when all external disturbances have been damped out, and the remaining motion is due only to collisions with the gas molecules, or in other words, we observe the Brownian motion around the position of equilibrium and not around an already existing vibration.

From this, we find for the time-average of $\phi_k{}^2$:

$$\overline{\phi_k{}^2} = \frac{1}{2} \frac{A_k{}^2 + B_k{}^2}{(\omega^2 - \omega_k{}^2)^2 + r^2\omega_k{}^2}. \tag{12}$$

In the case of very low pressure it is now possible to predict from the three properties (*a*), (*b*) and (*c*) of $M(t)$ (or $T(t)$) the value of $A_k{}^2$ and $B_k{}^2$. From (10) we have

$$A_k{}^2 = \frac{4}{\tau^2} \sum_{i=1}^{Z} \sum_{j=1}^{Z} T(t_i) T(t_j) \cos \omega_k t_i \cos \omega_k t_j \cdot \Delta t_i \Delta t_j. \tag{13}$$

Consider first in this double sum the terms with $i \neq j$. As a consequence of property (*b*), in the case of low pressure $T(t_i)$ and $T(t_j)$ are completely independent; hence these terms will have equal chances of being positive or negative and for large Z their sum will vanish. Consider next the terms with $i = j$, which are all positive. Due to our choice of Δt_i, for all frequencies ω_k of the order of magnitude of ω (and only those give according to (12) an appreciable $\overline{\phi_k{}^2}$,) $2\pi/\omega_k$ will be very large with respect to Δt_i, so that $\cos{}^2 \omega_k t$ changes very little over many time-elements Δt_i. We may therefore replace $T^2(t_i)$ by its average value and obtain:

$$A_k{}^2 = \frac{4}{\tau^2} \overline{T^2(t)} \sum_{i=1}^{Z} \cos^2 \omega_k t_i (\Delta t_i)^2. \tag{14}$$

Finally, replacing the sum once more by an integral, we have:

$$A_k{}^2 = 2/\tau \, \overline{T^2(t)} \cdot \Delta t \tag{15}$$

Obviously the value of $B_k{}^2$ is the same.

III. DISCUSSION OF THE FINAL FORMULA

Formula (6), which will be developed in §5, together with equation (3) gives:

$$\overline{T^2(t)} = 4m\bar{c}p/I\rho\Delta t. \tag{16}$$

In §6 we will prove, that for the case of low pressure, the friction-coefficient is given by:

$$f = 2m\bar{c}p\rho I/kT. \tag{17}$$

Substituting (15), (16), (17) in (12), we get *the final formula:*

$$\overline{\phi_k{}^2} = \frac{\pi^{1/2} m^{1/2} (8kT)^{3/2} \cdot p}{\rho I \cdot \tau} \cdot \frac{1}{\pi k T (\omega^2 - \omega_k{}^2)^2 + 32 p^2 \rho^2 \omega_k{}^2} \tag{18}$$

in which the well-known relation is used that:

$$\bar{c} = (8kT/\pi m)^{1/2}.$$

From the analysis in Section II it is clear that this formula may be interpreted in the *two* following ways:

1. If we resolve into Fourier series *a great number of curves*, each observed over *a relatively short time* τ (which however must still fulfill the fundamental inequality (7)), the mean square of the amplitudes of the kth components will be given by (18).

2. If we analyse *one curve*, observed over *a very long time* τ, then the square of the amplitudes of the kth component will also be given by (18).

The formula (18) shows the noteworthy result, that $\overline{\phi_k{}^2}$ depends not only on the temperature, but also explicitly on *the pressure* and *the molecular weight* of the surrounding gas. As a test we must of course show, as we will do in §4, that *by summing over all values of k*, we obtain for the mean potential energy $\frac{1}{2} D \overline{\phi^2}$ the equipartition value $\frac{1}{2} kT$ which is *independent* of the pressure and the molecular weight of the surrounding gas.

The dependence on the pressure is rather complicated. For frequencies ω_k very near to ω, the $\overline{\phi_k{}^2}$ becomes inversely proportional to p, and for ω_k very large compared with ω, the $\overline{\phi_k{}^2}$ becomes almost directly proportional to p. These latter terms of course contribute very little to the total motion, the denominator being so large. When we plot therefore $\overline{\phi_k{}^2}$ against k, the resulting curve has a maximum in the neighborhood of ω, which rapidly becomes very sharp as the pressure decreases. The motion of the mirror than becomes more and more "monochromatic."

APPENDIX

IV. PROOF OF THE EQUIPARTITION THEOREM.

The average potential energy of the vibrating mirror is equal to:

$$\tfrac{1}{2} D \overline{\phi^2} = \tfrac{1}{2} D \sum_{k=0}^{\infty} \overline{\phi_k{}^2} \tag{19}$$

because the different Fourier components are independent of each other. Though we restricted ourselves to values of ω_k small with respect to $2\pi/\Delta t$, it is permissible to extend the summation to infinity, because the components with ω_k large compared to ω contribute very little to the sum.

Equation (15) shows, that $A_k{}^2$ and $B_k{}^2$ are independent of k; hence from (12) and (15):

$$\overline{\phi^2} = \sum_{k=0}^{\infty} \overline{\phi_k{}^2} = \frac{2}{\tau} \overline{T^2(t)} \cdot \Delta t \sum_{k=0}^{\infty} \frac{1}{(\omega^2 - \omega_k{}^2)^2 + r^2 \omega_k{}^2}. \tag{20}$$

The last sum we now replace by an integral, substituting:

$$x_k = \omega_k/\omega = 2\pi k/\tau\omega$$

which gives:

$$\sum_{k=0}^{\infty} \frac{1}{(\omega^2 - \omega_k{}^2) r^2 + r^2 \omega_k{}^2} \cong \frac{\tau}{2\pi\omega^3} \int_0^{\infty} \frac{dx}{(1-x^2)^2 + (r^2/\omega^2) x^2}$$

with very good approximation. The value of the integral is $\pi\omega/2r$,[8] so that we obtain:

$$\overline{\phi^2} = \overline{T^2(l)} \cdot \Delta t/2\omega^2 r. \tag{21}$$

Introducing the relations (16) and (17), and substituting from (2) and (4) the values of ω^2 and r, we obtain immediately:

$$\tfrac{1}{2}D\overline{\phi^2} = \tfrac{1}{2}kT. \tag{22}$$

V. PROOF OF THE FLUCTUATION FORMULA (6) OR (16).

This relation follows from a consideration of *the fluctuations in time* of the pressure exerted upon a wall by a rarefied gas. Using Maxwell's distribution law one easily derives an expression for the probability that a molecule of a gas within a volume V at the temperature T gives to a portion Δo of the wall a momentum normal to the wall lying between G and $G+\Delta G$ during the time Δt. It is:[9]

$$W\Delta t\Delta o\Delta G = \frac{\pi}{2} \cdot \frac{1}{(2\pi mkT)^{3/2}} \cdot \frac{kT}{V} \cdot Ge^{-G^2/8mkT}\Delta t\Delta o\Delta G. \tag{23}$$

Let n_{ij} be the number of molecules, which in the time-element Δt_i give a momentum lying between G_j and $G_j+\Delta G_j$ to the portion Δo of the wall. Then the total momentum given to Δo during Δt_i becomes:

$$G(t_i) = \sum_{j=0}^{\infty} G_j n_{ij}.$$

Using the bar to denote the average over all time-elements, we find easily:

$$\overline{G^2(t_i)} - \overline{G(t_i)}^2 = \overline{(\Sigma_j G_j n_{ij})^2} - (\overline{\Sigma_j G_j n_{ij}})^2 = \Sigma_j G_j^2(\overline{n_{ij}^2} - (\overline{n_{ij}})^2) \tag{24}$$

because the cross-terms cancel, and the average over the time-elements Δt_i extends only over the n_{ij}. In general the fluctuation formula holds:

$$\overline{n_{ij}^2} - (\overline{n_{ij}})^2 = \overline{n_{ij}} \tag{25}$$

and $\overline{n_{ij}}$ follows immediately from (23), after multiplying by the total number of molecules N. Substituting then (25) in (24), and replacing the sum by an integral, we obtain:

$$\overline{G^2(t_i)} - \overline{G(t_i)}^2 = \frac{\pi}{2} \cdot \frac{p}{(2\pi mkT)^{3/2}}\Delta o\Delta t \cdot \int_0^{\infty} G^3 \exp[-G^2/8mkT]dG = 2m\overline{c}p\Delta o\Delta t \tag{26}$$

for:

$$p = NkT/V.$$

---

[8] See W. Schottky, Ann. der Phys. **68**, 157 (1922).

[9] Integrating over G from 0 to ∞, we get for the probability that a molecule hits in the time Δt the surface element Δo:

$$w\Delta t\Delta o = \overline{c}\Delta t\Delta o/4V$$

corresponding to the well-known result for the mean number $\overline{n}$ striking 1 cm^2 of the wall per second:

$$\overline{n} = N\overline{c}/4V.$$

In the same way we find for the mean momentum given to the wall taken over all the molecules striking it:

$$\overline{G} = (2\pi mkT)^{1/2}$$

and for the mean square:

$$\overline{G^2} = 8mkT$$

This, divided by Δt^2, expresses the fluctuation in time of the pressure on the portion Δo of the wall.[10] From this it follows obviously that for a disc of surface o inside the gas, the mean of the square of *the force* $K(t_i)$ taken over all the time-elements Δt_i is given by:

$$\overline{K^2(t_i)} = 4m\bar{c}po/\Delta t \tag{27}$$

as for such a disc $\overline{K(t_i)} = 0$, and the fluctuations on the right and left side are independent of each other.

For a case like the experiment of Gerlach we must consider the moment of momentum around the mirror axis instead of the momentum. The analogous formula for *the torque* is then:

$$\overline{M^2(t_i)} = \frac{4m\bar{c}p}{\Delta t} \int\int x^2 do = \frac{4m\bar{c}pI}{\rho\Delta t}$$

where x denotes the distance from the axis. This is equation (6).

VI. Proof of Formula (17) for the Friction Coefficient.[11]

Consider a portion Δo of the mirror, which moves, say to the right in the direction of the x-axis with the velocity u. The number of molecules per second, which strike this from the left, and which lie within a certain velocity-range $d\xi d\eta d\zeta$ is:

$$dN_1 = \left(\frac{m}{2\pi kT}\right)^{3/2} \frac{N}{V}(\xi - u)e^{-mc^2/2kT}\Delta o d\xi d\eta d\zeta \tag{28}$$

where we have used Maxwell's distribution law, because *in our case of very low pressure*, the mean free path is large with respect to the dimensions of the mirror, so that the motion of the mirror *does not disturb the velocity distribution* of the molecules. If x is the distance from Δo to the axis of the mirror, then the moment of momentum imparted per second by these molecules is:

$$dM_1 = \left(\frac{m}{2\pi kT}\right)^{3/2} \frac{2Nm}{V} \cdot (\xi - u)^2 \cdot x \cdot e^{-mc^2/2kT}\Delta o d\xi d\eta d\zeta. \tag{29}$$

Neglecting the term with u^2 and integrating over η and ζ from $-\infty$ to $+\infty$, and over ξ from 0 to $+\infty$, we get:

$$M_1 = px\Delta o - m\bar{c}Nux\Delta oV^{-1}. \tag{30}$$

In the same way, we find for the moment of momentum given to Δo per second by molecules striking from the right:

$$M_2 = -px\Delta o - m\bar{c}Nux\Delta oV^{-1} \tag{31}$$

so that the total moment of momentum given to Δo per second is:

$$M_1 + M_2 = -2m\bar{c}pux\Delta o/kT. \tag{32}$$

Now $u = x\dot{\phi}$, so that we find for the friction coefficient:

$$f = \frac{2m\bar{c}p}{kT}\int\int x^2 do = \frac{2m\bar{c}pI}{\rho kT}$$

which is formula (17).

---

[10] This can be written in the form:

$$\frac{\overline{p^2} - (\bar{p})^2}{(\bar{p})^2} = \overline{\delta_p{}^2} = \frac{16}{\pi} \cdot \frac{1}{n} \cdot \frac{1}{\bar{c}\Delta t\Delta o}$$

when n is the number of molecules per cc. It has then the same form as the expression for the fluctuation in pressure of a gas inside a volume element Δv (see R. Furth, Die Schwankungserscheinungen in der Physik, Vieweg, Braunschweig, 1920, p. 58):

$$\overline{\delta_p{}^2} = \frac{C_p}{C_v} \cdot \frac{1}{n} \cdot \frac{1}{\Delta v}$$

but it cannot be derived from it.

[11] Comp. H. A. Lorentz, Les theories statistiques en thermodynamique, Leipzig, 1916, p. 53.

Fundamental Noise Limits for Miniature Acoustic and Vibration Sensors

T. B. Gabrielson

NAWC Aircraft Division,
Code 4.5.5.4 MS07
Warminster, PA 18974

Recent technological advances in microfabrication and fiber optics have made practical the construction of very small, sensitive sensors for acoustic or vibration measurements. As the sensitivity is increased or the size is decreased, a sensor becomes more susceptible to mechanical noise resulting from molecular agitation. Traditional noise analysis is often focused exclusively on electrical or optical noise; consequently, mechanical-thermal noise may not be considered in new types of sensors until the prototype testing reveals an unexpectedly high noise floor. Fortunately, mechanical-thermal noise is relatively easy to estimate early in the design process because the equivalent noise force is only a function of the temperature and the mechanical losses in the sensor. There are a number of specific techniques that are applicable for evaluating either the total mechanical-thermal noise or the spectral distribution of that noise for simple or complex sensors. These techniques are presented and, in addition, a summary of other noise components is given in the context of design guidelines for high-sensitivity sensors.

Introduction

When designing high-sensitivity sensors, the fundamental processes that limit performance must be considered. Although it is commonly assumed that the first-stage electronics controls the noise floor, unavoidable fluctuation phenomena within the sensor itself can sometimes dominate the noise performance. If these phenomena are not understood, unrealistic claims may be made for the sensor design and the resultant performance can be disappointing. Economical production of very small sensors is now practical through techniques such as microfabrication (for example, Hohm and Hess, 1989; Bergqvist et la., 1991; Kühnel and Hess, 1992; Bernstein, 1992; Rockstad et al., 1993; Henrion et al., 1990; Roylance and Angell, 1979; and Petersen et al., 1982); however, as the size of such sensors decreases, the moving elements become increasingly affected by molecular agitation. To insure successful designs, this mechanical-thermal noise must be considered.

While the focus of this paper is on miniature sensors, it should not be assumed that physically large sensors are immune from the effects of molecular agitation. The critical issue is sensitivity: a large sensor of extremely high sensitivity may be affected as much by molecular agitation as a very small device with a much lower sensitivity. For example, one type of sensor that is routinely operated near the limits set by molecular agitation is the transient gravity-wave sensor. The anticipated signal levels for such sensors are so small that cryogenically cooled detectors with proof masses of thousands of kilograms are used to reduce the molecular-motion noise to an acceptable background level (Misner, et al.,

1973). At the other extreme, the biological gravity sensor in the protozoan *Loxodes* (Fenchel and Finlay, 1984) is only required to roughly determine the orientation of the organism with respect to local gravity. The sensor consists of a 1 to 2 μm barium sulfate granule suspended by a bundle of cilia inside a fluid-filled cavity. This sensor also operates near the limits imposed by thermal molecular motion: on this size scale, molecular agitation is so severe that, if the barium granule (the proof mass) were only a factor of four smaller, the organism would be incapable of distinguishing up from down!

Mechanical-thermal noise is a direct consequence of the molecular motion associated with thermal equilibrium (Callen and Welton, 1951; Hofler and Garrett, 1988; Uhlenbeck and Ornstein, 1930; Uhlenbeck and Goudsmit, 1929; Kittel, 1958; and Marton and Hornyak, 1969). The analysis techniques for equilibrium-noise processes are simple and completely analogous with the techniques for evaluating Johnson noise in electrical systems. In addition, there are also important nonequilibrium processes that result in sensor noise. Of these, shot noise (Kittel, 1958) is also relatively simple to analyze; however, 1/f noise (Press, 1978; Weissman, 1988; and Horowitz and Hill, 1989) is poorly understood (although its impact can be reduced by an understanding of its spectral distribution). This paper summarizes the basic methodologies for estimating the magnitude of equilibrium noise and briefly considers other noise mechanisms relevant to sensor design.

Fundamentals

According to the classical equipartition theorem (Callen and Welton, 1951; and Kittel, 1958), if an object is in thermal equilibrium with its surroundings, then each independent

component of its energy will have an average value of $k_B T/2$ where k_B is Boltzmann's constant (1.38×10^{-23} joules per kelvin) and T is the absolute temperature. For example, the average kinetic energy for a simple harmonic oscillator "at rest" would be $m <v^2>/2 = k_B T/2$ where m is the mass; the average potential energy of that oscillator would be $k <x^2>/2 = k_B T/2$ where k is the spring constant. Consequently, the mean-square speed $<v^2>$ or the mean-square displacement $<x^2>$ that results from molecular agitation can be immediately determined.

More often than not, the spectral distribution of noise is more useful than the overall mean-square value for acoustic or vibration sensors (Hofler and Garrett, 1988; and Marton and Hornyak, 1969). While the integral of the noise spectral density over all frequencies must equal the equipartition value, the spectral distribution depends on the mechanical characteristics of the system. Fortunately, the relationship between the system characteristics and the noise spectral density is simple: if a noise-force generator is associated with each dissipation element in the system (see Fig. 1), the proper system noise output is produced. Nyquist's relation (Callen and Welton, 1951) gives the proper value for this force generator: the generator should have a source spectral density of $\sqrt{4k_B TR}$ newtons/$\sqrt{}$ Hz (where R is the mechanical resistance—force divided by velocity—of the associated damper). The noise-force generator can be converted to an equivalent pressure-noise source by dividing by the area of the sensor face.

Simple Sensors

Often the mechanical behavior of a sensor is modeled quite well by a single, damped mass-spring system (Fig. 1). In this case, there are very simple expressions for the signal-to-noise ratio for mechanical-thermal noise (Gabrielson, 1993). For a simple pressure sensor, in which the pressure compresses a diaphragm against some restoring force, the signal-to-noise (power) ratio is given by the square of the ratio of the signal force ($p_s S$) to the noise force:

$$SNR = \frac{(p_s S)^2}{4k_B TR_M df} = \frac{(p_s S)^2 Q}{4k_B T df \omega_0 m} \qquad (1)$$

where p_s is the signal pressure, S is the diaphragm area, and df is the system or measurement bandwidth. In the form on the right, the mechanical resistance has been replaced by $\omega_0 m/Q$ where Q is the quality factor, ω_0 is 2π times the resonance frequency, and m is the mass.

For a simple accelerometer, in which a mass is suspended inside a case, the signal-to-noise ratio is also the square of the ratio of signal force to noise force but the signal force is now equal to the proof mass times the signal acceleration:

$$SNR = \frac{(m a_s)^2}{4k_B TR_M df} = \frac{a_s^2 m Q}{4k_B T df \omega_0} \qquad (2)$$

where a_s is the acceleration signal. Frequently, the df factor is absorbed into the signal quantity so that the equivalent pressure becomes pressure (in Pa) per root Hz and the equivalent acceleration becomes acceleration (in either m/s^2 or "g") per root Hz.

Dissipation

The relationship between damping in a system and noise is expressed by the fluctuation-dissipation theorem for systems in thermal equilibrium (Callen and Welton, 1951). If there is a path by which energy can leave a system, then there is also a route by which molecular-thermal motion in the surroundings can introduce fluctuations into that system. It is impor-
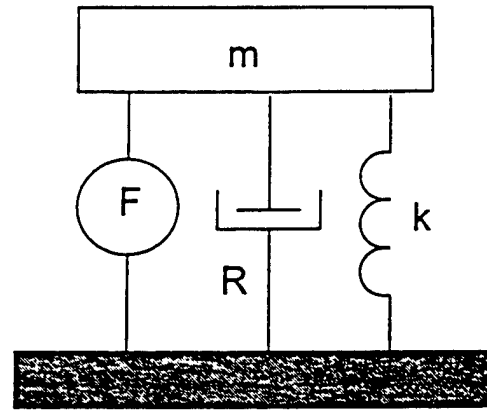
Fig. 1 Schematic diagram for a simple harmonic oscillator with mass, m, spring constant, k, and damper, R. Also shown is the noise force generator, F, that represents the mechanical-thermal noise.

tant to realize that energy is removed from a system not only by damping but, for example, by transfer to a load or radiation. One of the keys to evaluating mechanical-thermal noise is in understanding the mechanisms by which energy can leave the system. These mechanisms can include mechanical damping in the spring and supports, viscous drag, acoustic reradiation, electrical leakage, thermal radiation, and magnetic eddy currents.

Since it is often difficult to separate various damping mechanisms in a device, measurement of the system's Q is a valuable technique for noise assessment. As long as there is a single primary resonance and the damping is independent (or nearly so) of frequency, the Q gives the mechanical resistance directly in terms of the resonance frequency and either the mass or stiffness ($Q = \omega_0 m/R = k/\omega_0 R$). ($Q$ is also the reciprocal of twice the damping factor; a Q of 0.5 corresponds to critical damping.) Many times, measurements of a vibrating system's dominant mass and Q are simple; the resistance and, therefore, the fluctuating force can be calculated from these measurements.

There are instances in which the damping can be directly estimated. For example, microfabricated sensors often have very small gaps between moving parts. This results in large damping losses from squeeze-film damping—the viscous loss associated with squeezing the fluid out between moving surfaces. Squeeze-film damping can easily dominate the dissipation mechanisms for gaps of tens of microns or less. For two parallel disks of area, S, with average spacing, h, the equivalent mechanical resistance is (Starr, 1990)

$$R_{film} = \frac{3\mu S^2}{2\pi h^3} \qquad (3)$$

where μ is the fluid's viscosity. The dependence on spacing is strong.

If one disk is perforated, the damping can be reduced considerably. In this case, the mechanical resistance is given approximately by (Bergqvist et al., 1991; and Skvor, 1967)

$$R_{perf} = \frac{12\mu}{N\pi h^3} G(A) S^2 \qquad (4)$$

where N is the total number of holes in the perforated plate, A is the fraction of open area in the plate, and

$$G(A) = \left[\frac{A}{2} - \frac{A^2}{8} - \frac{\ln A}{4} - \frac{3}{8} \right] \qquad (5)$$

Radiation resistance can be a significant dissipation mechanism above 10 kHz (Mellon, 1952). This resistance is ap-

proximately equal to that for an unbaffled piston (Kinsler et al., 1992) of radius, a,

$$R_{rad} = \rho c \pi a^2 (ka)^2 / 4 \qquad (6)$$

where c is the sound speed and k is the acoustic wave number (ω/c). Also, the effective radiation resistance from thermal radiation may be important for sensors operating at very high temperatures (He and Cuomo, 1992) since the thermal radiation resistance increases as the fourth power of temperature.

Solution Methods

If the sensor and processor are not frequency selective, then the mechanical-thermal noise floor can be determined directly from the equipartition theorem. This has already been described for the mean-square displacement or velocity for a simple harmonic oscillator. For a torsional oscillator with moment of inertia, I, and torsional spring constant, K, the mean-square angular displacement, θ, or angular velocity, Ω, can be found because the associated energies $- K < \theta^2 > /2$ and $I < \Omega^2 > /2$ – are equal to $k_B T/2$. For an electrical oscillator with inductance, L, and capacitance, C, the fluctuation voltage or current can be found by setting $C < V^2 > /2$ or $L < i^2 > /2$ equal to $k_B T/2$.

When the spectral distribution of the thermal noise is required, a sensor can often be evaluated quickly for mechanical-thermal noise by determining the damping and then calculating the associated noise from Nyquist's relation. Once the direct noise force is determined, the equivalent pressure or acceleration (or force, or whatever) that would be required to produce the same level can be calculated and compared to the expected signal level. The equivalent noise levels for signal quantities can be calculated directly from Eq. (1) or Eq. (2) by setting the signal-to-noise ratio equal to one. This process is illustrated by two examples in the next section.

In any case, it is not the absolute value of noise power that determines the usefulness of a sensor; instead, the ratio of signal to noise power is the critical quantity. If a design modification reduces the noise but, at the same time, equally reduces the signal, there is no net benefit. An increase in signal responsivity often helps if the noise performance is limited by the electrical preamplifier; however, if the sensor's intrinsic thermal noise limits the performance, further increases in responsivity are unproductive.

Two other techniques, which are useful in certain circumstances, are described below. The first method—determination of the noise from the sensor's frequency response—is useful if little information is available about the sensor mechanics. The second method—electronic circuit simulation—is useful for mechanically complex sensors.

Noise Estimation from Sensor Frequency Response. One consequence of equipartition is that the details of damping need not be known to calculate the total thermal-noise energy. The total thermal energy is fixed by the system temperature; the system's frequency response can only redistribute that energy. This is illustrated in Fig. 2 where the spectral distribution of noise-displacement power is shown for two simple oscillators with the same spring constant and resonance frequency but different damping. For a high-Q oscillator, most of the noise power is concentrated around the resonance, while for the critically damped $(Q = 1/2)$ case, the noise power is distributed over the band below resonance. In each case, the area under the curves is the same. If the frequency response curve (measured or theoretical) is given for a sensor, this curve can be translated into the noise spectral distribution curve by adjusting the vertical scale so that the area under the curve is $k_B T/2$.

In order for this to work, the spectral shape of the signal
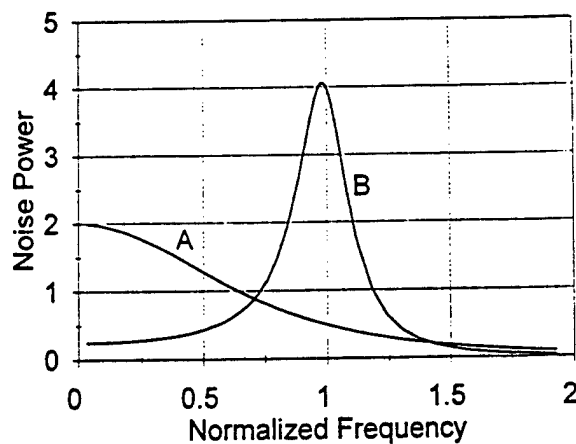
Fig. 2 Distribution of noise power for two mass-spring systems with identical spring constant and resonance frequency but different damping. System A has a Q of 0.5 and system B has a Q of 4. The noise power is normalized so that the area under the curve is 1.

response of the sensor must be the same as the spectral shape of the output of the sensor due to thermal agitation of the sense element. For the simple accelerometer, the spectral shape of the acceleration response is identical to the shape of the noise response; for the simple pressure sensor, the shape of the pressure response is identical to the shape of the noise response. This may not be true for more complicated sensors but, if the behavior is dominated by a single mass-spring system, then the following procedure may be suitable as a first approximation to the noise characteristics.

The spectral density of the noise is generally not constant with frequency because the mechanical spring-mass system shapes the spectrum but the broadband noise is still governed by equipartition so

$$< x^2 > = \int_0^\infty x^2(f) df = k_B T / k \qquad (7)$$

This expression says that the total energy associated with the mean-square displacement is constant regardless of its spectral distribution. (Of course, for some sensors it might be more appropriate to equate the integral of velocity-squared to $k_B T/m$.)

If the given sensor power response function is called $G(f)$ and the displacement noise has the same shape, then $x^2(f) = c_1 G(f)$ and all that is needed is the value of the constant c_1. This is found directly from Eq. (7): if A_f is the area under the response curve, $G(f)$, then

$$c_1 = k_B T / k A_f \qquad (8)$$

and

$$X^2(f) = G(f) k_B T / k A_f \qquad (9)$$

(When the area is calculated, the curve must be expressed in a power-like quantity—displacement squared, pressure-squared—and certainly never in dB). Once the displacement noise is known, the transfer constant relating sense mass displacement to sensor output can be used to calculate the sensor output noise.

Circuit Simulation. The more complex a mechanical system becomes, the more tedious an analytical solution becomes. A convenient alternative is to draw the electrical equivalent circuit for the mechanical system and then use a software circuit simulator like SPICE (Tuinenga, 1988) to do the analysis. SPICE, for example, has a noise analysis command that automatically calculates the equivalent noise from
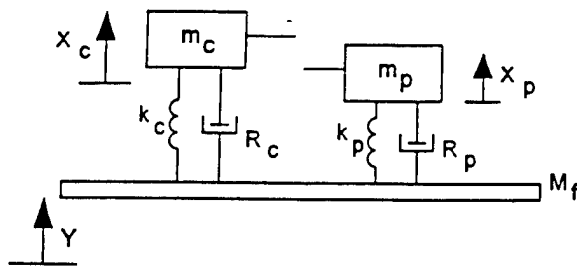
Fig. 3 Schematic diagram for a compound accelerometer consisting of two damped mass-spring systems
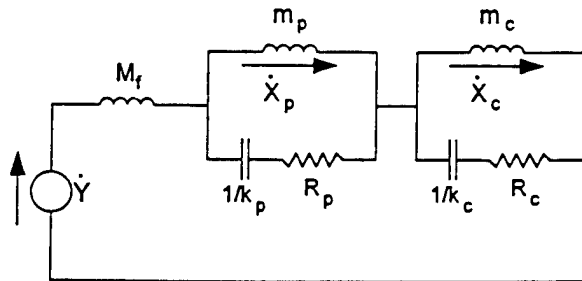
Fig. 4 Impedance-analogy equivalent circuit for the mechanical system shown in Fig. 3.

all resistors in the circuit. This way, both mechanical-thermal and electrical-thermal (Johnson) noise contributions can be included.

To illustrate, consider the two-element accelerometer shown in Fig. 3. Here, the output would be the difference in displacement between the two masses rather than between either mass and the case. The equivalent circuit (impedance analog) for this accelerometer is drawn in Fig. 4. For the impedance analog, current is velocity and voltage is force.

An inductor (M_F) representing the frame mass has been included primarily to provide a convenient way of monitoring the input acceleration. In the impedance analogy, force and velocity are the direct equivalents of voltage and current, respectively. Acceleration is equal to the force (voltage) across a mass divided by that mass and displacement is equal to the force across a stiffness element divided by that stiffness. In this way, both displacement and acceleration can be monitored from "voltage" measurements on the circuit. For example, the output quantity for this compound device is the displacement difference, $X_c - X_p$. This differential displacement is equal to the difference between the voltages across k_c and k_p divided by the respective stiffnesses.

Examples

High-Leverage Optical Accelerometer. The first example is a fiber-optic accelerometer (Gardner et al., 1987) that is limited by mechanical-thermal noise not because of small size but because of the high sensitivity that results from large optical leverage combined with an interferometric detector. This device consists of two arms each of which is a proof mass mounted on a compliant cylinder. Each elastomer cylinder functions both as a spring and as a mechanism to couple the displacement of the mass to strain in an optical fiber wrapped around the cylinder. When the proof mass compresses the cylinder axially, the cylinder expands radially, thereby stretching the fiber. The arms are arranged so that the proof masses move out of phase and, therefore, one fiber stretches while the other shrinks (in length); the two fibers are the two legs of a Michelson interferometer. The responsitivity can be controlled by varying the number of turns of fiber on the compliant cylinders. The combination of the Poisson's ratio coupling through the elastic cylinder, the

push-pull configuration of the legs, and the Michelson interferometer lead to high signal responsivity with reasonable fiber lengths.

The prototype device has a proof mass of 0.575 kg, a resonance frequency of 327 Hz, and a Q of 11. Calculation of the noise floor that results from mechanical-thermal noise is simple: the equivalent signal acceleration that would produce a signal-to-noise ratio of one is, from Eq. (2), 0.23 ng/√Hz. If thermal noise is ignored, the calculated noise floor based on the noise of a state-of-the-art interferometer demodulator is about 0.1 ng/√Hz with the apparent potential for lowering this even further merely by winding more turns of optical fiber on the compliant cylinders. In reality, any such improvements are illusory: the thermal noise sets the noise floor and even cooling to liquid nitrogen temperature (77 K) would only lower the equivalent noise acceleration by a factor of two.

Micromachined Microphone. Structurally, at least, construction of a very small capacitor microphone is feasible through silicon micromachining (Hohm and Hess, 1989; Bergqvist et al., 1991; Kuhnel and Hess, 1992; and Bernstein, 1992). One principal advantage would be the ability to maintain a small gap between the capacitor plates which would, in turn, permit a low bias voltage and relatively small plate area for a given capacitance. A reasonable design goal might be to require a 3 volt bias (to facilitate battery operation) and no less than 5 pF capacitance (to avoid exceptional problems with high impedance and stray capacitance). Using a conservative value of 10 kV/cm for the dielectric breakdown of air, the minimum plate spacing for 3 volts would be 3 μm. The minimum plate size for a 5 pF capacitor would then be 1.3 mm by 1.3 mm (since capacitance is ϵ times plate area divided by plate spacing and ϵ is 8.85 pF/m for air). From Eq. (3), the mechanical resistance resulting from squeeze-film damping is 0.9 N s/m; from Eq. (1), the pressure for a signal-to-noise ratio of one is 70 μPa/√Hz. This corresponds, roughly, to an A-weighted (Kinsler et al., 1982) level of 53 dB. (The effective noise bandwidth of the A-weighting function is about 15 000 Hz). This is more than 25 dB noisier than the background noise in a good recording studio and is about the average background level in a restaurant (Anderson, 1989). Application of such a microphone would clearly be limited.

If one of the plates is perforated, the squeeze-film damping is reduced markedly. In the above example, if 1600 holes were etched in one of the plates with an open-area to total-area ratio of 0.5 (and the plate dimensions were increased to maintain the same capacitance), then the mechanical resistance would be reduced to 2.8×10^{-4} N s/m and the noise-equivalent pressure would be 0.6 μPa/√Hz. The effective A-weighted level is about 12 dB which is more than 10 dB below the recording-studio background. Such plate perforation was originally explored in order to produce a usable responsitivity and frequency response for such microphones; in fact, the reduction in damping is more critical from the standpoint of producing an acceptable noise floor.

Checklist for Noise Design. Good engineering design of a sensor should embody, among other things, the following philosophy: sufficient (but not excess) sensitivity for the application. Certainly if there is a fundamental noise limit that would prevent detection of a desired signal, the sensor must be redesigned (larger, more complex, more expensive, heavier, etc.); however, these efforts can be taken to excess. There is no point in expending effort to reduce the sensor noise far below any anticipated signals; neither is there any point in reducing one particular noise component if some other source of noise is dominant. With this in mind, the following list of the common noise components can be used

as either a starting point for noise-floor design for new sensors or as a checklist for evaluating proposed sensors. Certainly, if a designer is claiming improvements over conventional technology of an order of magnitude (in size, or responsivity, or cost, etc.) or more, the evaluator should consider each of these sources of noise seriously.

Mechanical-Thermal Noise. Any moving elements in a sensor are subject to molecular agitation. This should always be considered if the sensor is pushing the state-of-the-art in sensitivity. Because it is, perhaps, the most frequently neglected source of noise, most of this paper has been devoted to its characteristics and analysis.

Shot Noise. If the electrons (or any other carriers like photons) in the sensor or the associated electronics move independently and randomly, then there will be a shot noise associated with that motion. Common sources of shot noise are photodetectors, semiconductor PN junctions, and electron tunneling. No optical system can achieve noise levels lower than shot noise if there is a stage of optical-to-electrical conversion because this always involves independent, random, photon-to-charge conversion. For electrical currents, the shot-noise current density is $i_n^2 = 2qIdf$, where q is the unit charge (1.6×10^{-9} C) and I is the average current (Kittel, 1958) (i.e., the current from a photodiode or the current into a PN junction).

Normal current flow in resistors, capacitors and inductors is strongly coherent because of the long-range interaction of the fields of the electrons. In a metal, the relaxation time for perturbations in charge density is about 10^{-8} seconds (Gray, 1967). Consequently, on any practical time scale, the charge carriers do not introduce fluctuations of their own: they merely image the surrounding lattice vibrations (Johnson noise). If there is no mechanism for destroying this coherence (like a PN junction), then there is no shot-noise component (Horowitz and Hill, 1989; Pippard, 1989; and Braddick, 1966).

1/f Noise. Noise with a power spectrum that drops with increasing frequency at about 1/f is commonly observed (Press, 1978; Weissman, 1988; and Horowitz and Hill, 1989). There is no general unifying principle to describe this noise as there is for shot noise or equilibrium thermal noise, so its magnitude is difficult to predict. Since 1/f noise is not an equilibrium noise, it is only present where there is a source of power (however small) to sustain it. Consequently, it is associated with polarization voltages, bias voltages, currents through components (carbon resistors, especially), currents through oxidized contacts (particularly, aluminum contacts), and currents through semiconductor devices. Since it is not easily predicted, it is normally measured for the specific device in question.

The designer should be aware that 1/f noise exists and that its most serious consequences are at low frequency (because of the 1/f spectral distribution). This noise can often be eliminated or greatly reduced by translating the signal to a frequency well above the 1/f-affected region. For example, a high-frequency AC bias applied to a capacitive sensor produces a modulated signal that is much less affected by 1/f noise than the baseband signal that would be produced by the same sensor with DC bias. Because of the ubiquity of 1/f noise, such modulation techniques should always be at least considered for sensors intended for very low frequency.

Preamplifier Voltage and Current Noise. Usually only the first stage of preamplification of a sensor is important from a noise point of view. Amplifiers can be characterized by equivalent input current and voltage noise, which are in direct competition with the signal. For example, the 2N4338 low-noise JFET has a minimum voltage noise of 8 nV/$\sqrt{\text{Hz}}$

and a minimum current noise of 0.8 fA/$\sqrt{\text{Hz}}$ (Siliconix, 1991). High-impedance sensors (e.g., capacitive sensors at low frequency) are particularly affected by the amplifier current noise as a large equivalent noise voltage can result when this noise current is forced through the sensor. Preamplifier selection should be based on both the current and voltage noise and the reaction of these noise "sources" with the attached components. Merely buying a "low noise" amplifier does not necessarily solve an electronics noise problem.

Johnson Noise in Circuit Resistors. Any electrical resistance in the circuitry contributes an equivalent voltage noise given by $v_n^2 = 4 k_B T R\, df$. There are often one or two resistors in the input stage that can contribute significant noise to the circuit. If any electrical equivalent circuit model is being used for mechanical-thermal noise analysis, the preamplifier can be included and the Johnson noise calculated at the same time.

Laser and Optical Detector Noise. If an optical scheme is being used, then the device should at least be examined for shot noise. However, intrinsic laser noise is often much higher than shot noise (Lax, 1991; Agrawal 1991; Dandridge et al., 1981; and Henry 1986) and so needs to be considered on a case-by-case basis. Fiber-optic systems that use two-way transmission in one or more fiber legs (e.g., Fabry-Perot or Michelson arrangements) are susceptible to coherent scattering noise generated in the fiber (Wood et al., 1988). In fact, fiber-optic systems without large optical leverage are generally not capable of reaching the mechanical-thermal noise limit because of the difficulties associated with reducing the optical noise.

Other Sources of Noise. The preceding list is not, by any means, a complete list of noise mechanisms but it is a starting point for sensor design. Of course, poor choice of components and inattention to electromagnetic interference can render an intrinsically good sensor ineffective.

References

Agrawal, G., 1991, "Noise in Semiconductor Lasers and Its Impact on Optical Communication Systems," *Laser Noise*, Rajarshi Roy, ed., Proc. SPIE, Vol. 1376, pp. 224–235.

Anderson, H., ed., 1989, *A Physicist's Desk Reference*, American Institute of Physics, New York.

Bergqvist, J., Rudolf, F., Maisana, J., Parodi, F., and Rossi, M., 1991, "A Silicon Condensor Microphone with a Highly Perforated Backplate," *1991 Int. Conf. on Solid-State Sensors and Actuators, Dig. Tech. Papers*, New York, IEEE, pp. 266–269.

Bernstein, J., 1992, "A Micromachined Condenser Hydrophone," presented at the IEEE Solid-State Sensor and Actuator Workshop, Hilton Head, SC, pp. 21–25.

Braddick, H., 1966, *The Physics of Experimental Method*, Chapman and Hall, London.

Callen, H., and Welton, T., 1951, "Irreversibility and Generalized Noise," *Phys. Rev.*, Vol. 83, pp. 34–40.

Dandridge, A., Tveten, A., Miles, R., Jackson, D., and Giallorenzi, T., 1981, "Single-Mode Diode Laser Phase Noise," *Appl. Phys. Lett.*, Vol. 38, pp. 77–78.

Fenchel, T., and Finlay, B., 1984, "Geotaxis in the Ciliated Protozoan Loxodes," *J. Exp. Biol.*, Vol. 110, pp. 17–33.

Gabrielson, T., 1993, "Mechanical-Thermal Noise in Micromachined Acoustic and Vibration Sensors," *IEEE Trans. Electron Devices*, Vol. 40, pp. 903–909.

Gardner, D., Hofler, T., Baker, S., Yarber, R., and Garrett, S., 1987,

"A Fiber-Optic Interferometric Seismometer," *J. Lightwave Tech.*, Vol. LT-5, p. 953.

Gray, P., 1967, *Introduction to Electronics*, Wiley, New York.

He, G., and Cuomo, F., 1992, "The Analysis of Noises in a Fiber Optic Microphone," *J. Acoust. Soc. Am.*, Vol. 92, pp. 2521-2526.

Henrion, W., DiSanza, L., Ip, M., Terry, S., and Jerman, H., 1990, "Wide Dynamic Range Direct Digital Accelerometer," *1990 Solid-State Sensor and Actuator Workshop, Tech. Dig.*, New York, IEEE, pp. 153-157.

Henry, C., 1986, "Phase Noise in Semiconductor Lasers," *J. Lightwave Tech.*, Vol. LT-4, pp. 298-311.

Hofler, T., and Garrett, S., 1988, "Thermal Noise in a Fiber Optic Sensor," *J. Acoust. Soc. Am.*, Vol. 84, pp. 471-475.

Hohm, D., and Hess, G., 1989, "A Subminiature Condenser Microphone with Silicon Nitride Member and Silicon Backplate," *J. Acoust. Soc. Am.*, Vol. 85, pp. 476-480.

Horowitz, P., and Hill, W., 1989, *The Art of Electronics*, 2nd ed., Cambridge University Press, New York.

Kinsler, L., Frey, A., Coppens, A., and Sanders, J., *1982 Fundamentals of Acoustics*, 3rd. ed., Wiley, New York.

Kittel, C., 1958, *Elementary Statistical Physics*, Wiley, New York.

Kühnel, W., and Hess, G., 1992, "Micromachined Subminiature Condenser Microphone in Silicon," *Sensors and Actuators A*, Vol. 32, pp. 560-564.

Lax, M., 1991, "The Theory of Laser Noise," *Laser Noise*, Rajarshi Roy, ed., Proc. SPIE, Vol. 1376, pp. 2-20.

Marton, L., and Hornyak, W., 1969, *Methods of Experimental Physics*, Vol. 8, Academic Press, New York.

Mellon, R., 1952, "The Thermal Noise Limit in the Detection of Underwear Acoustic Signals," *J. Acoust. Soc. Am.*, Vol. 24, pp. 478-480.

Misner, C., Thorne, K., and Wheeler, J., 1973, *Gravitation*, Freeman, NY.

Petersen, K., Shartel, A., and Raley, N., 1982, "Micromechanical Accelerometer Integrated with MOS Detection Circuitry," *IEEE Trans. Electron Devices*, Vol. ED-29, pp. 23-27.

Pippard, A., 1989, *The Physics of Vibration*, Cambridge University Press, New York.

Press, W., 1978, "Flicker Noises in Astronomy and Elsewhere," *Comments on Astrophysics*, Vol. 7, pp. 103-119.

Rockstad, H., Kenny, T., Reynolds, J., Kaiser, W., and Gabrielson, T., 1992, "A Miniature High-Sensitivity Broad-Band Accelerometer Based on Electron Tunneling Transducers," DSC Vol. 40, D. Cho, J., Peterson, A. Pisano, and C. Friedrich, eds., ASME, pp. 41-52.

Roylance, L., and Angell, J., 1979, "A Batch-Fabricated Silicon Accelerometer," *IEEE Trans. Electron Devices*, Vol. ED-26, pp. 1911-1917.

Siliconix, 1991, *Low Power Discretes Data Book*, Siliconix Inc., Santa Clara, CA.

Skvor, Z., 1967/1968, "On the Acoustical Resistance Due to Viscous Losses in the Air Gap of Electrostatic Transducers," *Acustica*, Vol. 19, pp. 295-299.

Starr, J., 1990, "Squeeze-Film Damping in Solid-State Accelerometers," *1990 Solid-State Sensor and Actuator Workshop, Tech. Dig.*, IEEE, NY.

Tuinenga, P., 1988, *SPICE: A Guide to Circuit Simulation and Analysis Using PSpice*, Prentice-Hall, Englewood Cliffs, NJ.

Uhlenbeck, G., and Goudsmit, S., 1929, "A Problem in Brownian Motion," *Phys. Rev.*, Vol. 34, pp. 145-151.

Uhlenbeck, G., and Ornstein, L., 1930, "On the Theory of the Brownian Motion," *Phys. Rev.*, Vol. 36, pp. 823-841.

Weissman, M., 1988, "1/f Noise and Other Slow, Nonexponential Kinetics in Condensed Matter," *Rev. Mod. Phys.*, Vol. 60, pp. 537-571.

Wood, T., Linke, R., Kasper, B., and Carr, E., 1988, "Observation of Coherent Rayleigh Noise in Single-Source Bidirectional Optical Fiber Systems," *J. Lightwave Tech.*, Vol. LT-6, pp. 346-351.

RESONANT ULTRASOUND SPECTROSCOPY

Albert Migliori
Los Alamos National Laboratory

ABSTRACT

We describe Resonant Ultrasound Spectroscopy (RUS) for the measurement of elastic moduli. Techniques, data analysis procedures and applications to solid state physics will be covered. Examples of recent measurements, selected for their ability to showcase the usefulness of RUS will be discussed.

REFERENCE

Resonant Ultrasound Spectroscopy, A. Migliori and J. L. Sarrao. (John Wiley, New York, 1997).

ATMOSPHERIC AND METEOROLOGICAL ACOUSTICS

Kenneth E. Gilbert
National Center for Physical Acoustics
University of Mississippi

ABSTRACT

The past 10 years have seen remarkable progress in our ability to understand and predict sound propagation outdoors at audible frequencies over ranges of kilometers. The progress was made possible by two developments that have taken place since 1970. The first development is an improved understanding of the atmospheric boundary layer, which is the medium through which audible sound propagates. The second is a dramatically increased numerical modeling capability resulting from the parabolic equation approximation (a one-way wave equation) for the Helmholtz equation. (a two-way wave equation). The parabolic equation or "PE" has allowed, for the first time with realistic atmospheric models, propagation predictions that can be meaningfully compared to experiment. In the present lecture we will first discuss the basic ideas of boundary-layer meteorology that are needed to understand the dramatic differences between sound propagation in the turbulent daytime boundary layer and the stable nocturnal boundary layer. Once realistic models for the atmosphere have been established, we will outline the physical and mathematical foundations of the PE method, beginning with a one-dimensional Helmholtz equation and progressing to a three-dimensional parabolic equation. Due to time limitations, a simplified approach based on the original PE formulation of Tappert will be followed for most of the lecture. The emphasis will be primarily on physical insight and not mathematical rigor. Generalizations of the Tappert PE that allow for the incorporation of a finite impedance ground surface will be presented but not discussed in detail. Finally, comparisons between experiment and theory will be presented. The extent to which realistic atmospheric models are needed to explain observed acoustic levels will be discussed in some detail.

REFERENCES

R.B. Stull, *An Introduction to Boundary Layer Meteorology*. (Kluwer Academic Publishers, Boston, reprinted 1994).

F.D. Tappert, "The parabolic approximation method," in *Wave Propagation and Underwater Acoustics*, Lecture Notes in Physics, Vol. 70, edited by J.B. Keller and J.S. Papadakis (Springer-Verlag, New York, 1977), Chap. V, pp. 224-287.

THERMOACOUSTICS

Robert M. Keolian
Applied Research Laboratory
Pennsylvania State University

ABSTRACT

It's a bit surprising, but you can cool a six pack with sound. Two ways of doing this will be described. In the first, the traditional standing wave method, we use the fact that heat (entropy to be more correct) is just itching to crawl along the walls of a resonator containing a standing wave. The effect is strongest about halfway between the velocity antinode and the pressure antinode with the heat flowing from the velocity to the pressure antinode. Since the heat pumping occurs in the gas a fraction of a millimeter from a wall, we enhance the effect by adding a lot of surface area in a region between the antinodes, in the form of a stack of plates with gaps lined up along the acoustic axis for the sound to pass through. Heat exchangers, similar to car radiators, are placed on either side of the stack. The one facing the velocity antinode gets cold and the one facing the pressure antinode gets hot, forming a refrigerator. The cold exchanger is used to transfer heat out of a load, such as the six pack, onto the cold end of the stack. The stack pumps the heat up to a higher temperature with the sound oscillating in its gaps. Heat is then deposited on the hot exchanger, which then transmits it out of the resonator to be exhausted externally. A lot of heat can be pumped from cold to hot temperatures this way— enough to cool a house.

A second way of cooling something is with the recently invented thermoacoustic Stirling refrigerator. The Stirling cycle is one of the traditional thermodynamic cycles, often with a gas compressing and expanding and passing through a structure called a regenerator. The regenerator is similar to the stack of plates just described, but with gaps which are quite a bit smaller. It turns out that the desired phasing between the pressure and motion of the gas is the same as that of a traveling acoustic wave. So in the acoustic version of a Stirling cycle, a traveling wave is made to go through the regenerator. To enhance the efficiency of the refrigerator it is also important to increase the pressure swings and decrease the velocity swings of an ordinary traveling wave because the velocity leads to viscous loss in the tight pores of the regenerator. To do this, a high amplitude standing wave is superimposed on the traveling wave

with the pressure swings of both constructively interfering. Heat exchangers are placed on both sides of the regenerator, one getting cold the other getting hot, and used the as described above for the traditional thermoacoustic refrigerator. The Stirling version has quickly achieved rather impressive efficiencies, about the equivalent of a household refrigerator.

Both of these thermoacoustic refrigerators can be used "backwards"—instead of using sound energy to pump heat from cold to hot, they can generate sound energy by allowing heat to flow from hot to cold. This can be used to generate sound, which can then be used to power a thermoacoustic refrigerator, making a heat powered refrigerator. Such a device could be powered by fuel, sunlight, or the waste heat of some other process, instead of electricity.

All of these devices are relatively simple in their construction, with few or no moving parts. Plus they do not use any of the various chlorofluorocarbons or their alternatives, which are both harmful to the ozone layer and contribute to global warming. Instead, the working gas is typically helium, or helium mixed with argon or xenon, or even air. Refrigeration is a huge industry, $750 billion per year worldwide, and thermoacoustics is one of the very few alternatives to conventional vapor compression refrigeration, which is under increasing environmental pressure.

For references that you may look at in preparation for the summer school, I have included two short articles. The Physics Today review covers the state of affairs as of five years ago. The recent Letter to Nature briefly describes the Stirling thermoacoustic heat engine, which is configured as a sound source rather than a refrigerator. You might also download thermoacoustic animations from the Los Alamos Thermoacoustics web site at http://www.lanl.gov/thermoacoustics/. They are quite nice and I intend on using them in the summer school. Those should keep you busy. However, if you want more, there is another review available, G. W. Swift "Thermoacoustic Engines and Refrigerators," Encyclopedia of Modern Physics, V. 21, pp. 245-264, 1997, which contains more detail than the 1995 review. And at the web site you can also download a draft of Greg Swift's textbook on thermoacoustics.

PHYSICS TODAY

THERMOACOUSTICS
50

THERMOACOUSTIC ENGINES AND REFRIGERATORS

On the heels of basic research, commercial developers are harnessing acoustic processes in gases to make reliable, inexpensive engines and cooling devices with no moving parts and a significant fraction of Carnot's efficiency.

Gregory W. Swift
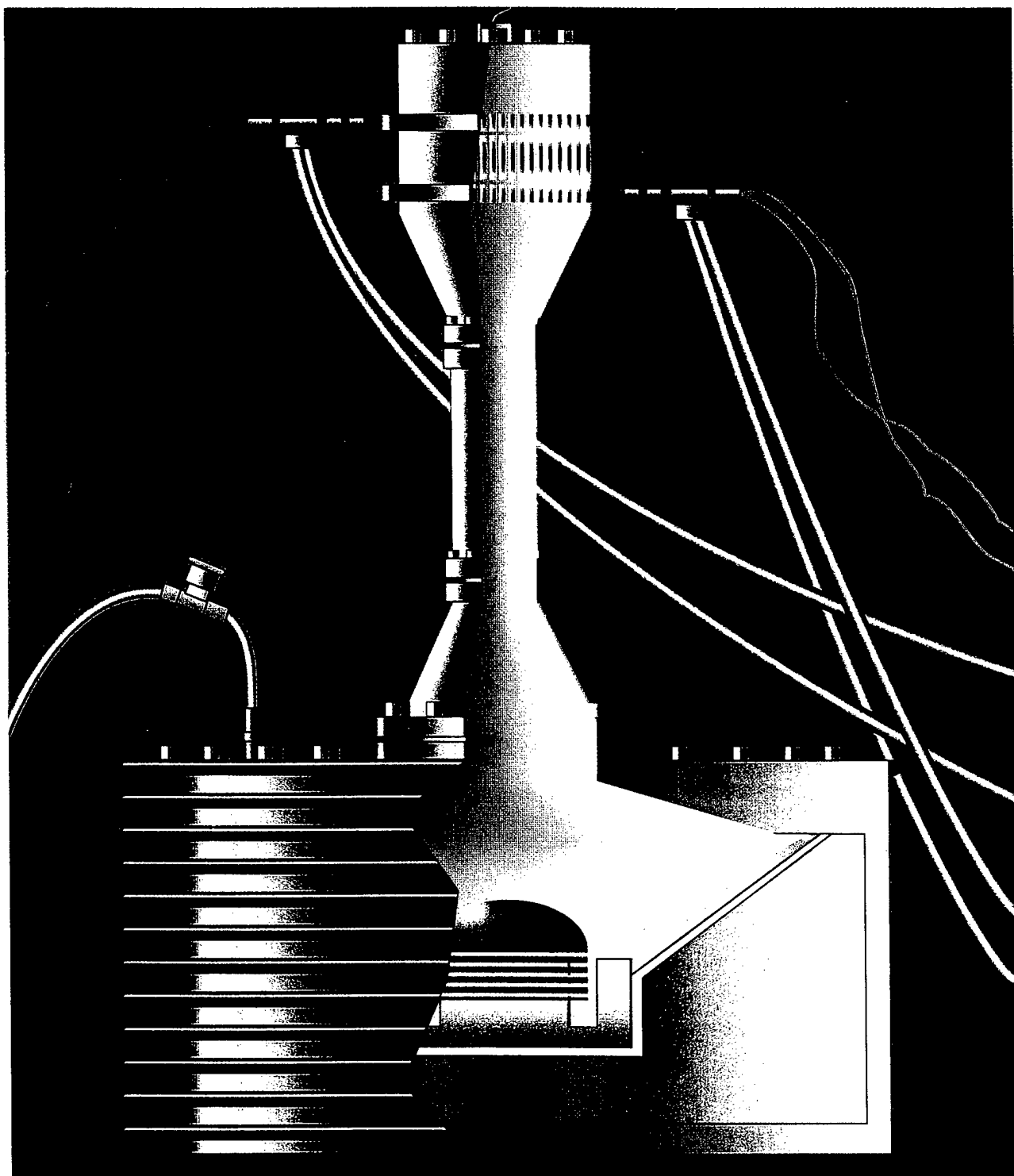
We ordinarily think of a sound wave in a gas as consisting of coupled pressure and displacement oscillations. However, temperature oscillations always accompany the pressure changes. The combination of all these oscillations, and their interaction with solid boundaries, produces a rich variety of "thermoacoustic" effects. Although these effects as they occur in everyday life are too small to be noticed, one can harness extremely loud sound waves in acoustically sealed chambers to produce powerful heat engines, heat pumps and refrigerators. Whereas typical engines and refrigerators have crankshaft-coupled pistons or rotating turbines, thermoacoustic engines and refrigerators have at most a single flexing moving part (as in a loudspeaker) with no sliding seals. Thermoacoustic devices may be of practical use where simplicity, reliability or low cost is more important than the highest efficiency (although one cannot say much more about their cost-competitiveness at this early stage).

The basics: Thermoacoustic engines

A thermoacoustic engine converts some heat from a high-temperature heat source into acoustic power, rejecting waste heat to a low-temperature heat sink. The heat-driven electrical generator shown in figure 1 illustrates the basic principle of operation. The overall view, shown at the top of figure 1a, is reminiscent of the appearance of a heat engine in many introductory thermodynamics texts: The apparatus absorbs heat per unit time Q_h from a heat source at high temperature T_h, rejects heat per unit time Q_c to a heat sink at low temperature T_c and produces acoustic power W. The first law of thermodynamics tells us that $W + Q_c = Q_h$; the second law shows that the efficiency W/Q_h is bounded above by the Carnot efficiency $(T_h - T_c)/T_h$. (I will use Q and W for heat power and acoustic power, and q and w for the corresponding energies.)

One of the most important scales in a thermoacoustic device is the length of its resonator, which (together with the gas sound speed) determines the operating frequency, just as the length of an organ pipe determines its pitch. This length typically falls between 10 cm and 10 m. In figure 1a, with both ends of the resonator closed, the lowest resonant mode is that which fits a half-wavelength

standing wave in the resonator, with displacement nodes and pressure antinodes at the ends, as shown in the lower portion of figure 1. The heat-exchange elements—a hot heat exchanger, a cold heat exchanger and a "stack" between them—are located where both oscillating pressure and oscillating gas displacement are nonzero. Each of the two heat exchangers is typically a set of copper fins, as open to gas flow as possible (like a car radiator), and is thermally anchored to its reservoir by metallic heat conduction or circulating fluids. The stack is simply a well-spaced stack of solid plates with high heat capacity, also quite open to gas flow, supporting the smooth temperature profile between the two heat exchangers as shown at the bottom of figure 1a. Most of the "parallel plate" stacks constructed so far have in fact been spirally wound, a low-cost configuration.

To understand in some detail the conversion of heat to acoustic power by this simple structure, consider the magnified view of part of the stack in figure 1b, which shows a typical parcel of gas at four instants of time during one cycle of the acoustic wave. The standing wave carries the parcel left and right, compressing and expanding it, with phasing such that it is at its most compressed state when at its farthest left position, and its most expanded state at its farthest right position. In typical thermoacoustic engines and refrigerators the amplitude of the pressure oscillation is 3–10% of the mean pressure, and the displacement amplitude is a similar percentage of the length of a plate in the stack.

The presence of an externally imposed temperature gradient in the stack adds a new feature to what would otherwise be a simple acoustic oscillation: oscillatory heat transfer between the parcel of gas and the stack. (To simplify this discussion, I will neglect the adiabatic temperature oscillations that accompany the pressure oscillations.) When the parcel is at its leftmost position, heat flows from the relatively hot stack plate to the parcel, expanding it; when the parcel is at its rightmost position, heat flows from it to the relatively cool stack plate, contracting the parcel. The parcel does net work on its surroundings, because the expansion takes place at the high-pressure phase of the cycle and the contraction at the low-pressure phase, as shown in figure 1c.

(Readers with Internet access are encouraged to view our computer animations of this process and of thermoacoustic refrigeration as described below. The thermoacoustics home page is at http://rott.esa.lanl.gov/; select "educational

GREGORY SWIFT *works in the condensed matter and thermal physics group at Los Alamos National Laboratory, in New Mexico.*

51
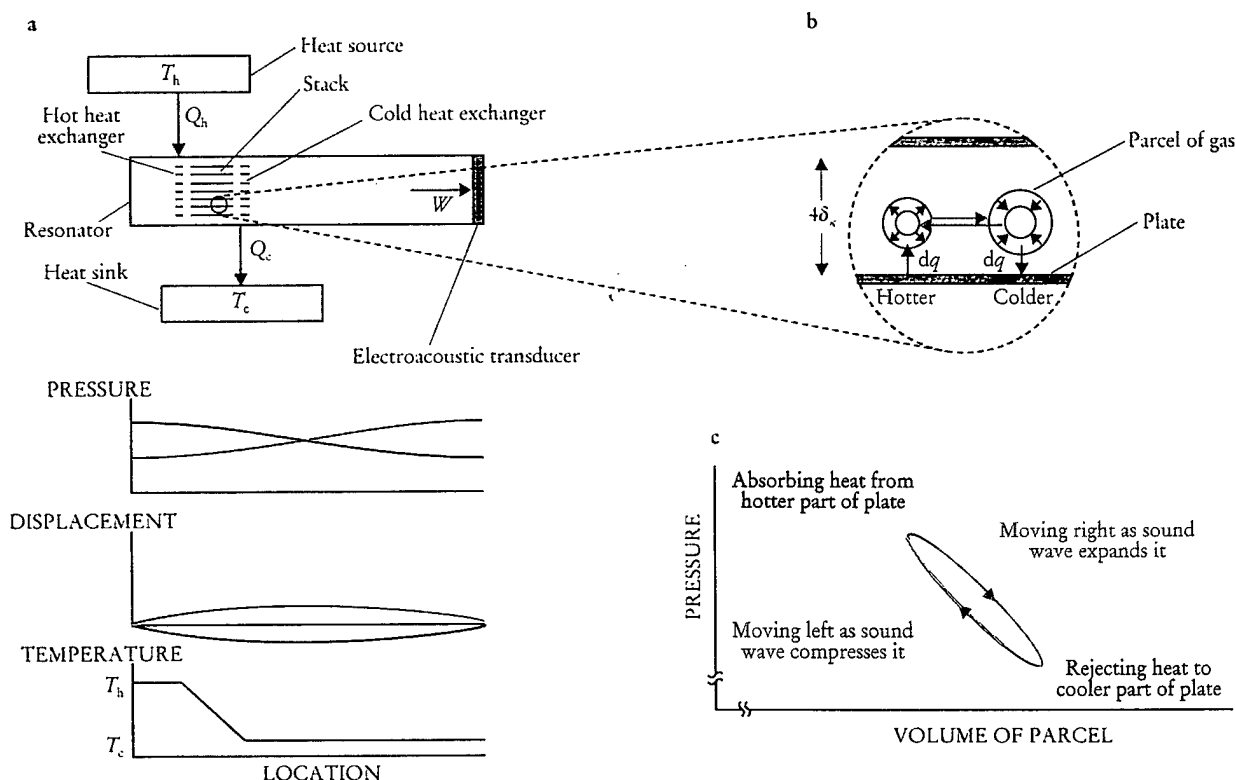
SIMPLE THERMOACOUSTIC ENGINE. a: Heat exchangers and a stack in a half-wavelength acoustic resonator convert some of the heat power Q_h from a thermal reservoir at temperature T_h into acoustic power W, rejecting waste heat power Q_c to another reservoir at T_c. The acoustic power is delivered to an electroacoustic transducer, which converts it to electricity. Plots below show gas pressure, gas displacement in the horizontal direction and average temperature as functions of location in the resonator. Pressure and displacement are each shown when the gas is at the leftmost extreme of its displacement (red), with density and pressure highest at the left end of the resonator and lowest at the right end, and 180° later in the cycle (blue). b: Magnified view of part of the stack shows a typical parcel of gas (greatly exaggerated in size) as it oscillates in position, pressure and temperature, exchanging heat dq with the nearby plates of the stack. Plates are separated by about four thermal penetration depths δ_κ. c: Pressure–volume (p–V) diagram for the parcel of gas shows how it does net work $\delta w = \oint p\, dV$ on its surroundings. FIGURE 1

demonstrations." For DOS-based computers, the executable file FANCY.EXE and text file FANCY.TXT can be downloaded.)

The net work that the parcel does on its surroundings is delivered in each cycle of the acoustic oscillation. The parcel and all others like it within the stack deliver acoustic power W to the standing wave; the standing wave delivers it in turn to the electroacoustic transducer. Each parcel absorbs a little heat from one location in the stack and deposits a little heat farther to the right, at a cooler location in the stack. With respect to heat, all the parcels act like members of a bucket brigade, with the overall effect being absorption of Q_h at the hot heat exchanger and rejection of Q_c at the cold heat exchanger.

A second important scale in a thermoacoustic engine is the separation between plates in the stack, which determines the nature of thermal contact between the plate and the typical parcel of gas. Imperfect thermal contact is needed to accomplish the cycle shown in figure 1, because it is desirable to have good thermal contact when the parcel is stationary or nearly so, but poor thermal contact while it is moving. Detailed analysis shows that a spacing between plates of about four thermal penetration depths $\delta_\kappa = \sqrt{\kappa/\pi f \rho c_p}$ is best, where κ is the thermal conductivity of the gas, ρ is its density, c_p its isobaric specific heat per unit mass and f the frequency of the acoustic oscillation; δ_κ is roughly the distance heat can diffuse through the gas during a time $1/\pi f$. In today's

thermoacoustic systems, δ_κ is typically a fraction of a millimeter.

Heat-driven acoustic oscillators such as that shown in figure 1 have been known for over a century. The earliest and simplest, known as the Sondhauss tube, was discovered accidentally by European glassblowers; a later example, the Taconis oscillator, is well known today to users of liquid helium. In each of these early thermoacoustic engines, the resonator itself was only several δ_κ in diameter, and its walls also served the functions of stack and heat exchangers. The use of an explicit stack (with multiple parallel passages) and heat exchangers in larger-diameter resonators to increase overall power began with Robert L. Carter in the 1960s.[1]

Although progress toward a theoretical understanding of these phenomena began with Lord Rayleigh 120 years ago, a quantitatively accurate theory of thermoacoustics was not developed until the 1970s, through the efforts of Nicholas Rott and coworkers.[2] This theory is based on a low-amplitude linearization of the Navier–Stokes, continuity and energy equations with sinusoidal oscillations of all variables. It is remarkable that such qualitatively simple classical phenomena went without a quantitatively accurate explanation until late in this century.

The basics: Thermoacoustic refrigerators

Another chapter in the development of thermoacoustics began at Los Alamos National Laboratory in the early

52
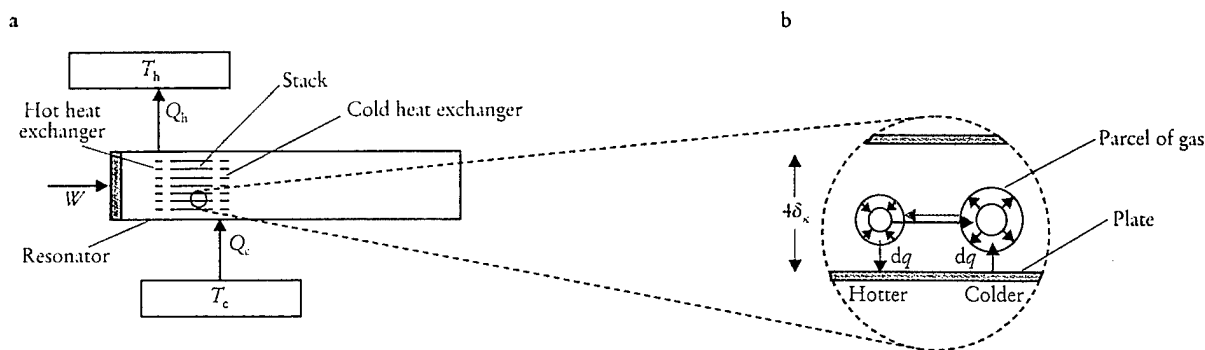
SIMPLE THERMOACOUSTIC REFRIGERATOR. a: Electroacoustic transducer at the left end delivers acoustic power W to the resonator, producing refrigeration Q_c at low temperature T_c and rejecting waste heat power Q_h to a heat sink at T_h. As in figure 1, this is a half-wavelength device with a pressure node at the midpoint of the resonator. The temperature gradient in the refrigerator's stack is much less steep than that in the stack for the engine shown in figure 1. b: Magnified view of part of the stack shows a typical parcel of gas as it moves heat dq up the temperature gradient. Here $\oint p\,dV < 0$, so the pressure–volume cycle analogous to figure 1c goes counterclockwise, and the parcel absorbs work·from its surroundings. FIGURE 2

1980s with the invention of thermoacoustic refrigeration.[3] The basic principle of operation, illustrated in figure 2, is very similar to that of thermoacoustic engines, but here the temperature gradient in the stack is much lower. As the gas oscillates along the stack, it experiences changes in temperature. Much of the gas's temperature change comes from adiabatic compression and expansion of the gas by the acoustic pressure, and the rest is a consequence of heat transfer with the stack. At the leftmost position of the parcel of gas shown in figure 2b, it rejects heat to the stack, because its temperature was raised above the local stack temperature by adiabatic compression caused by the standing wave. Similarly, at its rightmost position, the parcel absorbs heat from the stack, because adiabatic expansion has brought its temperature below the local stack temperature. Thus the parcel of gas moves a little heat from right to left along the stack, up the temperature gradient, during each cycle of the acoustic wave.

All the other parcels in the stack behave similarly, so that the overall effect, again as in a bucket brigade, is the net transport of heat from the cold heat exchanger to the hot heat exchanger, with Q_c absorbed at T_c and Q_h rejected at T_h. The parcel absorbs acoustic work from the standing wave, because the thermal expansion of the parcel of gas occurs during the low-pressure phase of the acoustic wave and the thermal contraction during the high-pressure phase. The resulting acoustic power W absorbed by all the parcels in the stack can be supplied by a loudspeaker, a thermoacoustic engine or other means. The first law of thermodynamics once again determines that $W + Q_c = Q_h$; the second law shows that the relevant efficiency, known as the coefficient of performance, is bounded above by the Carnot coefficient $T_c/(T_h - T_c)$.

The steepness of the temperature gradient in the stack determines whether a thermoacoustic device is a refrigerator (which has work done on it) or an engine (which does work). In an engine, with a steep temperature gradient as shown in figure 1, the gas parcel finds itself cooler than the local stack temperature after its adiabatic compression during displacement to the left, so it absorbs heat from the stack at high pressure and expands. In contrast, in a refrigerator, with a shallow gradient, the gas parcel finds itself warmer than the local stack temperature after its adiabatic compression during displacement to the left, so it rejects heat to the higher-temperature part of the stack and contracts.

Figure 3a shows schematically the first efficient thermoacoustic refrigerator,[4] designed, built and studied by Tom Hofler. It illustrates several features of many of today's thermoacoustic devices. The resonator had a slightly complicated geometry, which maintained the desired frequency, pressure amplitude and displacement amplitude at the stack while reducing the total length to much less than half the wavelength. This geometry also reduced viscous and thermal losses on the resonator walls and suppressed the harmonic content so that the sound wave remained purely sinusoidal in time. The pressure antinode is at the driver piston, and the pressure node is at the widening neck near the sphere, so this is essentially a quarter-wavelength apparatus, even though the spatial dependence of the pressure is not exactly a cosine. High-pressure helium gas was used: High pressure increases the power per unit volume of apparatus, and helium, having the highest sound speed and thermal conductivity of the inert gases, further increases the power density and allows spacings within the stack and heat exchangers to be as large as possible, for ease of fabrication. The loudspeaker-like driver was located at a pressure antinode of the standing wave, so that the acoustic power was delivered with high force and small displacement, easing engineering difficulties associated with the flexing portion of the driver. This location also placed it next to the hot heat exchanger, where heat generated in the driver could be removed most efficiently.

Figure 3b shows some of the data obtained with this refrigerator, which reached a T_c of −70 °C and had a cooling power of several watts with acoustic pressure amplitudes of 3% of the mean pressure. The curves in the figure were calculated using publicly available software[5] based on the theory developed by Rott and are in reasonable agreement with the data. The calculations have no adjustable parameters; they simply use the geometry of the apparatus and the properties of helium gas.

Commercial developments

Attempts to develop practical devices based on thermoacoustics began just a few years ago, throughout the US and on four other continents. This surge of interest was due to the interaction of several factors: the new "tech transfer" emphasis at government laboratories; the engineering development of some thermoacoustic refrigerators at the Naval Postgraduate School in Monterey, California,

53

under the enthusiastic leadership of Steve Garrett; the crisis in the refrigeration industry caused by the destruction of stratospheric ozone by chlorofluorocarbons; and the marriage of thermoacoustic engines with orifice pulse-tube refrigerators (discussed below). To illustrate the breadth of applications under way, I have chosen four examples from among the corporate-sponsored thermoacoustics projects that I know of.

The thermoacoustic refrigerator shown in figure 4a is a prototype for a food refrigerator. Built at CSIR (formerly called the Council for Scientific and Industrial Research) in the Republic of South Africa with corporate support, it is a direct descendant of a thermoacoustic refrigerator[6] that was originally intended for preserving blood and urine samples on the space shuttle. It is a symmetrical, essentially half-wavelength device driven by modified loudspeakers on both ends, with two stacks, each with two heat exchangers. The pressure node is at the center of the bottom section. Use of two stacks maximizes cooling power for a given resonator size, all other things being equal. For compactness, the fiberglass resonator is formed in a "U" shape, with little effect on the acoustics. Cooling power (typically 100 W) and temperatures are appropriate for residential food refrigeration in most of the world. (American refrigerators are larger than most and hence require about twice as much cooling power.)

Scientists at Ford Motor Company built the thermoacoustic refrigerator depicted on the cover of this issue. The driver is at the displacement maximum of the quarter-wavelength standing wave (instead of at the pressure maximum as in the refrigerators of figures 3a and 4a). Thus in this refrigerator acoustic power is delivered with small pressure and large volumetric displacement, accom-

plished by using a large area in the driver. The driver's losses flow to the cold heat exchanger, but this is a minor problem if the driver is efficient and T_c is not too far below T_h. Water inlet and outlet tubes (gray in the diagram), essentially serving as the hot and cold thermal reservoirs, are clearly visible at the heat exchangers. This device operates at 10 bars with either helium driven at 430 Hz or a mixture of 80% helium—20% argon driven at 260 Hz.

At Tektronix Corporation in Beaverton, Oregon, researchers are developing a system for cooling electronics to cryogenic temperatures. A thermoacoustic engine drives an orifice pulse-tube refrigerator,[7] which is related to both Stirling and thermoacoustic refrigerators. The system thus constitutes a heat-driven cryogenic refrigerator having no moving parts; it has cooled to 150 K. It has a half-wavelength resonator with resistively heated thermoacoustic engines near both ends. In a sidebranch, 500 W of acoustic power from these engines is delivered to the pulse-tube refrigerator.

The largest thermoacoustic engine to date, under construction at Cryenco Inc in Denver, Colorado, will also drive a pulse-tube refrigerator. The heat source for the engine will be natural gas combustion. Intended for industrial and commercial liquefaction of natural gas it will measure 12 meters long, and will use two ½-meter-diameter spiral stacks (figure 4b) to produce 40 kW of acoustic power at 40 Hz in 30-bar helium gas. The device should be completed this year.

Power and efficiency

The power of thermoacoustic devices is roughly proportional to $p_{avg} A a (p_{osc}/p_{avg})^2$, where p_{avg} is the average pressure, A the cross-sectional area of the stack, a the sound
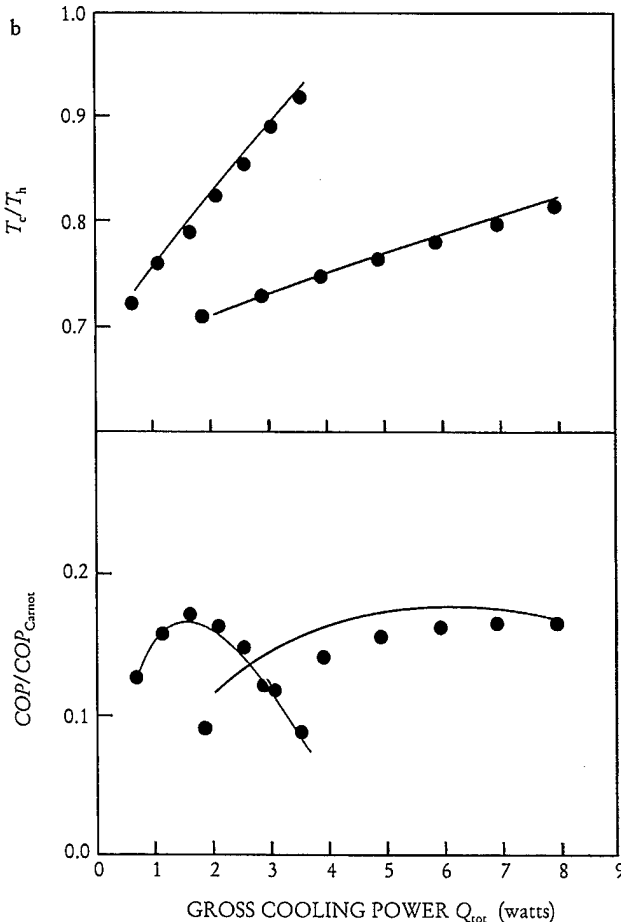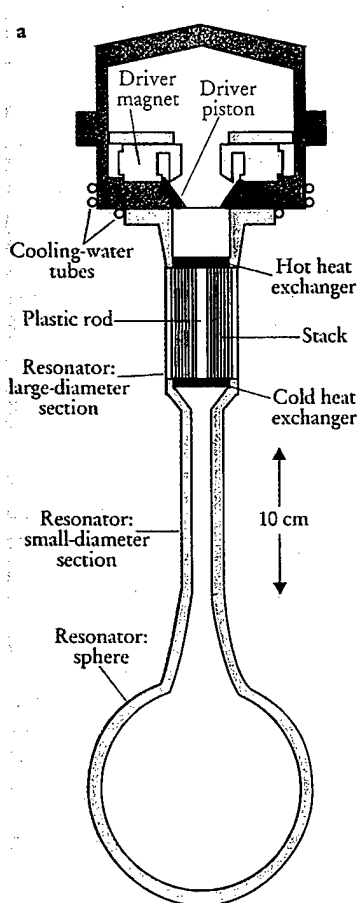
FIRST EFFICIENT THERMOACOUSTIC REFRIGERATOR (a) and some of its performance parameters (b) as measured[4] (data points) and calculated[5] (curves) for operation with 500-Hz pressure oscillations in 10-bar helium gas, and with T_h = 300 K. Blue circles are data for 1.5% pressure oscillations; red circles, 3%. The gross cooling power Q_{tot} includes the deliberately applied load plus some small parasitic loads such as heat leak from room temperature. The coefficient of performance (COP) equals Q_{tot}/W, with W the acoustic power delivered to the resonator. FIGURE 3

a

b

▷ Inherent loss arises from the heat transfer to and from each parcel of gas in the stack as shown in figures 1 and 2: Whenever heat dq is transferred across a nonzero temperature difference δT, the entropy of the universe increases[8] by $dq\, \delta T/T^2$. This irreversibility is unavoidable in the thermoacoustic process, relying as it does on imperfect thermal contact for the correct phasing between pressure oscillations and thermal expansion–contraction.

▷ Viscous loss in the stack occurs because work must be done to overcome viscous shear forces as the gas oscillates between the plates. The viscous penetration depth $\delta_\mu = \sqrt{\mu/\pi f \rho}$ (where μ is viscosity) is comparable to the thermal penetration depth, so most of the space between the plates experiences significant viscous shear (and the parcels in figures 1 and 2 actually experience significant shape distortions).

▷ Simple heat conduction from the hot heat exchanger to the cold one through the stack material and the gas is a further loss.

▷ These first three losses also occur in auxiliary parts of a thermoacoustic system: Viscous and inherent losses in the heat exchangers and conduction loss in the portion of the resonator case surrounding the stack are usually the most important auxiliary losses in large systems, while viscous and inherent losses on other surfaces in the resonator are important in small systems.

▷ Electroacoustic power transducers introduce additional loss. For the refrigerators shown on the cover and in figures 3a and 4a, the dominant transducer loss is Joule heating in the copper wires of the loudspeakers.

For many high-power-density designs, the first four sources of irreversibility contribute roughly equally to the inefficiency of thermoacoustic devices. About 40% of Carnot's efficiency is typical of the best current designs, using computer modeling based on Rott theory, for both engines and refrigerators; higher efficiencies are possible if power density is sacrificed, and lower efficiencies are the reality when electroacoustic transduction losses, losses in auxiliary equipment and deviations from Rott theory at high amplitudes are included. The most efficient engine built to date delivered acoustic power to its load at 23% of Carnot's efficiency (based on total heater power); the most efficient refrigerator[9] provided gross cooling power at 20% of Carnot (based on acoustic power delivered to the resonator). These efficiencies are impressive for devices with no moving parts, and they are comparable to the efficiencies of small, inexpensive commercial equipment. They

speed of the gas and p_{osc} the amplitude of the oscillatory pressure. Helium (with high sound speed) is often used, typically at a pressure above 10 bars. In the examples cited in the previous section, p_{osc}/p_{avg} values range from 0.03 to 0.10, chosen as design compromises between the high power density achieved at high amplitude and the high confidence in the quantitative accuracy of Rott-based calculations at low amplitude.

The efficiency of thermoacoustic devices falls below Carnot's efficiency because of five major sources of irreversibility—"inherent," viscous, conduction, auxiliary and transduction losses:
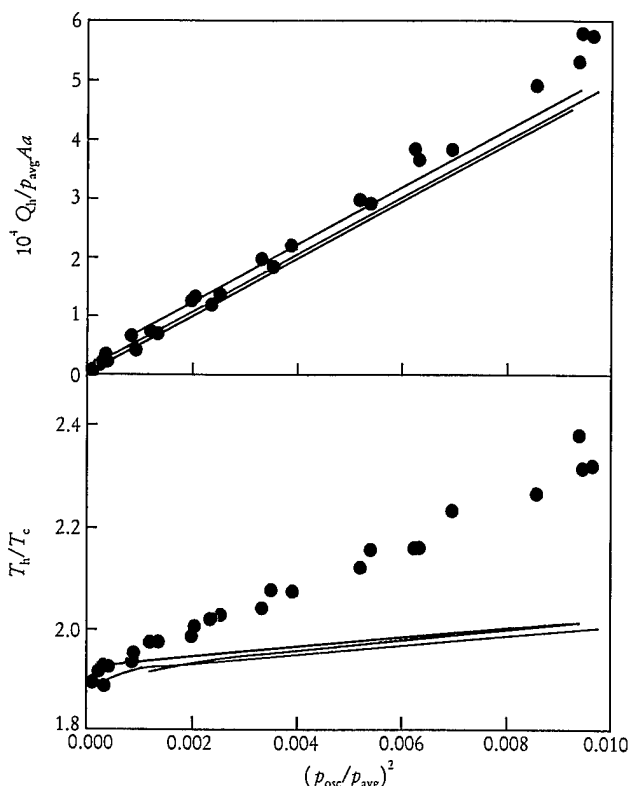
RECENT MEASUREMENTS AND CALCULATIONS for a thermoacoustic engine similar to that shown in figure 1, but with no transducer. The heater power Q_h, hot temperature T_h and oscillating pressure amplitude p_{osc} are all normalized, but note the different vertical scales. Circles are measurements from ref. 16; lines are calculations done using ref. 5. Red is for helium at 0.96 megapascals; green, neon at 0.70 MPa; blue, argon at 0.359 MPa. These pressures were chosen to make the thermal penetration depth δ_κ equal to 0.22 mm at the cold end (T_c) in all cases. FIGURE 5

---

fall far short of the efficiencies of well-engineered, expensive steam turbines or large-scale vapor-compression refrigeration equipment, for which over 80% of Carnot's efficiency has been achieved.

If future inventions and improvements to basic understanding can improve the efficiency or raise the power density of thermoacoustic engines and refrigerators without sacrificing their simplicity, they will find more widespread use. One way to increase efficiency, first demonstrated by Hofler,[4] is to use a mixture of helium and a heavier inert gas as the working substance. The Prandtl number $\sigma = \mu c_p / \kappa = \delta_\mu^2 / \delta_\kappa^2$ is a dimensionless measure of the ratio of viscous to thermal effects in fluids; lower Prandtl numbers give higher efficiencies in thermoacoustics. Kinetic theory predicts $\sigma = \frac{2}{3}$ for hard-sphere monatomic gases, and indeed real monatomic gases have values very close to this. (For instance, helium at room temperature has $\sigma = 0.68$.) Fortunately mixtures of a heavy and a light monatomic gas have Prandtl numbers significantly lower than $\frac{2}{3}$. The thermoacoustic refrigerator intended for the space shuttle that was mentioned above[6] used 89% helium and 11% xenon, with $\sigma = 0.27$, to achieve its 20% efficiency, compared with 17% efficiency for the similar apparatus shown in figure 3 when optimized for pure helium gas. However, with a sound speed less than half that of pure helium, the gas mixture reduced the power density.

Beyond the basics

In the US our understanding of thermoacoustics is advancing beyond the foundations established by Rott, thanks to physicists at many universities and national laboratories.

Rott and his collaborators considered two geometries for thermoacoustic processes: parallel-plate channels (most commonly used, as we have discussed above) and circular channels. Wondering if some geometries might be better than others, W. Patrick Arnott, Henry Bass and Richard Raspet[10] at the University of Mississippi added rectangular and triangular channels, established a common formalism for all channel geometries and concluded that parallel-plate channels are the most efficient. The reason is subtle: Viscous losses occur mostly at and near channel walls, within a characteristic distance equal to the viscous penetration depth δ_μ, while the desirable thermoacoustic effects portrayed in figures 1 and 2 occur mostly away from walls, at a characteristic distance equal to the thermal penetration depth δ_κ from them. Thus for the usual case of $\delta_\mu \approx \delta_\kappa$, extremely concave channels (imagine triangles) squeeze the desirable effects into a small fraction of the channel cross-sectional area in the center, leaving a relatively large area near the perimeter causing viscous loss. Capitalizing on this analysis, Ulrich Müller has proposed that the "channels" formed by the space in a two-dimensional array of parallel wires[11] (aligned along the direction of acoustic oscillation and spaced by a few δ_κ) would give even higher efficiency than parallel plates. Tapered channels[12] and modifications of the phase between pressure and velocity[13] are also being studied for improving efficiency.

The most promising route to higher power densities is increasing $(p_{osc}/p_{avg})^2$, but doing so will take us further from the range of small oscillations on which Rott theory and its current extensions are fundamentally based. Rott's assumptions include the following:
▷ a gas displacement amplitude much smaller than the length of the stack and other components
▷ a Reynolds number of the oscillations small enough to avoid turbulence
▷ $p_{osc} \ll p_{avg}$.
Extensions beyond each of these limitations have begun.

At the Naval Postgraduate School, Anthony Atchley and his colleagues[14] have undertaken high-amplitude experiments on the simplest possible thermoacoustic device, a short stack with no heat exchangers in a loudspeaker-driven resonator. Their data extend into the large-gas-displacement regime, with amplitudes approaching the length of the stack.

A growing body of literature is establishing the characteristics of several regimes of turbulent oscillatory flow[15] at high Reynolds numbers, although as yet there are no fundamental studies of heat transfer under these conditions.

A similitude study has shown[16] how to organize and correlate experimental data in the high-amplitude range, allowing meaningful experimental studies of scale models of thermoacoustic devices reminiscent of wind-tunnel studies of model aircraft.

Researchers at several institutions, including Johns Hopkins University and Los Alamos and Livermore National Laboratories, are beginning numerical and analytical studies that seek to illuminate other features of high-amplitude thermoacoustics.

56

Figure 5 illustrates the amplitude dependence of the accuracy of our current understanding of thermoacoustic phenomena. The data shown as points were taken from a no-load thermoacoustic engine.[16] The plots can be interpreted as displaying the required heater power Q_h and temperature T_h at the hot heat exchanger for maintaining steady oscillations at a given pressure amplitude p_{osc}. Three monatomic gases were used, with average pressures selected to make δ_κ the same for all three cases, ensuring similarity; the data for all three gases do indeed fall along the same curves. The lines are the results of calculations based on Rott's theory, the dimensions of the apparatus and the properties of the gases. The calculations agree well with the measurements in the limit of small p_{osc}, as expected from the assumptions in the theory. However, as p_{osc}/p_{avg} approaches 0.1, the measurements deviate significantly from calculations. The deviations are not surprising, in that they are of the same order as p_{osc}/p_{avg}, but they are disturbing from a practical point of view because both Q_h and T_h deviate in directions that decrease the efficiency.

The fundamentals of thermoacoustics at low amplitudes are reasonably well understood, and a few practical uses of thermoacoustics have been tentatively identified. Much study, engineering and especially invention remains to be done before these simple, elegant devices reach their full potential.

References

1. K. T. Feldman, J. Sound Vib. **7**, 71 (1968).
2. N. Rott, Z. Angew. Math Phys. **20**, 230 (1969); **26**, 43 (1975). Reviewed by G. W. Swift, J. Acoust. Soc. Am. **84**, 1145 (1988).
3. J. C. Wheatley, T. J. Hofler, G. W. Swift, A. Migliori, J. Acoust. Soc. Am. **74**, 153 (1983).
4. T. J. Hofler, PhD dissertation, U. Calif., San Diego (1986). T. J. Hofler, in *Proc. 5th Int. Cryocoolers Conf.*, P. Lindquist, ed., Wright–Patterson Air Force Base, Ohio (1988), p. 93.
5. W. C. Ward, G. W. Swift, J. Acoust. Soc. Am. **95**, 3671 (1994). Fully tested software and users guide available from Energy Science and Technology Software Center, US Dept. of Energy, Oak Ridge, Tenn. For a beta-test version, contact ww@lanl.gov (Bill Ward) via Internet.
6. S. L. Garrett, D. K. Perkins, A. Gopinath, in *Heat Transfer 1994: Proc. 10th Int. Heat Transfer Conf.*, G. F. Hewitt, ed., Inst. Chem. Eng., Rugby, UK (1994), p. 375.
7. R. Radebaugh, Adv. Cryogenic Eng. **35**, 1191 (1990).
8. A. Bejan, *Entropy Generation Through Heat and Fluid Flow*, Wiley, New York (1982).
9. S. L. Garrett, J. A. Adeff, T. J. Hofler, J. Thermophys. Heat Transfer **7**, 595 (1993).
10. W. P. Arnott, H. E. Bass, R. Raspet, J. Acoust. Soc. Am. **90**, 3228 (1991).
11. U. A. Müller, US patent 4 625 517 (1986). G. W. Swift, R. M. Keolian, J. Acoust. Soc. Am. **94**, 941 (1993).
12. N. Rott, G. Zouzoulas, Z. Angew. Math. Phys. **27**, 197 (1976). U. A. Müller, PhD dissertation 7014, Eidgenössische Technische Hochschule, Zurich, Switzerland (1982).
13. R. Raspet, H. E. Bass, J. Kordomenos, J. Acoust. Soc. Am. **94**, 2232 (1993). P. H. Ceperley, J. Acoust. Soc. Am. **66**, 1508 (1979).
14. A. A. Atchley, T. J. Hofler, M. L. Muzzerall, M. D. Kite, C. Ao, J. Acoust. Soc. Am. **88**, 251 (1990).
15. R. Akhavan, R. D. Kamm, A. H. Shapiro, J. Fluid Mech. **225**, 395, 423 (1991).
16. J. R. Olson, G. W. Swift, J. Acoust. Soc. Am. **95**, 1405 (1994). ■

A thermoacoustic Stirling heat engine

S. Backhaus & G. W. Swift

Condensed Matter and Thermal Physics Group, Los Alamos National Laboratory, Los Alamos, New Mexico 87545, USA

Electrical and mechanical power, together with other forms of useful work, are generated worldwide at a rate of about 10^{12} watts, mostly using heat engines. The efficiency of such engines is limited by the laws of thermodynamics and by practical considerations such as the cost of building and operating them. Engines with high efficiency help to conserve fossil fuels and other natural resources, reducing global-warming emissions and pollutants. In practice, the highest efficiencies are obtained only in the most expensive, sophisticated engines, such as the turbines in central utility electrical plants. Here we demonstrate an inexpensive thermoacoustic engine that employs the inherently efficient Stirling cycle[1]. The design is based on a simple acoustic apparatus with no moving parts. Our first small laboratory prototype, constructed using inexpensive hardware (steel pipes), achieves an efficiency of 0.30, which exceeds the values of 0.10–0.25 attained in other heat engines[5,6] with no moving parts. Moreover, the efficiency of our prototype is comparable to that of the common internal combustion engine[2] (0.25–0.40) and piston-driven Stirling engines[3,4] (0.20–0.38).

We plan to acoustically couple our thermoacoustic Stirling engines to pulse tube refrigerators[7], to provide efficient and maintenance-free combustion-powered cryogenic refrigeration having no moving parts, in order to liquefy natural gas[8]. This would enable economic recovery of 'associated gas', a by-product of oil production, which is currently burned ('flared') in vast quantities at remote oil fields worldwide, wasting fossil fuel and contributing to global warming. We expect our engine to find many additional uses throughout the global power-production environment, ranging from the separation of air into nitrogen and oxygen to the generation of electricity.

Ceperley[9,10] made the initial step towards this new engine, when he realized that gas in an acoustic travelling wave propagating through a regenerative heat exchanger (regenerator) undergoes a thermodynamic cycle similar to the ideal Stirling cycle; this is because the oscillations of pressure (p_1) and volumetric velocity (U_1) are temporally in phase in a travelling wave. We use the conventional anticlockwise phasor notation[11], so that time-dependent variables are expressed as

$$\xi(t) = \xi_m + \mathrm{Re}[\xi_1 e^{i\omega t}] \tag{1}$$

with the mean value ξ_m real, and with ξ_1 complex, to account for both the magnitude and phase of the oscillation at angular frequency ω. The net work performed in the cycle manifests itself as an increase in the time-averaged acoustic power $\dot{W} = \mathrm{Re}[p_1 \tilde{U}_1]/2$ of the wave as it passes through the regenerator. (The tilde denotes complex conjugate.) Although Ceperley's experiments never achieved power gain, he provided a key insight[12] for constructing a useful thermoacoustic Stirling engine. If a pure travelling wave were used, the ratio of acoustic pressure to volume velocity would be

58
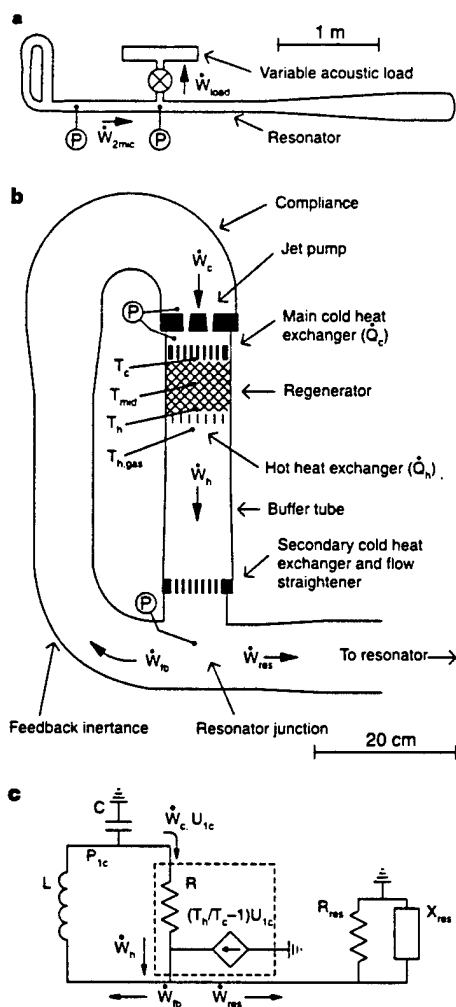
Figure 1 The thermoacoustic Stirling heat engine, constructed from steel pipe. **a,** Scale drawing of the engine. The variable acoustic load consists of an adjustable valve leading to a 2.2-l tank[20]. The valve setting controls the acoustic power flowing into the load $\dot{W}_{load}$, and hence T_h. Piezoresistive pressure sensors 'P' allow measurement of[20] the acoustic power flowing past their midpoint, $\dot{W}_{2mic}$. **b,** Details of the torus-shaped section. The regenerator is a stack of 120-mesh stainless-steel screen whose hydraulic radius is ~42 μm. This is smaller than the average thermal penetration depth of the helium (300 μm), ensuring the good thermal contact between the helium gas and the screen necessary for thermo-dynamic reversibility. The two cold heat exchangers are of shell-and-tube con-struction, with the oscillating helium in the tubes and flowing cooling water in the shell. The hot heat exchanger is electrically heated Ni-Cr ribbon wound in a zig-zag fashion on an alumina frame. The buffer tube provides thermal insulation between the hot heat exchanger and ambient temperature while transmitting the acoustic power out of the hot zone. Its internal surface is slightly tapered and polished to reduce boundary-layer streaming, which would otherwise convect heat from the hot heat exchanger[16]. Thermal insulation around the hot compo-nents is not shown. The two tapered channels of the jet pump are 51 mm long and 34 mm high, and their short, tapered dimensions are adjustable, typically set in the range 1–2 mm. The lower edges of the channels are rounded with a 0.8-mm radius, to reduce K_{in} to nearly zero (see text). The taper increases the cross-sectional area at the upper end, thereby decreasing the velocity there and preventing the upper end from developing an equal and opposite $\overline{\Delta p}_{jp}$ (see text). The tempera-ture of the helium is measured at locations labelled 'T' using 1.6-mm-diameter type-K thermocouples. **c,** Impedance model of the engine. The dashed lines enclose the regenerator; its volumetric-velocity source $(T_h/T_c - 1)U_{1c}$ is due to the temperature gradient in the regenerator and causes the acoustic power gain. The resonator and variable acoustic load are modelled as a parallel combination of R_{res} with a reactive impedance X_{res}.

fixed at[13] $p_1/U_1 = \rho_m c/A$ where ρ_m is the mean gas density, c is the speed of sound, and A is the cross-sectional area of the waveguide containing the wave. For realistic gases, U_1 would then be large enough to cause significant viscous losses, which would overwhelm any power gain. Hence, it is crucial to make $p_1/U_1 \gg \rho_m c/A$ within the regenerator, while maintaining travelling-wave phasing, to achieve a large acoustic power gain with a minimum of viscous loss.

Scale drawings of our engine, which achieved such an unusual condition, are shown in Fig. 1 a and b. Overall, it comprises a 1/4-wavelength acoustic resonator filled with helium at a pressure of 30 bar. The torus-shaped section contains the heat exchangers, regenerator, inertance, L (due to the inertia of the helium) and compliance, C (due to the compressibility of the helium) necessary to force the helium to execute the Stirling cycle. The inlet to the torus is near a pressure antinode (velocity node) which helps achieve $p_1/U_1 \gg \rho_m c/A$ within the regenerator. Applying heat to the hot heat exchanger creates an intense acoustic wave at the resonance frequency, 80 Hz.

Figure 1c shows a simplified acoustic impedance diagram of the engine, which captures the essential dynamics of the engine operation but removes the complicated spatial dependence of the acoustic wave. Each acoustic component is analogous to a similar electrical compo-nent, with p_1 analogous to a.c. voltage and U_1 analogous to electrical current[13]. Following Ceperley[9], the regenerator and adjacent heat exchangers are modelled as a resistance R and a volumetric-velocity source $(T_h/T_c - 1)U_{1c}$, where U_{1c} is the volumetric velocity into the cold end of the regenerator, and T_h and T_c are the temperatures of the hot and cold faces of the regenerator, respectively.

The study of this simple model provides basic insights into the operation of the engine. Solving for U_{1c}, we find:

$$U_{1c} = \frac{\omega^2 LC}{R} \frac{p_{1c}}{1 + i\omega L/R} \qquad (2)$$

If the impedance ωL of the feedback inertance L is small compared with the resistance R of the regenerator, p_{1c} and U_{1c} are nearly in phase, corresponding to the travelling-wave phasing necessary to drive the helium through the Stirling cycle, yet the ratio $|p_{1c}/U_{1c}|$ is no longer determined by $\rho_m c/A$. Here, p_{1c} is the oscillating pressure at the cold end of the regenerator. In our experiments, the physical dimensions of the inertance, compliance and regenerator are chosen so that $|p_{1c}/U_{1c}| \approx 30\rho_m c/A$ so that viscous dissipation in the regen-erator is reduced to an acceptable level. As the simple model in Fig. 1c shows, the LRC acoustic network of Fig. 1b provides both the travelling-wave phasing necessary to produce the Stirling cycle and the large value of $|p_{1c}/U_{1c}|$ necessary to avoid large viscous losses.

As this wave propagates through the regenerator, it is amplified by the imposed temperature gradient, resulting in $\dot{W}_h > \dot{W}_c$, where $\dot{W}_c$ and $\dot{W}_h$ are the acoustic powers flowing into the cold end and out of the hot end of the regenerator, respectively. To maintain the acoustic oscillation, part of $\dot{W}_h$ is fed back through the inertance to the cold end of the regenerator, W_{fb}. (Due to dissipation in the inertance and compliance, $\dot{W}_{fb} > \dot{W}_c$). The remainder of the power, $\dot{W}_{res}$, is available to maintain the wave throughout the resonator and per-form useful work.

In this process, heat $\dot{Q}_h$ is absorbed from the hot heat exchanger and $\dot{Q}_c$ is rejected at the cold heat exchanger. But, in our initial measurements, the $\dot{Q}_h$ needed to sustain the oscillation was far greater than we estimated using a detailed computer model[14] of the system. Also, the temperature profile in the regenerator was far from the estimated linear profile. Both of these effects may be understood by considering the second-order, time-averaged mass flux circulat-ing down through the regenerator and up through the inertance, an effect that was not anticipated by Ceperley. Gedeon[15] has discussed how a mass flux $\dot{M}_2$ can exist in Stirling systems which contain such a closed-loop path. Gedeon argues that $\dot{M}_2$ is given by:

$$\dot{M}_2 = \tfrac{1}{2}\mathrm{Re}[\rho_1 \tilde{U}_1] + \rho_m U_{2,0} \qquad (3)$$

59

Here, $U_{2,0}$ would be the next term in the expansion of equation (1) for volumetric velocity and represents the second-order, time-averaged volume velocity[16]. In acoustic oscillations, $\rho_1 \propto p_1$. Therefore, the first term in equation (3) is non-zero whenever acoustic power flow is non-zero; for example, around the LRC loop of Fig. 1c. This mass flux carries heat away from the hot heat exchanger and deposits it at the secondary cold heat exchanger, creating an unwanted heat leak $\dot{Q}_{leak} = \dot{M}_2 c_p (T_h - T_c)$ where c_p is the constant-pressure heat capacity of the helium. $\dot{Q}_{leak}$ can more than double the $\dot{Q}_h$ needed to maintain the acoustic oscillation, seriously degrading the engine's efficiency. The same $\dot{M}_2$ also injects cold gas into the cold end of the regenerator, causing its axial temperature profile to fall below the predicted linear profile.

Equation (3) shows that $\dot{M}_2$ can be forced to zero if a $U_{2,0}$ is imposed such that $\rho_m U_{2,0} = -\mathrm{Re}[\rho_1 \tilde{U}_1]/2$. A time-averaged pressure drop, $\overline{\Delta p_2}$, imposed across the regenerator will drive such a $U_{2,0}$. The $\overline{\Delta p_2}$ required to suppress $\dot{M}_2$ is given by:

$$\overline{\Delta p_2} = \frac{R}{2\rho_m} \mathrm{Re}[\rho_1 \tilde{U}_1]. \qquad (4)$$

Such a $\overline{\Delta p_2}$ can be generated using the asymmetry of hydrodynamic end effects[17]. When flow of high Reynolds number encounters an abrupt transition from a channel of small cross-sectional area to one of much larger area, the transition is accompanied by jetting and turbulence[17]. In this flow, Bernoulli's equation does not hold, and an additional pressure head loss given by $\Delta p_{ml} = (K_{out}/2)\rho v^2$ occurs, where v is the velocity of the jet as it leaves. The constant $K_{out} \approx 1$ is termed the 'minor loss coefficient'. When the flow changes direction, entering the small channel, the minor loss coefficient K_{in}

depends on the geometrical details. If the perimeter of the entrance to the small channel is sufficiently rounded[17,18], K_{in} can be as small as 0.04. With $K_{out} \neq K_{in}$, a time-averaged pressure drop of

$$\overline{\Delta p_{jp}} = \frac{\rho_m |U_{1jp}|^2}{8a^2} [K_{out} - K_{in}] \qquad (5)$$

develops across the transition. Here, U_{1jp} is the volume velocity at the transition and a is the area of the small channel. The device labelled 'jet pump' in Fig. 1a utilizes these minor losses by channelling the flow above the cold heat exchanger through two parallel tapered rectangular channels that open abruptly into the larger space just above the exchanger. By adjusting the jet area a, $\overline{\Delta p_{jp}}$ can be set to the pressure given in equation (4), thereby completely eliminating $\dot{M}_2$ and the large, unwanted $\dot{Q}_{leak}$.

Figure 2 demonstrates the effectiveness of the jet pump. The lowest curve ('lowest' refers to the curves at $\phi = 120°$) in Fig. 2b shows the time-dependent $\Delta p_{jp}(t)$, displayed as a function of the time phase of the acoustic cycle, with a at its fully open value of 3 cm^2. When time-averaged, this curve does not yield a significant $\overline{\Delta p_{jp}}$, so a large $\dot{M}_2$ flows down through the regenerator and buffer tube causing a large $\dot{Q}_{leak}$. To maintain the oscillation at $|p_1/p_m| = 0.036$, nearly 1,500 W of $\dot{Q}_h$ is necessary, with more than half of this $\dot{Q}_h$ carried away by $\dot{M}_2$. Also, the temperature at the axial midpoint of the regenerator, T_{mid}, is held significantly below $T_{avg} = (T_h + T_c)/2$ due to the flux of cold gas entering the cold end of the regenerator. The middle curve in Fig. 2b corresponds to $a = 1.8$ cm^2 in Fig. 2a. The resulting $\overline{\Delta p_{jp}}$ generated by the jet pump enforces $\dot{M}_2 = 0$. $\dot{Q}_{leak}$ is eliminated, and the $\dot{Q}_h$ needed to maintain $|p_1/p_m| = 0.036$ is at its minimum of 630 W. At this operating point $T_{mid} = T_{avg}$, demonstrating a linear temperature profile through the regenerator. The highest curve in Fig. 2b corresponds to $a = 0.8$ cm^2 in Fig. 2a. The resulting $\overline{\Delta p_{jp}}$ exceeds that required by equation (4), so $\dot{M}_2 < 0$, implying that the time-averaged mass flux flows up through the buffer tube and regenerator. Now, T_{mid} is greater than T_{avg} due to the hot gas entering the hot end of the regenerator. These data demonstrate that $\dot{M}_2$ causes a significant and unwanted heat load that can be completely eliminated by $\overline{\Delta p_{jp}}$. Also, the broad minimum in $\dot{Q}_h$ in Fig. 2a shows that the cancellation of $\dot{M}_2$ is insensitive to small variations in a.
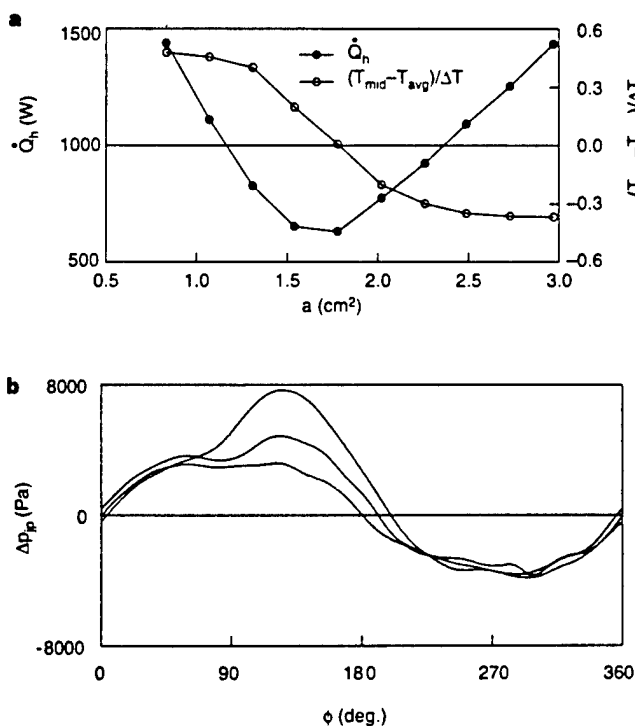
Figure 2 Effectiveness of the jet pump. **a**, Measurements of Q_h and $(T_{mid} - T_{avg})/\Delta T$ as a function of the jet area a. Here, $\Delta T = T_h - T_c$. As a is varied, Q_h is adjusted to maintain $|p_1/p_m| = 0.036$, and hence $\mathrm{Re}[\rho_1 \tilde{U}_1]$ nearly constant within the regenerator. With $a = 1.8$ cm^2, $T_{mid} = T_{avg}$ indicating that $\dot{M}_2$ is completely suppressed. With $\dot{M}_2 = 0$, $\dot{Q}_{leak} = 0$ and the heat input needed to maintain the oscillations, Q_h, is at a minimum. **b**, Measurements of $\Delta p_{jp}(t)$ as a function of the time phase of the acoustic cycle $\phi(t)$. The lowest curve, obtained with $a = 3.0$ cm^2, has $\overline{\Delta p_{jp}} = 120$ Pa; the middle curve, obtained with $a = 1.8$ cm^2, has $\overline{\Delta p_{jp}} = 630$ Pa; the highest curve, obtained with $a = 0.8$ cm^2, has $\overline{\Delta p_{jp}} = 1160$ Pa. The middle setting suppresses $\dot{M}_{2,0}$ as shown in **a**.
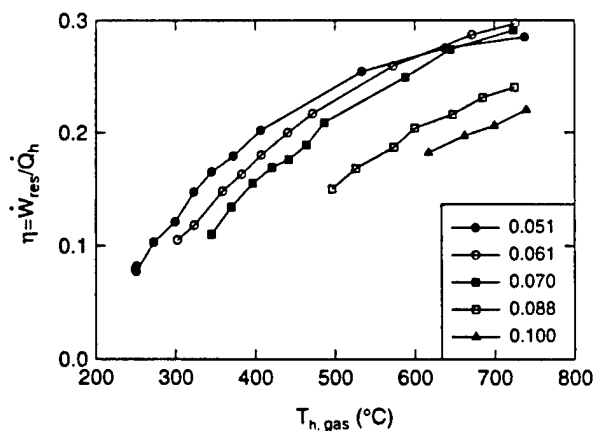
Figure 3 Thermal efficiency of the engine as a function of $T_{h,gas}$. To make a fair comparison with other thermoacoustic engines[6], the thermal efficiency $\eta = \dot{W}_{res}/Q_h$ is reported in terms of the power entering the resonator, $\dot{W}_{res}$, instead of the directly measured $\dot{W}_{2mic}$. A detailed computer model (ref.14; model available at ⟨http://rott.esa.lanl.gov/⟩) duplicating $\dot{W}_{2mic}$ and the magnitude of the measured pressures is used to extrapolate back to the resonator junction to determine $\dot{W}_{res}$. At the maximum $T_{h,gas}$, the difference between $\dot{W}_{2mic}$ and $\dot{W}_{res}$ is typically 4% and never more than 14%. During these measurements, the cooling water in the main cold heat exchanger is typically 15 °C. The maximum efficiency obtained corresponds to 42% of theoretical maximum Carnot efficiency[2].

60

With $\vec{M}_2$ suppressed, the performance of the engine is measured as a function of p_{1c} and the temperature of the helium immediately below the hot heat exchanger, $T_{h,gas}$. Figure 3 shows the thermal efficiency[2], $\eta = \dot{W}_{res}/\dot{Q}_h$, where $\dot{W}_{res}$ is the acoustic power delivered to the resonator. The maximum thermal efficiency of $\eta = 0.30$ occurs near $|p_1/p_m| = 0.06$ at $T_{h,gas} = 725\,°C$ with the engine delivering 710 W to the resonator. This corresponds to 42% of the theoretical maximum Carnot efficiency[2]. At the most powerful operating point, $|p_1/p_m| = 0.10$, 890 W is delivered to the resonator with $\eta = 0.22$.

Although this engine already shows a large increase in efficiency over previous heat engines without moving parts, we anticipate further improvements through research on flow separation losses[17,18] and regenerator inefficiency. We have also built one refrigerator[19] according to the same principles, and we expect that it will give performance comparable to that of commercially successful refrigeration equipment. □

1. Walker, G. *Stirling Engines* (Clarendon, Oxford, 1960).
2. Bejan, A. *Advanced Engineering Thermodynamics* 2nd edn (Wiley, New York, 1997).
3. Mechanical Technology Inc., Latham, NY *Automative Stirling Engine-Mod II Design Report* (Tech. Rep. CR-175106, NASA Lewis Research Center, Cleveland, Ohio, 1986).
4. Slaby, J. G. in *21st Intersociety Energy Conversion Engineering Conf.* Vol. 1, 420–429 (Am. Chem. Soc., Washington DC, 1996).
5. *Proc. 29th Intersociety Energy Conversion Engineering Conf.* (Am. Inst. of Aeronautics and Astronautics, Washington DC, 1994).
6. Godshalk, K. M. *et al.* Characterization of 350 Hz thermoacoustic driven orifice pulse tube refrigerator with measurements of the phase of the mass flow and pressure. *Adv. Cryogen. Eng.* **41**, 1411–1418 (1996).
7. Radebaugh, R. A review of pulse tube refrigeration. *Adv. Cryogen. Eng.* **35**, 1191–1205 (1990).
8. Swift, G. W. in *Proc. DOE Natural Gas Conf.* Paper 7.1 (Federal Energy Technology Center, Morgantown, West Virginia, 1997).
9. Ceperley, P. H. A pistonless Stirling engine—the traveling wave heat engine. *J. Acoust. Soc. Am.* **66**, 1508–1513 (1979).
10. Yazaki, T., Iwata, A., Maekawa, T. & Tominaga, A. Traveling wave thermoacoustic engine in a looped tube. *Phys. Rev. Lett.* **81**, 3128–3131 (1998).
11. Swift, G. W. Thermoacoustic engines. *J. Acoust. Soc. Am.* **84**, 1145–1180 (1988).
12. Ceperley, P. H. Gain and efficiency of a short traveling wave heat engine. *J. Acoust. Soc. Am.* **77**, 1239–1244 (1985).
13. Kinsler, L. E., Frey, A. R., Coppens, A. & Sanders, J. V. *Fundamentals of Acoustics* (Wiley & Sons, New York, 1982).
14. Ward, W. C. & Swift, G. W. Design environment for low amplitude thermoacoustic engines (DeltaE). *J. Acoust. Soc. Am.* **95**, 3671–3672 (1994).
15. Gedeon, D. in *Cryocoolers 9* (ed. Ross, R. G.) 385–392 (Plenum, New York, 1997).
16. Olson, J. R. & Swift, G. W. Acoustic streaming in pulse tube refrigerators: tapered pulse tubes. *Cryogenics* **37**, 769–776 (1997).
17. Streeter, V. L. *Handbook of Fluid Dynamics* (McGraw-Hill, New York, 1961).
18. Idelchik, I. E. *Handbook of Hydraulic Resistance* 3rd edn (CRC Press, Boca Raton, FL, 1994).
19. Swift, G. W., Gardner, D. L. & Backhaus, S. Acoustic recovery of lost power in pulse tube refrigerators. *J. Acoust. Soc. Am.* **105**, 711–724 (1999).
20. Fusco, A. M., Ward, W. C. & Swift, G. W. Two-sensor power measurements in lossy ducts. *J. Acoust. Soc. Am.* **91**, 2229–2235 (1992).

Correspondence and requests for materials should be addressed to S.B. (e-mail: backhaus@lanl.gov).

61

POROUS MEDIA

James M. Sabatier
National Center for Physical Acoustics
University of Mississippi

ABSTRACT

The physics of the interaction of airborne sound with the surface of the earth[1] will be presented. The ground is an example of a fluid-filled, porous material. When sound in the atmosphere is incident upon the ground surface, vibrational energy is transferred to both the fluid and solid phases. This coupling has been referred to as acoustics-to-seismic coupling[2,3] and will be discussed in the light of the Biot model.[4] The relevant pore parameters, air-porosity, permeability and pore tortuosity, can be determined from acoustic measurements. Experimental techniques used to study porous soils include buried microphones, geophones and laser Doppler vibrometers. Specific measurements of the acoustics-to-seismic coupling ratio and the physics that can be extracted will be presented. The principle components of the Biot model, including Type I and II phase velocity and attenuation and boundary conditions at various interfaces, will be described and compared to measured data. Since air-filled soils approximate the light-fluid limit of the Biot theory, rigid-framed porous media models can also be used to describe the fluid phase physics and these models will be described.

REFERENCES

1. Sabatier, *et al.*, "The interaction of airborne sound with the porous ground: The theoretical formulation," J. Acoust. Soc. Am. **79**, 1345-1352 (1986).

2. Attenborough, *et al.*, "The acoustic transfer function at the surface of a layered poroelastic soil," J. Acoust. Soc. Am. **79**, 1353-1358 (1986).

3. Sabatier, *et al.*, "Acoustically induced seismic waves," J. Acoust. Soc. Am. **80**, 646-649 (1986).

4. M.A. Biot, "Theory of propagation of elastic waves in a fluid saturated porous solid. I. Low frequency range. II. High frequency range," J. Acoust. Soc. Am. **28**, 168-191 (1956).

MEDICAL APPLICATIONS OF ACOUSTICS

Lawrence A. Crum
Applied Physics Laboratory
University of Washington

ABSTRACT

Medical ultrasound technology is experiencing a rebirth as methods and applications extend beyond current diagnostic imaging to include novel therapeutic and surgical uses. These applications broadly include: Tissue ablation, cautery, lipoplasty, and hemostasis via targeted non-invasive thermal deposition; site-specific and ultrasound mediated drug activity; novel imaging approaches using ultrasound contrast agents and signal processing; extra-corporeal lithotripsy; and enhancement of natural physiological functions such as wound healing and tissue regeneration. This general lecture will address some of the basic scientific questions and future challenges in the areas listed above. We shall particularly emphasize the use of High Intensity Focused Ultrasound (HIFU) in the treatment of hemorrhagic trauma and related pathological conditions, especially in organs that are difficult to treat using conventional medical and surgical techniques. Direct applications include combat casualty care, as well as many civilian uses in non-invasive or minimally invasive trauma management, bloodless surgery, and ultrasound-mediated drug therapy. We shall also explores imaging and simulation techniques associated with treatment, targeting, and monitoring the effects of HIFU therapy. Finally, we shall describe our efforts to successfully transition the scientific developments in our laboratory to commercial products, and thus will describe our attempts to start new companies or work with existing ones to implement technology transfer.

REFERENCES

"Effect of high intensity focused ultrasound on whole blood with and without contrast agents," S. L. Poliachik, P. D. Mourad, W. Chandler and L. A. Crum, IEEE-Ultrasonics Symp. Proc. 2, 24-29, (1998).

"High intensity focused ultrasound and tissue heating: the effect of nonlinear sound propagation and vessel presence," F. P. Curra, P. D. Mourad, R. Cleveland, V. A. Khokhlova and L. A. Crum, IEEE-Ultrasonics Symp. Proc. 2, 1419-1422, (1998).

"Comparison of lithotripters with rigid and pressure-release ellipsoidal reflectors. I. Acoustic fields," M. R. Bailey, D. T. Blackstock, R. O. Cleveland, and L. A. Crum, J. Acoust. Soc. Am., **104**, 2517-2524 (1998).

"Comparison of electrohydraulic lithotripters with rigid pressure-release ellipsoidal reflectors: II. Cavitation fields," M. R. Bailey, D. T. Blackstock, R. O. Cleveland, and L. A. Crum, J. Acoust. Soc. Am. **106**, 1149-1160 (1999).

"Therapeutic ultrasound: A promising future in clinical medicine," L. Crum, M. Bailey, P. Kaczkowski, I. Makin, P. Mourad, K. Beach, S. Carter, U. Schmiedl, W. Chandler, R. Martin, S. Vaezy, G. Keilman, R. Cleveland, and R. Roy, Proceedings of the joint meeting of the 16th International Congress on Acoustics and the 135th Meeting of the Acoustical Society of America (P. Kuhl and L. Crum, eds.) 1, 719-720 (1998).

"Hemostasis using High Intensity Focused Ultrasound," S. Vaezy, R. Martin, P. Mourad, and L. A. Crum, European J. of Ultrasound **9**, 79-87 (1999).

"Use of High Intensity Focused Ultrasound to control bleeding," S. Vaezy, R. Martin, P. Kaczkowski, G. Keilman, B. Goldman, H. Yaziji, S. Carter, M. Caps, and L. A. Crum, J. Vascular Surgery **29**, 534-542 (1999).

"Ultrasound Detection of Acute Parenchymal Injury in an Experimental Porcine Model of Renal Hemorrhage: Gray Scale Imaging using an Ultrasound Contrast Agent," Udo P. Schmiedl, Stephen Carter, Roy Martin, William Eubanks, Thomas Winter, Peter P. Chang, Albrecht Bauer, and Lawrence Crum, Amer. J. Radiology **173**, 1289-1294 (1999).

"Hemostasis of punctured vessels using Doppler-guided treatment," R. Martin, S. Vaezy, P. Kaczkowski, G. Keilman, S. Carter, M. Caps, K. Beach and L. Crum, Ultrasound in Medicine and Biology **25**, 985-990 (1999).

SONOLUMINESCENCE

Thomas J. Matula
Applied Physics Laboratory
University of Washington

ABSTRACT

If an intense acoustic field is applied to a liquid, the liquid can fail under the tensile, or negative portion of the sound field; weak sites within the liquid, probably preexisting gas pockets, called "cavitation nuclei", are caused to rapidly grow, thereby producing vapor and gas-filled cavities (i.e., bubbles). These bubbles continue to grow during the negative portion of the sound field, until the sound field turns positive. The resulting inertial implosion of the bubbles (now mostly filled with vapor and thus unable to provide stiffness) can be extremely violent, leading to an enormous concentration of energy within the small residual volume of the collapsed bubble. Consequently, the temperatures and pressures achieved by the compressed bubble contents can be respectively several tens of thousands of degrees (perhaps even higher) and several kilobars (perhaps even much higher). At the final stages of bubble collapse intense shock waves are emitted, chemical bonds are broken, and even light is emitted, called "sonoluminescence."

Thus, cavitation leads to sonoluminescence. I should point out however, that sonoluminescence is not restricted to bubbles (cavitation) in fluids. Ultrasonic vibrations of piezoelectric crystals and semiconductors can also generate luminescence of the gas near the crystal surface.[1] Although this form of sonoluminescence involves ultrasonic waves interacting with a medium (the crystal), we will not delve too deeply into this subject. Instead, we will focus on sonoluminescence occurring from ultrasonic irradiation of a liquid. That is, cavitation-induced luminescence.

Sonoluminescence was discovered nearly 65 years ago,[2,3] and since then a variety of explanations have been given for the origin of the electromagnetic emissions. Electrical discharge theories of various types were at first quite popular. As early as 1940, Frenkel[4] suggested that electrical charges known to exist on the surfaces of bubbles (see for example, Ref. 5) were somehow made to discharge. This model, though seriously challenged by recent

experiments[6,7] and theories,[8,9] even has its modern advocates. Other, more exotic theories have surfaced in order to explain the experimental findings.

For most of the past 65 years, most sonoluminescence studies were carried out by generating large fields of cavitation bubbles with high-intensity ultrasonic generators. Because the number of bubbles was large, and the size distribution of the bubbles was not known, it was, and still is, difficult to study these systems. Only statistically averaged information can be obtained from these systems, and thus, interpreting experimental data can be difficult.

In 1990, Felipe Gaitan (then, a graduate student) discovered a form of sonoluminescence, which we now call Single-Bubble sonoluminescence (SBSL), whereby a single bubble levitated in a container of fluid can be forced to emit light. This fortuitous discovery has led to a remarkable explosion of experiments and theoretical models. The explosion of new data is directly due to our ability to make measurements of this single, isolated bubble.

The idea is to trap (levitate) a single bubble using a standing acoustic wave field in a liquid. Under moderately applied drive pressure amplitudes (near 1 bar) the bubble undergoes highly nonlinear volume mode pulsations. Figure 1 illustrates the nonlinear radial response of a sonoluminescence bubble to an applied sound field, obtained with our light-scattering system, and modeled with one of our computer codes of bubble dynamics. When the pressure within the bubble falls below the vapor pressure of the liquid, the bubble begins to grow while the bubble fills with vapor. When the pressure turns positive, the vapor condenses and the bubble accelerates rapidly inward. This collapse phase was first studied by Lord Rayleigh and found to be extremely violent. Consider that even for the modest applied pressure amplitude illustrated in Fig. 1 (we used 0.14 MPa), the temperature (assuming adiabatic compression) within the bubble can exceed 7,000 K. More precise calculations suggest that temperatures on the order of tens of thousands of degrees can be achieved.
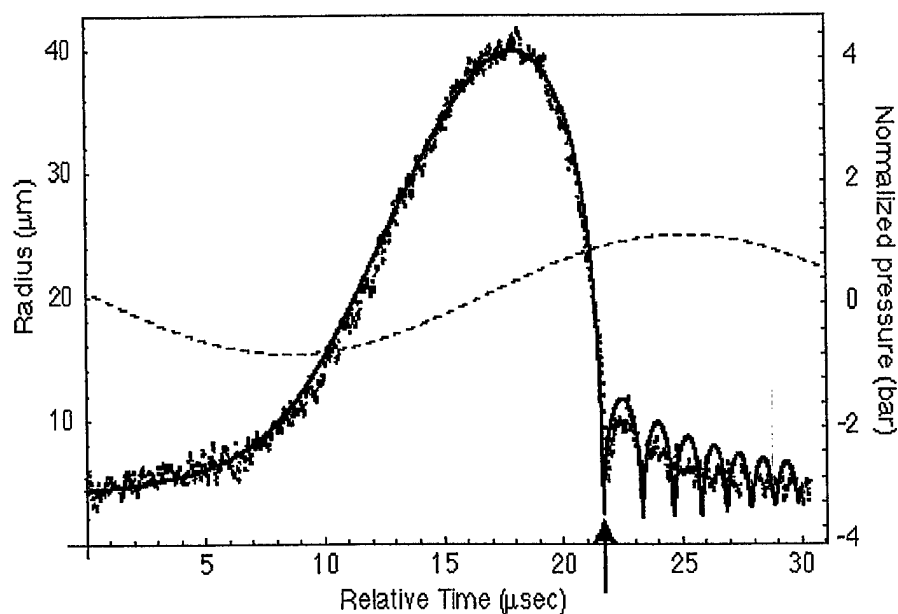
Fig. 1. The nonlinear, radial response of a bubble subject to an oscillating acoustic pressure field of 0.14 MPa. The heavy line is the calculated bubble radius, the dashed line is the normalized acoustic drive pressure, and the solid points are the experimentally measured bubble radius (in the physical optics limit). The arrow indicates where the light flash occurs.

The dynamics of the bubble can be modeled using a form of the Rayleigh-Plesset equation. This equation describes how a (presumed spherical) bubble oscillates when subjected to a time-varying pressure field. Although the bubble's motion can be described by this equation, the equation does not show us how light can be emitted. We must therefore couple some emission mechanism model to the bubble's dynamical motion. The form of the mechanism model is dependent on the experimental findings. That is, the model must agree with experimental data.

To guide us in developing a model for sonoluminescence, we have available several key experimental findings: First, the duration of the sonoluminescence flash is much less than 1 nsec, in some cases, less than 50 psec! This implies that the physics must occur on very rapid time scales. Second, the spectra observed in many systems are void of line or band emissions, indicating that either temperatures are too hot for simple line and band emission mechanisms involving radiative recombination, or there exists some exotic physics that governs the emission mechanism. Third, the light emission depends greatly on the type of gas dissolved in the liquid. Any emission mechanism must show a dependence on the gas.

This talk will cover the experimental techniques used to observe sonoluminescence behavior, and theoretical formulations that have been developed to explain sonoluminescence.

REFERENCES

1. I. V. Ostrovskii, "Observation of a new class of crystal sonoluminescence at piezoelectric crystal surface," Appl. Phys. Lett. **70**, 167 (1997).

2. N. Marinesco J. J. Trillat, C. R. Acad. Sci. **196**, 858 (1933).

3. H. Frenzel and H. Z. Schultes, Phys. Chem. **27B**, 421 (1935).

4. J. Frenkel, Acta Phys-Chim (U.R.S.S.) **12**, 317 (1940).

5. D. J. Watmough,*et al.*, "Evidence that ultrasonically-induced microbubbles carry a negative charge," Ultrasonics **30**, 325 (1992).

6. K. S. Suslick, "The chemical effects of ultrasound," Sci. Amer. **260**, 80 (1989)

7. K. S. Suslick, "Sonochemistry," Science **247**, 325 (1990).

8. W. C. Moss, *et al.*, "Calculated pulse widths and spectra of a single sonoluminescing bubble," Science **276**, 1398 (1997).

9. S. Hilgenfeldt, *et al.*, "A simple explanation of light emission in sonoluminescence," Nature **398**, 402 (1999).

DEFINING THE UNKNOWNS OF SONOLUMINESCENCE

Bradley P. BARBER[a], Robert A. HILLER[b], Ritva LÖFSTEDT[c], Seth J. PUTTERMAN[b],
Keith R. WENINGER[b]

[a] Lucent Technologies, Murray Hill, NJ 07974, USA
[b] Physics Department, University of California, Los Angeles, CA 90095, USA
[c] Institute for Theoretical Physics, University of California, Santa Barbara, CA 93106, USA

Defining the unknowns of sonoluminescence

Bradley P. Barber[a], Robert A. Hiller[b], Ritva Löfstedt[c], Seth J. Putterman[b],
Keith R. Weninger[b]

[a] *Lucent Technologies, Murray Hill, NJ 07974, USA*
[b] *Physics Department, University of California, Los Angeles, CA 90095, USA*
[c] *Institute for Theoretical Physics, University of California, Santa Barbara, CA 93106, USA*

Contents:

Abstract

As the intensity of a standing sound wave is increased the pulsations of a bubble of gas trapped at a velocity node attain sufficient amplitude so as to emit picosecond flashes of light with a broadband spectrum that increases into the ultraviolet. The acoustic resonator can be tuned so that the flashes of light occur with a clocklike regularity: one flash for each cycle of sound with a jitter in the time between flashes that is also measured in picoseconds. This phenomenon (sonoluminescence or "SL") is remarkable because it is the only means of generating picosecond flashes of light that does not use a laser and the input acoustic energy density must be concentrated by twelve orders of magnitude in order to produce light. Light scattering measurements indicate that the bubble wall is collapsing at more than 4 times the ambient speed of sound in the gas just prior to the light emitting moment when the gas has been compressed to a density determined by its van der Waals hard core. Experiments indicate that the collapse is remarkably spherical, water is the best fluid for SL, some noble gas is essential for stable SL, and that the light intensity increases as the ambient temperature is lowered. In the extremely stable experimental configuration consisting of an air bubble in water, measurements indicate that the bubble chooses an ambient radius that is not explained by mass diffusion. Experiments have not yet been able to map out the complete spectrum because above 6 eV it is obscured by the cutoff imposed by water, and furthermore experiments have only determined an upper bound on the flash widths. In addition to the above puzzles, the theory for the light emitting mechanism is still open. The scenario of a supersonic bubble collapse launching an imploding shock wave which ionizes the bubble contents so as to cause it to emit Bremsstrahlung radiation is the best candidate theory but it has not been shown how to extract from it the richness of this phenomenon. Most exciting is the issue of whether SL is a classical effect or whether Planck's constant should be invoked to explain how energy which enters a medium at the macroscopic scale holds together and focuses so as to be emitted at the microscopic scale.

1. Why is sonoluminescence interesting?

The equations of fluid mechanics (Landau and Lifshitz, 1987) describe an extraordinarily wide range of phenomena. These include the behavior of sound waves and surface waves, the formation of shock fronts, the localization of energy in solitons (Dodd et al., 1982; Wu et al., 1984), the randomization of energy in the transition to turbulence, and pattern formation, such as observed in convection cells (Cross and Hohenberg, 1993). Among fluid phenomena sonoluminescence (SL), the transduction of sound into light is unique in that the energy enters the fluid at low energy and long wavelengths, where the equations of fluid mechanics apply, but the resulting fluid mechanical motion sets up a transformation of the sound energy into degrees of freedom, visible photons, which are not describable by the original equations of fluid mechanics. In sonoluminescence, the sound energy is concentrated by twelve orders of magnitude and emitted as a flash of light.

Fig. 1 displays the extraordinary range of length and time scales characterizing SL. Trace "b" is the sound field near the center of a flask containing partially degassed water, driven (sinusoidally) at its acoustic resonance (which is here about 26 kHz). The acoustic radiation pressure (King, 1934) of the sound field traps a gas bubble at the pressure antinode in the center of the flask where it pulsates in response to the pressure swings of the drive. These pulsations are displayed in trace "a", which shows
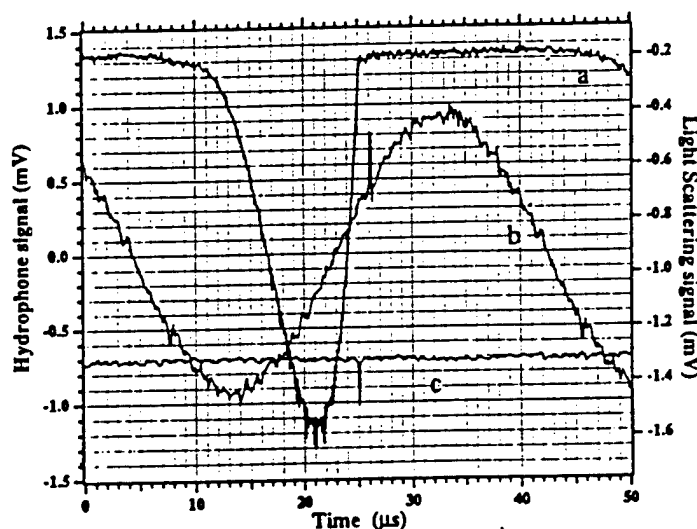
Fig. 1. Relative timing of sonoluminescence (c) from the stressed interior of a collapsing air bubble whose radius squared is proportional to the magnitude of the intensity of scattered laser light (a). The high pressures reached during the collapse launch an outgoing spike recorded by a microphone that measures the driving sound field (b) inside the acoustic resonator. The scale for SL has been offset and the phase of the 26 kHz sound wave has been shifted by 3 μs to correct for the phase delay introduced by the AC-coupled preamplifier. The needle microphone is located about one mm from the bubble, and this accounts for the 1 μs delay between the flash of light and the spike. The flash of SL is less than 50 ps long, and the spike is less than 20 ns wide. The maximum radius of the bubble is about 45 μm and the amplitude of the sound field is about 1.2 atm. This process repeats with each cycle of sound. For an air bubble in water each flash of SL yields about 2×10^5 photons.
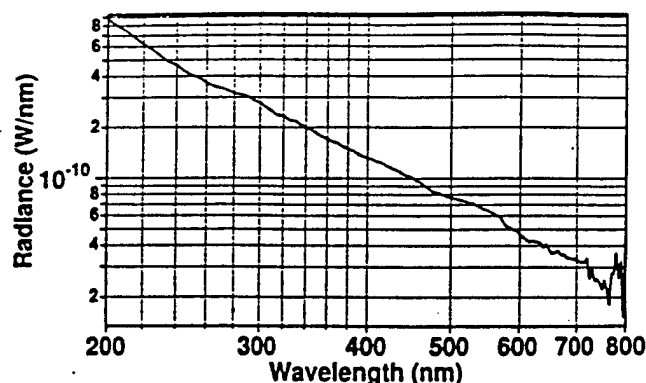
Fig. 2. Spectrum of light emitted by a sonoluminescing bubble of ⁴He gas, which is formed from water with.helium gas dissolved at a partial pressure of 150 mm. The high-energy cutoff at 6 eV (200 nm) is due to the transmission cutoff imposed by water. How far the energy focusing extends beyond 6 eV is a major unknown. The measured spectrum has been corrected for the attenuation of light by the flask and the water, and for the quantum efficiency of the photodetector and spectrometer. The resolution is 10 nm FWHM.

the amount of light scattered out of a laser beam trained on the bubble (Barber and Putterman, 1992). The larger the negative signal, the larger is the bubble radius. The expansion of the bubble from its ambient radius (~ 4.5 μm) occurs on hydrodynamic time scales during the rarefaction half-cycle of the pressure swing. It brings the bubble to its maximum radius of about 45 μm. The ensuing collapse accelerates the bubble wall to supersonic velocities and compresses the bubble's interior (Barber et al., 1994). By mechanisms yet unknown, the high stresses and high energy densities inside the bubble generated by this collapse result in the emission of a flash of light (in trace "c"). The high pressures built up inside the bubble during the collapse launch an outgoing acoustic pulse (Barber et al., 1997), which is the spike riding the sound field in trace "b". Plotted on this hydrodynamic timescale, the flash of light and the acoustic spike are deltafunctions and the collapsing radius is a theta function. To the best of our resolution, which has only established upper bounds, the light flash is less than 50 ps in duration and it occurs within 0.5 ns of the minimum bubble radius (Barber et al., 1992, 1997). The SL flashwidth is thus 100 times shorter than the shortest (visible) lifetime of an excited state of a hydrogen atom. Each flash is roughly spherically symmetric and contains about one million photons (Barber and Putterman, 1991). The outgoing acoustic spike is less than 20 ns wide and the collapse velocity is over 1.4 km/s (or four times the ambient speed of sound in the gas, $c_0 = 3.3 \times 10^4$ cm/s) (Barber et al., 1997). This violent bubble motion and resultant light emission repeat in clocklike synchronicity with the sound field; each acoustic cycle yields one flash of light, and the jitter in time between consecutive flashes can be made less than 50 ps (Barber et al., 1992). The unaided eye can easily see the sonoluminescing bubble as a steady starlike light.

Fig. 2 shows the spectrum (Hiller et al., 1992) of the light emitted by a helium bubble in water at 0°C with helium dissolved in it at a partial pressure of 150 Torr. The broadband, featureless spectrum extends into the ultraviolet; higher-frequency electromagnetic radiation cannot propagate through water. The extent of the energy focusing achieved in SL is estimated by comparing the average acoustic energy delivered to an atom of the fluid by the sound field, $\langle \rho v^2 \rangle \cdot (\text{volume/atom}) \approx$

4×10^{-12} eV/atom, where p is the density of water and v is the velocity amplitude in response to the sound wave, to the most energetic of the observed photons, which have an energy of 6 eV. Assuming that the light emission stems from a region of atomic dimensions, one is led to interpret SL as a process where the energy concentration spans twelve orders of magnitude (Barber et al., 1991). (Here we used a pressure amplitude of one atm, so that the rms Mach number, $M = v/c = 10^{-5}$, where the velocity of sound in water is $c = 1.482 \times 10^5$ cm/s at 20°C and 1.403×10^5 cm/s at 0°C.) Noting that 1 eV = 11 600 K and that spectral lines have yet to be observed we conclude that the region from which the broadband 6 eV radiation is originating is very hot and very stressed.

In order to study the properties of an audible sound field we have had to use photodetectors which are faster than those used in elementary-particle experiments. Not only is this mixing of macroscopic and microscopic regimes interesting physics, but an understanding of SL might reveal a useful paradigm for energy-concentrating phenomena, and since the wavelength of the outgoing light is larger than the light-emitting region inside the collapsed bubble (of radius $\sim 0.5 \ \mu$m) some type of photon correlation might be present in SL. Our attempts to characterize this phenomenon have led us to pose the following questions and experimental challenges which we will discuss, but not resolve, in this review.

- Why is SL so sensitive to the temperature of the fluid, the light intensity increasing a hundredfold when the temperature is decreased from 40°C to 0°C?
- Why is water the friendliest fluid for SL?
- Why are noble gases so essential for producing stable, bright bubbles? Why do pure diatomic gas bubbles jitter and give such dim light?
- What determines the radius of the SL bubble?
- What determines the upper and lower sound pressure thresholds between which one can observe SL?
- How can one measure a time-resolved spectrum of the light emission?
- Can one measure the spectrum of SL beyond the ultraviolet cutoff of water?
- What is the limit of the energy focusing that can be achieved with SL?
- What is the light-emitting mechanism?

2. How does one produce a sonoluminescing bubble?

An overview of the basic SL apparatus is shown in Fig. 3 (Gaitan, 1990; Hiller and Barber, 1995). An oscillating voltage across a piezoelectric ceramic (PZT) causes it to vibrate and acts as a transducer to drive the water-filled flask at an acoustic resonance. The lowest breathing mode of a spherical resonator is described by $\varphi = j_0(kr)$, where φ is the velocity potential such that $v = \nabla \varphi$ and j_0 is the spherical Bessel function. The wavenumber k is chosen to satisfy the pressure-release boundary condition presented by the air-glass interface, viz. $\varphi(R_f) = 0$, where R_f is the radius of the flask. This solution is perturbed slightly by the differences in acoustic impedance between the fluid and the glass. In this geometry, a gas bubble in the water will be forced to the pressure antinode at the center of the flask by the acoustic radiation pressure of a sufficiently intense sound field (Löfstedt et al., 1995). The second spherically symmetric resonance of the flask creates a spherical velocity-nodal shell which can trap many bubbles at once. This shell is located at about $0.7R_f$ and appears when $kR_f = 2\pi$. The corresponding resonance frequency ω_a is determined by $\omega_a/k = c$.
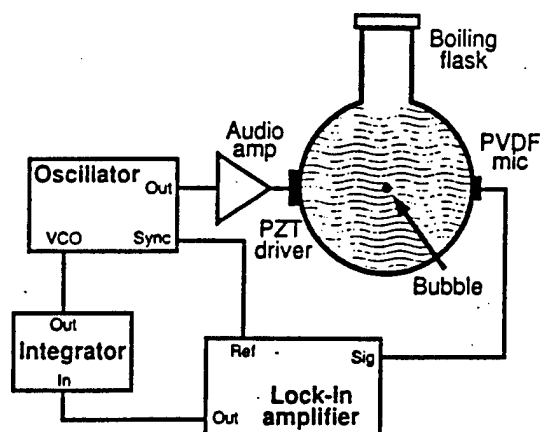
Fig. 3. Basic apparatus for generating and modelocking sonoluminescence. The amplified output of a sine-wave generator drives a water-filled flask at resonance so that a trapped bubble of gas pulsates at sufficient amplitude to generate light. The modelocking circuit tracks the resonance.

At the lowest acoustic drive level at which a bubble is trapped, the bubble will slowly dissolve away. At higher drive levels, the trapped bubble is stable against dissolution but emits no light. Still higher drive levels are the parameter space for stable SL: the bubble suddenly shrinks in size and emits light. Increasing the drive level leads to more intense light emission. Eventually an upper drive threshold is reached, at which pressure the sonoluminescing bubble will abruptly disappear (Gaitan, 1990; Barber and Putterman, 1991). Sometimes, the abrupt upper threshold is replaced by the tendency for the bubble to wander away from the center of the flask with increasing drive levels; whether this is a property of the specific resonator design is unknown.

The resonant frequency of the flask is determined by searching for peaks in the amplitude of the sound field in the flask by means of a microphone, or by tracking the phase difference between voltage and current of the PZT (Barber, 1992). Various spurious resonances, such as flexing modes of the glass flask do not trap a bubble. Variations in the ambient temperature of a few degrees Celsius correspond to shifts in the resonant frequency by 200 Hz which is larger than the width of the resonance of a typical flask. The drive frequency may be continuously adjusted to accommodate such changes in the resonance by using a mode-locking scheme, as shown in Fig. 3 (Hiller, 1995). Underlying the operation of such a method is the fact that the phase of the response of an oscillator relative to a sinusoidal drive shifts by π as the frequency is tuned through resonance. At low frequencies of drive the response is dominated by the spring constant so that it is "in" phase, whereas at high frequency the response is dominated by inertia and is therefore "out" of phase with the drive. The phase shift occurs over a frequency range determined by the damping coefficient of the oscillator. To maintain SL as the drive frequency drifts off resonance, the phase difference between the output of the signal generator, which drives the PZT, and the standing wave in the resonator, as measured by a PVDF microphone, is determined by means of a lock-in amplifier. This phase difference is integrated and used as the voltage-controlled oscillator input to the signal generator. The quality factor of a typical SL apparatus is between 300 and 1500 (Barber and Putterman, 1991). Typical voltages across the PZT required to drive the acoustic resonance and sustain a sonoluminescing bubble are 50 to 150
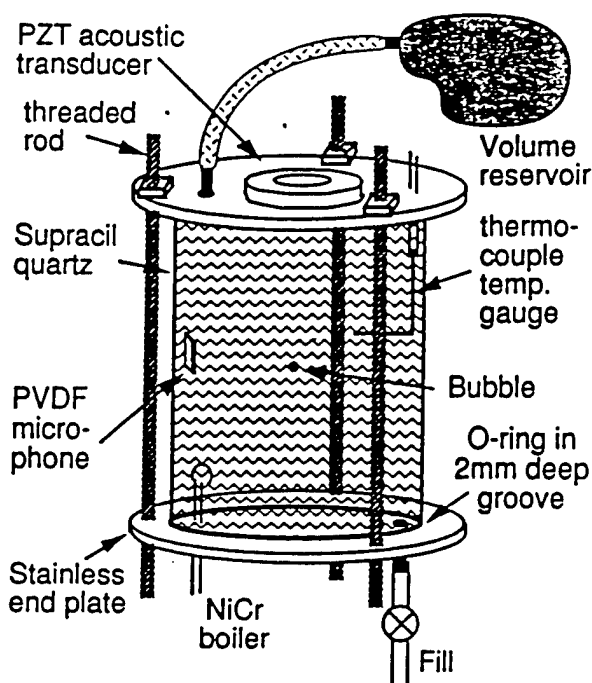
Fig. 4. Cylindrical resonator for obtaining sonoluminescence from a sealed system. This is important for controlling the composition and the partial pressure of the gas content in the resonator. The NiCr (toaster) wire is used to seed a bubble by boiling the liquid locally. The vaporous cavity fills with whatever gas is dissolved in the liquid and is at the same time yanked to the velocity node of the sound field where it emits light at a sufficiently high acoustic drive.

V (which can be generated easily, but expensively. with high voltage linear amplifiers). Alternatively, impedance-matching the capacitance-dominated PZT with inductors allows the SL cell to be driven with less than 10 V (Barber, 1992).

A spherical flask such as the one in Fig. 3 can be seeded with bubbles by simply poking the open surface. However, the quality of the resonance is very sensitive to the level of fluid in the neck. Achieving some degree of experimental reproducibility requires a sealed system, which allows the liquid and the gas contents to be controlled accurately. Such a system is shown in Fig. 4, where a sealed cylindrical resonator is driven by piezoelectrics mounted on the steel endcaps (Hiller et al., 1994). In this apparatus the free surface is eliminated by filling the system entirely; changes in density are accommodated by a variable volume which is provided by a polyethylene bag. The bubble is seeded by passing a brief current through a loop of NiCr wire, which boils the surrounding fluid, leaving vaporous bubbles, into which flows the gas dissolved in the fluid. These gas bubbles are then carried to the pressure antinode by acoustic radiation pressure, where they coalesce into a single bubble. The ambient fluid temperature is measured by means of thermocouple gauges.

The fill lines of the resonator are connected to the gas manifold shown in Fig. 5 (Battino et al., 1972; Hiller, 1995). The designated fluid is degassed to tens of millitorr of partial pressure of
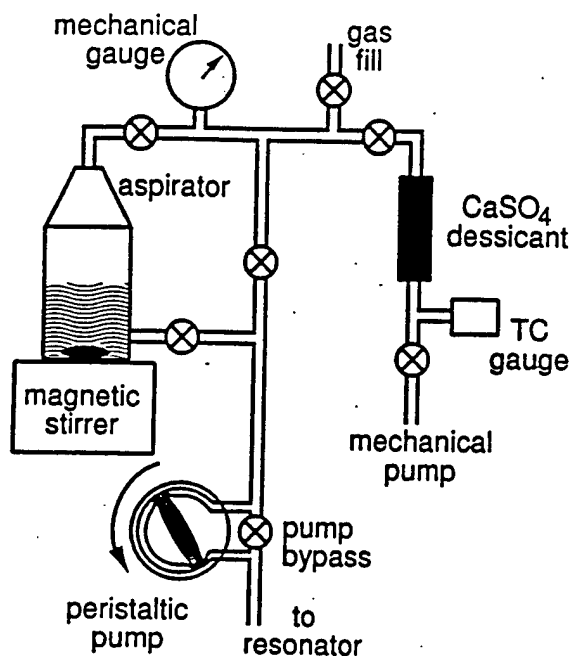
Fig. 5. Gas manifold apparatus used for the purpose of degassing water or another liquid and then preparing it with a desired partial pressure of a particular gas mixture.

gas (plus the vapor pressure) by means of a mechanical pump. A magnetic stirrer accelerates the degassing by creating turbulent voids which increase the area of the fluid/gas interface. The chosen gas mixture is prepared in a large reservoir, and admitted to the degassed fluid through the gas fill line at the chosen pressure. Stirring the fluid accelerates the establishment of equilibrium between the gas dissolved in the fluid and the gas pressure above it. Although equilibrium appears to be established in less than 5 min we stir for about 20 min. The fluid finally pumped into the SL resonator has a partial pressure of gas dissolved in it which is accurate to about 1/2 Torr.

The modal structure which can trap bubbles in the cylindrical cell in Fig. 4 are approximated by the pressure amplitudes

$$P_a = P_a' J_0(k_n r) \cos(2q\pi z/H) \cos(\omega_a t)$$

where H is the height of the cylinder and

$$\omega_a^2 = c^2 \left(k_n^2 + \frac{4q^2\pi^2}{H^2} \right)$$

and the surface of the cylinder is taken as a pressure node, so that $J_0(k_n R_f) = 0$, and the z dependence has been chosen so that $z = 0, +H/2$, and $-H/2$, are all velocity nodes. This fixes q to be an integer,

as can be seen from the velocity potential, φ, which is related to the pressure by

$$P_a = -\rho \partial\varphi/\partial t.$$

3. How does one measure the bubble motion?

Underlying SL is a small bubble whose pulsations absorb the long-wavelength sound energy during half of the sound cycle and then quickly concentrate it so as to emit a flash of light. The dynamics of this bubble, in particular its radius as a function of time, $R(t)$, constitute an essential parameter in characterizing SL. The experimental impediments to overcome in measuring the radius include the wide range of timescales of the bubble motion (~ 10 μs for the absorption of energy to sub-nanosecond for the collapse) and the fact that the bubble's radius ranges from 50 μm at its maximum to 1/2 μm, the wavelength of visible light, at its minimum (Barber and Putterman, 1992). The features of SL which come to the experimentalist's aid in determining $R(t)$ include the flash of light which accompanies each cycle of the sound field. The flash can be used to set the zero of time for the purpose of averaging several acquisitions and reducing the noise level. As mentioned above, the light flash comes at the same point in every cycle and these cycles repeat with a clocklike synchronicity (Barber et al., 1992).

Mie scattering has proven to be a valuable and versatile technique for measuring $R(t)$ (van de Hulst, 1957; Dave, 1969; Kerker, 1969; Marston 1979, 1991; Wiscombe, 1980; Hansen, 1985; Gaitan, 1990; Barber and Putterman, 1992; Holt and Crum, 1992). In this approach laser light with a beam width larger than the bubble's radius is trained on the bubble. In the classical, or ray optics limit, the light scattered within a given angle is simply proportional to $R^2(t)$. Since the voltage on the photodetector is proportional to the intensity of the scattered light, the square root of this signal is proportional to R. This scattered light is also proportional to the difference in the dielectric constant at the gas-fluid interface presented by the surface of the bubble. Surprisingly, as the size of the bubble is increased, the ray optics limit is approached only very slowly. As shown in Fig. 6, for a bubble of radius 20 μm, the light scattered within a specific angle displays many diffraction peaks which can be seen straddling the classical limit (solid line). The signal is clearly very sensitive to angular alignment. Experimentally we converge on the classical limit by collecting the scattered light from a range of angles, typically 25° around 60° from the forward direction, which averages out the fringes, as shown in Fig. 6.

A Mie scattering apparatus is shown in Fig. 7 (Barber and Putterman, 1992). Light from a He-Ne or He-Cd laser irradiates the bubble. A filter which blocks the wavelength of the laser light is placed between the bubble and a photodetector, which is therefore sensitive only to the flash of SL. This serves as the trigger for the zero of time and enables us to average about 500 runs to obtain a final plot. The light scattered by the bubble in a large angle is collected by a lens and passes through a laser line pass filter (which blocks the broadband SL flash) onto a photodetector whose signal $V(t)$ is proportional to $R^2(t)$ plus the background level $\bar{V}(t)$. The signal and the noise level are shown in Fig. 8. The noise level is measured by shining the laser light through the flask in the absence of a bubble. We presume that the noise is due to stray light and scattering from impurities. The radius is obtained by evaluating $\sqrt{|V(t) - \bar{V}(t)|}$ which is proportional to the radius, as plotted in Fig. 9 for one cycle of the sound field.
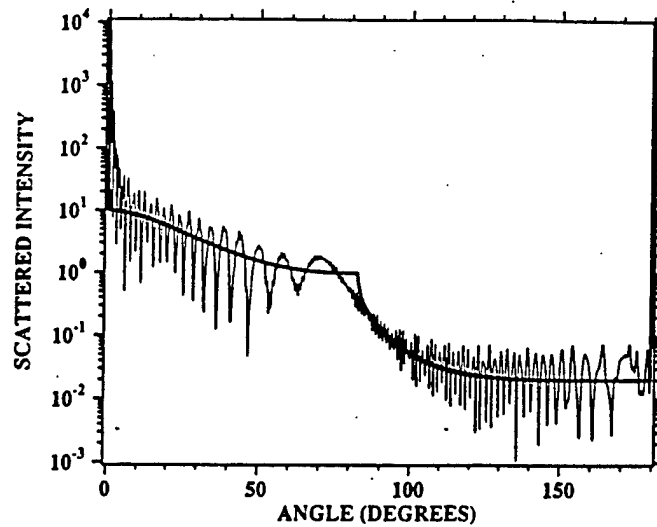
Fig. 6. Intensity of light as a function of angle of scattering. The exact Mie theory (jagged curve) and the WKB or ray optics limit (smooth curve) for a 20 μm air bubble in water illuminated by a He-Ne laser are compared. The intensity is normalized such that geometric reflection from a mirrorlike sphere gives an intensity of 1.
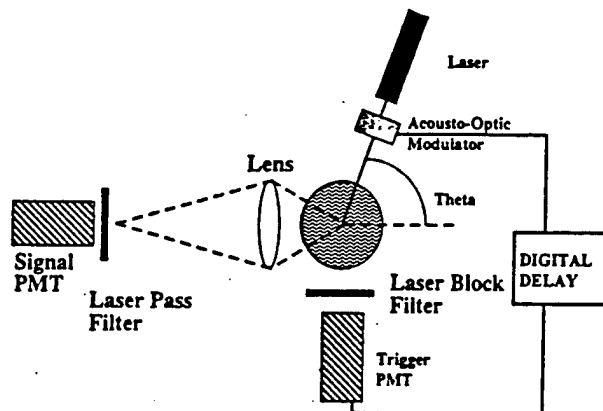
Fig. 7. Apparatus for Mie scattering measurements of a sonoluminescing bubble. By collecting light from a large solid angle the detected intensity becomes proportional to the square of the radius of the bubble. The flash of SL provides a trigger which sets the zero for time and which can be used in conjunction with a pulse delay generator to pick out various portions of the cycle.

Apparent in Fig. 9 are four different timescales of the bubble motion: t_A is the slow expansion of the bubble in response to the rarefaction of the indicated sound field ($\sim 15\ \mu$s), t_B is the turnaround time at the maximum bubble radius, R_m, which is due to inertia of the bubble ($\sim 5\ \mu$s), t_C is the runaway collapse of the bubble wall, which leads ultimately to the flash of light (the time for the bubble to collapse from $\frac{1}{2}R_m$ to R_c, the minimum radius is on the order of 1/2 μs), and t_D is
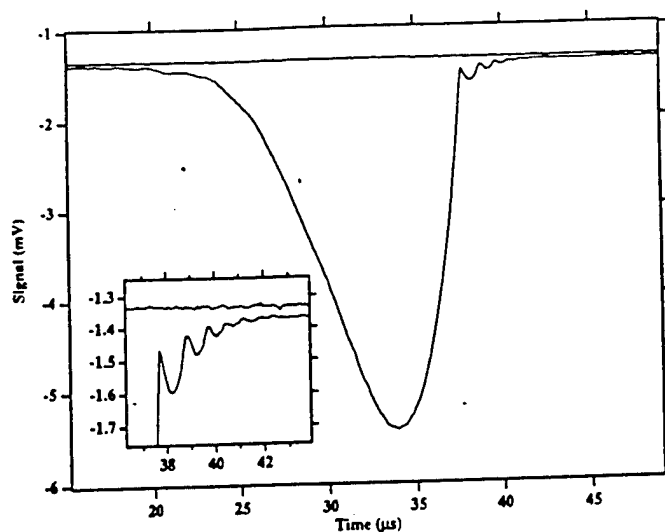
Fig. 8. Signal $V(t)$ and noise level $\hat{V}(t)$ for light scattered by a sonoluminescing bubble during one cycle of the driving sound field. The inset blows up the difference between signal and noise. These data show more detail than Fig. 1 because it is the average of 512 as compared to 32 sweeps.

the order 1 μs period of the breathing resonance oscillations of the bubble around its ambient size, $R_0(P)$ which is the size of the bubble when it is in static mechanical equilibrium with a gas pressure P on the inside. For $P = P_0$ (which is usually 1 atm) we will simply write $R_0 = R_0(P_0)$. The total pressure P will be due to the externally imposed static pressure P_0 plus the acoustic pressure. It turns out that in the region of the afterbounces P/P_0 is about 2.

A fifth timescale which cannot be obtained from this graph governs the approach to the minimum radius (the time to go from R_0 to R_c). The region of interest can be expanded by using an acousto-optic modulator to select the appropriate portion of the cycle (Barber and Putterman, 1992). By deflecting the laser beam from the bubble during the portion of the cycle when the bubble is near its maximum radius (i.e., when it scatters the most light), one can operate the photomultiplier tube at a higher gain without exceeding its anode current limit. The blowups, Fig. 10, are scaled to the ambient radius, $R_0(P)$, which is the radius approached as the oscillations die out. According to this data the timescale t_E is between 5 and 10 ns. The absolute calibration of such blowups relies on fixing the value of the radius at one instant by a comparison with the larger picture, Fig. 9. The large picture in turn is calibrated by matching it to the theoretical Rayleigh-Plesset equation, discussed in the following section. Suffice it to say here that in view of the wide range of timescales characterizing the SL bubble motion, this fit is highly constrained. For this data one finds $R_m = 38$ μm so that $R_0 \approx 4.0$ μm (Barber and Putterman, 1992).

Alternative measurements of R and $\dot{R}$ at certain points in time can be obtained by fitting data to structure in Mie scattering (Lentz et al., 1995) and by interfering scattered and unscattered light (Delgadino and Bonetto, 1996). By backlighting the bubble Tian et al. (1996) obtained R from video images. Whether these techniques can improve on the calibrations obtained from hydrodynamics
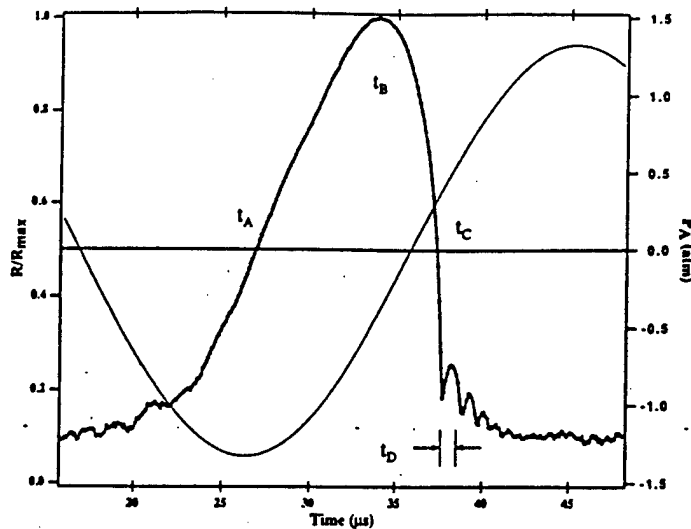
Fig. 9. The radius $R(t)$ scaled to the maximum radius R_m during one cycle of the sound field. If $V(t)$ is the signal on the photodetector and $\tilde{V}(t)$ is the noise level, this plot is given by $\{|[V(t) - \tilde{V}(t)]|/V_m\}^{1/2}$, where V_m is the maximum voltage. Note that for a SL bubble $R_m/R_0 \approx 10$, where R_0 is the ambient radius which is the radius the bubble would have in the absence of a driving pressure. The driving sound field is superimposed. This figure is constructed from the data in Fig. 8, for an air bubble in water. A comparison to the Rayleigh-Plesset equation of bubble dynamics indicates that for these data $R_0 = 4.0$ μm, and the amplitude of the sound field is 1.35 atm.

remains to be seen. Altough all of these methods lack the bandwidth of the Mie scattering technique described in this section, the video images point the way towards the direct detection of deformations in the shape of the bubble.

The measurements shown in Figs. 8–10 are made possible by the nanosecond response time of the photomultiplier tube used to detect the scattered light. However, this response time is still not fast enough to avoid convolving light scattered from different times during the rapid final collapse to the minimum radius, shown in Fig. 10. To determine more accurately this key interval of time leading up to the flash of light, we replaced the CW laser used above with the short flashes of a titanium-sapphire laser (Barber et al., 1997). This laser produces 200 fs wide pulses with a repetition rate of 76 MHz, which corresponds to about 13 ns between flashes. Now the instant at which the light was scattered by the bubble is precisely labelled by the pulse of laser light, and the integrated response of the photomultiplier tube can be attributed to a precise moment in time. Fig. 11 shows the scattered light and the noise level using this apparatus. The width of the peaks is due to the PMT's finite response time (5 ns), which is shorter than the time between consecutive laser pulses (13 ns), so there is no spillover of the tube response from one pulse to the next. The height of the peaks is proportional to the square of the instantaneous radius of the bubble. The SL flash again serves as a temporal reference point in the alignment of many traces.

The traces, such as in Fig. 11, are acquired on a digital oscilloscope with a bin separation of 0.5 ns. The integrated area of each peak is ascribed to the bin corresponding to the time difference between the maximum of the peak and the flash of SL. As data is acquired at different phases relative to the
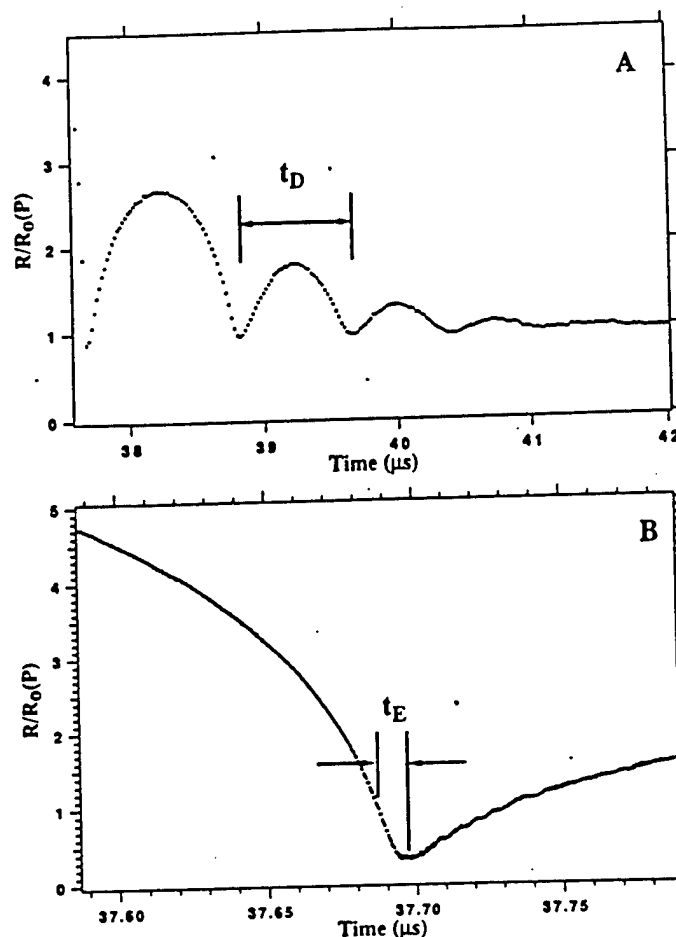
Fig. 10. Detail of the bubble motion $R(t)$ near the minimum radius R_c, taken with continuous laser illumination. These curves, (A) and (B), are taken at the same gain level of the photodetector, which is higher than the gain level used to obtain Fig. 9. The observation that $R_c/R_0(P) \le 1/8$ indicates that the van der Waals hard core of the gas plays a role in limiting the collapse of the bubble. The breathing period is t_D and the time to go from the ambient radius to the collapse radius is t_E.

SL flash (note that the repetition rate of the laser is not commensurate with the frequency of the sound field), the graph in Fig. 12 is obtained. The calibration of these traces proceeds in the same way as in the CW laser scattering. The complete sound cycle is matched to the theoretical equation, and the blowups are calibrated by using the value of the radius at a point on the large picture.

From Fig. 12 we can conclude that the bubble is collapsing inward at Mach 4, relative to the ambient speed of sound in the gas, and that the acceleration which brings the bubble to a halt at its minimum radius exceeds 10^{11} g (Barber et al., 1997). In addition, as shown in Fig. 13, the SL light
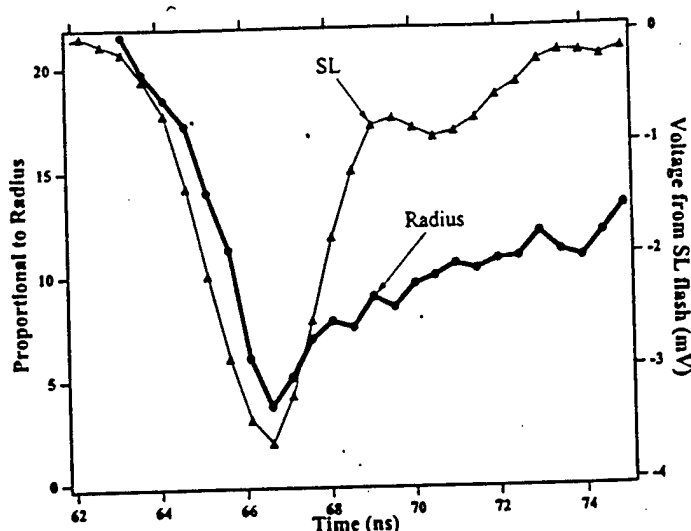
Fig. 13. Flash of SL and light scattering as resolved by the same photomultiplier tube. Each radius measurement is ascribed to that point in time when the response shown in Fig. 11 is a maximum. Thus for comparison the flash of SL must be ascribed to that point in time when the response to the flash is a maximum. As shown by these data the flash occurs within 500 ps of the minimum radius. This improves on the 8 ns resolution of Barber and Putterman (1992) (see their Fig. 4) and the 100 ns resolution of Lentz et al. (1995) (see their Fig. 11).

flash is localized to within 0.5 ns of the minimum. In this experiment the light flash was acquired with the same photodetector that acquired the scattered light and as with the individual scattering peaks of laser light, the time of the flash in Fig. 13 must be ascribed to the location of its maximum. (Using CW scattering led to an incorrect interpretation of the light coming a few ns before the minimum bubble radius R_c (Barber and Putterman, 1992).) The fastest known timescale characterizing SL is the width of the flash (< 50 ps) and this time scale is not resolved or apparent in this light scattering data.

Laser scattering from a non-light-emitting bubble ("bouncing") bubble is more difficult because there is no intrinsic trigger like the SL light flash. The synchronous output of the sine-wave generator, which drives the PZT, serves as a trigger with 10 ns jitter. While this is not nearly enough resolution to characterize the timescales of the SL bubble motion, it suffices to describe the slower bouncing bubble motion (Barber and Putterman, 1992).

4. How does one describe the bubble dynamics?

Except for an interval of time of about 200 ns when the bubble is near its minimum radius, R_c, the speed of the bubble wall, $\dot{R}(t)$, is less than one-tenth of the ambient speed of sound of gas in the bubble and less than one-fortieth of the speed of sound in water. Thus, during 99.5% of the acoustic cycle, one would expect low Mach number hydrodynamics to provide an accurate description of the motion. This expectation is indeed met, and these solutions indicate how the bubble absorbs energy

from the sound field and then begins its runaway collapse. Already in 1917, Rayleigh (1917) made major analytic progress in finding and interpreting the equations which apply in this circumstance. His starting point was fluid mechanics for a barotropic equation of state so that pressure, P, is a function only of the density, ρ. These equations (Landau and Lifshitz, 1987) are

$$\frac{\partial \rho}{\partial t} + \nabla \cdot \rho v = 0 \tag{1}$$

and

$$\frac{\partial \rho v_i}{\partial t} + \frac{\partial}{\partial r_j}[P(\rho)\delta_{ij} + \rho v_i v_j + \tau_{ij}] = 0, \tag{2}$$

where $v(r,t)$ is the velocity, and the viscous stress tensor is given by

$$\tau_{ij} = -\eta\left(\frac{\partial v_i}{\partial r_j} + \frac{\partial v_j}{\partial r_i} - \frac{2}{3}\delta_{ij}\nabla \cdot v\right), \tag{3}$$

where η is the shear viscosity. These equations apply to both the gas in the bubble and the surrounding fluid; the only adjustment is to use the appropriate equation of state for the pressure and value for the shear viscosity. At a spherically symmetric interface the surface tension σ leads to a discontinuity in the perpendicular component of stress:

$$P_g(R,t) - P(R,t) - \frac{4\eta\dot{R}}{R} = \frac{2\sigma}{R} \tag{4}$$

where P_g is the pressure in the gas, P is the pressure in the fluid, and viscous effects lead to $\tau_{rr} = -4\eta\dot{R}/R$, the viscous effects due to the gas being negligible. The center of the bubble is at the origin of the spherical coordinates. To close the equations also requires use of the kinematic boundary condition $v_r(R,t) = \dot{R}(t)$.

In the limit where the imposed sound field $P_a(r,t)$ has a small Mach number, such that $|P_a/\rho c^2| \ll 1$, where c is the speed of sound in the fluid (c_g will denote the speed of sound in the gas), and the Mach numbers and accelerations of the bubble are small,

$$\frac{\dot{R}}{c} \ll 1, \quad \frac{R\ddot{R}}{c^2} \ll 1, \quad \frac{\dot{R}}{c_g} \ll 1, \quad \frac{R\ddot{R}}{c_g^2} \ll 1,$$

and the wavelength of the sound field, $\lambda = 2\pi/k$, is large compared to the bubble radius, $kR \ll 1$, one is led to the leading order Rayleigh-Plesset equation (Rayleigh, 1917; Plesset, 1949; Noltingk and Neppiras, 1950; Prosperetti, 1984; Prosperetti et al., 1988; Löfstedt et al., 1993)

$$R\ddot{R} + \frac{3}{2}\dot{R}^2 = \frac{1}{\rho}(P_g(R) - P_0 - P_a(0,t)) - \frac{4\eta\dot{R}}{\rho R} - \frac{2\sigma}{\rho R}$$

$$+ \frac{R}{\rho c}\frac{d}{dt}(P_g - P_a). \tag{5}$$

The left-hand side of this equation represents the inertia of the accelerating bubble in response to the net force on it, which, as on the right hand side, is due to the difference in pressures inside and
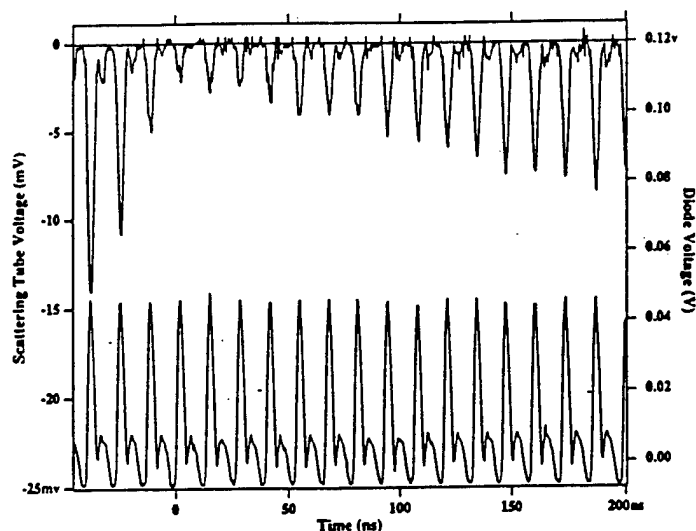
Fig. 11. Pulsed light scattering from a collapsing bubble as probed by 200 fs pulses of light with a repetition rate of 76 MHz (upper trace). The scattering data are generated by a single sweep. The noise floor is obtained from 512 averages. Essential to this method is that the response of the detector return to the noise floor between pulses. In this way each peak can be ascribed to a single, precisely timed scattering event. Shown on the lower trace is the output of the photodiode that tracks the timing of the laser pulses.
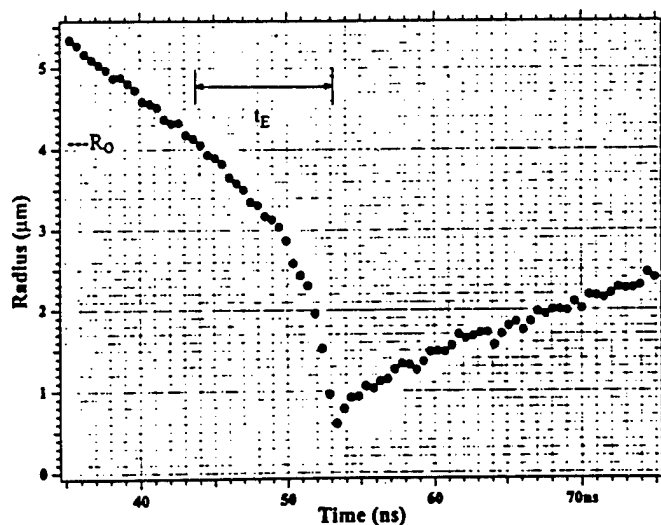
Fig. 12. Radius of a sonoluminescing bubble (1% xenon in oxygen at 150 mm) as the moment of collapse is approached. These points are obtained by averaging together many traces of the type shown in Fig. 11, for various phases of the laser relative to the flashes of SL. According to these data the bubble is collapsing over 4 times the ambient speed of sound in the gas. For this bubble $R_0 \approx 4.1$ μm, $P_a' \approx 1.45$ atm.

outside it. At leading order the damping is due to viscous effects and the radiation of sound into the fluid by the bubble's motion. When next-order terms in a Mach number expansion (Prosperetti, 1984; Löfstedt et al., 1993) are included in the inertial terms, the left-hand side of (5) becomes

$$R\ddot{R}\left(1 - \frac{2\dot{R}}{c}\right) + \frac{3}{2}\dot{R}^2\left(1 - \frac{4\dot{R}}{3c}\right).$$

For small Mach numbers these corrections are obviously small. But also when the Rayleigh-Plesset equation is used beyond its region of applicability so that $\dot{R}/c \sim O(1)$, these terms present the problem that the effective mass becomes negative. Although these corrections provide a slightly more accurate model for small Mach numbers, we will continue to use Eq. (5) to describe the bubble motion. The externally imposed (sinusoidal standing wave) sound field at the bubble is

$$P_a(0, t) = P_a'\cos(\omega_a t) \tag{6}$$

where P_a' includes the response of the resonator to the drive.

The Rayleigh-Plesset equation needs to be supplemented with an equation of state for the gas, so that it becomes a closed equation for $R(t)$. For rapid changes in the bubble radius we will use the adiabatic equation of state (Löfstedt et al., 1993)

$$P_g(R) = \frac{P_0 R_0^{3\gamma}}{(R^3 - a^3)^\gamma}, \quad T_g(R) = \frac{P_0 R_0^{3(\gamma-1)}}{(R^3 - a^3)^{\gamma-1}} \tag{7}$$

where $\gamma = C_P/C_V$, the ratio of specific heats, and we have allowed for the possibility that the collapse is sufficiently strong that the hard core radius of the bubble contents, a, is probed. This radius is related to the van der Waals excluded volume, b, by $\frac{4}{3}\pi a^3 = \mathcal{N}b$, where $\mathcal{N}$ is the number of moles in the bubble and for air $b = 0.04$ ℓ/mole. R_0 is the radius at which the pressure inside the bubble is the ambient pressure, $P_0 = 1$ atm, so that for air $R_0/a = 8.54$. For slow motion we will assume an isothermal equation of state, $P_g(R) = P_0 R_0^3/R^3$; $T_g(R) = T_0$, where T_0 is the ambient temperature. (In general the subscript "g" will denote properties of the gas and the subscript "0" will denote properties of the gas at ambient conditions.)

We typically use the isothermal equation of state for radii larger than the ambient radius, and the adiabatic equation of state for smaller radii. The crossover timescale τ between the two equations of state may be evaluated by calculating the diffusive penetration depth in the gas. If this depth is comparable to the radius of the bubble, the contents will be isothermal; if it is much smaller than 1/3 the radius of the bubble, the adiabatic equation of state is more appropriate. The expression for the diffusive penetration depth (Prosperetti, 1984) is

$$\delta_T = \left(\frac{\kappa_g \tau}{\pi \rho_g C_g}\right)^{1/2}.$$

At ambient density and at an ambient radius of a few microns, the timescale for the crossover is microseconds. The resonant breathing frequency of such bubbles corresponds to this ambiguous regime.

A typical fit of the RP equation to data is shown in Fig. 14 (Barber and Putterman, 1992). The sensitivity of the fit is demonstrated in Fig. 15. Here the fitting parameters, viz. R_0 and P_a, are
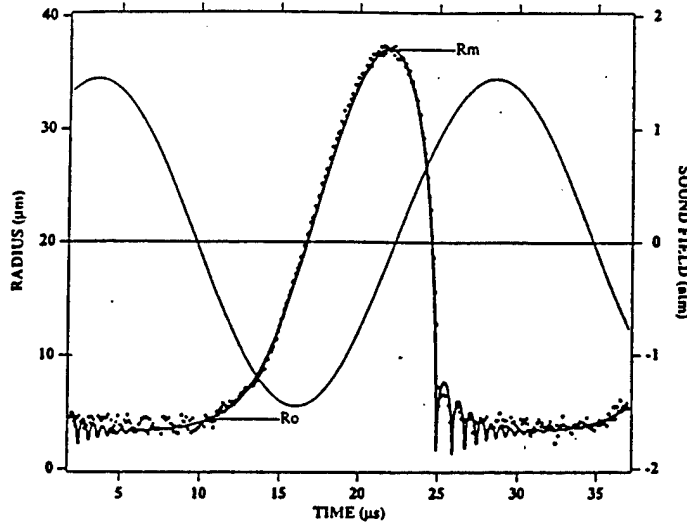
Fig. 14. Radius of a 3 mm xenon bubble as a function of time for one cycle of the sound field. When the acoustic pressure is negative the bubble expands. This is followed by a collapse and ringing before the bubble sits dead in the water waiting for the next cycle. According to a calibration of the data by Rayleigh-Plesset equation (solid line) the ambient radius is 4.3 μm and the driving pressure is 1.45 atm.

varied. Surface tension is typically taken as 50 dyne/cm, and fits generally use an effective damping $\eta \approx 4\eta_{water} \approx 0.04$ g/cm s due to impurities in the water. In Fig. 14 it is apparent that the fit to the afterbounces is not in very good agreement with the experimental data. The expanded data, Fig. 16, however, shows a good fit to the RP equation. To obtain accurate experimental measurements of these afterbounces, use of the acousto-optic modulator is essential; the PMT cannot resolve the magnitude of the relatively small bounces after being exposed to scattered light from the expansion of the bubble to its maximum size.

The RP equation enables us to calculate the various timescales governing the SL bubble's dynamics (Löfstedt et al., 1993). To characterize the expansion of the bubble from its ambient radius to the maximum radius, we expand the RP equation around the maximum rarefaction of the drive. The expansion is found to be accurately linear in time (Apfel, 1986; Löfstedt et al., 1993), with a slope

$$\dot{R}_A = \left(\frac{2}{3}\frac{P'_a - P_0}{\rho}\right)^{1/2} \tag{8}$$

corresponding to a Mach number relative to the ambient speed of sound in gas $M = 0.01$ for typical $P'_a \approx 1.4$ atm. The time scale t_A is therefore given approximately by

$$t_A \approx (R_m - R_0)/\dot{R}_A \tag{9}$$

and we note that the slope given by (8) is in good agreement with Fig. 14. Due to the inertia of its expansion the bubble continues to grow even after the net pressure acting on it is no longer negative.
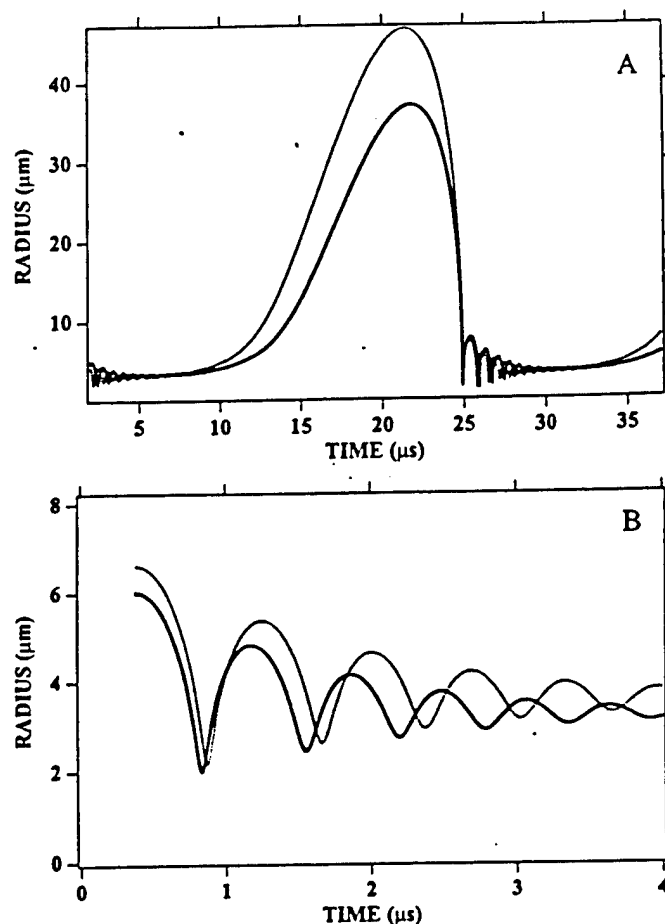
Fig. 15. Sensitivity of solutions to the Rayleigh-Plesset equation. In (a) solutions with the same R_0 but drive pressures differing by 10% are compared. In (b) the amplitude and phasing of the afterbounces are compared for the same drive amplitude but ambient radii differing by 10%. A comparison of light scattering data to the Rayleigh-Plesset equation yields a fit to R_0 accurate to 0.25 μm and to P'_a accurate to 0.05 atm.

This is the timescale t_B associated with its turnaround at the maximum radius. Expanding the RP equation around this radius yields

$$t_B \approx \left(\frac{\rho R_m^2}{P_0}\right)^{1/2} \tag{10}$$

which is on the order of 5 μs (again in good agreement with Fig. 14). If this timescale is comparable to the time t_- required for the sound field to go from $-P_0$ to zero, then the bubble will find itself perched at its maximum radius with a vacuum on the inside and P_0 on the outside. So if
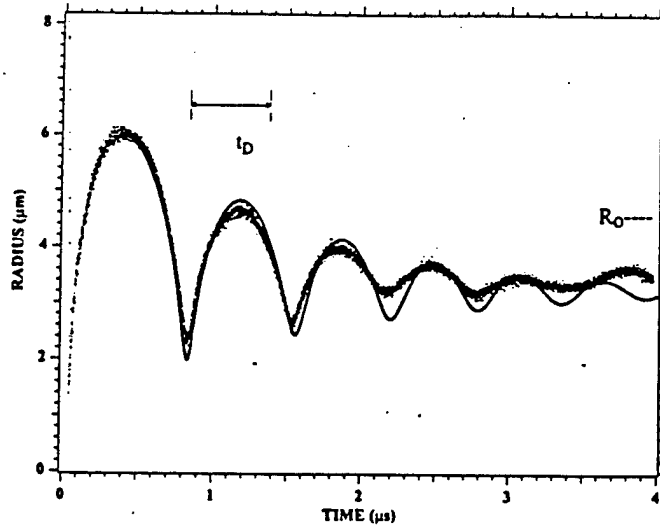
Fig. 16. Comparison of data and fit to the Rayleigh-Plesset equation for the afterbounces of a 3 mm xenon bubble. To account for impurities in the water we interpret the viscosity as an effective damping and take its value as 0.04 g cm/s (four times the tabulated viscosity of pure water), and for surface tension the value 50 dyne/cm is taken.

$$t_B \sim t_- = (1/\omega_a)\sin^{-1}(P_0/P'_a) \tag{11}$$

the bubble at $R = R_m$ will be unstable against the collapse, which was first calculated by Rayleigh (1917). The time required for the bubble to collapse from its maximum radius to its minimum radius can be evaluated by first transforming (5) to obtain (Löfstedt et al., 1993)

$$\frac{d}{dt}\left(\frac{1}{2}R^3\dot{R}^2 + \frac{P_0R^3}{3\rho} - \frac{1}{\rho}\int P_g(R)R^2\,dR\right) = 0 \tag{12}$$

which applies when damping and surface tension are negligible. Integrating this equation from R_m, where $\dot{R} = 0$, to R, and noting that unless R is within a percent of the hard core a the back pressure of the gas is negligible, yields

$$\frac{1}{2}R^3\dot{R}^2 + \frac{P_0(R^3 - R_m^3)}{3\rho} = 0. \tag{13}$$

For values of $R < R_m/2$ we have to about 10% accuracy

$$\dot{R} = -(2P_0/3\rho)^{1/2}R_m^{3/2}/R^{3/2} \tag{14}$$

so that the time to go from $R_m/2$ to R_0 is

$$t_C \approx \frac{R_m}{10\sqrt{P_0/\rho}} \tag{15}$$

and the time to go from R_0 to the minimum radius is

$$t_E \approx \frac{\sqrt{6}\, R_0^{5/2}}{5 R_m^{3/2} (P_0/\rho)^{1/2}}. \tag{16}$$

For typical parameters $t_C \approx 500$ ns and $t_E \approx 8$ ns, also in good agreement with experiment (Barber and Putterman, 1992; Löfstedt et al., 1993). This calculation involves only the approximations that the Mach number relative to the speed of sound in the fluid is small, $\dot{R}/c \ll 1$, so that the radius of the bubble must be larger than about $3a$. For such radii one can also easily verify that the damping effects are small and that P_g can be neglected. Even when $\dot{R}/c \ll 1$ it is possible that $\dot{R}/c_g \sim 1$. In this limit (12) still applies but the equations of state (7) become a very poor description of the gas inside the bubble (Greenspan and Nadim, 1993; Löfstedt et al., 1993); in particular the gas becomes nonuniform so that $P_g(r, t) \neq P(R(t))$.

A linearization of (5) around the ambient radius R_0 yields the dispersion law for the (adiabatic) radial pulsations of a free bubble with a frequency (Prosperetti, 1984).

$$\omega_0(P) = [3\gamma P/\rho R_0^2(P)]^{1/2} \tag{17}$$

so that $t_D \approx 2\pi/\omega_0(P)$. Approximating P with P_0 and $R_0(P)$ with R_0 yields $t_D \sim 1.3$ μs for $R = 4.5$ μm. The difference between this estimate and the actual period (~ 0.75 μs) can be accounted for by the factor:

$$\omega_0(P)/\omega_0 = [R_0/R_0(P)]^{5/2} = (P/P_0)^{5/6}$$

where P is the total pressure acting on the ringing bubble and $R_0(P)$ is the asymptote in Fig. 16.

Finally, one can also use the RP equation to estimate the time for the bubble to turn around at its minimum radius by expanding (5) around R_c. Using the parameters appropriate to SL, one finds a timescale of about a hundred picoseconds (Löfstedt et al., 1993). However, this short timescale clearly lies outside of the validity of the hydrodynamic approximations which led to the derivation of the RP equation. Such calculations serve only to show that these approximations are violated, and that while the RP is rich in mathematical implications at these parameters, it misses the physics essential to SL.

As the bubble collapses the increasing pressure in the interior becomes a pressure source for an outgoing acoustic wave. To lowest order in the Mach number relative to the fluid, the scattered field takes the form (Löfstedt et al., 1993),

$$P_{scat}(r, t) = \rho \left(\frac{2R\dot{R}^2 + R^2 \ddot{R}}{r} \right)_{t-(r-R)/c}. \tag{18}$$

Using the RP equation for $R(t)$, one can readily reproduce the acoustic spike, depicted in Fig. 1, trace "a" (Barber et al., 1997). In particular the spike is a compression, it is delayed by the time that it takes the pulse to travel the 1 mm from the bubble to the microphone, and the spike width is due to the response of the microphone to the nanosecond bubble dynamics. A blow-up of the spike is shown in Fig. 17. Based upon the calibration of the manufacturer (Precision Acoustics), the peak has an amplitude of 3 atm at 1 mm from the bubble. The initial amplitude of the outgoing acoustic spike may be obtained by correcting for the spreading and damping of the high frequency waves as they travel from the bubble wall (at 0.5 μm) to the microphone.
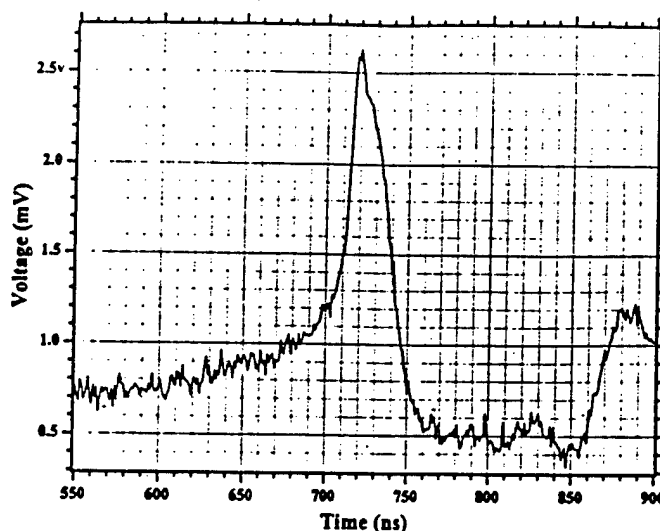
Fig. 17. Response of a PVDF needle hydrophone to the short pulse of sound emitted by the collapsing bubble. This is the spike shown on trace (b) of Fig. 1 with an expanded timescale. The rise time of 10 ns is instrument limited and indicates the presence of frequencies greater than 30 MHz. (Hallaj et al. (1996) report the measurement of a 5 ns risetime that is still instrument limited.) According to the calibration of the hydrophone, the signal at 1 mm from the bubble is about 3 atm. Correcting for geometric dispersion the amplitude at the point of emission (0.5 μm) is over 6000 atm. The attenuation of sound is also considerable for high frequency pulses. For instance a 300 MHz pulse is reduced in amplitude by a factor of 10000 after having travelled 1 mm. Inclusion of this effect would substantially increase the estimate of the launching amplitude of the outgoing pulse.

Interpreting Eq. (12) as an energy equation (Noltingk and Neppiras, 1950; Löfstedt et al., 1993), one can show that the quantity of energy absorbed by the bubble from the sound field during its expansion is $\frac{4}{3}\pi R_m^3 P_0$. About half of this energy is radiated as sound during the bubble's collapse, and the rest is dissipated by the viscosity. In fact, by equating the energy absorbed to the energy radiated at the minimum, one can obtain an analytic estimate of the bubble's minimum radius, with reasonable accuracy. The energy of the radiated light from the brightest bubble represents only 0.01% of the acoustic drive input. However, the energy radiated as light is comparable to the acoustic energy dissipated in the resonator, *in the absence of a bubble*, by the shear viscosity. To see this consider the ratio of the energy stored in the bubble to the energy stored in the sound field in the flask (Löfstedt et al., 1993)

$$\frac{E_b}{E_a} = \frac{P_0 R_m^3}{\rho M^2 c^2 R_f^3}.$$ (19)

The ratio of the rate at which these quantities dissipate is then

$$\frac{\dot{E}_b}{\dot{E}_a} = \frac{P_0 R_m^3}{2\pi M^2 \omega \eta R_f^3}.$$ (20)

which is order 10^4! The huge rate at which bubbles scatter sound energy is the reason why bubbles make outstanding contrast agents for acoustic radiology (Feinstein, 1989; de Jong et al., 1992; D'Arrigo et al., 1993).

A key feature of the SL bubble dynamics is the asymmetry of the expansion and collapse (Löfstedt et al., 1993). The origin of this asymmetry is the inertia of the bubble which allows it to expand even after the net pressure acting on it is no longer negative. This overshoot of the bubble expansion (as described by Eq. (10)) implies that when the bubble reaches its maximum size, the external sound field has already turned compressive, and thus there is no force to resist the bubble wall's runaway collapse into its evacuated interior. This asymmetry sets the arrow of time for the SL process by leading to such a fast collapse that the radiation damping then causes the bubble to sit dead in the water waiting for the next cycle.

An empirical criterion for SL derives from the observation that the collapse toward the minimum radius for a sonoluminescing bubble attains Mach 1, relative to the ambient speed of sound in air, at its ambient radius (Barber et al., 1994). From Rayleigh's equation (1917) for the collapse (14), this condition can be written as

$$\frac{\dot{R}(R_0)}{c_s} \approx \left[\frac{2}{3\gamma}\frac{\rho_0}{\rho}\left(\frac{R_m}{R_0}\right)^3\right]^{1/2} \approx O(1). \qquad (21)$$

Solving this equation for the expansion ratio of maximum radius to ambient radius gives $R_m/R_0 \approx 10$ as the condition for SL. This condition is lent additional support by "waterfall" plots of the bubble dynamics as a function of drive pressure (Fig. 18) (Barber et al., 1994). At low drive levels, a stably-trapped, but non-light-emitting, "bouncing" bubble obeys the RP equation, and its motion throughout the acoustic cycle is well-described by low Mach number hydrodynamics. The expansion ratio is about 3, and thus the criterion for SL is not met. At a certain drive level, the lower threshold, the bubble suddenly shrinks, the expansion ratio increases, and the bubble begins to emit light. As shown in Fig. 19, which is a detail of Fig. 18, the lower threshold for SL is related to the sudden change in the ambient size in the bubble, a parameter which is undetermined by the RP equation.

Interaction with the standing wave sound field also determines the time averaged force of trapping of the bubble (King, 1934; Löfstedt and Putterman, 1991; Löfstedt et al., 1995)

$$F_a = -\langle V\nabla P_a\rangle \qquad (22)$$

where V is the volume of the bubble. For small oscillations the acoustic radiation (or Bjerknes) forces are second-order effects in the drive amplitude (Bjerknes, 1906). For an SL bubble, the time averaged force is dominated by the expansion of the bubble, which is when the volume is largest and the drive pressure passes through an ascending node (Löfstedt et al., 1995). In this way (22) becomes, to a good approximation

$$F_a = \frac{1}{24}\pi R_m^3 P_a' k_z^2 z \qquad (23)$$

where k_z is the z component of the sound field and z is the distance of the bubble from the pressure antinode. The force is directed toward the pressure antinode. It is remarkable that the great nonlinearity of the bubble motion leads to a radiation force that is linear in the external drive. This force must balance the force of buoyancy due to gravity which acts in the z direction
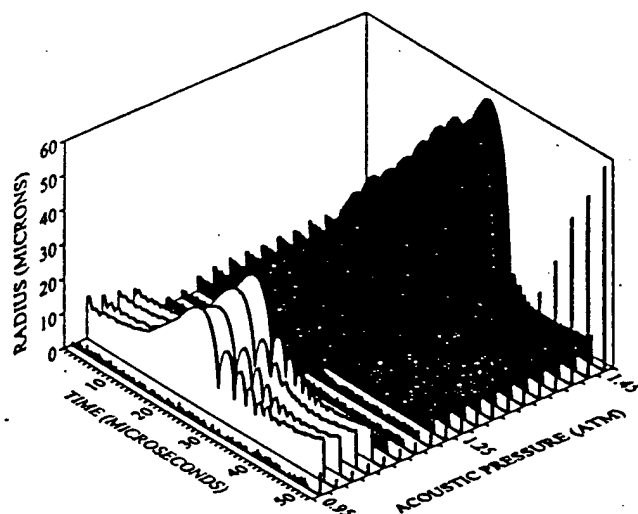
Fig. 18. Bubble radius verus time for about one cycle of the imposed sound field as a function of increasing drive level. The shaded area represents the light emitting region. The relative intensity of the emitted light as a function of drive level is indicated by the vertical lines. For the unshaded region, the air bubble is trapped, but no light is emitted. At drive levels below the unshaded region the bubble dissolves over a long time scale ($\sim$ 1 s). The lowest amplitude sweep (no bubble present) indicates the noise level.
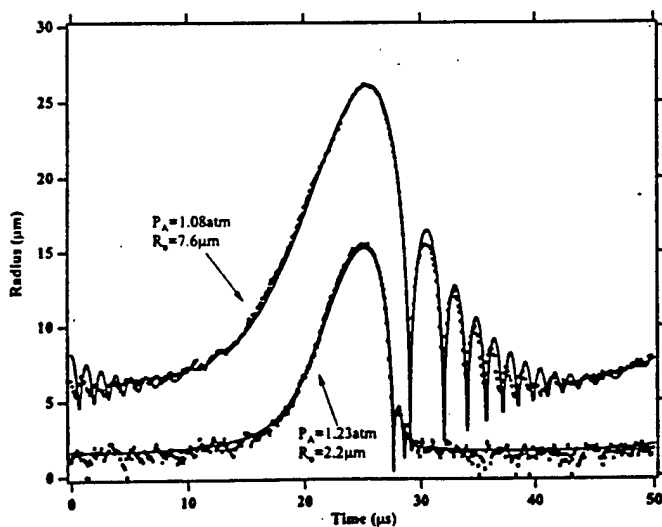
Fig. 19. Plot of radius versus time for bubble motion just above and below the threshold for the onset of sonoluminescence. Note that the expansion ratio R_m/R_0 increases from 3.5 to 9 as the system goes from a non-light-emitting bubble to an SL bubble.

$$F_b = \dot{\rho}g\langle V\rangle \approx \tfrac{1}{3}\pi R_m^3\rho g. \tag{24}$$

The distance of the bubble from the velocity node then is

$$\langle z\rangle \approx 8\rho g/P_a'k_z^2 \tag{25}$$

which is typically less than 1 mm. The motion around this average is reduced by an additional factor of $P_a'/2\pi\rho c^2$. If the sound field is turned off, the bubble radius drops to R_0 and the bubble floats up with the terminal velocity

$$v_F = \frac{2R_0^2 g}{9\eta/\rho} . \tag{26}$$

which for typical values is 5×10^{-3} cm/s.

In general the role of surface tension in SL bubble dynamics is small and for this reason it was neglected in the above discussions. However for sufficiently small bubbles, surface tension becomes a sizable correction to the ambient properties of the bubble (Löfstedt et al., 1995). For instance the frequency of ringing of a bubble becomes

$$\omega_0 = (3\gamma P_0/\rho R_{0\sigma}^2)^{1/2} \tag{27}$$

where the radius $R_{0\sigma}$ of the bubble when it is in mechanical equilibrium with the externally imposed pressure P_0 is determined by

$$P_g(R_{0\sigma}) = P_0 + \frac{2\sigma}{R_{0\sigma}} \tag{28}$$

so that to a very good approximation

$$\Delta R_\sigma = R_0 - R_{0\sigma} = 2\sigma/3P_0 \approx 0.35 \ \mu\text{m}. \tag{29}$$

In particular the expansion of the bubble, which commences when the net pressure acting on it is negative, can be delayed because the negative pressure of the acoustic drive must overcome both the ambient pressure and the extra pressure due to surface tension. The criterion for expansion becomes

$$|P_a(t)| > P_0 + \frac{2\sigma}{R(P_a \approx -P_0)} \tag{30}$$

where $R(P_a = -P_0)$ is the radius of the bubble when the net external pressure goes through zero (i.e. when $P_a \approx -P_0$). At negative net pressure stationary mechanical equilibrium is impossible and the bubble wall acquires a velocity. Substituting for R in (30) yields the magnitude of the rarefaction that must be exceeded so that the bubble rapidly expands

$$|P_a| > P_0 + \frac{2\sigma}{R_0}\left(\frac{2\sigma}{R_0 P_0}\right)^{1/2} . \tag{31}$$

For 2 μm bubbles this threshold is increased by 35%. The maximum velocity of bubble expansion (see Eq. (8)) is similarly reduced to:
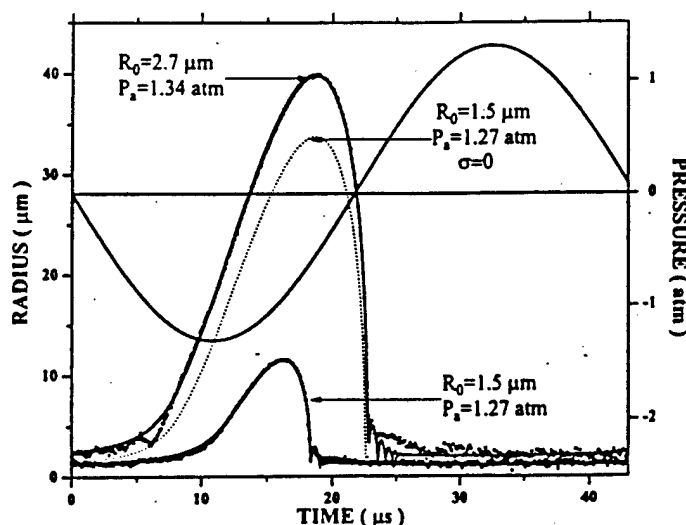
Fig. 20. Radius versus time for 1% xenon in nitrogen bubbles at 150 mm partial pressure of solution. Shown is the transition to SL from a small bubble whose dynamics are dominated by surface tension. The dashed line is a solution to the Rayleigh-Plesset equation with surface tension set equal to zero. It differs dramatically from the actual motion of the small ($R_0 = 1.5$ μm) bubble, which does, however, match the same equation when surface tension is included.

$$\dot{R} \approx \sqrt{\frac{2}{3} \frac{P'_a - P_0 - (2\sigma/R_0)(2\sigma/R_0 P_0)^{1/2}}{\rho}}. \tag{32}$$

This effect is displayed in Fig. 20 which shows the light scattering measurements of a bubble formed from a 1% xenon-doped nitrogen mixture in water at a partial pressure of 150 mm (Löfstedt et al., 1995). According to this data the surface tension for this small bubble ($R_0 = 1.5$ μm) reduces R_m from 35 μm to 10 μm. It should be clear that surface tension can suppress the onset of light emission in these bubbles because the critical expansion ratio is not reached. In addition surface tension is associated with hysteresis in the ramping up and down of the acoustic drive pressure (Löfstedt et al., 1995). For example the transition to SL for a 0.1% xenon in nitrogen bubble at 150 Torr is shown in Fig. 21. Note that SL is separated from the non-light-emitting regime by a region where there is no steady-state bubble motion. Within the non-SL region an upward sweep in drive amplitude marches from bubble to bubble regardless of the rate of increase of the acoustic pressure. However, an infinitesimal step to lower P'_a will cause the bubble to disappear. Nor can such a bubble be reseeded at the drive level at which it disappeared; to recover the stable small bubble, one must start with a lower-amplitude bubble and increase the drive level.

The Rayleigh-Plesset equation of bubble dynamics shows how the bubble takes energy from the sound field and then accelerates to a velocity comparable to the speed of sound. At that point more complete equations of state (or microscopic theories) and nonlinear dynamics must be employed. Furthermore, the ambient radius R_0 and the allowed range of acoustic drives P_a are not determined a priori by this equation.
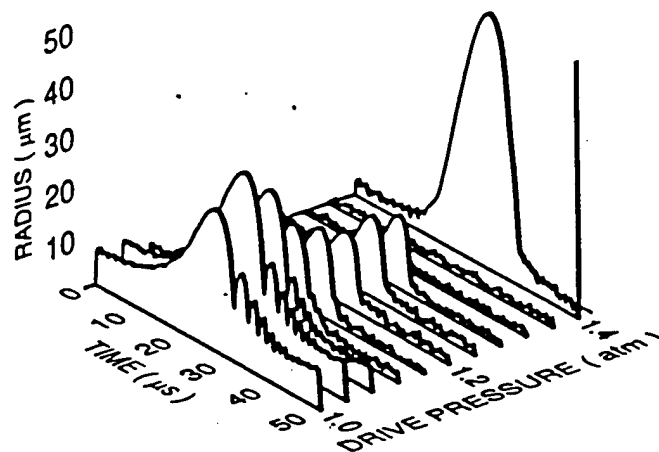
Fig. 21. Transition to SL for a 0.1% xenon in nitrogen bubble at 150 mm. These radius versus time curves were taken as a function of increasing drive level. With this system bubbles cannot be seeded between 1.1 and 1.35 atm. Those states must be approached from the lower amplitude, bouncing bubble regime.

5. Why is a small percentage of noble gas essential to stable, visible sonoluminescence?

To learn about SL we initially tried to expand the available parameter space by obtaining light from air bubbles in non-aqueous fluids such as alcohols and low-viscosity silicone oils (Weninger et al., 1995). The difficulties faced in this endeavor led us instead to search for light emission from water with gases other than air dissolved in it (Hiller et al., 1994; Hiller and Putterman, 1995). This led to the design of the sealed acoustic resonator and gas manifold system described in Figs. 4 and 5 (Hiller et al., 1994; Hiller, 1995).

The first experiments in this line of research used pure nitrogen gas, since it comprises 80% of air. To our surprise neither pure N_2 nor pure O_2 nor an 80 : 20 mixture of the two yielded a stable or visible signal. After convincing ourselves that there were no problems with the vacuum transfer system, we realized that air is 1% argon, and indeed, as shown in Fig. 22, a small amount of noble gas is essential for the activation of stable bright (i.e. visible to the eye) SL (Hiller et al., 1994). The effect of doping nitrogen with argon as a function of partial pressure is shown in Fig. 23.

It should be emphasized that when we speak of a gas mixture of a certain composition, we are referring to the mixture dissolved in the water. As of yet, we have not been able to determine the contents of the bubble. For instance, we cannot experimentally rule out the possibility that a 1% argon in nitrogen solution in water at 150 mm yields a bubble that is filled with pure argon. Of course such a scenario would violate the theoretical predictions of diffusion, the applicability of which will be discussed in the next section.

In Fig. 23 we see that at high and low partial pressures the SL intensity from a 1% argon in nitrogen mixture decreases (Hiller et al., 1994). As the saturation concentration of this mixture is approached, the light emission disappears; by contrast, pure argon bubbles yield SL at all partial pressures, although such bubbles are the most stable near 3 mm.
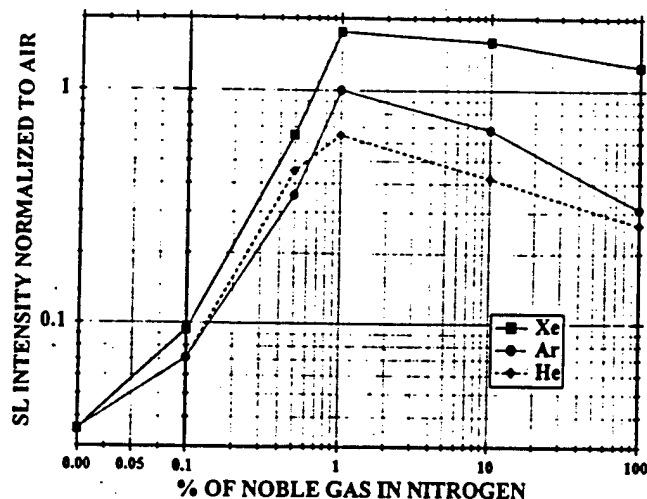
Fig. 22. Intensity of light emission from a sonoluminescing bubble in water as a function of the percentage (mole fraction) of noble gas mixed with nitrogen. The gas mixture was dissolved into water at a pressure head of 150 mm. The data are normalized to the light emission of an air bubble in 24°C purified water with a resistance greater than 5 MΩ cm dissolved at 150 mm. Such an air bubble emits about 2×10^5 photons per flash.
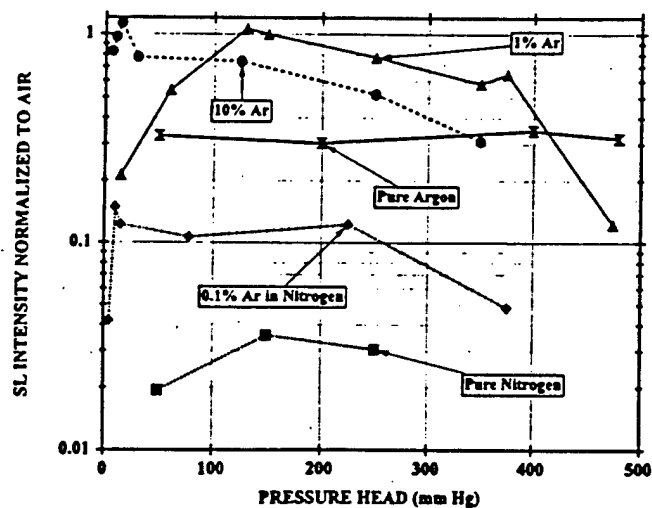
Fig. 23. Intensity of SL from an argon-doped nitrogen bubble as a function of the degree of saturation of the gas in the water. To observe SL from an air bubble requires some degree of degassing but a pure argon bubble can glow at concentrations approaching saturation. Since tap water is saturated with air it will not yield SL, but if tap water is pressurized to about 5 atm the concentration of air falls to 20% (which is comparable to a 150 mm solution at 1 atm) and SL can then be observed.
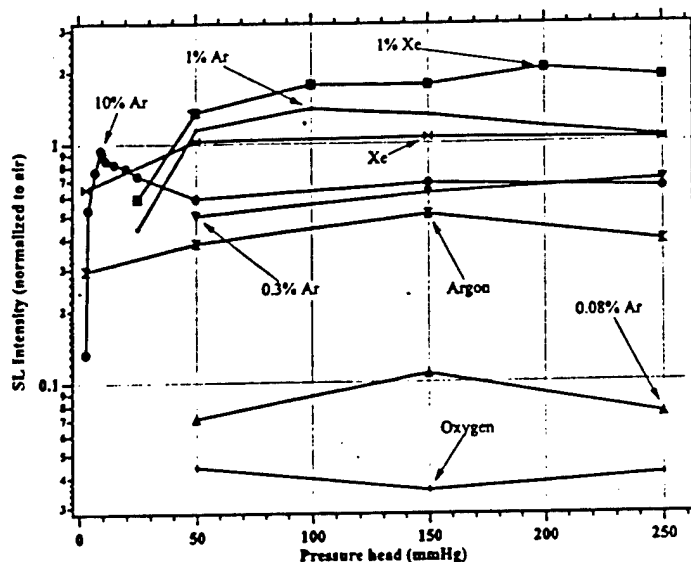
Fig. 24. Sonoluminescence from noble-gas doped-oxygen bubbles. The enhancement effect in oxygen is very similar to that which occurs in nitrogen.
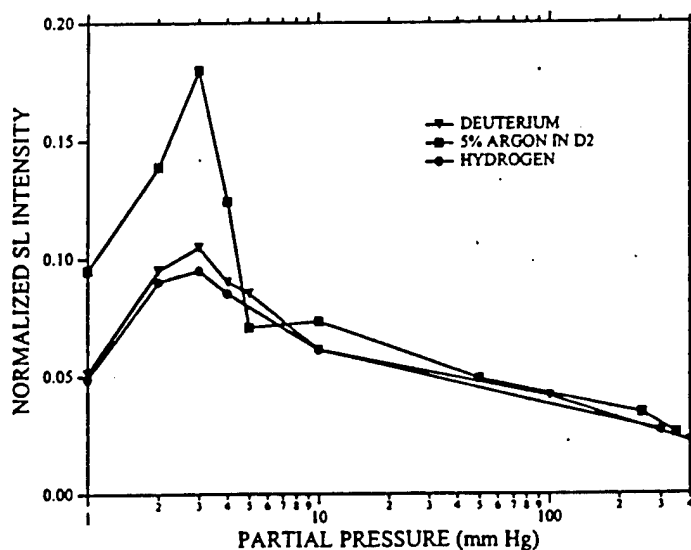
Fig. 25. Sonoluminescence from hydrogenic bubbles and argon-doped deuterium. Hydrogenic bubbles are very unstable, and they do not exhibit the enhancement effect displayed by oxygen and nitrogen.

As shown in Fig. 24 we have found that the noble gas doping effect also works for oxygen (Chow et al., 1996). This indicates that we are here dealing with the physics of atoms and plasmas as opposed to, say, effects of chemical reactions (Griffing, 1952; Suslick and Flint, 1987; Verrall and Sehgal, 1987; Lohse et al., 1996), or the properties of gas scintillators (Birks, 1964; Tornow, 1996). With regard to gas discharge physics an analogy can perhaps be found in the Penning effect (Penning and Addink, 1934) where various gas mixtures can dramatically alter discharge characteristics. However, with SL the gas compressions approach solid densities, and the system is far from the parameter space where the Penning effect is usually studied.

The enhancement effect observed with N_2 and O_2 is not observed with H_2 or D_2 as shown in Fig. 25 (Barber et al., 1995). These bubbles are very dim and unstable. It may turn out that as higher degrees of water and gas purity are achieved, and in particular any air leaks from the gas manifold system are removed, the bubbles of hydrogen and deuterium will be even dimmer than shown in Fig. 25. An outstanding question remains how to enhance SL from hydrogenic gases. There is of course a large parameter space to probe, including the ambient temperature, the ambient pressure, the partial pressure, and the possibility of adding surfactants to the water. As of yet, the brightest and most stable room-temperature bubble appears to be a 1% mixture of xenon in oxygen at a partial pressure of 150 Torr.

6. What determines the ambient radius?

For given experimentally controllable parameters, such as the drive pressure, the ambient temperature, the gas and fluid composition, Nature determines the ambient radius (Löfstedt et al., 1995). It is not in the experimentalist's power to scale up the size of the SL bubble. In fact, it is not yet theoretically possible to predict the size of the SL bubble, or the range of drive pressures for which SL exists. Since the transition to SL is accompanied by a change in the ambient radius, it is clearly an important object of study.

Simple diffusion theory does predict a stable, stationary value for the ambient radius (Eller and Flynn, 1965; Fyrillas and Szeri, 1994; Löfstedt et al., 1995). This value is determined by requiring a balance between the gas flow into and out of the bubble during its oscillatory cycle. A gas-fluid interface achieves thermodynamic equilibrium when a certain partial pressure of gas is dissolved in the fluid; this partial pressure, at least in the dilute gas limit, is proportional to the pressure of the gas above the fluid. Consider now the oscillation of the SL bubble. When the bubble expands, the pressure of the gas inside it goes down, and gas will flow out of the surrounding fluid into the bubble. When the bubble size is smaller than a certain radius, the gas pressure is higher than would be in equilibrium with the surrounding fluid, and gas will flow out of the bubble interior into the surrounding fluid. A steady-state size of the bubble is achieved if these flows of mass are balanced. Thus, diffusion theory predicts a distinct ambient radius for a fixed acoustic drive amplitude and fixed concentration of gas dissolved in the fluid.

Mathematically, this picture is expressed by the diffusion of equation of gas in the fluid (Landau and Lifshitz, 1987),

$$\frac{\partial C}{\partial t} + \frac{\dot{R}R^2}{r^2}\frac{\partial C}{\partial r} = D\nabla^2 C \tag{33}$$

where $C(r, t)$ is the concentration of gas in the fluid, D is the diffusion constant for gas in the fluid ($\sim 2 \times 10^{-5}$ cm^2/s for air in water), and the convective term takes into account the pulsations of the bubble. This equation is subject to the boundary condition at the bubble wall

$$C(r = R) = C_0 P_g(R)/P_0 \qquad (34)$$

where $C(r, t)$ is the saturated concentration of gas dissolved in the fluid at 1 atm (for air in water $C_0/\rho_0 \approx 0.02$ where $\rho_0 \approx 1.3 \times 10^{-3}$ g/cm^3 (Battino et al., 1984)). This boundary condition expresses Henry's law for the fluid-gas interface (Fermi, 1936). The concentration of gas in the fluid at infinity, $C(r = \infty) = C_\infty$, is determined by the preparation of the fluid, $C_\infty/C_0 = P_\infty/P_0$ where P_∞ is the partial pressure of the gas in solution as is established by the methods discussed in Section 2.

A solution of (33) for steady-state motion determines the ambient radius which would be in equilibrium with a given partial pressure of gas dissolved in the fluid (Fyrillas and Szeri, 1994; Löfstedt et al., 1995)

$$C_\infty = \frac{1}{T_a} \int_0^{T_a} \frac{C_0 P_g(R)}{P_0} d\tau' \qquad (35)$$

where T_a is the acoustic period and

$$\tau(t) \equiv \int^t R^4(t') \, dt'. \qquad (36)$$

This result applies in the limit where the diffusive penetration depth is small compared to the maximum radius or $\delta_D = \sqrt{2D/\omega_a} \ll R_m$.

Since the integral in (35) is dominated by the maximum size of the bubble, C_∞ is determined by that part of the motion when the bubble is isothermal (Löfstedt et al., 1993). Using the isothermal equation of state one finds that the bubble which is in diffusive equilibrium with the surrounding fluid obeys (Löfstedt et al., 1995)

$$\frac{C_\infty}{C_0} \approx 3 \left(\frac{R_0}{R_m}\right)^3. \qquad (37)$$

A comparison of this formula (or more precisely Eqs. (35), (36)) with the ambient size of low drive "bouncing" bubbles shows that diffusion determines the size of these bubbles as in Fig. 26.

However, if we return to the waterfall plot of the transition to SL, it is clear that both the bouncing bubble and the SL bubble cannot be in diffusive equilibrium at the same partial pressure. Yet this is precisely what is found for air bubbles in water. In Fig. 27 is plotted the phase of the SL light emission relative to the driving sound field (Barber et al., 1995). The 150 Torr air bubble in water shows no jitter on such a plot, indicating that it is stably maintained at that partial pressure. For this bubble the transition to SL is accompanied by the appearance of an as yet undetermined mass flow process that enables the system to violate Eq. (37) by a factor of about 50.

Given the expansion ratio of about 10 : 1 which is characteristic of SL, one finds from Eq. (37) that SL bubbles should be in diffusive equilibrium at around 3 Torr. This turns out to be the partial pressure where pure noble gas bubbles are stable, as is also indicated in Fig. 27 (Barber et al., 1995).
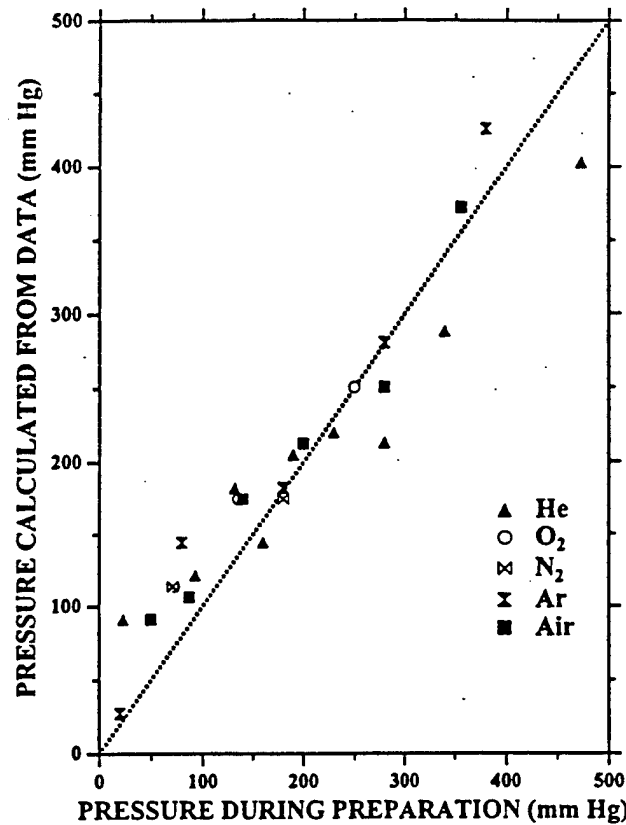
Fig. 26. Static versus diffusive equilibrium partial pressures. The abscissa shows the pressure at which gas has been stirred into the water, and the ordinate shows the pressure calculated from the application of the diffusion equation to the measured low amplitude, steady state bubble motion.

At this partial pressure there is no bouncing bubble, in agreement with the predictions of diffusion. All trapped noble gas bubbles are light emitting at 3 mm! At higher partial pressures noble gas bubbles can be driven to high enough amplitude to make light, but the bubble motion is unstable (see Figs. 27 and 28). We interpret the phase jitter of the pure noble gas bubbles at higher partial pressures as obeying the diffusion equation. At these higher partial pressures, the bubbles grow in size with every cycle of the drive in accordance with the diffusion equation, until they somehow become unstable and split off microbubbles (Barber et al., 1995), suddenly shrinking in size, as evidenced by the rapid glitches of Fig. 27. (This process has been called "recycling" by Holt and Gaitan (1996).) These phase glitches also show up as fluctuations in the light intensity of these noble gas bubbles, as shown in Fig. 28. The timescales of the growth of the bubble is however still in accord with the diffusion equation which can be used to calculate the amount of mass to flow into a bubble during one cycle of the drive (Löfstedt et al., 1995):
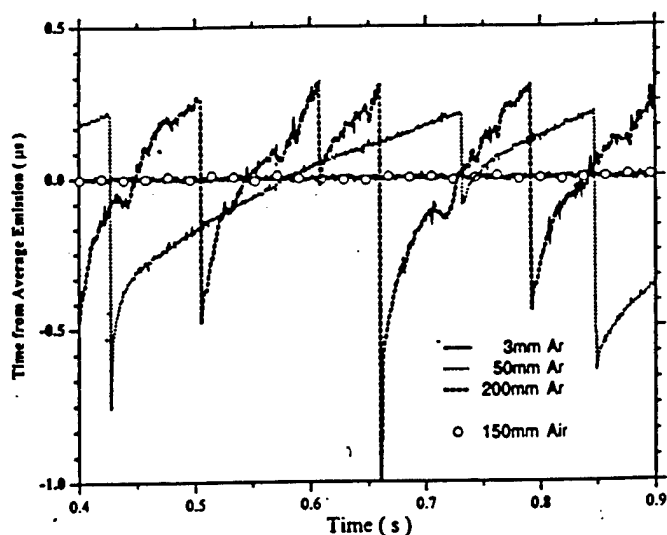
Fig. 27. Phase of light emission from an argon bubble. Shown is the time during the acoustic cycle at which light is emitted for 200, 50, and 3 mm argon bubbles. A data point was collected every tenth acoustic cycle. An air bubble at 150 mm is also shown for reference. Note that an air bubble is stable at partial pressures where diffusion is disobeyed, but argon bubbles are most stable where diffusion is obeyed.
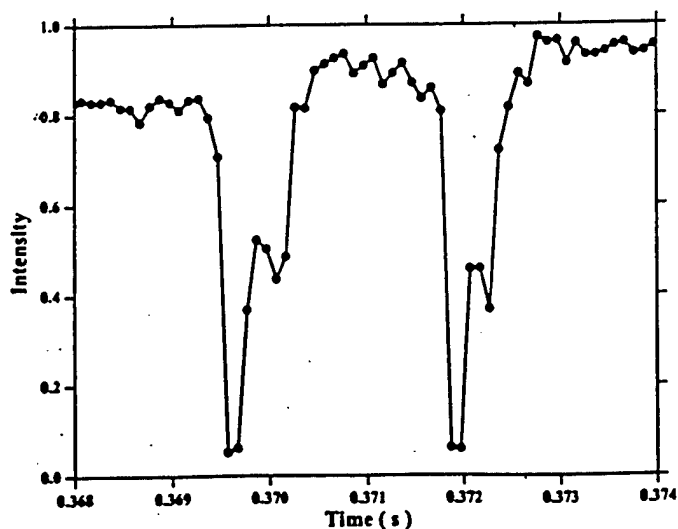
Fig. 28. Intensity of light emission from an argon bubble as a function of time at a partial pressure of 150 mm. Each cycle of the motion is captured. Large changes in the light intensity occur on the time scale of a single acoustic cycle.

$$\frac{\Delta M}{M} \approx \frac{3}{2} \left(\frac{T_a D}{R_0^2}\right) \frac{C_\infty - C_\infty(D)}{C_0} \frac{C_0}{\rho_0} \frac{R_m}{R_0} \approx 10^{-4} \tag{38}$$

where ρ_0 is the ambient density of the gas and $C_\infty(D)$ is the calculated equilibrium concentration from Eq. (34). To obtain this result one must supplement Eq. (33) with the rate of mass flow across the wall of the bubble due to diffusion,

$$\left(\frac{dM}{dt}\right)_D = 4\pi R^2 D \left(\frac{\partial C}{\partial r}\right)_{r=R}. \tag{39}$$

The time scales calculated from (38) are in qualitative agreement with the glitching rate displayed in Fig. 27.

Any theory of the ambient radius has to reconcile the stability of a sonoluminescing air bubble at 150 Torr and the stability of pure noble gas bubbles at 3 Torr, which is consistent with mass diffusion. Our logical, but unproven, deduction is that there is some unknown non-diffusive mass flow mechanism controlling the size of the sonoluminescing air bubble in water. The mass discrepancy might be accounted for by gas discharged along with the outgoing shock as the bubble reaches its most stressed point in time (Löfstedt et al., 1995), or, following quite the opposite reasoning, the hydrodynamic pulsations of the bubble might set up a macroscopic mass convection cell that breaks the spherical symmetry (Gould, 1973; Asaki et al., 1993). In any case the discharge must compensate for the diffusional influx given by (38).

Ethane bubbles were also found to give light at low partial pressures where the 10 : 1 expansion ratio is in diffusive equilibrium with the surrounding fluid. However, as the partial pressure is reduced below these levels, the ethane bubbles can sustain a 17 : 1 expansion ratio and again violate mass diffusion arguments (Barber et al., 1995). These radius–time curves are displayed in Fig. 29. The waterfall plot for ethane at 2 mm is shown in Fig. 30. All of these bubbles are light-emitting.

A consideration of waterfall plots (Löfstedt et al., 1995) of gas bubbles of various compositions reveals that the transition to light emission can occur after the (non-diffusive) decrease in size of a bouncing bubble as shown in Fig. 31. This graph is a detail of the waterfall plot of Fig. 32 which shows the transition to SL in a 5% argon in nitrogen mixture dissolved at 150 mm. The same situation can be seen for a 1% xenon in nitrogen bubble as shown in Figs. 33 and 34.

The diffusion equation enables us to calculate the time it would take a quiescent gas bubble in a fluid to dissolve away. This timescale (Epstein and Plesset, 1950)

$$t_D \approx \frac{1}{2} \frac{\rho_0 R_0^2}{D(C_0 - C_\infty)} \tag{40}$$

is about 1/3 s for a 5 μm air bubble in undersaturated water. One can compare this timescale with the "turn-on" times for sonoluminescing bubbles shown in Fig. 35 (Löfstedt et al., 1995). This is the time it takes the seeded bubble to start to glow. Pure noble gas bubbles start to glow immediately, even before they have reached the pressure antinode of the resonator. Noble-gas doped nitrogen bubbles turn on gradually (with time scales comparable to Eq. (40)) to reach their final steady intensity. An argon-doped nitrogen bubble driven near its upper threshold also shows modulations on the time scale of Eq. (40) as shown in Fig. 36. The time scale for a sonoluminescing air bubble to respond to an increased drive level is also measured in seconds as shown in Fig. 37, but the turnoff which acompanies a large boost in drive can occur over a hundred times faster than this time. When the
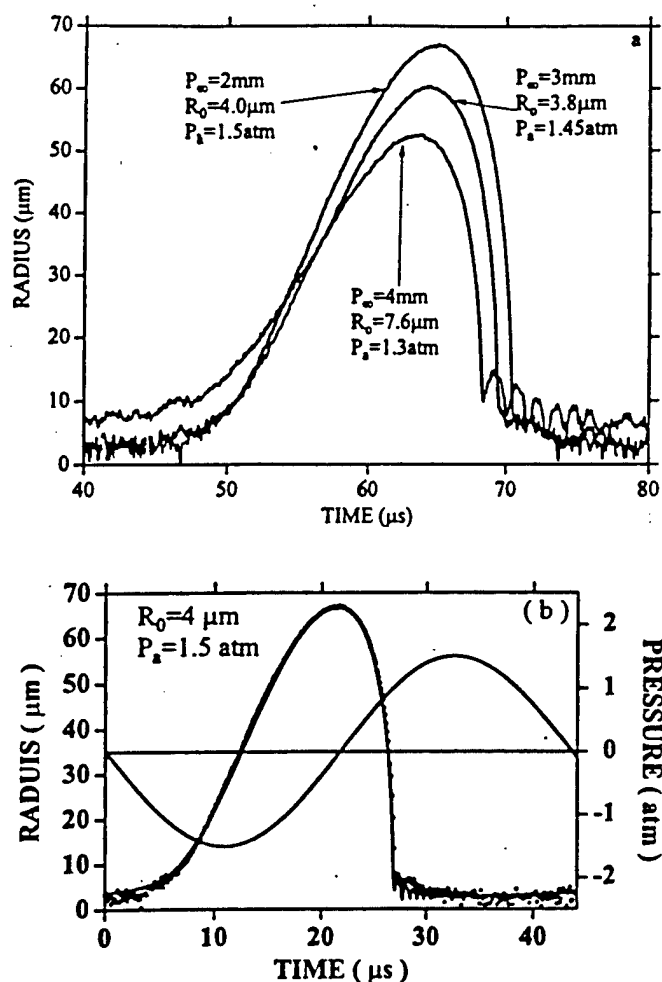
Fig. 29. Radius versus time curves for an ethane bubble at various partial pressures. In (a) are shown 2, 3, and 4 mm bubbles aligned with their proper phases relative to the sound field. The parameters for the 4 mm bubble obey diffusion whereas the 17 : 1 expansion ratio of the 2 mm (see (b), (c)) bubble is inconsistent with the steady state diffusion equation. In (b) the driving sound field is also displayed. The intensity of SL from these bubbles is so weak that its use as a trigger for the acquisition of traces yields spurious signals. To minimize this false triggering and allow for averaging of data a joint gate set by the SL flash and a 100–500 ns window, determined by the phase of the sound field at which SL should occur, was employed.

sound field is switched off the bubble returns to its ambient radius with the decay time of the sound field (5–10 ms) and then dissolves into the surrounding fluid as shown in Fig. 37C. Note that the bouncing bubble decays in about 1/3 of a second whereas the SL bubble decays in about 1/10 s. The difference in these times is consistent with the R_0^2 dependence in (40) but the absolute rates are
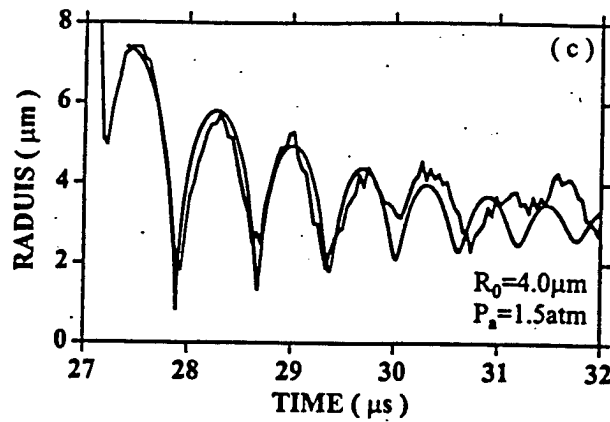
Fig. 29. Continued
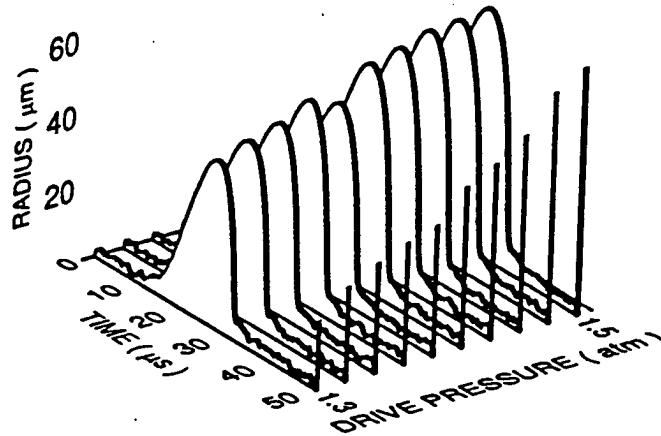
Fig. 30. Waterfall plot for a 2 Torr ethane bubble. The height of the vertical bars is proportional to the intensity of the emitted light. Note that all trapped bubbles emit light.

about twice as fast as the simplest diffusion approximation.

When the effects of surface tension are included, Eq. (37) is still the correct estimation of the consequences of the diffusion equation, however, R_0 is no longer the radius of the bubble when it is in equilibrium with the ambient pressure. The equilibrium radius is now $R_{0\sigma}$ as determined by Eq. (28). In terms of this quantity the scaling law (37) can be written in the equivalent form

$$\frac{C_\infty}{C_0} = 3 \left(1 + \frac{2\sigma}{R_{0\sigma}P_0}\right) \frac{R_{0\sigma}^3}{R_m^3}.$$

(41)

A detailed comparison of the diffusion equation to the behavior of a 5% argon in nitrogen bubble at 150 Torr is shown in Fig. 38A. At low drive levels the measured and calculated ambient radii are in fairly good agreement. But as the drive level is increased the measured radius displays a
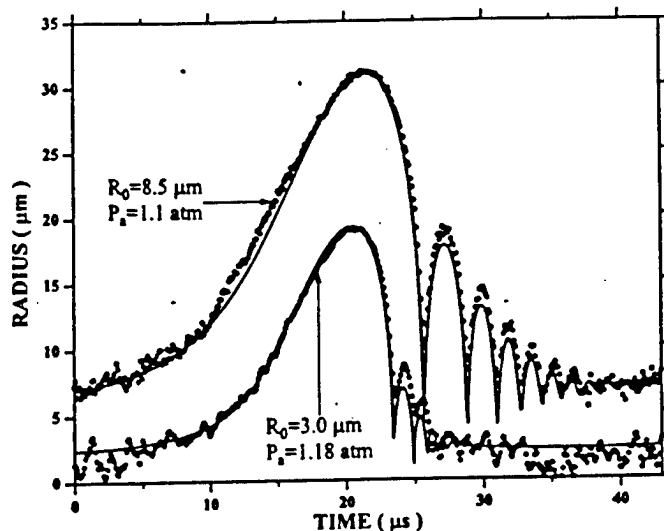
Fig. 31. Radius versus time for an argon-doped nitrogen bubble. As the drive is increased the larger bubble abruptly shrinks, and the expansion ratio increases. This bifurcation due to a non-diffusive mass flow mechanism occurs here below the transition to SL. The bubble has 5% argon in nitrogen and the gas is dissolved into the water at 150 mm.
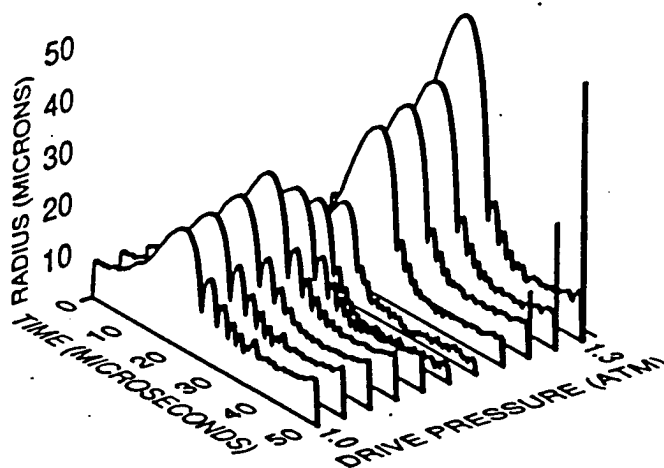
Fig. 32. Transition to SL for a 5% argon in nitrogen bubble. The vertical bars indicate the relative intensity of SL.

marked deviation from the requirements of diffusion. There is a drop and subsequent increase in R_0. The thick solid line indicates those bubbles which yield light. It is important to appreciate that the deviation from diffusive equilibrium already occurs for non-light-emitting bubbles. The maximum temperature reached when these bubbles collapse is about 1000 K. At such relatively low temperatures only a handful of nitrogen molecules are dissociated so that (at least for the bouncing bubble) an
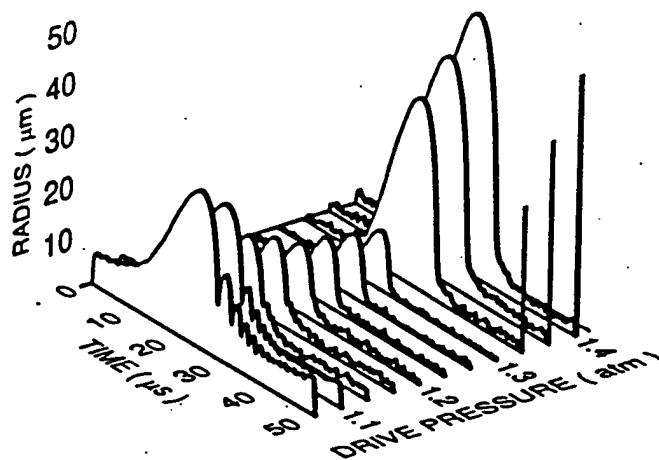
Fig. 33. Waterfall plot showing the transition to SL for a 1% xenon-doped nitrogen bubble The relative intensity of SL is indicated by the vertical lines. The transition to SL occurs only after the force of surface tension on the small bubbles is overcome by the driving sound field. The partial pressure of solution is 150 mm.
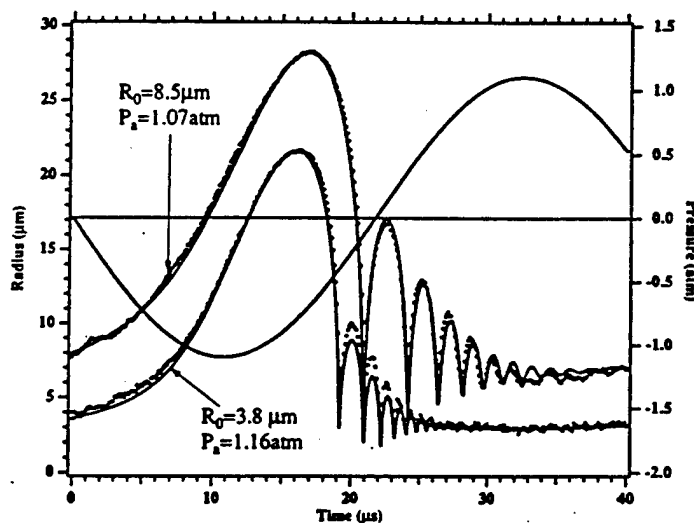
Fig. 34. Effect of anomalous mass flow on the radius of a 1% xenon in nitrogen bubble as the drive level is increased.

understanding of the non-diffusive mechanism lies outside chemistry (compare with Lohse et al. (1996)). We suggest that the additional mass flux originates with the outgoing acoustic spike (Figs. 1, 17) launced by the collapsed bubble. This spike is observed for both the SL and bouncing bubbles.

The curves which yield the equilibrium ambient radii for given sound field and concentration of gas in the water are calculated from the diffusion equation by substituting a solution to the RP equation
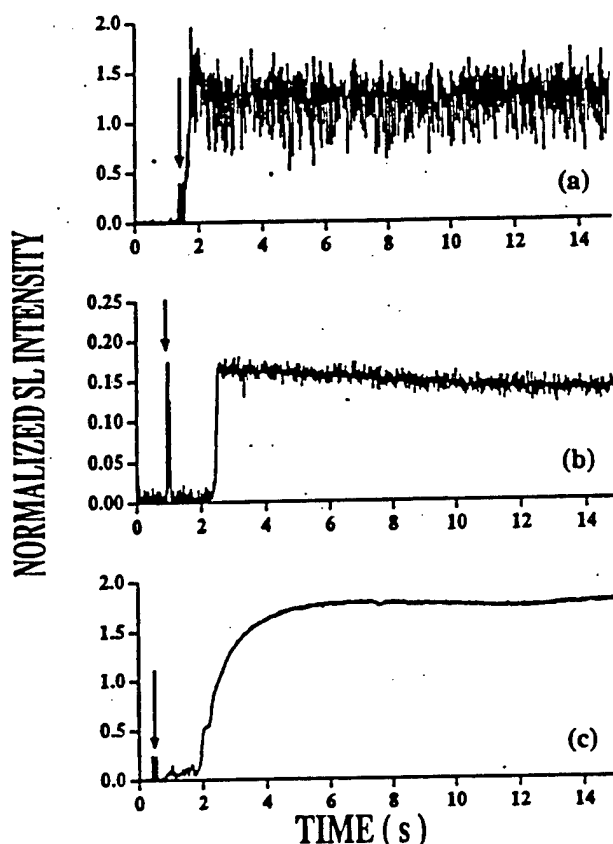
Fig. 35. Turn-on times for SL. Shown is the light intensity (normalized to an air bubble in water) as a function of time after seeding a bubble into an acoustically driven resonator. In (a) a pure xenon bubble at high drive levels lights up almost instantaneously. In fact, these bubbles are glowing as they leave the NiCr wire on their way to the velocity node of the sound field. (b) and (c) show the response of a xenon-doped nitrogen bubble. An arrow indicates a flash of light from an LED that is activiated by the current through the nichrome wire. This is the moment at which the bubble is seeded. Note the plethora of time scales that characterize the bubble driven at a high amplitude (c).

into Eq. (35) (Church, 1988, Crum and Cordry, 1994; Brenner et al., 1996). These curves are shown in Fig. 39 for drive pressures between 0.9 and 1.2 atm. For given C_∞/C_0 one picks off an equilibrium R_0. Since multiple solutions are possible, the issue of stability becomes important. It turns out in fact that the calculated equilibrium points plotted in Fig. 38, even at low amplitude where experiment and diffusion agree, are unstable according to diffusion. When the slope in Fig. 39 is negative, a fluctuation that increases the bubble radius brings it to a higher expansion ratio and thus further away from equilibrium with the surrounding gas fluid mixture, so that more gas will flow in causing the bubble to grow even larger. So for these bubbles the non-diffusive mechanism not only determines the size but also the stability even at low drive levels. For comparison, in Fig. 38B also are plotted the first stable solutions to the diffusion equation together with experimental values.
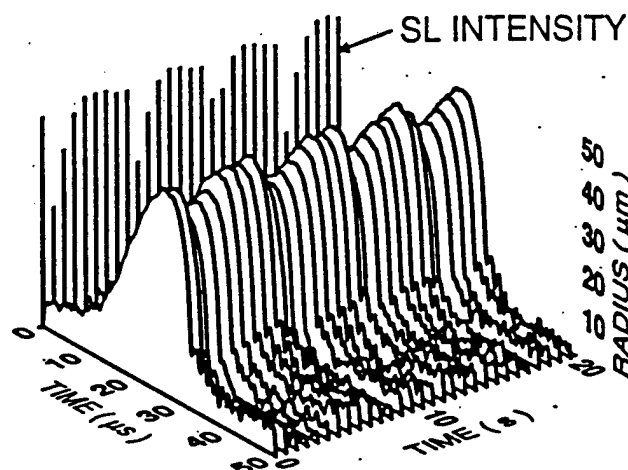
Fig. 36. SL intensity and bubble radius as a function of time for a nitrogen bubble with 5% argon at 150 mm. At a drive level just below the upper threshold of SL this bubble shows a variation on a long time scale of the order of 4 s. The acoustic frequency is 23 kHz.

For bubble radii under about 8 μm the cause of this instability is the surface tension as shown in Fig. 40 which compares bubbles with and without surface tension. For bouncing bubbles there remains the issue of whether multiple equilibria can be observed and why diffusively unstable bubbles are observed at low drive levels. An experiment aimed at observing multiple equilibria will have to be run in very pure water because as seen from the dashed line in Fig. 39 a realistic choice of damping washes out many of the wiggles. Also note that use of the isothermal equation of state for the slower parts of the cycle (as was used here) reduces the chances for multiple equilibria (This should be compared to Brenner et al. (1996) who used the adiabatic equation of state for the whole cycle.) Regarding the instability, it is important to realize that the corresponding growth rate is very slow. The time constant for exponential growth is

$$\left[\frac{D}{2R_0} \frac{d(C_\infty/C_0)}{dR_0} \left(3\frac{C_\infty}{C_0} \right)^{1/3} \frac{C_0}{\rho_0} \right]^{-1} \tag{42}$$

which for a 7 μm bubble at 1 atm is about 1/2 min. Finally, as we have emphasized, the onset of the non-diffusive mass flow mechanism will affect these comparisons.

According to the graphs in Fig. 41A multiple equilibria are also possible in the SL regime. Here there are two categories of such equilibria. We see that at $C_\infty/C_0 = 0.004$ there are two intersections with the response at 1.3 atm, with bubbles with ambient radii of 2.1 and 4.6 μm. The smaller bubble is strongly dominated by surface tension and is diffusionally unstable with a short time constant. The larger bubble is in fact the one observed in experiments. The other category is a true stable multiple equilibrium as can be seen where this partial pressure intersects the 1.4 atm drive level response at $R_0 = 7.0$ and 7.2 μm. These multiple equilibria again wash out at higher levels of damping, leaving one stable equilibrium state in the parameter range of interest. Furthermore, as shown in Fig. 41B the radius-time curves for these bubbles are not typical of SL. The afterbouncing rings through until
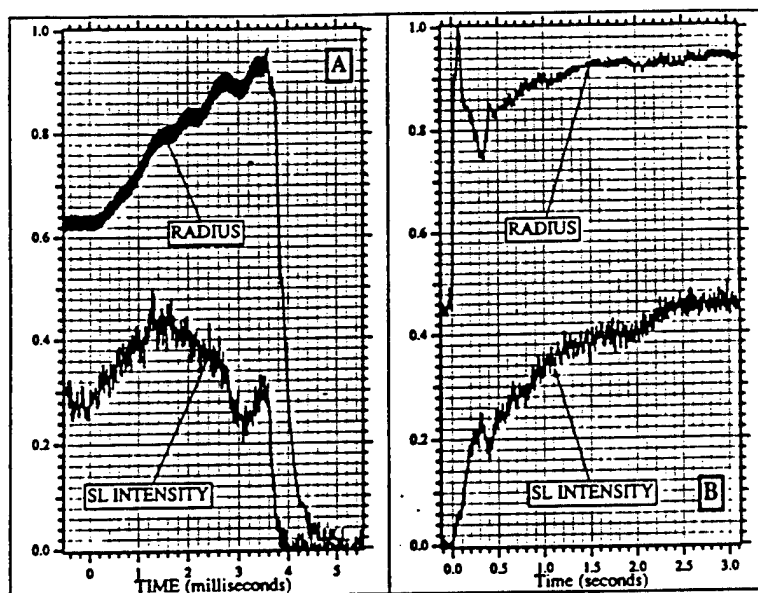
Fig. 37. Dynamic response of the intensity of sonoluminescence and of the bubble radius to a sudden change in the drive level. In (A) the drive is boosted above the upper threshold and after becoming brighter for a short time, the bubble disappears. In (B) the drive is boosted from weak to strong SL. After "gagging" (which can also be seen in (A)) the bubble achieves a new steady state during a long time scale measured in seconds. The signal has been averaged with a time constant of 100 μs for (A) and 10 ms for (B). Strictly speaking the results labeled "radius" are proportional to the product of R_m and the duration of the expansion. In (C) and (D) is plotted the square of the ambient radius as a function of time after the sound field is turned off. After an acoustic time of about 5-10 ms the bubble drops to its ambient radius and then dissolves. The bouncing bubble (D) (7 μm) dissolves in about 1/3 s and the SL bubble (C) (4 μm) dissolves in about 1/10 s. The 50% deviation of these times from Eq. (40) might be accounted for by surface tension and increased resolution.

the next acoustic cycle. It is in fact the variation in the afterbounce resonances that accounts for the calculated multiple equilibria. As a rule the SL bubbles are sitting dead in the water as the next cycle begins. (The transition to SL for the systems studied to date is therefore not explained in terms of multiple diffusive equilibria, in constrast to the conclusions of Crum and Cordry (1994) and Brenner et al. (1996).)

Consider again the noble gas bubbles which are experimentally stable at 3 mm where diffusion theory also allows for an equilibrium bubble with an expansion ratio large enough for SL. A waterfall plot of such a bubble of argon is shown in Fig. 42. The experimental data for R_0 and P_a for this argon bubble are compared to the 150 mm, 5% argon in nitrogen bubble in Fig. 43. In the region of SL the data for these two systems are remarkably similar and in good experimental agreement with the parameters calculated from diffusion theory for a pure argon bubble. This again suggests that some rectification process that concentrates one of the gases in the bubble may exist (Löfstedt et al., 1995); however, the requirements of diffusion theory apply to each gas separately, and the general issue remains.

In conclusion, the stability and size of light emitting air bubbles (and higher amplitude bouncing
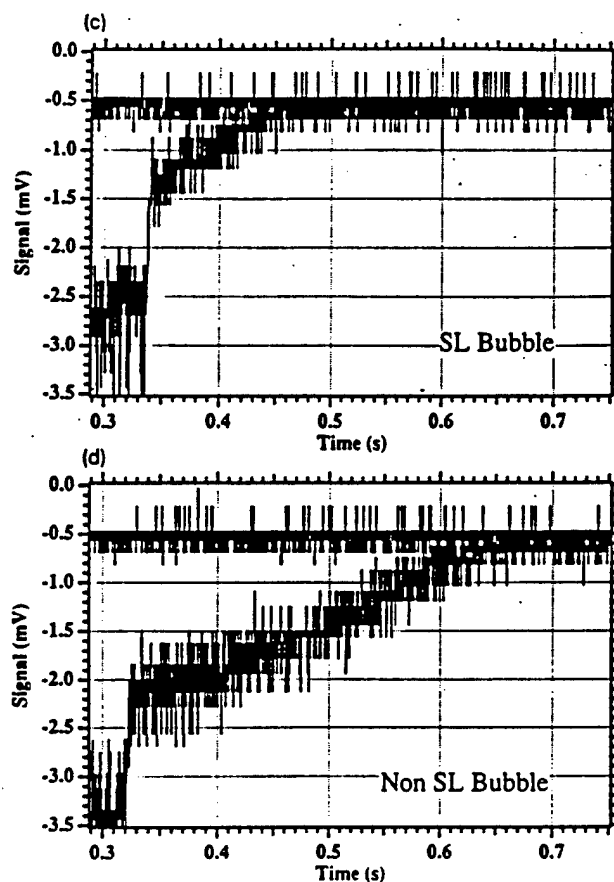
Fig. 37. Continued

bubbles) requires that a non-diffusive mass flow mechanism operates during each cycle of the sound field. The stability of light emitting noble gas bubbles at 3 mm is consistent with diffusion. At higher partial pressures the motion is also consistent with diffusion from cycle to cycle but after many cycles a "catastrophic" non-diffusive event occurs, such as a piece of the bubble splitting off. Although the diffusion equation permits multiple stability, experiments in water have not observed this effect. Whether other regions of parameter space will suppress the nondiffusive effects so as to make these states physically accessible remains to be seen.

7. Why is water the friendliest fluid for sonoluminescence?

One's ability to observe SL in a non-aqueous fluid is greatly enhanced by the use of xenon as the dissolved gas (Weninger et al., 1995). Pure helium and pure argon bubbles do not give light in
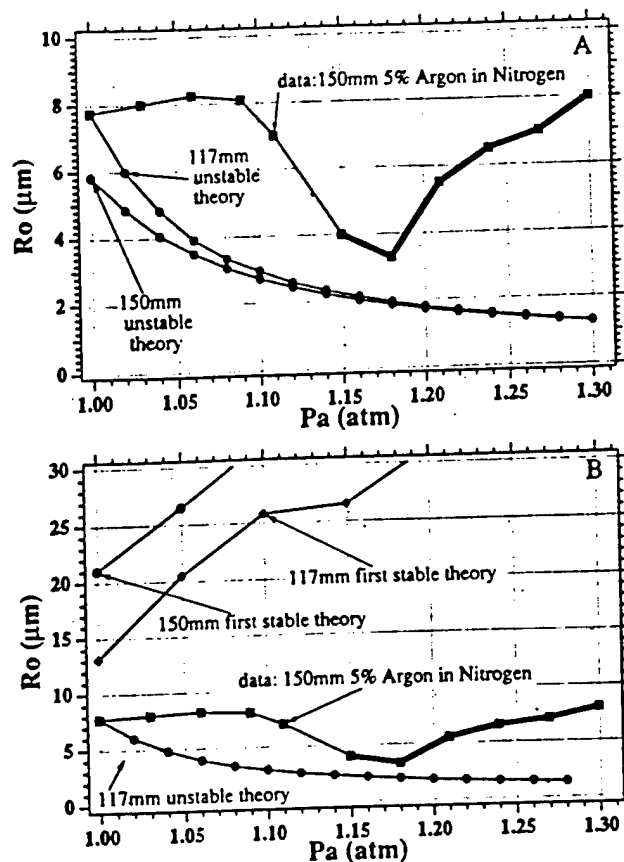
Fig. 38. Measured and calculated values of the ambient radius at which a 5% argon in nitrogen bubble at 150 mm would be in diffusive equilibrium, as a function of increasing drive level. In (A) is plotted the first (unstable) theoretical equilibrium point for 117 mm and 150 mm. The bubbles which make light are indicated with the thick solid line. In (B) is plotted the first theoretically stable equilibrium point. The deviation from the diffusion equation for this "air type" bubble is dramatic. At low drive levels, where bubbles do not make light, the deviation is much less and tends to zero. Similar measurements of the phase diagram of SL for air bubbles in nearly saturated water have been made by Holt and Gaitan (1996).

these fluids. Even in the xenon gas arrangement, the light emission is not nearly as stable as, say, air bubbles in water. In the non-aqueous fluids which we have studied (Fig. 44) the bubbles tend to jitter spatially a few mm around the pressure antinode which traps them. The phase of the light emission with respect to a trigger from the synthesizer that generates the sound field is typically spread over a few hundred nanoseconds, about a hundred times the phase wander for air bubbles in water. Yet another difference between the SL bubbles in non-aqueous fluids and air bubbles in water is that the maximum drive at which bubbles in non-aqueous fluids emit light is not well defined. Sometimes these bubbles simply stop emitting light after a short time (without being destroyed) and in other cases increasing drive amplitudes cause the bubbles to change their location in the resonant sound
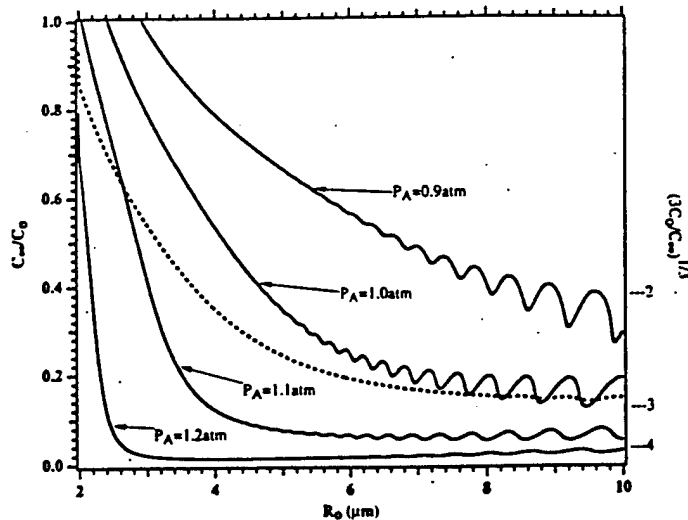
Fig. 39. Equilibrium concentrations as a function of ambient radius for various drive levels ranging from 0.9 to 1.2 atm. For the solid lines the viscosity is 1 centistokes and the surface tension is 70 dyne/cm. The dashed line has been calculated with a viscosity of 4 cSt and a surface tension of 50 dyne/cm. The wiggles indicate the presence of multiple equilibria, and the negative slopes are unstable if diffusion were the dominant process. These graphs have been calculated for $\gamma = 1.4$; the isothermal equation of state has been used for radii larger than the ambient radius and the adiabatic equation of state otherwise. On the right axis is plotted $(3C_0/C_\infty)^{1/3}$ which according to the scaling law Eq. (37) is the theoretically predicted value of R_m/R_0. This figure was calculated for an acoustic frequency of 26 kHz.

field while maintaining the same level of light emission. This tendency to wander away from the pressure antinode at increased drive is also achieved in non-light-emitting helium bubbles in silicone oil (Löfstedt et al., 1995), xenon bubbles in water at temperatures close to 0°C, and air bubbles in water at static pressures less than one atm (Barber, 1994). Fig. 45 shows measurements of the light emission from xenon bubbles in 1-butanol for various partial pressures and temperatures; note the breaks in the curve such as at −5°C for 250 mm partial pressure. Fig. 46 shows the light emission curves for xenon in ethanol.

These experiments display another general but as yet unexplained feature of SL, viz. that it produces more light at low temperatures (Barber et al., 1994). This was first observed for air in water as shown in Fig. 47, where cooling the water from 40°C to −6°C results in an increase in the light emission of over a factor of 100 (the increased emission is correlated with an increase in the maximum value of sound level that can be imposed on the SL bubble without destroying it). It seems to be fortunate happenstance for the discovery of SL that room temperature is not 20°C hotter. In fact, it seems that a static (ambient) pressure of one atmosphere also provides the most stable SL (as shown for an ethane bubble in Fig. 48). Our goal in decreasing the ambient pressure, P_0, was to increase the energy amplification characteristic of SL (Barber et al., 1991). The drive level required for SL, P'_a, scales to the ambient pressure, and the acoustic energy density is proportional to the square of the drive level. At 1/4 atm of static pressure, the observation of SL would involve an energy focusing an order of magnitude greater than estimated in Section 1. The lowest ambient pressure at which SL
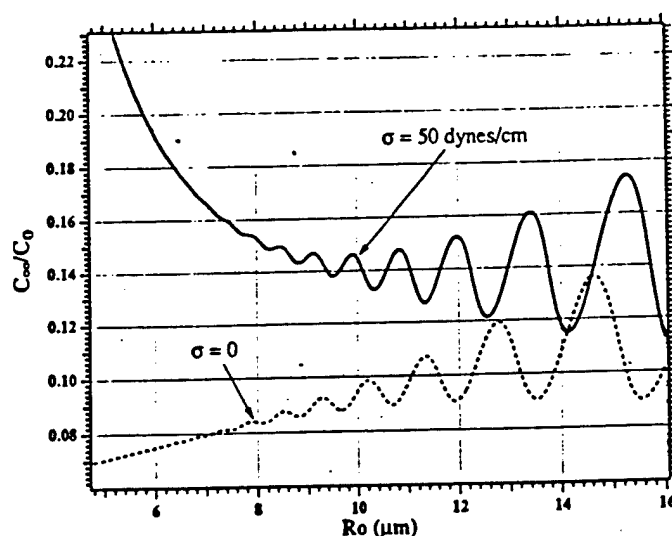
Fig. 40. Equilibrium concentrations for given radii showing the effect of surface tension. These curves are calculated from RP and the diffusion equation. The dashed line is for zero surface tension. The drive level is 1 atm and the viscosity is 4 cSt.

has been successfully observed is 1/3 atm (Barber, 1994). At these reduced pressures the bubble becomes not just dim but also poorly behaved. This observation suggests that SL from diatomics or non-aqueous fluids might be stabilized by increasing the static pressure. The experiment remains to be done.

Fig. 49 shows the dramatic reduction in SL that acompanies the addition of tiny amounts of impurity (butanol) to the standard air bubble in water (Weninger et al., 1995). In fact the strength of SL from such a fluid mixture is less than from an air bubble in the pure butanol, which as shown in Fig. 50 also yields a very faint signal.

The high solubility of xenon in nonaqueous fluids implies that diffusion processes lead to large fluxes of gas into and out of the bubble during each cycle. These oscillatory fluxes have an amplitude that is generally larger than the anomalous mass flow (38), and are given by (Löfstedt et al., 1995)

$$\left(\frac{\Delta M}{M}\right)_D \approx \frac{C_0}{\rho_0}\frac{\sqrt{DT_a}}{R_0}. \tag{43}$$

Since the solubility of xenon in butanol is 10^{-2} mole fraction as compared to air in water which is 1.3×10^{-5} mole fraction, one finds that $C_0/\rho_0 \approx 2.4$, which is so large that according to the diffusion equation, 20% of the gas in a xenon bubble in butanol must flow in and out during each cycle (for air in water the oscillatory mass flux is under a percent). Perhaps this effect accounts for the extreme jittering of these bubbles. However, gases with a lower solubility (such as helium for which C_0/ρ_0 is a factor of ten smaller) and presumably greater stability from the perspective of diffusion, do not yield SL from butanol, and so there is no simple interpretation of the role of the diffusion equation in SL from non-aqueous fluids.
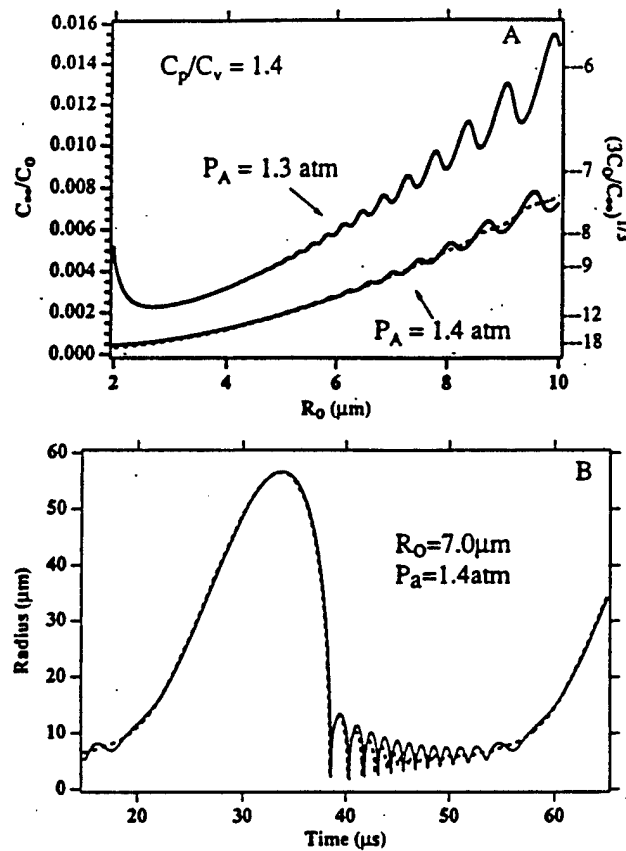
Fig. 41. (A) Equilibrium concentrations as a function of radii as calculated from diffusion for bubbles with SL parameters. Note that an increased viscosity (dashed line = 4 cSt, solid lines = 1 cSt) diminishes the multiple equilibria. On the right axis is plotted the expansion ratio as calculated from the scaling Eq. (37). The surface tension is 70 dyne/cm for the solid lines and 50 dyne/cm for the dashed line. (B) Calculated radius-time curve in the region of multiple equilibria for a 7.0 μm bubble driven at 1.4 atm at 30 kHz. Although the expansion ratio is about 8 : 1 the oscillations of this bubble persist until the next acoustic cycle. Such an effect has not yet been observed for an SL bubble. The solid line is for 1 cSt and the dotted line is calculated for 4 cSt. The ratio of the heat capacities is 1.4.

The wealth of parameters which characterize SL in these experiments tend to rule out a number of simple phenomenological correlations. For instance, the solubility of gases in fluids (Battino et al., 1984; Pollack et al., 1984; Fogg and Gerand, 1991) does not appear to be of crucial importance because the solubility of xenon in dodecane is over a thousand times greater than the solubility of air in water. Similar remarks apply to the fluid's vapor pressure, which for dodecane is 10^4 times smaller than for ethanol, and to the fluid's dielectric constant, which is 80 for water, 25 for ethanol and 2.3 for silicone oil. The relative insensitivity of SL to chemistry suggests that helium gas dissolved in liquid argon could constitute a simple and thus paradigmatic system for the study of SL. Unfortunately our
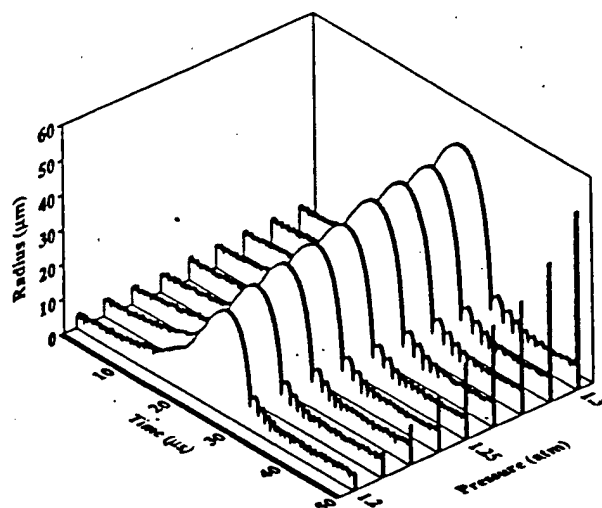
Fig. 42. Waterfall plot of an a 3 mm argon bubble in water. All of these bubbles emit light; the relative SL intensity is indicated by the vertical bars. At one pressure step above the highest level shown the bubble blinks and dies, and at one pressure step below the lowest drive level the bubble dissolves.
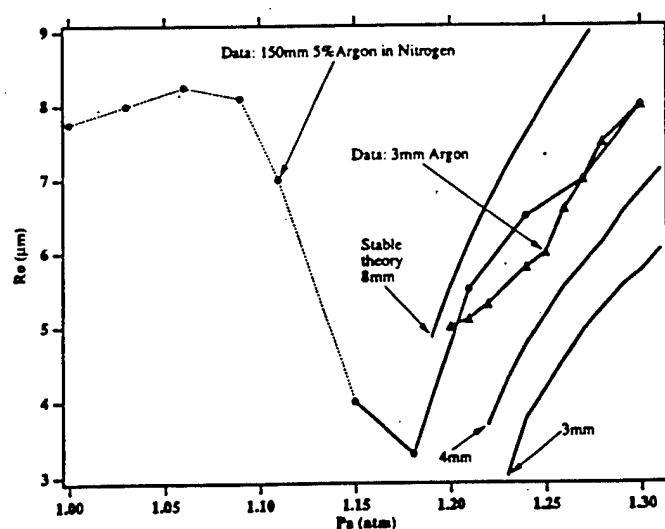
Fig. 43. A comparison of measured drive levels and ambient radii for a 3 mm argon bubble and a 150 mm 5% argon in nitrogen bubble. In the region of SL the bubble parameters overlap, and furthermore are in reasonable agreement with diffusion theory applied to a pure argon bubble. For the theory the frequency is taken to be 23 kHz, $\gamma = 5/3$, surface tension is 50 dyne/cm and kinematic viscosity is 0.04 cm²/s. Note that for the 3, 4, 8 mm theory plots there is no solution below the lowest value plotted.
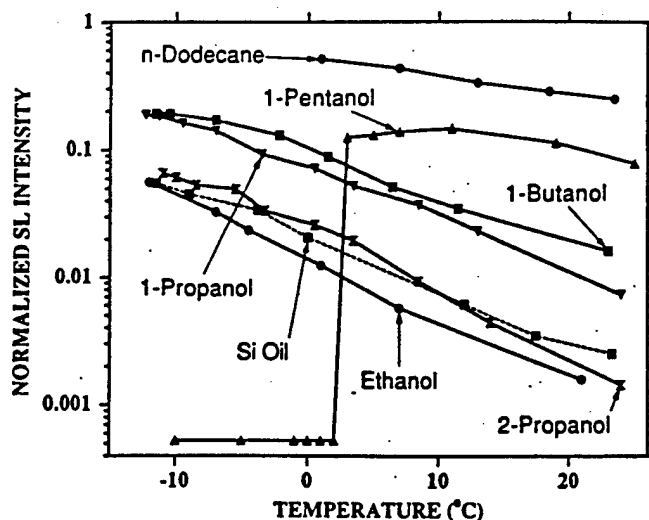
Fig. 44. Intensity of SL from a single xenon bubble trapped in various fluids as a function of temperature (normalized to 150 mm air in water at room temperature). These are the largest signals that can be observed for 30 s or longer. For 1-pentanol below 1°C non-light-emitting bubbles can be sustained. By sweeping the drive level a signal of 1–2 mV (0.1 normalized) can be attained for about 50 ms.
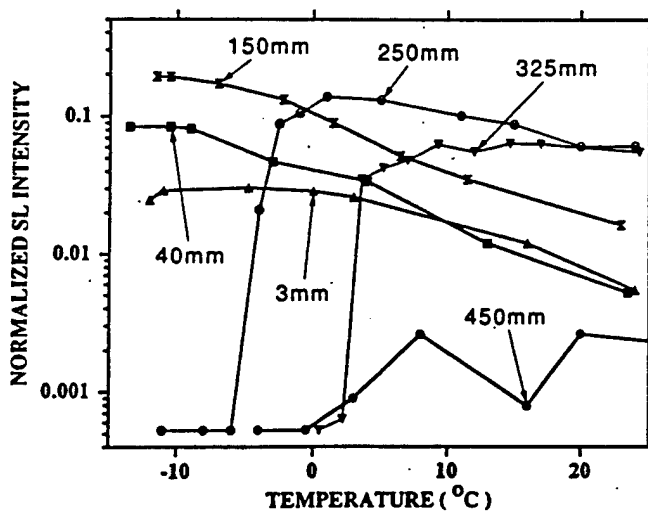
Fig. 45. Intensity of SL for a single xenon bubble in 1-butanol as a function of partial pressure and temperature. For the 250 mm and 325 mm curves at cold temperature the same comments given for 1-pentanol in Fig. 44 apply.

114
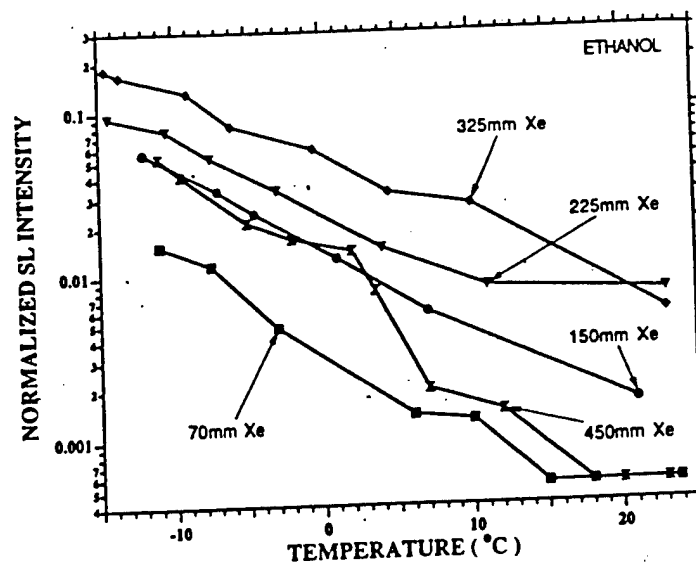
Fig. 46. Intensity of SL from xenon in ethanol.

$O = PRL$ Paper
Vol 72, 1994
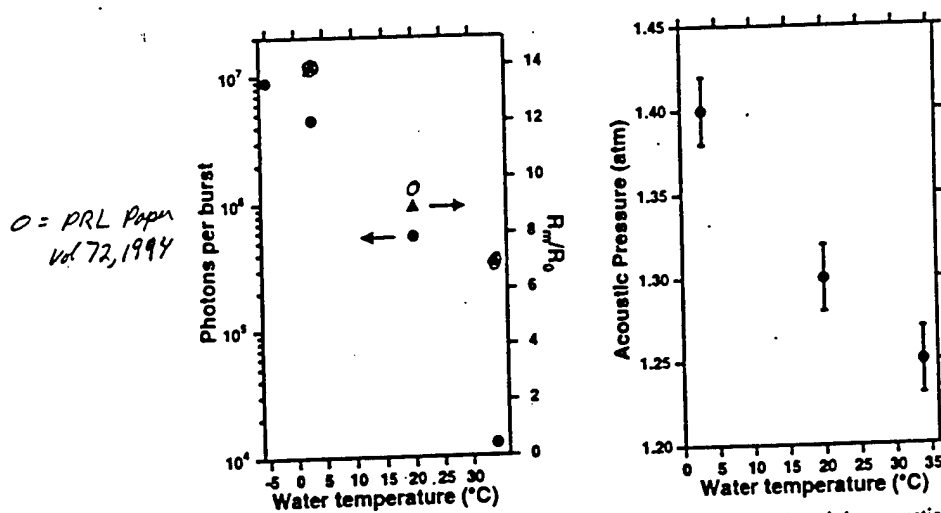
Fig. 47. Intensity of SL from an air bubble in water as a function of temperature (A) and the acoustic pressure (maximum drive levels at which SL is stable) for which these intensities are achieved (B). The increase in light output as the ambient temperature is lowered is correlated with the higher drive level at which SL can be maintained.

grasp of theory does not enable us to predict whether such an experiment would work. If it were attempted, a 3 mm partial pressure solution of helium in liquid argon would be the logical starting point of the search through that portion of parameter space.
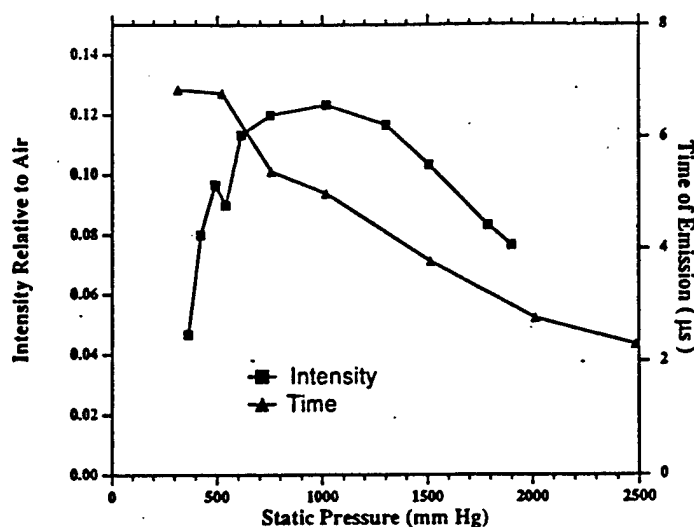
Fig. 48. Intensity of SL for an ethane bubble (dissolved into water at a partial pressure of 2 mm) as a function of the ambient (static) pressure. Also shown is the phase of emission of SL. The earlier time of emission at higher pressure is due to the fact that those bubbles spend less time at the maximum radius. At a static pressure of 4–5 atm "tap" water can display stable SL. Although tap water is saturated as it comes out of the faucet it becomes degassed relative to $C(P_0)$ as P_u increases.
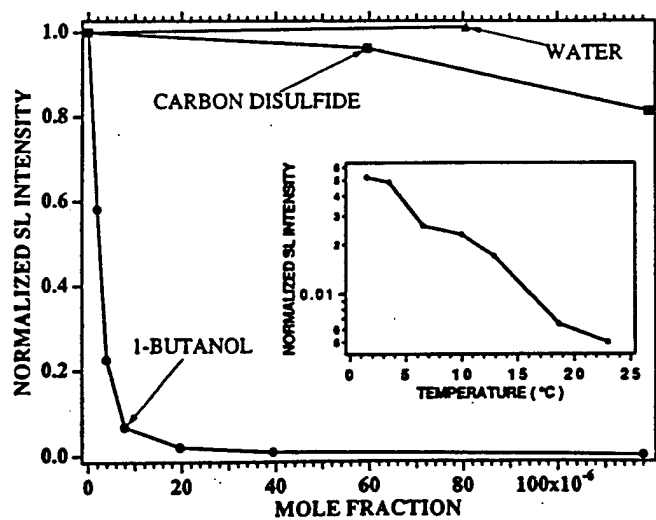
Fig. 49. Intensity of SL as a function of impurity concentration in the water.
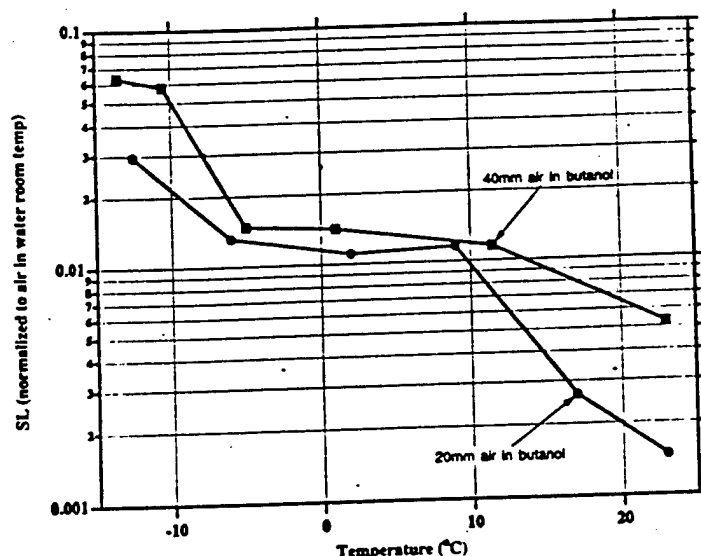
Fig. 50. SL from an air bubble in butanol as a function of ambient temperature.

8. How energetic are the emitted photons?

Fig. 51 displays the uncalibrated spectrum of a helium bubble in water, taken with an ARC 0.275 m spectrometer with a 1200 lines/mm grating blazed at 300 nm and a Hamamatsu R2027 photomultiplier tube (Hiller et al., 1992, 1994, 1995; Gaitan et al., 1996). The key features are
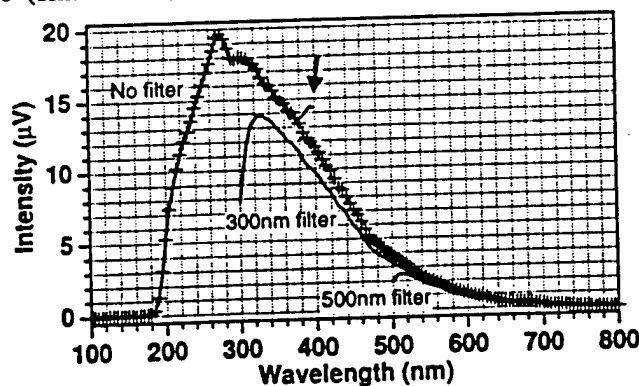
Fig. 51. Raw data showing the uncalibrated spectrum of light emitted by a sonoluminescing bubble of helium in water. Note that the spectral response turns on at about 185 nm (6.5 eV). Due to the broadband nature of the emission, order-sorting filters must be used to suppress second-order diffraction peaks. The arrow points to the onset of a deviation in the spectrum from its real value that would occur if such filters were not used. Here this effect sets in at about 380 nm. The physical spectrum is reconstructed from data taken with no filter as well as filters which cut off light below 300 nm and 500 nm. The actual spectrum must be corrected for the response of the grating, photodetector, and transmission through water and quartz.
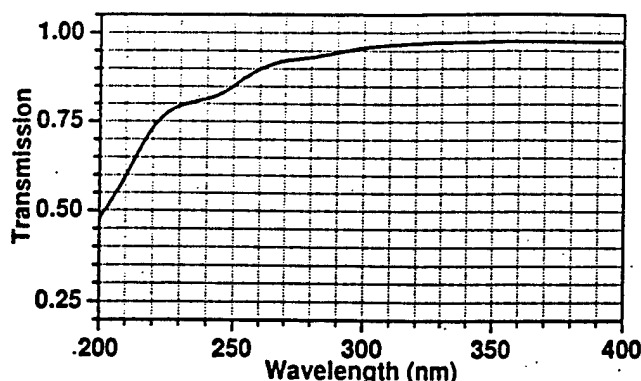
Fig. 52. Transmission of light through water and one wall of the GM quartz flask. Data which are corrected for transmission uses this curve.

already apparent in this plot: the broad band nature of the light (i.e. no spectral lines at the 10 nm FWHM resolution employed), and the persistence of a signal down to a wavelength of 190 nm which is up to an energy almost 6.5 eV. The loss of signal at this wavelength is in part due to the fall off in response of the grating at the diffraction angle corresponding to this wavelength. The fundamental cause for the cutoff of the spectrum at this point is due to the attenuation of light travelling through water. Water does not become transparent again until well into the X-ray regime (Robinson Painter et al., 1969). To obtain values for the spectral radiance which are corrected for the response of the grating, mirrors and photodetector, we use calibrated sources (quartz-tungsten-halogen and deuterium lamps). Even if water would not cut off light in the far UV there still would be no established procedure for calibrating the spectrum below 200 nm. It is also important to use order-sorting filters to suppress second-order scattering by the grating. The arrow in Fig. 51 shows the onset of a signal due to second-order scattering when such a filter is not used. Estimates of the effect of transmission through water and the resonator walls on the spectra are obtained by measuring the attenuation of light focused to pass through the center of the resonator. These correction factors, when used, are shown in Fig. 52. The noise level was reduced by acquiring data with a lock-in amplifier synchronized to the acoustic frequency, which is also the rate at which the SL light emission turns on and off. Putting all these effects together yields typical calibrated spectra for SL, as shown in Fig. 53 for helium dissolved at 150 mm at various temperatures.

The spectrum from various noble gases at room temperature and and 0°C are shown in Figs. 54 and 55 (Hiller et al., 1994). In these experiments the gas is dissolved in water at a partial pressure of 3 mm. Fig. 56 shows the spectrum from noble-gas-doped nitrogen mixtures. It is apparent that the long wavelength limit of virtually all of these gases is similar, but the bubbles with xenon yield a decreasing emission as 200 nm is approached. The broad spectral peak exhibited by xenon may be indicative of the light-emitting mechanism but it may also be due to an enhanced attenuation of the UV light in and near the bubble for this system. The spectral density of a xenon bubble increases slightly in the ultraviolet at lower drive as shown in Fig. 57. The spectrum of xenon in ethanol and butanol is shown in Fig. 58 together with the spectrum of an ethane bubble in water, Fig. 59 (Weninger et al., 1995). Aside from the similarity of these spectra to those already shown
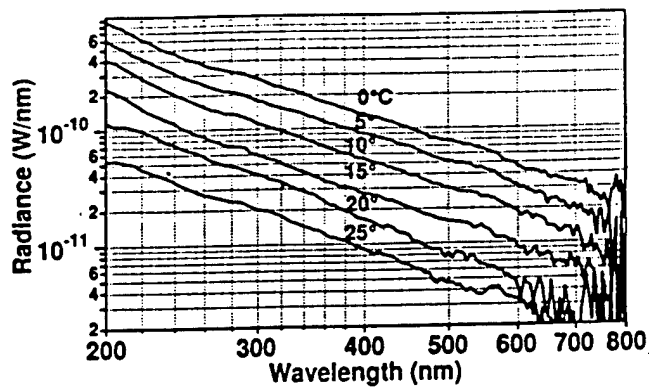
Fig. 53. Corrected spectra for a 150 mm bubble of helium in water at various temperatures.
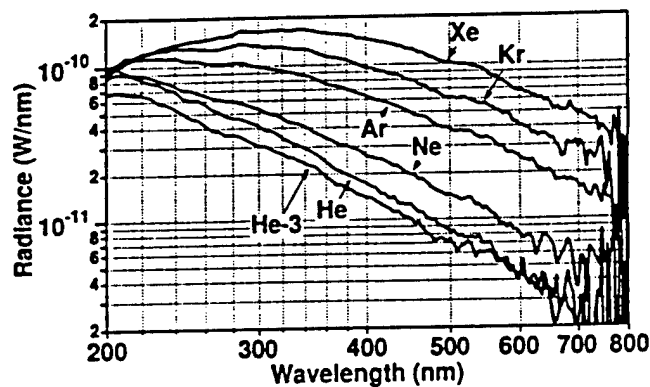
Fig. 54. Room temperature spectra of various noble gases in a cylindrical "supracil" resonator. No transmission corrections have been used. The gases have been dissolved at 3 mm.
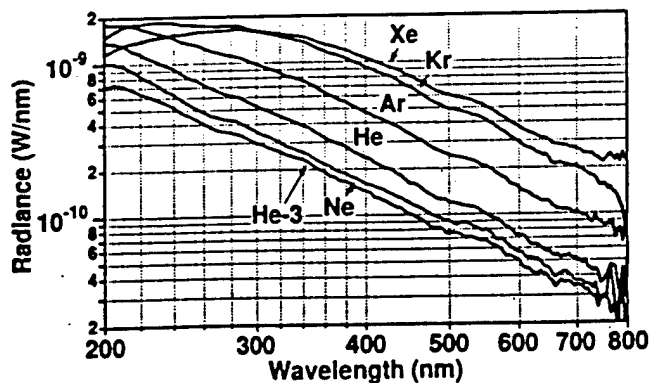
Fig. 55. Freezing point spectra of various noble gases in water. The gases have been dissolved at 3 mm, and the spectra are not corrected for transmission.
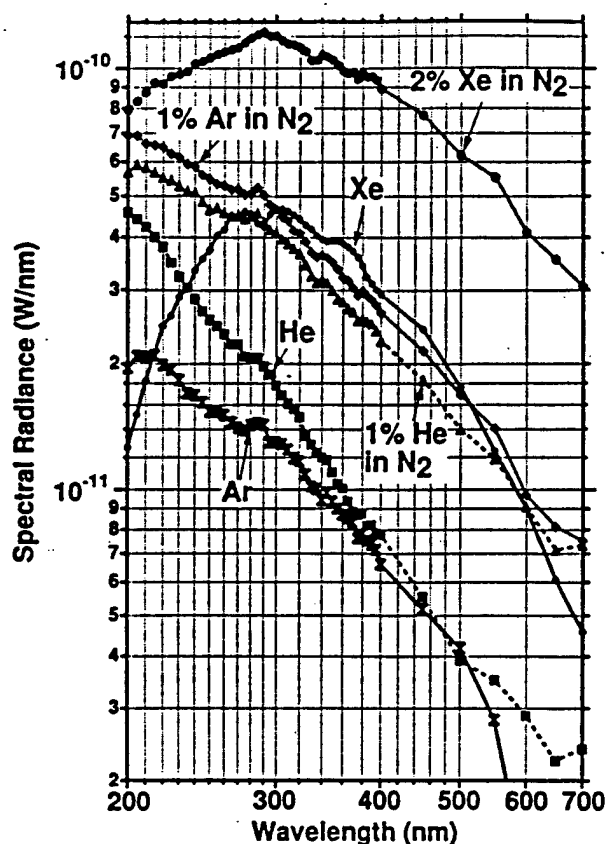
Fig. 56. Spectrum of SL for various gas mixtures dissolved into water at 150 mm and $T = 24°C$. Data have been corrected via use of Fig. 52. Note that although helium is dimmer than xenon it has a greater spectral density in the ultraviolet.

it is noteworthy that the Swan lines are absent (Suslick and Flynt, 1987). These are lines that are emitted by excited states of carbon molecules.

The similarity of the spectra raises the possibility that each spectrum in fact has the same shape, but its position on the wavelength axis is scaled. Then each measurement simply displays a different window of the same spectrum. In this case one can ask where the spectrum of, say, He at 20°C would reach its maximum so as to have the same energy as xenon-doped nitrogen at 0°C. That value turns out to be over 150 eV. The existence of such energetic photons cannot be ruled out experimentally at this time, because a technique for measuring the spectrum beyond the cutoff of various fluids has not yet been developed.
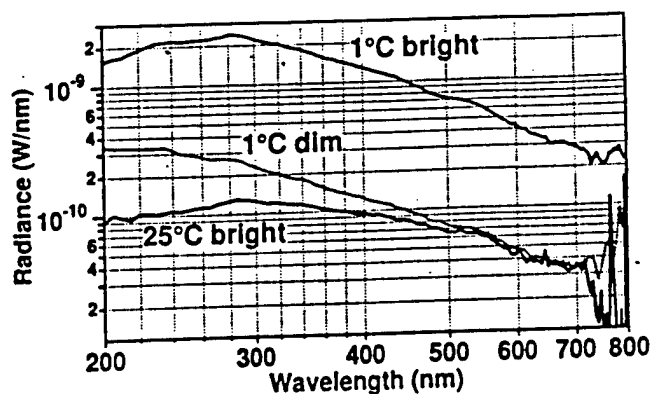
Fig. 57. Spectrum of 2% xenon in nitrogen dissolved at 150 mm showing the variation of the spectral density with drive level.
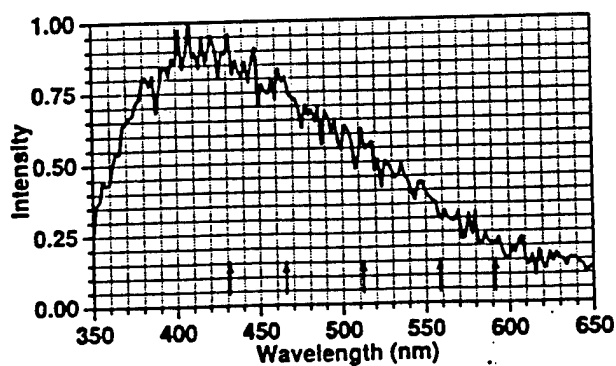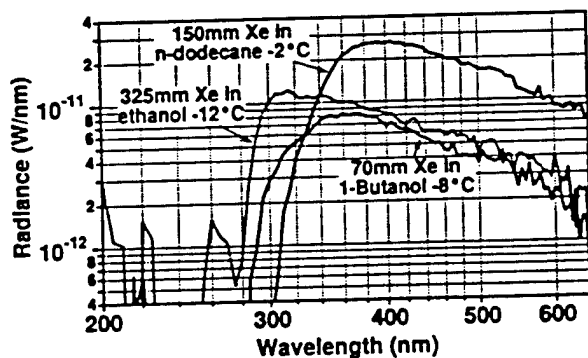
Fig. 58. Spectrum of xenon in various organic liquids. The lower graph (xenon in dodecane) was obtained at a resolution of 1 nm and shows no evidence of the Swan lines which are emitted by excited carbon molecules. These lines have been observed in experiments designed to measure transient SL.
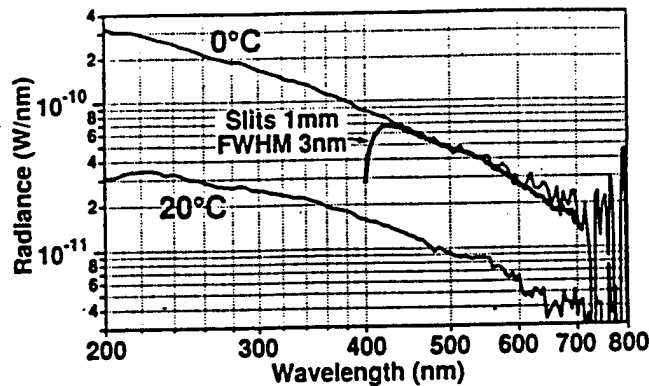
Fig. 59. Spectrum of a 2 mm ethane bubble in water.

9. How short are the flashes?

The fastest time scale for sonoluminescence is more than ten times shorter than the shortest time scale of 500 ps (Barber et al., 1997) that has been resolved in the bubble motion. This very short time scale is the width of the individual flashes of sonoluminescence (Barber and Putterman, 1991). Fig. 60 displays a comparison of the response of a microchannel-plate photomultiplier tube with a rise time of 170 ps to a flash of SL and a flash of purple light from a 34 ps laser pulser (Barber et al.,
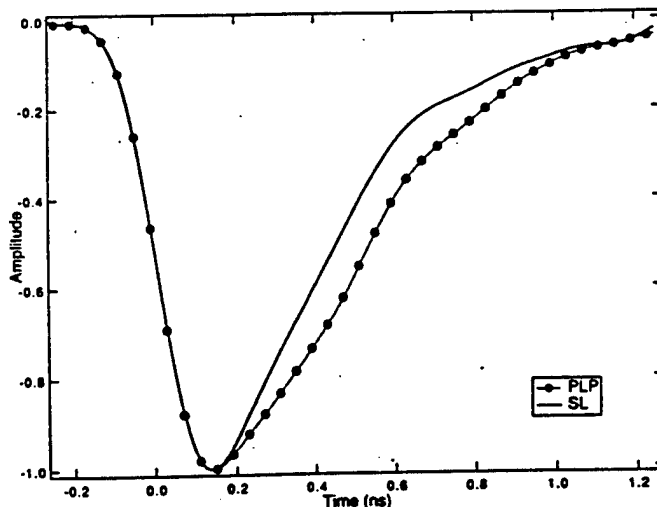
Fig. 60. Voltage versus time at the output of a two-stage microchannel-plate photomultiplier tube with a rated rise time of 172 ps. The solid line shows the response to SL, and the dashed line is the response to 410 nm pulses of 34 ps duration from a laser. These curves correspond to the recording of about 25 photoelectrons. After passing through the delay line and 20 dB attenuator a single photoelectron corresponds to a peak amplitude of 2 mV. A comparison of the graphs indicates that the flash of SL is shorter than 50 ps and furthermore the faster return towards zero of the SL signal indicates that the laser has some after-ringing. The reason for the quick turnoff of SL is unknown.

1992). On the graph the rise-times of the two responses are indistinguishable. Typically the measured rise time for the pulser is about 172 ps and for SL it is about 172–176 ps. From this comparison one can set an upper bound of 50 ps on the duration of the flashes of SL. It is interesting to note that the PMT response to the SL flash returns towards zero more rapidly than the response to the laser pulser. This occurs because the turn-off for SL is clean whereas the pulser is characterized by after ringing. To acquire these traces one must face the difficulty that the oscilloscope requires a trigger that is 20 ns in advance of the signal and that for SL there is no such advance trigger. To overcome this problem, the signal from the photodetector is split into a trigger pulse and a signal pulse. The signal is sent through a high bandwidth delay line so as to arrive after the trigger. The average of many such acquisitions is shown in the figure.

In view of the large parameter space for SL it would be valuable to have a means of resolving the flash width and measuring its value in various situations. To this end a streak camera should be able to resolve the width down to about 2 ps (Barber, 1992). There are two ways to apply this device. One is to collect enough light so that a single sweep catches enough photons to resolve the flash. The difficulty here is to overcome chromatic aberration or, if mirrors are used, to overcome various geometric distortions. The other method is to overlay many acquisitions. Here the problem faced is that the camera must be triggered prior to the arrival of the light. Now it is the light and not an electrical signal that must be delayed. If a signal is recorded at the resolution of the camera, it is essential to distinguish it from dark noise by dispersing it in time with a prism or an optical fiber. The noise will not disperse.[1]

If enough light from a bubble could be collected so that the flashes could be resolved by a streak camera, then it might be possible to measure a time-resolved spectrum of SL. Such data would show whether the UV portion of the spectrum preceded the red portion and would thus yield important information about the light-emitting mechanism and the energy focusing process.

If the output of the photodetector is sent to a time interval meter the jitter in the time between flashes of light can be measured (Barber et al., 1992). As shown in Fig. 61 the standard deviation of the time between flashes is shorter than 50 ps, which in fact is about equal to the stated jitter of the instruments used to measure the SL. It is surely remarkable that the successive supersonic implosions which generate SL should occur with a clock-like precision that is better than a part per million of the imposed acoustic frequency. For reference, the quality factor of the sound field is about only 1000 (Barber and Putterman, 1991).

The largest SL signal measured to date has over 10^7 photons per flash; assuming an average photon energy of 5 eV and a flash width of 50 ps yields a peak power over 100 mW. (The conversion factor of 1 joule $= 6.2 \times 10^{18}$ eV is useful.) Although ps lasers can be very powerful, a cheap UV picosecond light source still costs over $20 000, and has the same power as SL which can be built for $200.

The lowest frequency sound field for which SL has been observed is in the audible range under 10 kHz (Barber and Putterman, 1991). Due to the processes of fluid mechanics, this 100 μs input period results in the emission of a macroscopic pulse of light whose duration of 50 ps is shorter than the time scales that are resolved in high-energy physics experiments.

It was our measurement (Barber and Putterman, 1991) of the picosecond flash widths and synchronicity that fostered general interest in SL, even though SL had been discovered over 50 years

---

[1] According to this criterion, Moran et al. (1995) measured dark noise and not SL, and so their upper bound on the SL flashwidth is invalid.
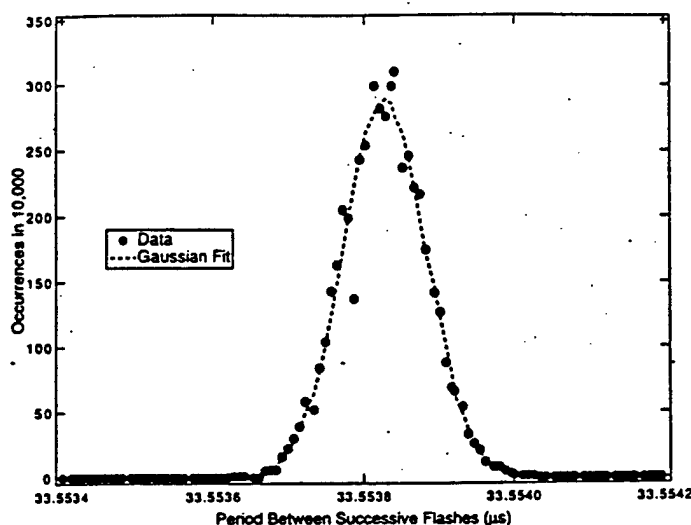
Fig. 61. Histogram of events versus period between flashes for SL. The jitter in the time between flashes is less than 50 ps.

earlier by Frenzel and Schultes (1934). In their apparatus, clouds of cavitating bubbles were generated by sound fields more intense than those quoted above. These bubbles would emit light in a transient and unpredictable fashion. It was the discovery (Gaitan, 1990; Gaitan et al., 1992) that, at least for air in water, SL could be obtained from a single bubble by degassing the water, that made our synchronicity (Barber et al., 1992) and light-scattering experiments (Barber and Putterman, 1992) possible and facilitated the measurements of the flashwidths (Barber and Putterman, 1991). The study of transient SL has a long history (Walton and Reynolds, 1984; Löfstedt, 1995; Putterman, 1995) and it remains to be seen if the physics of each bubble in the Frenzel and Schultes apparatus probes the same physics as a single bubble trapped at a velocity node. The long turn-on time for SL from a single bubble (Fig. 35) (Löfstedt et al., 1995) suggests that these phenomena are quite different. Nevertheless, a calibrated spectrum of transient SL in a resonant system has not yet been taken. The spectral lines observed in transient SL (Suslick and Flynt, 1987; Verrall and Sehgal, 1987; Matula et al., 1995) might be due to a fundamental difference between transient and synchronous SL (Crum, 1994) or perhaps to electrical discharges initiated by the tip of the cell disruptor that drives the fluid. The apparatus of Frenzel and Schultes (1934) was designed to avoid this ambiguity but, unfortunately, they abandoned this line of research after their first paper.

10. What is the light-emitting mechanism?

The transduction of sound into light was coined "sonoluminescence" by Harvey (1957). The reason for the use of the ending "luminescence" dates back to Wiedemann (1889), who defined luminescence as cold light, in contrast to hot light, such as fire. Instances of cold light included such long-established discoveries as light from frictional electricity (*Reibungselektrizitätsluminescenz*) and

124
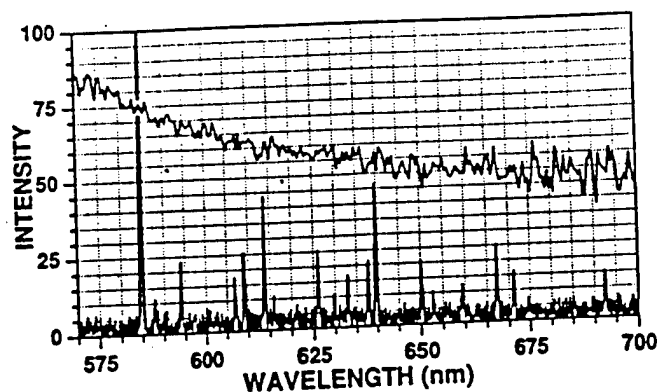
Fig. 62. A comparison of the spectrum of SL from a 3 Torr neon bubble and the spectrum of gas discharge through a 75 Torr neon atmosphere (generated by frictional electricity of mercury against glass (Picard, 1676)). Note that the dramatic peaks which give neon its characteristic orange-red color are absent for SL.

light emitted by fracturing crystals, "triboluminescence". A comparison of the spectra of frictional electricity and SL is shown in Fig. 62. The broadband spectrum is emitted by a neon gas bubble trapped in a sound field according to the procedures of Section 2. The line spectrum is emitted by the friction of mercury against glass in a neon atmosphere at a pressure of 75 mm (Budakian et al., 1996). The broadband nature of what we have been calling SL stands in strong contrast to the very bright spectral lines of the luminescence of frictional electricity. Indeed, the absence of lines in SL strongly suggests that the SL bubble is very hot and/or very stressed so that the comparison with other luminescence phenomena may be misleading. One can wonder if in fact SL is a thermal phenomenon and if its correct name would have been "sonoincandescence".

Explanations of the light-emitting mechanism of SL naturally seek to interpret the featureless spectrum in terms of emission from a hotspot, for example blackbody radiation if the radiation and matter are in near equilibrium (Noltingk and Neppiras, 1950) or Bremsstrahlung from accelerating unbound electrons if the light-emitting region is hot enough to be ionized yet sufficiently rarified so as to be transparent to radiation (Wu and Roberts, 1993). Another candidate mechanism, chemiluminescence, originates in molecular dissociation and recombination at a hotspot (Griffing, 1952).

The adiabatic heating which accompanies the collapse (Eqs. (5), (7)) can produce temperatures of about 5000 or 10 000 K (Noltingk and Neppiras, 1950; Löfstedt et al., 1993). Since 1 eV is about 12 000 K and since the spectrum of SL is generally rising at 6 eV (200 nm), it appears that adiabatic heating could lead to some light emission but that it does not focus energy sufficiently to explain the strongly ultraviolet SL spectrum. In Rayleigh's original investigation (1917) of the spherically imploding bubble, he assumed that the gas obeyed an isothermal equation of state, and so he missed his chance to predict SL.

The shock wave model (Jarman, 1960; Löfstedt et al., 1992; Greenspan and Nadim, 1993; Wu and Roberts, 1993, 1994; Barber et al., 1994; Moss et al., 1994) provides an extra stage of energy focusing by assuming that the supersonic inward collapse of the bubble wall launches a shock wave into the bubble's interior. This shock can run through the already compressed gas inside the bubble, increasing its amplitude and speed as it focuses towards the origin. As sketched in Fig. 63, there is now a surface of radius R_s (the radius of the shock front), within the bubble of radius R. As the
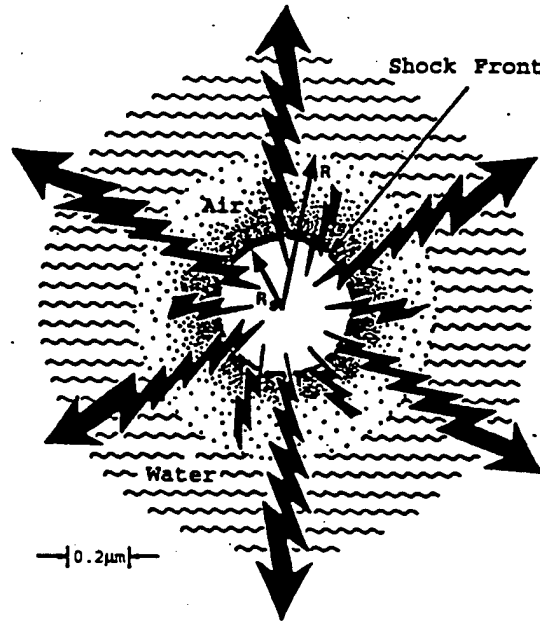
Fig. 63. Sketch of an imploding shock wave model of SL. The shock is launched by the supersonic motion of the bubble wall. The radius of the gas water interface is R and the radius of the shock is R_s. The shock first implodes to a focus and then explodes. This figure depicts the state reached about 100 ps after focusing.

shock moves towards the origin its strength increases until it becomes so strong that there exists a similarity solution to the Euler equations (i.e. the non-dissipative limit) of fluid mechanics. In this case Eq. (1) and (2) must be supplemented with (Landau and Lifshitz, 1987)

$$\frac{\partial s}{\partial t} + v \cdot \nabla s = 0 \tag{44}$$

where s is the entropy per gram, and effects of viscosity in (3) are neglected. In spherical coordinates, these radially symmetric equations are

$$\frac{\partial \rho}{\partial t} + \frac{\partial \rho v}{\partial r} + \frac{2\rho v}{r} = 0, \tag{45}$$

$$\frac{\partial v}{\partial t} + v\frac{\partial v}{\partial r} + \frac{1}{\rho}\frac{\partial P}{\partial r} = 0, \tag{46}$$

$$\left(\frac{\partial}{\partial t} + v\frac{\partial}{\partial r}\right) \log \frac{P}{\rho^\gamma} = 0 \tag{47}$$

where v is the radial component of the velocity, and the last relation expresses the conservation of the entropy of a polytropic gas. The similarity solution is obtained by assuming that the shock radius takes the form (Guderley, 1942)

$$R_s = A(-t)^\alpha \tag{48}$$

where time is measured from the time of the convergence of the shock, and A is the "launch" condition of the shock, which couples the shock to the bubble motion. A similarity solution is then sought in the variable $\xi = r/R_s(t)$, such that $v = (\alpha r/t)\bar{v}(\xi)$, $\rho = \rho_1 \bar{\rho}(\xi)$, and $c^2 = (\alpha^2 r^2/t^2)\bar{c}^2(\xi)$. The solution yields an exponent α of 0.72 in air and 0.69 for noble gases. Since the exponent is less than unity, the Mach number of the shock which goes as $M = \dot{R}_s$ becomes infinitely large as the shock implodes toward the origin. The temperature immediately behind the imploding shock front is given by $T/T_0 \sim M^2$. However, when the shock converges on the origin it explodes from the origin with the same similarity solution. Thus the gas which was compressed just behind the imploding shock front now finds itself in front of the shock front again. As the shock passes through these particles a second time, there is another burst of heating and the maximum temperatures reached by the exploding shock wave now goes roughly as $T/T_0 \sim M^4$ (Barber et al., 1994). (This is an approximation for the purpose of dimensional analysis since, even though it obeys the same scaling laws, the exploding shock is not strong.) The energy focusing ability of the shock front in this model is thus controlled by the extent to which the shock wave is stable upon implosion. Since the imploding shock gets stronger as it approaches the origin, the similarity solution, valid in the limit of high amplitude, always applies eventually. The same form of solution even works for a van der Waals gas (Wu and Roberts, 1994), but is invalidated when ionization effects become important.

Determination of the launch condition, A, connects the imploding shock solution to a particular bubble motion. This condition can be estimated by the (nonrigorous) extention to 3D waves of the concept of characteristics (Landau and Lifshitz, 1987). Consider for example a "characteristic" launched by the bubble wall into its interior when its radius passes through R. The location of this characteristic at time t is $\hat{R}(R, t)$ and its motion is described by

$$\frac{d}{dt}\hat{R} \approx -[c_s(R) + |\dot{R}(R)|]\frac{R}{\hat{R}} \tag{49}$$

where the velocity of the characteristic is the speed of sound in the gas plus the actual velocity of the bubble wall, and is adjusted by the amplification factor $1/\hat{R}$, appropriate to a three-dimensional disturbance as it approaches the origin. This characteristic reaches the origin in a time

$$\hat{t}(R) = R/2[c_s(R) + \dot{R}(R)]. \tag{50}$$

The time for the bubble wall itself to collapse from R to 0, for an ideal gas equation of state is

$$\tau(R) = \tfrac{2}{5}R/\dot{R} \tag{51}$$

where for $R < R_m/2$, $\dot{R}$ is given by (14). One possible criterion for shock formation is that there exists an R such that $\hat{t}(R) = \tau(R)$, or

$$\frac{\dot{R}(R_0)}{c_0} \geq 4\left(\frac{R_0}{R}\right)^{3\gamma/2-3} \tag{52}$$

so when $\dot{R}(R_0)/c_0 \sim 1$ this criterion yields $R = R_0/4$. If one restricts R to the range of validity of the ideal gas equation of state, then $R > R_0/8$ and the corresponding expansion ratio is $R_m/R_0 = 7$. The smallest expansion ratio at which SL has been observed is about 8 : 1. Other criteria (such as characteristics crossing) for shock formation are also possible. A computer calculation indicates that the shock appears about 100 ps before the bubble reaches its minimum radius and that the

shock forms at 1/2 the radius of the bubble when the bubble wall is collapsing at 4–5 times the ambient speed of sound (Wu and Roberts, 1993, 1994). In each case the dimensional analysis and the brute force calculation lead to Eq. (21) as being not only the criterion for shock formation but also the criterion for SL. So we will adopt, for the estimate of A, the criterion that the bubble wall is collapsing at the speed of sound when it is passing through its ambient radius. In this case (Barber et al., 1994)

$$R_s = R_0(-t/t_0)^a, \quad t_0 = \alpha R_0/c_0 \tag{53}$$

and in terms of the Mach number

$$M = |t_0/t|^{1-a} \tag{54}$$

one can estimate

$$R_s \sim R_0(1/M)^{a/(1-a)}, \quad t_s \sim (\alpha R_0/c_0)(1/M)^{1/(1-a)} \tag{55}$$

where t_s is the time scale for the shock to have a radius smaller than R_s. For $M = 4.3$ and $R_0 = 4.5$ μm, these scaling relations yield $T = 10^5$ K, $R_s = 0.15$ μm and $t_s = 100$ ps. For $M = 24$ these scaling relations yield $R_s = 30$ Å, $t_s = 0.3$ ps and $T = 10^8$ K (which would be hot enough for fusion if it happened in a deuterium bubble! (Barber et al., 1994)). Whether the shock can maintain itself down to such incredibly small radii remains to be seen. It should also be emphasized that, in contrast to the bubble wall, the shock surface has not yet been experimentally detected.

The temperatures reached by the shock heating suggest that the gas in the bubble forms a dense ionized region. The free electrons released by the heating will accelerate and radiate light as they collide with the ions. The Bremsstrahlung so generated has a spectral density per unit wavelength λ, per unit volume per second given by (Glasstone and Lovberg, 1960)

$$\frac{dP}{d\lambda} = \frac{16\pi^2 e^6 n_e n_i}{\sqrt{3k_BT}\, m_e^{3/2} c^2 \lambda^2} \exp(-hc/\lambda k_B T) \tag{56}$$

where e, m_e are the electron charge and mass, n_e, n_i are the density of free electrons and ions, and c is the speed of light. If we assume that the light is emitted during an interval of time t_s from a region with radius R_s and a temperature determined by the Mach number, we find for the light energy radiated per flash (per unit wavelength λ)

$$\frac{dE_\lambda}{d\lambda} = \frac{128\pi^2\alpha}{\sqrt{3}} \frac{Nk_BT}{\lambda} \frac{R_0}{\lambda} 145 q^2 \beta^2 n a_B^3 \left(\frac{e^2}{2a_B k_B T}\right)^3$$

$$\times M^2 (1/M)^{(3a+1)/(1-a)} \exp(-hc/\lambda k_B T) \tag{57}$$

where N is the total number of atoms in the bubble and n is their density in the region of the shock front, β is the ratio of the thermal electron velocity to the speed of light, a_B is the Bohr radius, $q = n_e/n$ is the degree of ionization, and for the ideal gas the maximal compression is $n = 145 n_0$. For q a good estimate is obtained from Saha's equation of state (Fermi, 1936)

$$q^2/(1-q) \approx 10^{-7} T^{3/2} \exp(-\chi/k_B T) \tag{58}$$

where χ is the ionization potential and the prefactor T is given in kelvin. The measured light ($\lambda > 200$ nm) is dominated by temperatures above 10^5 K. So if one substitutes the corresponding $M = 4$ into (57) and notes that the degree of ioniztion is almost unity (so that $n_e = n_i = n$) one finds that the total radiated energy per flash is about 10^7 eV in rather good agreement with experiment. In a more precise analysis, a van der Waals equation of state would be used for this calculation. Beyond that, one would employ equations of state that are themselves corrected for the degree of ionization. Finally, corrections to the Bremsstrahlung formula to account for the posibility that SL originates from a dense cold plasma should be considered.

Since the SL light emission occurs as a (mathematical) singularity is forming, any transport process which a theorist chooses to incorporate in this model can affect the result (Moss et al., 1994; Kondic et al., 1995; Vuong and Szeri, 1996). A closely related model ascribes the radiation to changes in molecular dipole moments that are induced by collisons (Frommhold and Atchley, 1994). These effects, however, would be suppressed in pure noble gas bubbles.

The launch of a shock wave by the Rayleigh-Plesset bubble dynamics with the subsequent Bremsstrahlung radiation from the hot ionized contents is the most complete candidate model of SL. This model, however, is far from satisfactory. It requires a number of key physical inputs such as the acoustic drive level and ambient radius (P_a and R_0) at which bubbles give SL and additional physical inputs are required in order to determine the minimum radius attained by the shock. Furthermore, it does not address compelling yet simply stated mysteries, such as why pure diatomic gases are bad sources of SL.

Another insight into the light-emitting mechanism is that it is relatively unaffected by a strong, 20 T, magnetic field (Young et al., 1996). Even though the cyclotron radius of 100 000 K electrons is 0.5 μm, which is close to the minimum bubble radius, and the cyclotron period is 1 ps, which is shorter than the current bound on the flashwidth, in first approximation SL appears to be unaffected.

According to (56), Planck's constant determines the high energy cutoff in the Bremsstrahlung spectrum. Since the spectrum beyond the cutoff of water has not yet been observed, the validity of this term has not been checked. Thus the shock wave-Bremsstrahlung model lies entirely within the range of classical mechanics and there still remains the exciting issue of whether Planck's constant will play a role in a phenomenon initiated by classical acoustics! In this direction Schwinger (1993) proposed that the change in electromagnetic zero point energy brought about as water filled in the gaseous cavity would show up as radiation. The "spectrum" of zero point energy in a volume V near wavenumber k is

$$dE_k = \tfrac{1}{2}\hbar ckV\,d^3k. \tag{59}$$

Due to a jump in the index of refraction n at the bubble interface, the collapsing wall sweeps out a changing zero point motion which then becomes observable. The rate of change of the zero point energy of water plus bubble is then

$$\frac{d}{dt}\frac{d\Delta E_\lambda}{d\lambda} = (2\pi)^5 \hbar c \frac{\Delta n}{\lambda^5}\frac{dV}{dt}. \tag{60}$$

Although the power law spectrum has similarities to SL, this source of energy transduction is a maximum when the rate of change of volume is a maximum which is near the maximum radius. In contrast, the rate of change of the surface is a maximum at the moment of light emission, but

attempts to interpret SL in terms of Unruh radiation from the surface (Eberlein, 1996; Knight, 1996) yield powers that are too small by many orders of magnitude.

Another light emitting mechanism that has been proposed is an electronic discharge from charge separation inside a plasma (Lepoint et al., 1996). This picture is reminiscent of "ball lightning" (Kapitza, 1956). Also, SL has been connected to triboelectric phenomena via a postulated cracking of a solid gas shell that forms on the bubble wall (Hickling, 1994) and by the "cracking" of the water by a supersonic jet launched by the collapsing bubble (Prosperetti, 1996). The value of these various models will be judged based upon their ability to make falsifiable predictions.

11. How spherical is the collapse?

One of the defining characteristics of electromagnetism is that spherically symmetric accelerations of charge distributions do not radiate (Ehrenfest, 1910; Stratton, 1941). Yet among picosecond light sources sonoluminescence is unique in that the flash intensities are uniform over a spherical shell and furthermore this light originates from a region that is smaller than its wavelength. Based upon these observations it is clear that a probe of possible angular correlations in SL would help to characterize the properties of this light source and possibly shed light on the light-emitting mechanism. Although we have observed dipole components that reach 10% of the total emitted intensity (Weninger et al., 1996), they can be interpreted as being due to the refraction of light by a nonspherical bubble wall that separates the hot gas near the center of the bubble from the surrounding host liquid. According to this interpretation, angular correlations in SL provide a diagnostic for the sphericity of the bubble collapse (and therefore they do not reflect the light-emitting mechanism). Since a more spherical collapse is more violent, this diagnostic should prove to be useful in attempts to reach higher levels of energy concentration with sonoluminescence.

These correlations were measured with multiple photodetectors as a function of their observation angle (Weninger et al., 1996). The angular dependence in the intensity of SL is characterized by a non-zero value of the correlation,

$$\Delta Q_{AB} = \frac{1}{\bar{Q}_A \bar{Q}_B} \langle [Q_A(i) - \bar{Q}_A][Q_B(i) - \bar{Q}_B] \rangle_i \tag{61}$$

as a function of the angle θ_{AB} formed by the detectors "A" and "B" and the bubble which is reckoned to sit at the vertex. In Eq. (61), $Q_A(i)$ is the total charge recorded in detector A on the ith flash, $\bar{Q}_A$ is the running average of $Q_A(i)$ and $\langle\ \rangle_i$ denotes an average over i. In addition to tubes A and B there is a trigger tube which monitors the SL so as to gate a digital oscilloscope which then acquires the tube outputs. From the data generated by 1000 flashes, the average and the correlation (61) are calculated. Twenty such data sets generate a "result" and the average and standard deviation of 3 results generate the plotted point and "error" bar at each angle. As experimental configurations were varied, the signal recorded in each phototube ranged from 5–8 photoelectrons per flash of SL.

The solid line in Fig. 64 displays the angle dependent correlation that is observed in most runs. It can be attributed to a dipole component in the detected photon field. If $\bar{\Omega}_A$ is the fraction of solid angle subtended by detector A, and N_I and N_D are the numbers of photons arriving isotropically and as a dipole, then the total number of photons to strike the detector is
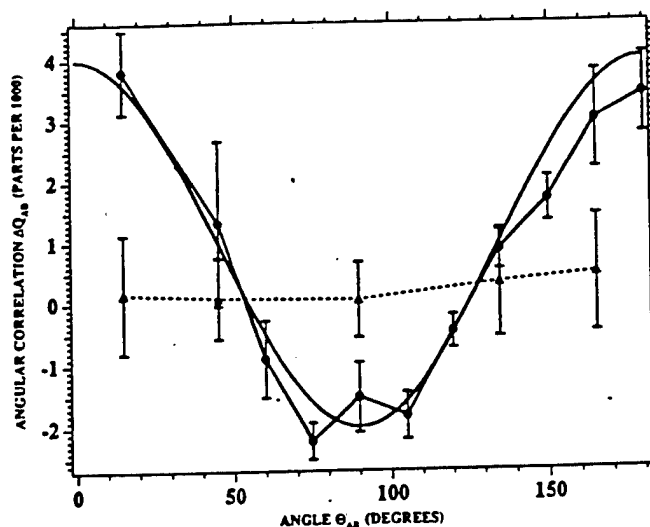
Fig. 64. Correlation of light intensity between two phototubes subtending an angle θ_{AB} with respect to a sonoluminescing bubble. The solid line corresponds to an SL bubble whose flash to flash intensity has a large variation. The flash to flash fluctuations for the dotted line are much less and are furthermore consistent with Poisson statistics. Note the appearance of a negative correlation at 90°. The maximum dipole observed is about 10 parts per thousand. If the dipole is due to refraction of light at the gas-fluid interface of the bubble then the ellipticity of the bubble in the state with large fluctuations is about 20%. The sine wave fit is $0.001(1 + 3\cos\theta)$.

$$N_A(i) = \bar{\Omega}(N_I + 3N_D \cos^2\theta_{iA}) \qquad (62)$$

(and similarly for B), where θ_{iA} is the angle between the direction of the dipole on flash i and the detector A. If one assumes that over time there is no preferred direction, then a physical dipole of strength N_D leads to the correlation

$$\Delta N_{AB} = \frac{\langle[N_A(i) - \bar{N}_A][N_B(i) - \bar{N}_B]\rangle_i}{\bar{N}_A\bar{N}_B}$$

which upon substitution of (62) yields

$$\Delta N_{AB} = \frac{N_D^2}{(N_I + N_D)^2}(\tfrac{1}{5} + \tfrac{3}{5}\cos 2\theta_{AB}). \qquad (63)$$

So according to the sine wave fit to the data in Fig. 64, this observed field has a dipolar component, N_D/N_I, of 7%.

In order to determine whether the dipole is due to the mechanism whereby the stress of implosion is converted into light, we measured the correlation (61) as a function of the time delay Δt between acquisitions in tubes A and B (Weninger et al., 1996). In the case that the dipole is due to the light-emitting mechanism each flash would be independent of the previous flash so that the correlation should fall abruptly to zero for $\Delta t \neq 0$. As shown in Fig. 65, however, the dipole correlation $\Delta Q_{AB}(\Delta t)$ has a long memory, about equal to the free decay time of the sound field.
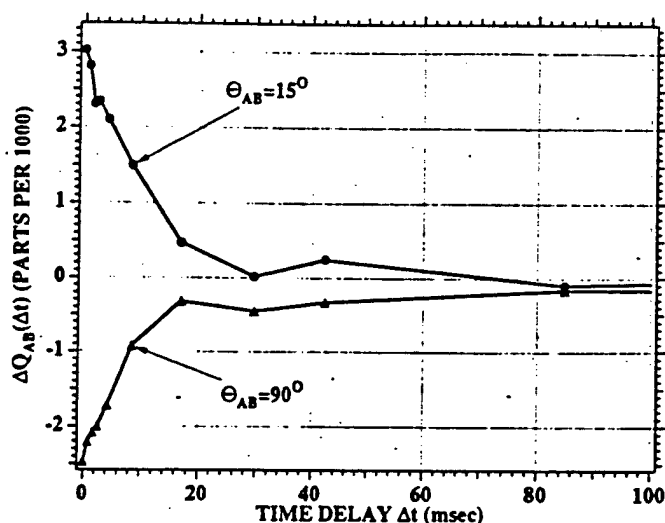
Fig. 65. The correlation of an SL flash in tube A with flashes in tube B at a later time. The time delay $\Delta t = nT_a$, where n is an integer and T_a is the acoustic period. The long-term memory of the dipolar component is comparable to the lifetime of the driving sound field. Typical quality factors for these sound fields range from 500–1500.

This long time decay of the angle-dependent correlation indicates that the dipole component is due to some aspect of the hydrodynamic motion. Such motions rearrange themselves on the same time scale for which the sound field changes. The various possibilities include (1) jitter in the location of the bubble, (2) bending of the emitted light by the sound field in the bulk of the fluid, and (3) refraction of the SL rays by the surface of a non-spherical bubble. Jitter gives the wrong sign of correlation and the effect of ray bending is too small since it goes as the Mach number of the sound field in the water squared.

The simplest explanation of the measured angular correlation is in terms of refraction, by the nonspherical bubble wall, of light that is emitted uniformly from a point source within the bubble's interior. Fig. 66 shows how light from a point source would be refracted by passage through an elliptical boundary in the ray optics limit. For an interface where the index of refraction jumps from 1.0 (on the gas side of the bubble's surface) to 1.35 (in water), a 7% dipolar component would require a 20% ellipticity. (We define ellipticity as $a/b - 1$ where a and b are the major and minor axis, respectively.) For demonstration purposes Fig. 66 was constructed for a jump in the index of refraction from 1.0 to 2.0 and a ratio of major axis to minor axis of 2.

Another insight into the origin of these correlations is provided by the observation that in some runs the dipole component vanishes, as shown by the dashed line in Fig. 64. According to Fig. 67 these states are in one to one correspondence with narrow pulse height distributions. The time record and histogram of SL flash intensities indicates that the state with a 7% dipolar component (and ellipticity of 20%) has over an order of magnitude more spread in flash intensities. (The spread is defined as the maximum divided by the width at half maximum.) For the state with a narrow pulse height distribution the dipole component (as determined by a least squares fit) is 1%, which corresponds to
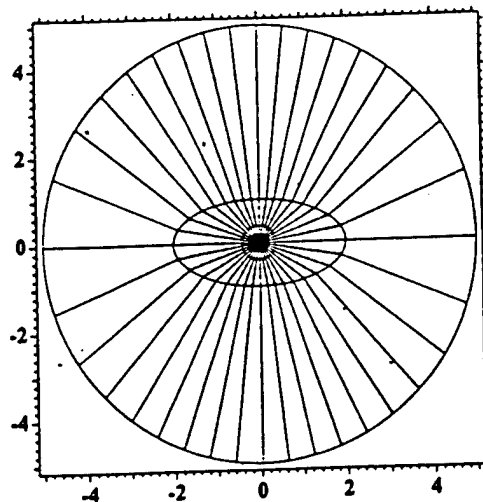
Fig. 66. Refraction of light from a point source by a surrounding elliptical interface. For purpose of demonstration this figure was generated with a major axis that is twice the minor axis. Such a surface introduces a dipole component into the far field.

an estimated upper bound on ellipticity of about 3%. Using three detector tubes we were also able to verify that the angle-dependent and angle-independent states occurred in the vertical and horizontal planes simultaneously. That is, when the longitude showed a large dipole so did the latitude, and similarly for the case of no dipole.

Control of the key parameters which determine whether the collapse is elliptical has been elusive as the system falls into and out of this state. Various candidate parameters are imperfections in the sound field such as coupling to nearby modes of the resonator, thermal drift, scattered sound biting back on the bubble, or dust particles in the vicinity of the bubble. Each of these hydrodynamic motions is coupled to the sound field and will tend to wander on the time scale determined by its bandwidth. In this way the direction of the measured dipole will change in space on the time scale shown in Fig. 65. Remarkably, we have found that the jitter (50–100 ps) in the time between flashes is the same for the two states shown in Figs. 64 and 67 (Weninger et al., 1996). So, these particular effects do not appear to explain the chaos observed in other experiments (Holt et al., 1994).

By inserting colored glass filters between the PMT and the bubble, the dependence of the angular correlations on color can be investigated (Weninger et al., 1996). Fig. 68 shows the angular correlation for "red" ($\lambda > 500$ nm) and "blue" ($260 < \lambda < 380$ nm) light for the same bubble state. The fact that the red correlation is suppressed indicates that these longer wavelengths diffract out of the bubble's interior on their way to the detector. This implies that the radius of the bubble at the moment of light emission is about equal to the wavelength of red light, consistent with light-scattering measurements (Barber and Putterman, 1992).

According to Hanbury-Brown and Twiss (HBT) (Hanbury-Brown, 1974), filtered light from an incoherent uniform emitter can display angular correlations in the intensity. This effect has been used to measure the radius of stars. If the dipole component in these broadband measurements is indeed due to the asphericity of the collapse, then this source of correlation will have to be monitored or
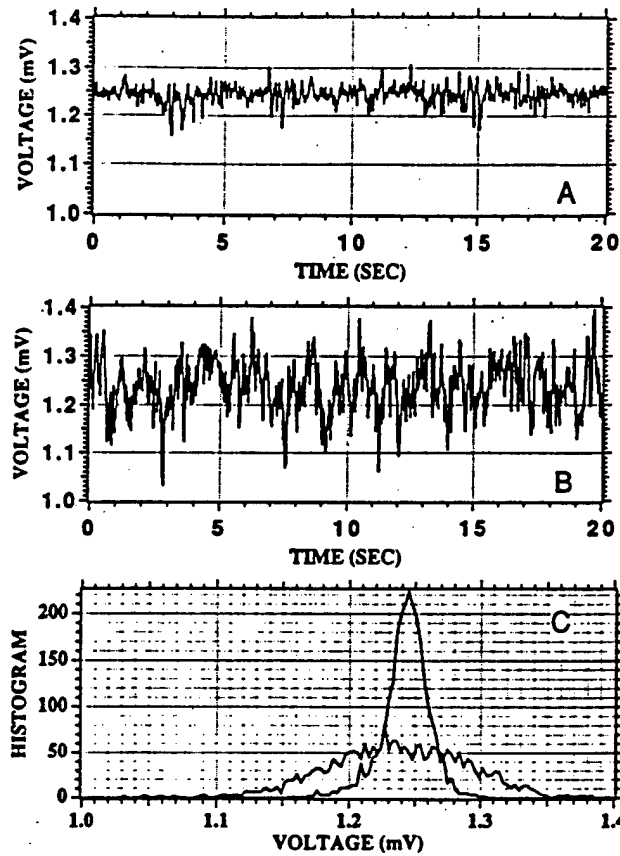
Fig. 67. Fluctuations in SL intensity for states with large and small dipolar components. Time records are displayed in (A), (B) and the pulse height distributions are compared in (C). The sound field has a frequency of 26.4 kHz, and the detectors each record an average of 5 photoelectrons per flash. The time constant for binning is 10 ms.

eliminated in an attempt to apply HBT to SL (Trentalange and Pandey, 1996).

The observed dipole in the light emission provides a probe of the degree of nonsphericity of the collapse. Ellipticity is the leading order, quadrupolar, form of a convolution instability. Such instabilities have also been studied with regard to bubble (Plesset and Mitchell, 1956; Prosperetti, 1977; Löfstedt et al., 1995; Brenner et al., 1995) and shock wave motion (Wu and Roberts, 1996a, 1996b) and inertial confinement fusion (Budil et al., 1996). For bubble motion the convolutions are expanded in terms of spherical harmonics so that

$$R(t) = \bar{R}(t) + \sum_{n=2}^{\infty} a_l(t) Y_l(\theta, \phi).$$ (64)

Requiring that pressure and velocity be continuous at the surface of the bubble yields to linear order in the amplitudes of convolution $a(t)$ (Prosperetti, 1977)
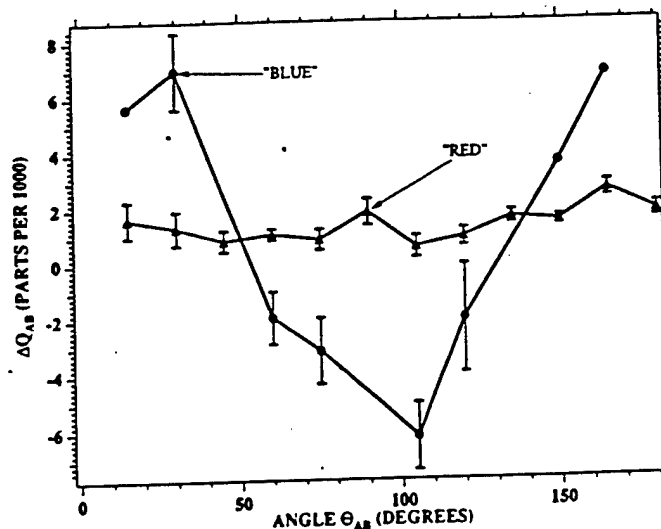
Fig. 68. Angular correlation for the long and short wavelength parts of the SL spectrum. According to the model presented in Fig. 66 the absence of correlation at long wavelength is attributed to the dominance of diffraction over refraction.

$$R\ddot{a}_l + \left(3\dot{R} + 2\frac{\nu(l+2)(2l+1)}{R}\right)\dot{a}_l$$

$$- \left((l-1)\ddot{R} - \frac{2\nu(l-1)(l+2)}{R^2}\dot{R} - \frac{(l^2-1)(l+2)\sigma}{\rho R^2}\right)a_l = 0 \tag{65}$$

where the bar has been dropped from R. This equation has the form of a Hill equation being a second order linear differential equation with coefficients that are periodic functions of time. There are three cases of interest. First, on the short time scale, one can ask if this equation develops an instability which leads to the rapid growth of a convolution during one cycle of the motion. This is the issue of whether the bubble suffers from Rayleigh-Taylor (RT) instability (Rayleigh, 1883; Taylor, 1950). Next one can ask if the convolution builds up from cycle to cycle. This question which is in the spirit of the Matthieu equation (Landau and Lifshitz, 1976) for a parametrically driven swing can be applied to the bouncing and SL bubbles. For the SL bubble a theory which connects the hydrodynamics on both sides of the collapse does not exist so Eq. (65) cannot be applied to this case. We now consider the RT instability within a cycle for SL and bouncing bubbles and the Matthieu type instability for the non-SL bubble.

First, we neglect the (stabilizing) effects of viscosity. For the SL bubble the cycle is divided into the expansion, the collapse and the time during which the bubble sits dead in the water. During the expansion of the bubble to R_m the growth is approximately linear and $a(t)$ decreases as $1/R^2$ from its initial value. During the collapse Eq. (14) applies so that (65) yields $a \sim (R_m/R)^{1/4}$ (Plesset and Mitchell, 1956). Up until the point where deviations from the ideal gas law come into play the enhancement of the convolutions is at most a factor of 3. That the motion is in fact RT stable can be appreciated by writing (65) in Hamiltonian form (Löfstedt et al., 1995),

$$H = \frac{p_l^2}{2\rho R^3} - \frac{\rho(l-1)}{2} R^2 \ddot{R} a_l^2 + \frac{(l^2-1)(l+2)}{2} \sigma a_l^2 \tag{66}$$

where, as mentioned, viscosity has been neglected. Since $\ddot{R}$ is negative during the collapse (see Fig. 12), the motion in the potential well of the Hamiltonian is stable, and the (factor of 3) magnification of a is due to the scaling of the effective mass and the potential through R in the spherical geometry. Following the collapse, the bubble is motionless at R_0 for half the acoustic cycle. During this part of the cycle convolutions decay due to the viscosity which we now include (Prosperetti, 1977)

$$a_l(t) = a_{l0} \cos(\omega_\sigma t + \delta_0) e^{-\alpha t} \tag{67}$$

where

$$\omega_\sigma^2 = \frac{(l-1)(l+1)(l+2)\sigma}{\rho R^3}, \quad \alpha = \frac{(l+2)(2l+1)\nu}{R^2}. \tag{68}$$

In particular, the time constant for a quadrupolar perturbation to decay for a bubble motionless at $R_0 = 4~\mu m$ is less than $1~\mu s$ which is very short when compared to this $15~\mu s$ portion of the acoustic cycle. So we conclude that during any given cycle, i.e. from flash to flash, harmonic convolutions do not build up (Löfstedt et al., 1995). The upper threshold of SL is due either to some other hydrodynamic instability or to an event occurring at the moment of collapse which is not describable by the hydrodynamics.[2]

The decay rate $\alpha_0 = \nu_0/R_0^2$ (where ν_0 is the ambient kinematic viscosity of the gas) for acoustic energy stored inside the bubble is also on the order of a microsecond. When other sources of damping such as acoustic radiation and bulk viscosity are included this time becomes even shorter. Therefore, there no usable energy is stored inside the bubble during a cycle, in contrast with a recent suggestion (Brenner, Hilgenfeldt, et al., 1996).

Fig. 69 shows the standard deviation in light scattering from a collapsing bubble of 1% xenon in oxygen. Note that for a given radius (a given average signal) the standard deviation after the collapse is larger than before the collapse. This can be interpreted as due to the generation of a convolution in the bubble as a result of the crash. Depending upon the orientation of the convolution relative to the laser, systematic variations in the scatter can occur which would not be present for a spherical bubble. Since a macroscopic theory that connects the bubble motion before and after the collapse has not yet been developed, this ringing convolution cannot be derived. Nevertheless this bubble is stable and so this convolution dies out before the next cycle, consistent with the above analysis. These collapse induced shape oscillations are not observed in all bubbles (e.g. air). Another type of asphericity that occurs in a collapsing bubble is the formation of a jet (Kornfeld and Suvorov, 1944; Kling and Hammit, 1972; Lauterborn and Bolle, 1975; Crum, 1979). The possible role of jets in SL has been proposed by Longuet-Higgins (1996) and Prosperetti (1996).

---

[2] The shape instabilities derived by Brenner et al. (1995) and Hilgenfeldt et al. (1996) resulted from the use of a coefficient of damping which is much smaller than that given by Eqs. (65), (68). Their unphysical damping term is due to the application of an asymptotic expansion beyond its range of validity (Roberts and Putterman, 1996). It remains to be seen whether SL is affected by non-RT sources of shape instability such as jets, bubble pinch-off, anomalous diffusion, or resonator imperfections. We regard Eq. (65) as being consistent with Lamb (1945), Prosperetti (1977), and Prosperetti and Seminara (1978), for subsonic bubble motion.
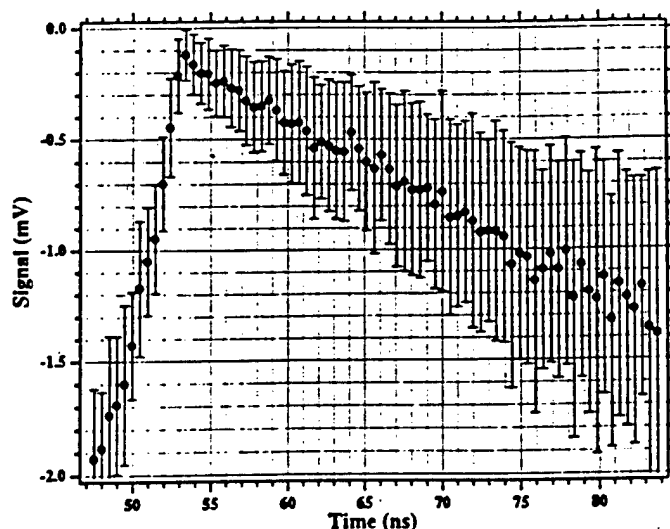
Fig. 69. Standard deviation in the intensity of light scattered from a bubble near the moment of light emission. The average value determines the radius, and the bar determines the standard deviation in a given 500 ps bin. (Note that the standard deviation of the mean is down by about a factor of 8 from the plotted values.) The larger standard deviation after collapse can be interpreted as due to nonspherical bubble oscillations whose orientation relative to the laser varies from shot to shot. For some gases the standard deviation does not increase as a result of the collapse. These data were taken for 1% xenon in oxygen at 150 mm.

12. How controllable are experiments on sonoluminescence?

There are two cultures of sonoluminescence. One culture, which includes the theorists, is intrigued by the picosecond timescales, the energetic spectrum, the upper and lower thresholds, and the effect of doping with a noble gas. There is, however, an experimental culture that expends substantial effort on the critical yet apparently disjoint issue of controlling this phenomenon. In this direction it can be said that we do not yet know the complete set of experimental parameters that must be controlled so as to render experiments on SL reproducible from lab to lab.

First on this list of challenges is the acoustic resonator. Our best resonator to date has been custom made by GM from GE quartz. We have worked with four such spheres each of which has a sphericity accurate to one percent. Three of these spheres have produced the most stable reproducible SL that we have measured. The fourth looks identical in every way to the other three yet it produces a lousy acoustic resonance and even for air in water the SL signal is highly unstable. Also the tendency of an SL bubble to walk off-center as the drive level is increased varies from resonator to resonator. Perhaps the appearance and disappearance of the dipole component is also connected with the input acoustics. Clearly, slight variations in the acoustical properties of the resonator can be critical. Substantial efforts have been expended on "resonator technology"; the next efforts will include metallic resonators with windows.

Although water is the friendliest fluid for SL it presents unique difficulties. When pure 19 MΩ cm water from the still comes into contact with air its resistance drops before your eyes as it dissolves
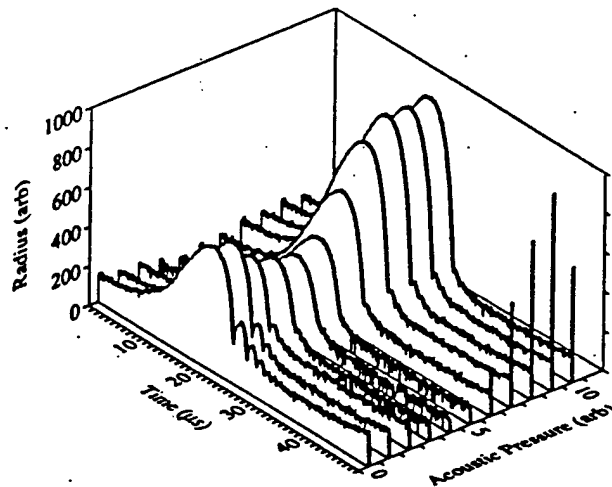
Fig. 70. Waterfall plot of a 150 mm, 1% xenon in nitrogen bubble in water with photoflow solution dissolved into the water at a concentration of 1/500. The photoflow goes to the bubble interface and changes the surface tension so that the bubble dynamics is affected. In particular the smaller bubbles reach a higher expansion ratio.
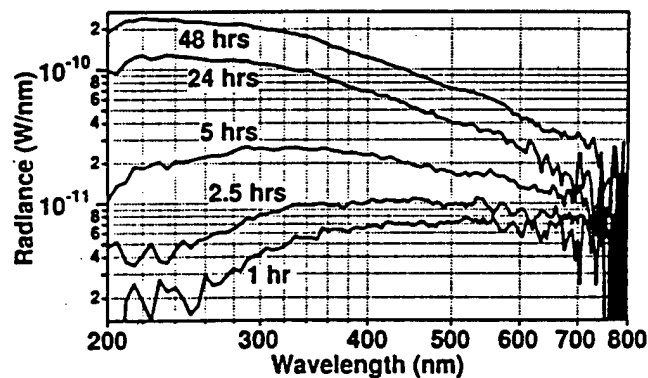
Fig. 71. Spectrum of a deuterium bubble in heavy water as a function of time from preparation of the 3 mm solution. The drift is due to an air leak either from the outside or outgassing from the RTV seals on the cylindrical resonator.

grime from the air. Within a few minutes the resistance is down to 5 MΩ cm and the effective damping and surface tension have been likewise affected. An example of how surface tension can change the bubble dynamics is shown in Fig. 70, which was taken for a 1% xenon in nitrogen bubble at 150 mm with commercial photoflow dissolved into the water at a concentration of 1/5000. The difference with Fig. 33 (no photoflow) is apparent. It would be interesting to carry out SL in a clean environment so as to achieve the lowest viscosity and highest surface tension, perhaps reproducibly.

Small gas leaks have a dramatic effect on the properties of SL. Shown in Fig. 71 is the time dependence of the spectrum of what we prepared to be a hydrogen bubble in heavy water. We do not know whether the leak is from the outside or whether it is due to outgassing RTV seals. This drift
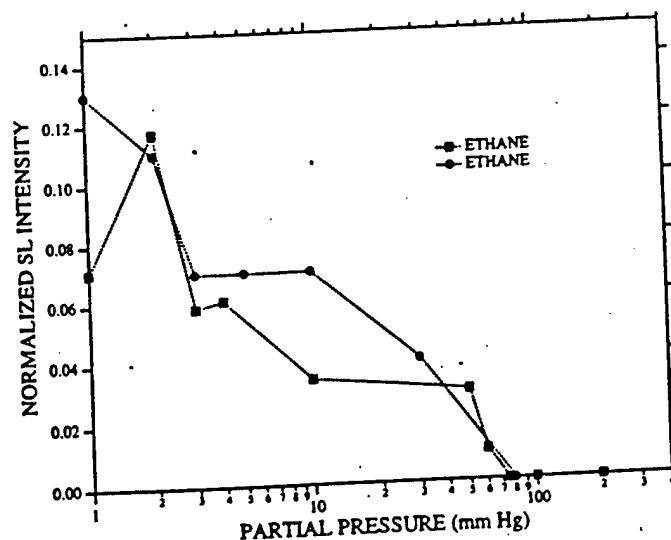
Fig. 72. Intensity of light emission from a 2 mm bubble of ethane in water. Two independent runs are shown.
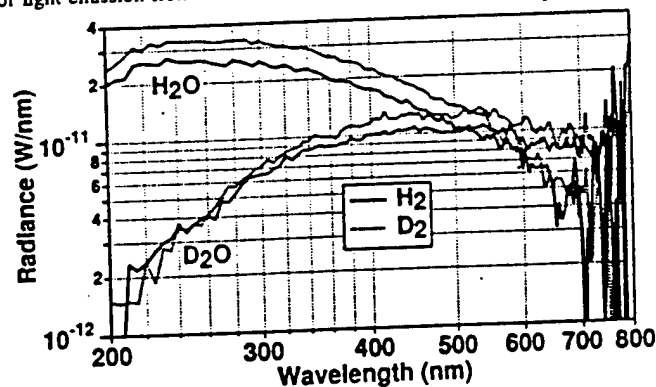
Fig. 73. Spectrum of 3 mm solutions of hydrogen and deuterium in light and heavy water. These are jittery bubbles. Whether these spectra are due to tiny levels of impurity remains to be seen. In any event the spectra in heavy water fit well to a black body spectrum at 6000 K.

is eliminated by rubber O rings. We are even ready to doubt whether *pure* diatomic gases give any light. It is possible that, as higher levels of purity are achieved, these bubbles will behave worse and worse. Fig. 72 shows the typical run to run variations in behavior that can be observed, in this case for a 2 mm ethane bubble in water.

Fig. 73 shows the spectrum of hydrogen and deuterium bubbles in light and heavy water (Hiller and Putterman, 1995). The difference can reasonably be attributed to a dramatic isotope effect due to the heavy water except that, as shown in Fig. 74, different batches of heavy water yield different spectra with xenon bubbles. Tiny impurities in the heavy water could be affecting the results.

Before all confidence is annihilated we should say that the experiments on noble gas doping have
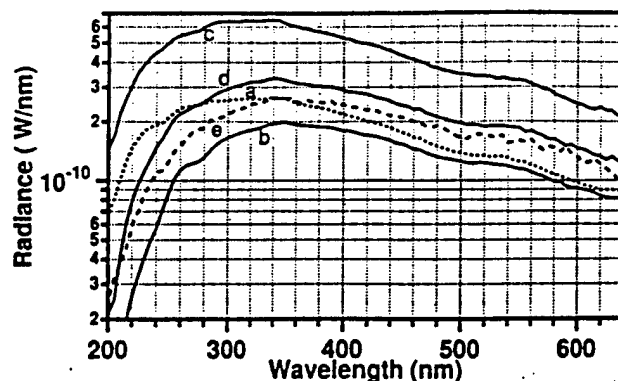
Fig. 74. Spectra of SL from xenon bubbles in light and heavy water prepared at a partial pressure of 3 mm: curves (a) and (b) are for light water and the first batch of heavy water in a spherical resonator, curves (c) and (d) are for other batches of heavy water in a cylindrical resonator and curve (e) is for water with 2.5 ppm 1-butanol, multiplied by 7.3 to align it with pure water at 340 nm.
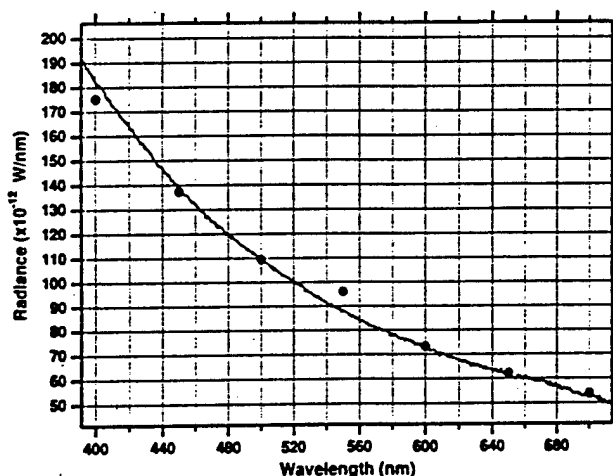
Fig. 75. High resolution spectrum of a 1% xenon in oxygen bubble (at 150 mm partial pressure) obtained via two different calibrations of the radiance. The points are determined by a calibration of the apparatus with a NIST traceable QTH lamp. The continuous line is obtained when the black body curve which provides the best fit to the QTH calibration is used to calibrate the apparatus. The expectation that the SL spectrum should be featureless suggests that the QTH calibration at 550 nm is incorrect.

been repeated from the bottom up by four different researchers, B.P. Barber, D. Chow, R. Hiller, K. Weninger on four different apparatuses with various gas mixtures (Hiller et al., 1994; Chow et al., 1996). Furthermore, some aspects of SL are so remarkably repetitive and reliable as to make SL useful in calibrating instruments! Matching bubble dynamics to hydrodynamics provides P_a and therefore a means of calibrating a hydrophone such as the one used to acquire the data in Fig. 1. The response of a PMT to SL can be used to calibrate after ringing in a picosecond light source (Section 9), and the lack of structure in the spectrum of SL can be used to check the calibration of
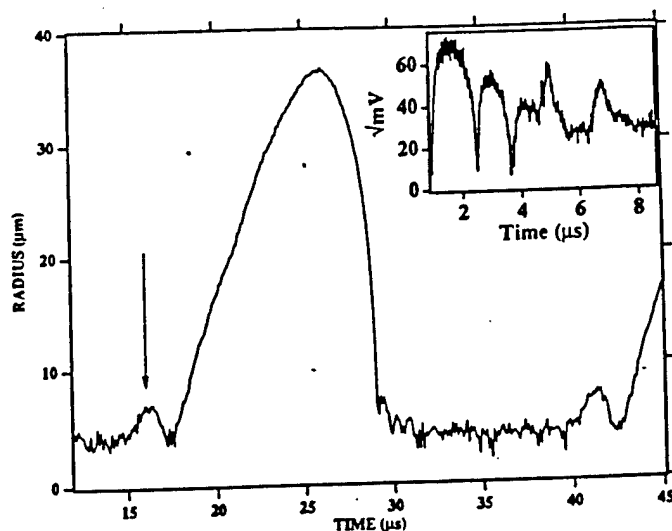
Fig. 76. Radius versus time curve at high drive level showing a glitch in $R(t)$ just as the bubble begins to expand. These data were taken for a 150 mm, 1% xenon in nitrogen bubble. The inset shows that glitches can also appear during afterbounces to SL (Chowet et al., 1996). In contrast with the complete $R(t)$ curve, the inset is not averaged.

light sources as shown in Fig. 75. In Fig. 75 the dots are the spectrum of SL as determined from a QTH lamp with a NIST traceable calibration and the continuous line is the measured SL spectrum as calibrated by the black-body curve that provides the best fit to the QTH calibration. Based upon the insight that the SL spectrum is featureless (on the scale of say 50 nm) one concludes that the light source was incorrectly calibrated at 550 nm.

Returning to the experimental difficulties we finally note that at high drive levels the light scattering experiments observe on occasion a glitch in the radius of the expanding bubble (see Fig. 76). Whether this is an insight into the key issues revolving around the mass flow mechanism, or thresholds for SL, remains to be seen.

Pending the ascendancy of a falsifiable theory, the next set of SL discoveries might instead be driven by engineering improvements that address the issues broached in this section.

Acknowledgments

References

Apfel, R., 1986, IEEE-UFFC 33, 139.

D'Arrigo, J.S., S.-Y. Ho, and R.H. Simon, 1993, Investigative Radiology 28, 218.

Asaki, T.J., P.L. Marston, and E.H. Trinh, 1993, J. Acoust. Soc. Am. 93, 706.

Barber, B.P., 1992, Ph.D. Thesis (University of California, Los Angeles).

Barber, B.P., 1994, J. Acoust. Soc. Am. 96, S3252.

Barber, B.P., R.A. Hiller, K. Arisaka, H. Fetterman, and S. Putterman, 1992, J. Acoust Soc. Am. 91, 3061.

Barber, B., R. Löfstedt, and S. Putterman, 1991, J. Acoust. Soc. Am. 89, S1885.

Barber, B.P. and S.J. Putterman, 1991, Nature 352, 318.

Barber, B.P. and S.J. Putterman, 1992, Phys. Rev. Lett. 69, 3839.

Barber, B.P., K. Weninger, R. Löfstedt, and S. Putterman, 1995, Phys. Rev. Lett. 74, 5276.

Barber, B.P., K. Weninger, and S.J. Putterman, 1997, Trans. Roy. Soc. (in press).

Barber, B.P., C.C. Wu, R. Löfstedt, P.H. Roberts, and S.J. Putterman, 1994, Phys. Rev. Lett. 72, 1380.

Battino, R., M. Banzhof, M. Bogan, and E. Wilhelm, 1972, Anal. Chem. 54, 806.

Battino, R., T.R. Rettich, and T. Tominaga, 1984, J. Phys. Chem. Ref. Data 13, 563.

Birks, J.B., 1964, Theory and Practice of Scintillation Counting (Pergamon, New York), p. 572.

Bjerknes, V.F.J., 1906, Fields of Force (Columbia, New York).

Brenner, M.P., D. Lohse, and T.F. Dupont, 1995, Phys. Rev. Lett. 75, 954.

Brenner, M.P., D. Lohse, D. Oxtoby, and T.F. Dupont, 1996, Phys. Rev. Lett. 76, 1158.

Brenner, M.P., S. Hilgenfeldt, D. Lohse, and R.R. Rosales, 1996, Phys. Rev. Lett. 77, 3467.

Budakian, R.O., R.A. Hiller, K.R. Weninger, and S.J. Putterman, 1996, unpublished.

Budil, K.S., B.A. Remington, T.A. Peyser, K.O. Mikaelian, P.L. Miller, N.C. Woolsey, W.M. Wood-Vasey, and A.M. Rubenchik, 1996, Phys. Rev. Lett. 76, 4536.

Chow, D., K. Weninger, and S. Putterman, 1996, unpublished.

Church, C., 1988, J. Acoust. Soc. Am. 83, 210.

Cross, M.C. and P.C. Hohenberg, 1993, Rev. Mod. Phys. 65, 851.

Crum, L.A., 1979, J. Phys. (Paris) 40, 285.

Crum, L.A., 1994, J. Acoust. Soc. Am. 95, 559.

Crum, L.A. and S. Cordry, 1994, in Bubble Dynamics and Interface Phenomena, edited by J.Blake et al. (Kluwer, Dordrecht).

Dave, J.V., 1969, IBM J. Res. Dev. 13, 302.

Delgadino, G.A. and F.J. Bonetto, 1996, preprint.

Dodd, R.K., J.C. Eilbeck, J.D. Gibbon, and H.C. Morris, 1982, Solitons and Nonlinear Wave Equations (Academic, New York).

Eberlein, C., 1996, Phys. Rev. Lett. 76, 3842.

Ehrenfest, P., 1910, Phys. Z. 11, 708.

Eller, A. and H.G. Flynn, 1965, J. Acoust. Soc. Am. 37, 493.

Epstein, P.S. and M.S. Plesset, 1950, J. Chem. Phys. 18, 1505.

Feinstein, S.B., 1989, Echocardiography 6, 27.

Fermi, E., 1936, Thermodynamics (Dover, New York).

Fogg, P.G.T. and W. Gerand, 1991, Solubility of Gases in Liquids (Wiley, New York).

Frenzel, H. and H. Schultes, 1934, Z. phys. Chem. B27, 421.

Frommhold, L. and A.A. Atchley, 1994, Phys. Rev. Lett. 73, 2883.

Fyrillas, M.M. and A.J. Szeri, 1994, J. Fluid Mech. 277, 381.

Gaitan, D.F., A.A. Atchley, S.D. Lewis, J.T. Carlson, X.K. Maruyama, M. Moran, and D. Schweider, 1996, Phys. Rev. E 54, 525.

Gaitan, D.F., 1990, Ph.D. Thesis (University of Mississippi).

Gaitan, D.F., L.A. Crum, C.C. Church, and R.A. Roy, 1992, J. Acoust. Soc. Am. 91, 3166.

Glasstone, S. and U. Lovberg, 1960, Controlled Thermonuclear Fusion (Princeton University, Princeton).

Gould, R.K., 1973, J. Acoust. Soc. Am. 56, 1740.

Greenspan, H.P. and A. Nadim, 1993, Phys. Fluids A 5, 1065.

Griffing, V., 1952, J. Chem. Phys. 20, 939.

Guderley, G., 1942, Luftfahrtforschung 19, 302.

Hallaj, I.M., T.J. Matula, R.A. Roy, and L.A. Crum, 1996, J. Acoust Soc. Am. 100, 2717.

Hanbury-Brown, R., 1974, The Intensity Interferometer (Taylor & Francis, London).

Hansen, G.M., 1985, Appl. Opt. 24, 3214.

Harvey, E.N., 1957, A History of Luminescence from the Earliest Times until 1900 (Am. Phil.Soc. Press, Philadelphia).

Hickling, R., 1994, Phys. Rev. Lett. 73, 2853.

Hilgenfeldt, S., D. Lohse, and M.P. Brenner, 1996, Phys. Fluids 8, 2808.

Hiller, R.A., 1995, Ph.D. Thesis (University of California, Los Angeles).

Hiller, R. and B.P. Barber, 1995, Sci. Am. 272, 78.

Hiller, R.A. and S.J. Putterman, 1995, Phys. Rev. Lett. 75, 3549; 77, 2345 (E).

Hiller, R., S.J. Putterman, and B.P. Barber, 1992, Phys. Rev. Lett. 69, 1182.

Hiller, R., K. Weninger, S.J. Putterman, and B.P. Barber, 1994, Science 266, 248.

Holt, R.G., and L.A. Crum, 1992, J. Acoust Soc. Am. 91, 1924.

Holt, R.G., D.F. Gaitan, A.A. Atchley, and J. Holzfuss, 1994, Phys. Rev. Lett. 72, 1376.

Holt, R.G. and D.F. Gaitan, 1996, Phys. Rev. Lett. 77, 3791.

van de Hulst, H.C., 1957, Light Scattering by Small Particles (Wiley, New York).

Jarman, P., 1960, J. Acoust Soc. Am. 32, 1459.

de Jong, N., L. Hoff, T. Skotland, and N. Born, 1992, Ultrasonics 30, 95.

Kapitza, P.L., 1956, Collected Papers, edited by D. Ter Haar (Pergamon, New York).

Kerker, M., 1969, The Scattering of Light and Other Electromagnetic Radiation (Academic, NewYork).

King, L.V., 1934, Proc. Roy. Soc. A147, 212.

Kling, C.L. and F.G. Hammit, 1972, J. Basic. Eng. Trans. A.S.M.E. D94, 825.

Knight, P., 1996, Nature 381, 736.

Kondic, L., J.I. Gersten, and C. Yuan, 1995, Phys. Rev. E 52, 4976.

Kornfeld, M. and L. Suvorov, 1944, J. Appl. Phys. 15, 495.

Lamb, H., 1945, Hydrodynamics (Dover, New York).

Landau, L.D. and E.M. Lifshitz, 1976, Mechanics (Pergamon, Oxford).

Landau, L.D. and E.M. Lifshitz, 1987, Fluid Mechanics (Pergamon, Oxford).

Lauterborn, W. and H. Bolle, 1975, J. Fluid Mech. 72, 391.

Lentz, W.J., A. Atchley, and D.F. Gaitan, 1995, Applied Optics 34, 2648.

Lepoint, T., D. De Pauw, F. Lepoint-Mullie, M. Goldman, and A. Goldman, 1996, J. Acoust.Soc. Am. (in press).

Lohse, D., M.P. Brenner, T.F. Dupont, S. Hilgenfledt, and B. Johnston, 1996, "Single sonoluminescing bubbles as stable chemical reaction chambers".

Löfstedt, R., 1995, Ph.D. thesis (University of California, Los Angeles).

Löfstedt, R., B.P. Barber, and S.J. Putterman, 1992, J. Acoust Soc. Am. 92, S2453.

Löfstedt, R., B.P. Barber, and S.J. Putterman, 1993, Phys. Fluids A 5, 2911.

Löfstedt, R. and S. Putterman, 1991, J. Acoust. Soc. Am. 90, 2027.

Löfstedt, R., K. Weninger, S. Putterman, and B.P. Barber, 1995, Phys. Rev. E 51, 4400.

Longuet-Higgins, M.S., 1996, J. Acoust Soc. Am. 100, 2678.

Marston, P.L., 1979, J. Opt. Soc. Am. 69, 1205.

Marston, P.L., 1991, Appl. Opt. 30, 3479.

Matula, T.J., R.A. Roy, P.D. Mourad, W.B. McNamara, and K.S. Suslick, 1995, Phys. Rev. Lett. 75, 2602.

Moran, M.J., R.E. Haigh, M.E. Lowry, D.R. Sweider, G.R. Abel, J.T. Carlson, S.D. Lewis, A.A. Atchley, D.F. Gaitan, and X.K. Maruyama, 1995, Nucl. Instrum. Methods B96, 651.

Moss, W.C., J.W. White, R.A. Day, and D.B. Clarke, 1994, Phys. Fluids 6, 2979.

Noltingk, B. and E. Neppiras, 1950, Proc. Roy. Soc. B63, 674.

Penning, F.M. and C.C.J. Addink, 1934, Physica 1, 1007.

Picard, J., 1676, Mem. Acad. Roy. Science 2, 202.

Plesset, M., 1949, J. Appl. Mech. 16, 277.

Plesset, M.S. and T.P. Mitchell, 1956, Quart. Appl. Math. XIII, 419.

Pollack, G.L., J.F. Himm, and J.J. Enyeart, 1984, J. Phys. Chem. 81, 3239.

Prosperetti, A., 1977, Quart. Appl. Math. 34, 339.

Prosperetti, A., 1984, Rend. Sc. Int. Fis. XCIII, 145.

Prosperetti, A., 1996, "A new mechanism for sonoluminescence".

Prosperetti, A., L. Crum, and K. Commander, 1988, J. Acoust. Soc. Am. 83, 502.

Prosperetti, A. and G. Seminara, 1978, Phys. Fluids 21, 1465.

Putterman, S.J., 1995, Scientific American 272, 32.

Lord Rayleigh, 1883, Proc. London. Math. Soc. XIV, 170.

Lord Rayleigh, 1917, Phil. Mag. 34, 94.

Roberts, P.H. and S.J. Putterman, 1996, to be published.

Robinson Painter, L., R.D. Birkhoff, and E.T. Arakawa, 1969, J. Chem. Phys. 51, 243.

Schwinger, J., 1993, Proc. Natl. Acad. Sci. U.S.A. 90, 2105, 7285.

Stratton, J.A., 1941, Electromagnetic Theory (McGraw-Hill, New York).

Suslick, K.S. and E.B. Flint, 1987, Nature 350, 553.

Taylor, G.I., 1950, Proc. Roy. Soc. A201, 192.

Tian, Y.J., J.A. Ketterling, and R.E. Apfel, J. Acoust. Soc. Am. 100, 3976.

Tomow, W., 1996, Phys. Rev. E 53, 5495.

Trentalange S. and S.U. Pandey, 1996, J. Acoust. Soc. Am. 99, 2439.

Verrall, R. and C. Sehgal, 1987, Ultrasonics 25, 29.

Vuong, V.Q. and A.J. Szeri, Phys. Fluids 8, 2354.

Walton, A.J. and G.T. Reynolds, 1984, Adv. Phys. 33, 595.

Weninger, K., R. Hiller, B.P. Barber, D. Lacoste, and S.J. Putterman, 1995, J. Phys. Chem. 99, 14195.

Weninger, K., S.J. Putterman, and B.P. Barber, 1996, Phys. Rev. E. 54, R2205.

Wiedemann, E., 1889, Wiedemanns Ann. 37, 177.

Wiscombe, W.J., 1980, Appl. Opt. 19, 1505.

Wu, C.C. and P.H. Roberts, 1993, Phys. Rev. Lett. 70, 3424.

Wu, C.C. and P.H. Roberts, 1994, Proc. Roy. Soc. A445, 323.

Wu, C.C. and P.H. Roberts, 1996a, Phys. Lett. A 213, 59.

Wu, C.C. and P.H. Roberts, 1996b, Quart. J. Mech. Appl. Math. 49, 501.

Wu, J., R. Keolian, and I. Rudnick, 1984, Phys. Rev. Lett. 52, 1421.

Young, J.B., T. Schmiedel, and W. Kang, 1996, Phys. Rev. Lett. 77, 4816.

FORTHCOMING ISSUES

A.J. Hoff, J. Deisenhofer. Photophysics of photosynthesis. Structure and spectroscopy of reaction centers of purple bacteria

R. Casalbuoni, A. Deandrea, N.Di Bartolomeo, R. Gatto, F. Feruglio, G. Nardulli. Phenomenology of heavy meson chiral lagrangians

W. Grimus, M.N. Rebelo. Automorphisms in gauge theories and the definition of CP and P

V. Castellani, S. Degl'Innocenti, G. Fiorentini, M. Lissia, B. Ricci. Solar neutrinos: beyond the standard solar model

R. Redmer. Physical properties of dense, low-temperature plasmas

M. Cvetič, H.J. Soleng. Supergravity domain walls

H. Chen et al. Search for new massive particles in cosmic rays

M.V. Sadovskii. Superconductivity and localization

F.M. Marqués, G. Martínez, T. Matulewicz, R. Ostendorf, Y. Schutz. Two-photon correlations. From Young Experiments to heavy-ion collision dynamics

C. Jung, T.H. Seligman, Integrability of the S-matrix versus integrability of the Hamiltonian

U. Näher, S. Bjørnholm, S. Frauendorf, F. Garcias, C. Guet. Fission of metal clusters

L. Herrera, N. O. Santos. Local anisotropy in self gravitating systems

V. Barger, M.S. Berger, J.F. Gunion, T. Han. Higgs boson physics in the s-channel at mu^+mu^- colliders

B.R. Judd. Lie groups for atomic shells

S. Kailas. Heavy-ion induced fission at near-barrier energies

J.M. Overduin, P.S. Wesson. Kaluza-Klein gravity

L.N. Lipatov. Small-x physics in perturbative QCD

E.B. Starikov. Chemical physics of solid state nucleic acid: new intriguing horizons

M.E. Brandan, G.R. Satchler. The interaction between light heavy ions and what it tells us

A.M. Kamchatnov. New approach to periodic solutions of integrable equations and nonlinear theory of modulational instability

PHYSICS REPORTS
A Review Section of Physics Letters

Aims and scope: Physics Reports keeps the active physicist up-to-date on developments in a wide range of topics by publishing timely reviews which are more extensive than just literature surveys but normally less than a full monograph. Each Report deals with one specific subject. These reviews are specialist in nature but contain enough introductory material to make the main points intelligible to a non-specialist. The reader will not only be able to distinguish important developments and trends but will also find a sufficient number of references to the original literature.

Abstracted/indexed in: Current Contents: Physical, Chemical & Earth Sciences/INSPEC/Chemical Abstracts.

North-Holland, an imprint of Elsevier Science

PHYSICS REPORTS

REPORT DOCUMENTATION PAGE

1. AGENCY USE ONLY (Leave Blank)	2. REPORT DATE 30 Sep 01	3. REPORT DYPE AND DATES COVERED Final 22 June 98 – 30 Sep 01

4. TITLE AND SUBTITLE
Proceedings of the 2000 Physical Acoustics Summer School: Volume III. Background Materials

5. FUNDING NUMBERS
PE 61153N
G N00014-98-1-0044

6. AUTHOR(S)
Henry E. Bass and Elizabeth A. Furr

7. PERFORMING ORGANIZATION NAME(S) AND ADDRESS(ES)
Jamie L. Whitten National Center for Physical Acoustics
The University of Mississippi
University, MS 38677

8. PERFORMING ORGANIZATION REPORT NUMBER

9. SPONSORING / MONITORING AGENCY NAME(S) AND ADDRESS(ES)
Office of Naval Research
ONR 331
800 North Quincy Street
Arlington, VA 22217-5660

10. SPONSORING / MONITORING AGENCY REPORT NUMBER

11. SUPPLEMENTARY NOTES

12a. DISTRIBUTION / AVAILABILITY STATEMENT
Approved for public release; Distribution unlimited

12b. DISTRIBUTION CODE

13. ABSTRACT (Maximum 200 words)

Volume I of the Proceedings of the 2000 Physical Acoustics Summer School contains verbatim transcriptions of the lectures given at the summer school. Volume II of these proceedings contains copies of the transparencies used by the lecturers and Volume III contains background materials that were sent to student and discussion leader participants prior to the summer school.

14. SUBJECT TERMS Physical Acoustics, Nonlinear Acoustics, Acoustics Demonstrations, Noise and Sensors, Resonant Ultrasound Spectroscopy, Atmospheric and Meteorological Acoustics, Thermoacoustics, Medical Applications of Acoustics, Sonoluminescence

15. NUMBER OF PAGES
154

16. PRICE CODE

17. SECURITY CLASSIFICATION OF REPORT UNCLASSIFIED	18. SECURITY CLASSIFICATION OF THIS PAGE UNCLASSIFIED	19. SECURITY CLASSIFICATION OF ABSTRACT UNCLASSIFIED	20. LIMITATION OF ABSTRACT